Multi-carrier waveforms for 5G and beyond systems: from power amplifier impairments to energy efficiency enhancement

Hmaied Shaiek

Conservatoire National des Arts et Métiers | le cnam

École doctorale : SMI - Sciences des Métiers de l'Ingénieur $n°432$

Habilitation à Diriger des Recherches
Spécialité Télécommunications

Multi-carrier waveforms for 5G and beyond systems: from PA impairments to energy efficiency enhancement

Presented by

Hmaied SHAIEK

Defended on January 06^{th} 2022

Defense committee:

Reviewers:	Pr. Marie-Laure BOUCHERET	ENSEEIHT-Toulouse
	Pr. Jean-Pierre CANCES	University of Limoges
	Pr. Mohamed-Fadhel GHANNOUCHI	University of Calgary
Examinators:	Pr. Carlos-Faouzi BADER	ISEP-Paris
	Pr. Geneviève BAUDOIN	ESIEE-Paris
	Pr. Iyad DAYOUB	UPHF/INSA-H-d-H
	Pr. Mérouane DEBBAH	Huawei-Paris
Advisor:	Pr. Daniel ROVIRAS	CNAM-Paris

CEDRIC Laboratory (EA4629), LAETITIA Team

Acknowledgements

Writing this thesis is a very interesting and very fruitful experience, which allowed me to realize the difficulty of the synthesis exercise, especially when it relates to diversified activities ranging from teaching to research, including administrative responsibilities. After a brief overview of the research activities carried out during my PhD thesis, this synthesis exercise allowed me to establish the common thread of the research activities and scientific collaborations carried out since my arrival at CNAM in February 2011.

After a decade of work, exchanges, and collaborations, I would like to thank all the colleagues, researchers, administrative-staff, PhD students and technicians of the LAETITIA team of the CEDRIC laboratory and of the electrical engineering department of CNAM. I have had a lot of fun working with you and I have learned a lot, both scientifically and humanly, from the discussions I have had with each of you.

I would like to thank the reviewers on this work: Prof. Marie-Laure Boucheret, Prof. Mohamed-Fadhel Ghannouchi and Prof. Jean-Pierre Cances. It's also a great pleasure having: Prof. Geneviève Baudoin, Prof. Mérouane Debbah, Prof. Carlos-Faouzi Bader and Prof. Iyad Dayoub as examiners of my work. I have great admiration for the expertise of all the members of my jury, especially in the fields those corresponding to my research activities. I hope you will find pleasure in reading this report.

This work would not have happened without the help and support of several people to whom I wish to express my gratitude here.

To begin with, I have a hard time finding the words to thank Daniel, who has supported me in this process. Daniel, you know how much I appreciate working with you, for your human and scientific qualities, your efficiency, and the confidence you placed in me when I arrived at the laboratory. You have helped me a lot, advised me and I am very grateful to you.

I take this opportunity to thank colleagues with whom I have had the opportunity to work more closely in my department and laboratory. I would particularly like to thank Iness Ahriz, Mylène Pischellla, Anne-Laure Billabert, Catherine Algani, Michel Terré, Christophe Alexandre, Pascal Chevalier, Didier Le Ruyet, Christian Pautot and Pierre Provent. Colleagues who mean a lot to me, I thank my office colleague Salim Faci, my close friends Ali Dziri and Yahia Medjahdi and my dear Tarek Raissi.

This decade has enabled me to develop my research activities, also through the supervision of several PhD students and master's students. I thank very much Hanen, Hayfa, Xinying, Meryem, Krishna, the three Khaled: Tahkoubit, Tani, Ramdani and Saidou. I wish them every success in their personal and professional lives.

This work would not have seen the light without constant family support. To begin, I have a hard time finding the words to pay tribute to my father who passed away in 2017. Also, I thank very much my mother for her daily encouragement. I also thank my wife, my two princesses, my sister, and my brothers for everything you bring. Lobna, thank you for your support, for your understanding and for your patience throughout these last years.

Contents

List of Figures

List of Tables

Acronyms

Acronyms

3GPP 3^{rd} Generation Partnership Project

4G 4^{th} Generation

5G 5^{th} Generation

6G 6^{th} Generation

ACCENT5 Advanced Waveforms, MAC Design and Dynamic Radio Resource Allocation for Device-to-Device in 5G Wireless Networks

ACE Active Constellation Extension

ACPR Adjacent Channel Power Ratio

ADC Analog to Digital Converter

AI Artificial Intelligence

AM/AM Amplitude Modulation to Amplitude Modulation

AM/PM Amplitude Modulation to Phase Modulation

ANR Agence Nationale de la Recherche

ATOME5+ OptimisAtion de l'efficacité énergéTique des formes d'Ondes Multi-portEuses 5G+ en présence d'imperfections RF dans un contexte MIMO et massive MIMO

AWGN Additive White Gaussian Noise

BER Bit Error Rate

BF-OFDM Block-Filtered OFDM

BS Base Station

C3 Communications Cognitives et Coopératives dans les réseaux ad-hoc sans fil

CCDF Complementary Cumulative Distribution Function

C-MTC Critical Machine Type Communications

CP Cyclic Prefix

CS Cyclo Stationary

CSI Channel State Information

DAC Digital to Analog Converter

DC Direct Current

DFT Discrete Fourier Transform

DL Down Link

DoF Degrees of Freedom

DPD Digital Pre-Distortion

DSLM Dispersive SeLective Mapping

DSP Digital Signal Processing

DT Data Tone

eMBB enhanced Mobile BroadBand

EMPhAtiC Enhanced Multicarrier techniques for Professional Ad-hoc and cell-based Communications

ETSI European Telecommunications Standards Institute

EVM Error Vector Magnitude

FBMC-OQAM Filter Bank MultiCarrier with Offset Quadrature Amplitude Modulation

FBMC-QAM Filter Bank MultiCarrier with Quadrature Amplitude Modulation

FCC Federal Communication Commission

FFT Fast Fourier Transform

FFT-FBMC Fast Fourier Transform FBMC

FIR Finite Impulse Response

FMT Filtered MultiTone

f-OFDM filtered-OFDM

FPGA Field-Programmable Gate Array

Fresh Frequency shift

FSE Fractionally Spaced Equalization

FT Fourier Transform

FTN Faster Than Nyquist

GD Gradient Descent

GFDM Generalized Frequency Division Multiplexing

IB In-Band

IBO Input Back Off

ICI Inter-Carrier Interference

IDFT Inverse Discrete Fourier Transform

IDP Iterative Dichotomy PAPR

IFFT Inverse Fast Fourier Transform

IIR Infinite Impulse Response

INI Inter Numerology Interference

ISI Inter-Symbol Interference

ITU International Telecommunication Union

IU Interfering User

KPI Key Performance Indicators

LE Linear Equalizer

LINC LInear amplification using Nonlinear Components

LTE Long Term Evolution

LVDM Lagrange Vandermonde Division Multiplexing

MESANGES Metasurface-based Electronically Steerable Antenna arrays for Next Generation EHF Systems

MGF Moment Generating Function

MIMO Multiple Input Multiple Output

MLP Multi-Layer Perceptron

mMTC massive Machine Type Communications

mmWaves millimeter Waves

MSE Mean Square Error

MU Multi User

MUI Multi User Interference

MP Memory Polynomial

MWF Multi-Carrier Waveform

NL Non Linear

NN Neural Network

NR New Radio

NSOC Non-Second Order Circular

OBO Output-Back-Off

OFDM Orthogonal Frequency Division Multiplexing

OOB Out-Of-Band

OQAM Offset Quadrature Amplitude Modulation

OTFS Orthogonal Time Frequency Space

P2JO Ping-Pong Joint Optimization

PA Power Amplifier

PAE Power Added Efficiency

PAM Pulse Amplitude Modulation

PAPR Peak to Average Power Ratio

PCB Printed Circuit Boards

PMR Professional Mobile Radio

POCS Projection Onto Convex Sets

PPDR Public Protection and Disaster Relief

PRT Peak Reserved Tones

PSD Power Spectral Density

PTS Partial Transmit Sequence

QAM Quadrature Amplitude Modulation

QCQP Quadratically Constrained Quadratic Programs

QR Quasi-Rectilinear

RB Resource Block

RF Radio Frequency

RIS Reconfigurable Intelligent Surface

RTFs Room Transfer Functions

Rx Receiver

SC Sub Carrier

SCS Sub Carrier Spacing

SDR Software Defined Radio

SE Spectral Efficiency

SEL Soft Envelop Limiter

SER Symbol Error Rate

SI Side Information

SISO Single Input Single Output

SLM SeLective Mapping

SNR Signal to Noise Ratio

SO Second Order

SS Spectrum Sharing

SSD Solid State Disk

SSE Symbol Spaced Equalization

SSPA Solid State Power Amplifier

SVD Singular Value Decomposition

TEDS Tetra Enhanced Data Service

TETRA TErrestrial Trunked RAdio

TI Tone Injection

TR Tone Reservation

TSLM Treillis based SeLective Mapping

TWTA Travelling Wave Tube Amplifier

Tx Transmitter

UF-OFDM Universal Filtered OFDM

UHF Ultra High Frequency

UI User of Interest

UL Up Link

URLLC Ultra-Reliable and Low Latency Communications

U.S. United States of America

USRP Universal Software Radio Peripherals

WCP-COQAM Windowed Cyclic Prefix-based Circular-OQAM

WL Widely Linear

WOLA-OFDM Weighted Overlap and Add OFDM

WONG5 Waveforms MOdels for Machine Type Communication inteGrating 5G Networks

ZF Zero Forcing

ZP Zero Padding

Short introduction

This report draws my career as associate professor at Conservatoire National des Arts et Métiers (CNAM) since 2011. This document is structured in two parts. The first part consists of one chapter: chapter 1. This chapter is an extended CV presenting in addition to some personal information, my education, my professional experience, my administrative responsibilities, and my teaching activities. In this chapter, I will also present various information about my research activities, namely the supervision, publications, collaborations as well as the research projects in which I have been involved. The second part of this report corresponds to my research thesis. This part is structured in six chapters:

- In chapter 2, I will present the research activities carried out since 2003. First, I will review my contributions in the field of acoustics and digital audio to optimize the performance of high-fidelity loudspeaker systems by digital signal processing. In the second part of chapter 2, I will give an overview of the research activities carried at CNAM since 2011. During this decade I have been working on post-Orthogonal Frequency Division Multiplexing (OFDM) Multi-Carrier Waveforms (MWFs) for 5G and beyond systems, with important efforts to characterize and mitigate power amplifier (PA) distortions in Single Input Single Output (SISO) and massive Multiple Input Multiple Output (MIMO) scenarios. For each research activity, I will present the projects under which the work has been carried, along with the different collaborations carried out, the main achievements and related publications.

- The third chapter introduces my contribution to the efforts made to find the best candidate post-OFDM waveform for 5G. I will present a comparative study of many MWFs based on different key performance indicators (KPI), that suits well to 5G and beyond requirements. The interest of Filter Band Multi Carrier with Offset Quadrature Amplitude Modulation (FBMC-OQAM), in terms of spectral localization and robustness to asynchronous user access, has prompted us to work on advanced equalization structures for this MWF in the presence of frequency selective channels and mixed numerology.

- The time domain signals generated by the vast majority of the MWFs candidate for 5G exhibit significant fluctuations in instantaneous power, characterized by the Peak to Average Power Ratio (PAPR). This characteristic makes these MWFs very sensitive to the non-linearities induced by the PA. In Chapter 4, I will present the studies carried out to characterize the In-Band (IB) and Out-Of-Band (OOB) distortions induced by memoryless measured or modeled PA. A great originality of this contribution is its applicability to most of the MWFs candidate for 5G systems in presence of modeled or measured memoryless PAs.

- The high PAPR of MWFs strongly compromises the energy efficiency of 4G, 5G and beyond transceivers. In chapter 5, I will present the solutions that we proposed to improve the energy efficiency of several post-OFDM MWFs based transceivers. The first family of the proposed solutions aims to reduce the PAPR and/or pre-distort the signal before amplification in a dissociated or joint manner. The second approach that will be presented modifies the architecture of the PA and splits the multi-carrier signal into several sub-signals with lower PAPRs which can be amplified with better energy efficiency.

- Among the prominent technologies proposed to reach the 5G New Radio (NR) requirements, Massive MIMO and mixed numerology have been retained to support various configurations on top of OFDM waveform. In chapter 6, I will present two contributions to massive-MIMO systems. The first one is related to the analysis and cancellation of the interference caused by users using different numerologies in massive MIMO OFDM systems. The second contribution is the proposal of low complexity energy efficient emitter architecture combining MIMO precoding, PAPR reduction and Digital Pre-Distortion (DPD).

- Chapter 7: the last chapter of this report, will be dedicated to present the prospects and future directions of my research activities.

Part I

Part I: Summary of my career

Chapter 1

Curriculum Vitæ

1.1 Personal informations

First name, Name	Hmaied, SHAIEK
Born	April 29^{th}, 1979 in Menzel Abderrahmen (Tunisia)
Nationality	Tunisian & French
Address	Conservatoire National des Arts et Métiers Electrical engineering CEDRIC laboratory, LAETITIA team 292 Rue Saint-Martin 75141 Paris Cedex 03
Telephones	(+33) 1 40 27 24 99 (office) (+33) 6 30 89 05 89 (mobile)
Email address	hmaied.shaiek @cnam.fr
Web	https://cedric.cnam.fr/lab/en/author/shaiek/
Marital status	married, 2 children

Position since February 2011 : Associate professor at Conservatoire National des Arts et Métiers (CNAM)

1.2 Strong points with some indicators

- Contribution to the development of "La Sphère": the first full range and digitally controlled coaxial loudspeaker system (second INPI award in December 2006).
- Conversion of research activities, from the field of acoustics and digital audio to the field of digital communications applied to post-OFDM multi-carrier modulations.
- 2 co-supervised post-doctoral researchers, 6 co-supervised PhD students (2 defended in 2016 and 1 defended in 2019), 10 supervised and co-supervised master's students.
- 1 European FP7-STREP project $N°$318362 EMPhAtiC (2013-2015), 3 ANR projects: ACCENT5 (2014-2017) WONG5 (2015-2019) and MAESANGES (2021-2024), with a strong involvement in the setting up and coordination of the WONG5 project, 2 PHC projects : Utique C3 (2012-2014) and Tassili ATOME5+ (2018-2021), with very active participation in the setting up, administrative and scientific coordination of these projects.
- 17 publications in international peer-reviewed journals, 1 book chapter, 35 publications in international conferences.
- 3 patent filings with 1 extended to many countries.
- 8 projects deliverables.
- 617 citations, h-index[1]: 13, i10-index[2]: 17.
- Participation to 3 in thesis committees as co-supervisor.

[1] ref. Google Scholar, July 7^{th}2021
[2] ref. Google Scholar, June 15^{th}2021

- Participation to 3 selection committees for the recruitment of 1 associate professor and 2 research and teaching assistant positions (ATER).
- Several reviews of articles in international journals (IEEE Transactions on Signal Processing, IEEE Transactions on Vehicular Technology, IEEE Wireless Communication Letters, IEEE Communication Letters, IEEE Access).
- Participation to different teaching units, ranging from the first year of B.Sc. to the last year of master's degree. Modernization of some teaching units, given in French and in English.
- In charge of some teaching modules related to electronics and signal processing.
- Proposal, in collaboration with Pr. Daniel Roviras, of a Massive Online Open Access Course (MOOC) on "introduction to signal processing".
- In charge of 3 degrees at CNAM: 2 engineering degrees and 1 bachelor's degree.
- Doctoral supervision and research grant (PEDR) holder since September 2017.

1.3 Education

2003-2007 **PhD in acoustic and signal processing**
TELECOM Bretagne, Lab-STICC, UMR-3192 CNRS
Specialty: Physics and computer sciences

2002-2003 **Master degree in science and telecommunications technology**
Université de Bretagne occidentale (UBO)-TELECOM Bretagne
Option: Signal and circuits

1999-2002 **Electrical engineering degree**
Ecole nationale d'ingénieurs de Tunis (ENIT)
Option: Electronics and telecommunications

1.4 Professional experience

Since Feb. 2011 **Associate professor**
CNAM, Electrical engineering department
CEDRIC Laboratory (EA4629), LAETITIA team

Sept. 2010 Jan. 2011 **Postdoctoral researcher at CNRS**
LMA - Marseille (PA and SACADS teams)
- Study and design of a "broadband" listening and sound reproduction room (in collaboration with Guy Rabaud and Philippe Herzog)

2009-2010 **Assistant professor**
Laboratoire brestois de mécanique et des systèmes - ENIB
- Reducing the distortion of electrodynamic loudspeakers (in collaboration with Emmanuel Delaleau)

2007-2009 **Senior research engineer**
May - July 2009: Orange Labs-Lannion, TECH/OPERA team
- Objective and subjective evaluations of different headsets (in collaboration with Rozenn Nicol)
April 2007 - April 2009: Canon/Cabasse-Brest
- Transfer of technologies developed during my thesis

2007-2009 **Assistant professor**
TELECOM Bretagne - Signal and communications department

2003-2007 **PhD from TELECOM Bretagne**
Signal and communications department, in collaboration with Cabasse Acoustic Center

- *Title :* **Optimizing wide band co-axial loudspeaker systems using digital signal processing techniques**
- *Supervised by:* Jean-Marc Boucher
- *Defense date:* July 2^{nd}, 2007
- *Committee:*

President	Pr. Gilles Burel, UBO-Brest
Reviewer	Pr. Meriem Jaidane, ENIT-Tunisia
	Pr. Pascal Scalart, ENSSAT-Lannion
Examiner	Pr. Jean-Marc Boucher, TELECOM Bretagne
	Dr. Bernard Debail, Cabasse-Brest
	Pr. Philippe Herzog, CNRS-Marseille
Invited member	Dr. André Goalic, UBO-Brest
	Ing. Yvon Kerneis, Cabasse-Brest

1.5 Contribution to research and scientific projects

1.5.1 General context

In 2011, I joined CNAM, as an Associate Professor in electronics and signal processing. My research activities, carried within the CEDRIC laboratory, are related to the physical layer of radiocommunications systems with a special focus on performances analysis and comparison of OFDM and post-OFDM waveforms in 5G and beyond communications. In this context power amplifier nonlinearities were shown to severely impact the whole system performance in both SISO and MIMO scenarios. After deep analysis of power amplifier impairments, over many OFDM and post-OFDM waveforms, we have proposed different solutions based either on reducing the transmitted signal PAPR or on linearizing the power amplifier characteristics.

1.5.2 International projects

2020-2023 **ERASMUS+ program with Tunisian universities.**
CNAM submitted in January 2019 an ERASMUS+ exchange project, in partnership with several Tunisian universities, including the University of Carthage. This project was accepted in September 2020. As part of this project, hosting of master 2 and doctoral students are planned during the years 2022 and 2023. Also, I will be asked to spend a stay in Tunisia, to provide a seminar or a conference, related to my research activities.

2018-2021 **PHC-Tassili-ATOME5+ Project**
I contributed to the setting up of the Hubert Curien Partnership project (OptimisAtion de l'efficacité énergéTique des formes d'Ondes Multi-portEuses 5G+ en présence d'imperfections RF dans un contexte MIMO et massive MIMO) between the CEDRIC/LAETITIA team and the telecommunications laboratory at the University of Tlemcen, in Algeria. The objective of this project is to reduce the PAPR of post-OFDM multi-carrier modulations and compensate for power amplifier imperfections in MIMO and massive MIMO context, by using modern Deep Learning techniques.

A joint supervision of a PhD thesis has been initiated within the framework of this project: thesis of Meryem Benosman.

2013-2015 **FP7-STREP European project** $N°318362$ **EMPhAtiC**[3]
The aim of this project, involving thirteen partners, was to demonstrate the advantages of using filter bank based multi-carrier techniques: FBMC-OQAM, for allowing the coexistence between broad-band 4G/5G services with narrow-band legacy services dedicated to Professional Mobile Radio (PMR) applications. I worked on the reduction of FBMC-OQAM signals PAPR in the presence of nonlinear power amplifier. Our main contribution to this project was the adaptation of some PAPR reduction techniques proposed for OFDM: SLM and TR, by considering the overlapping between FBMC-OQAM symbols. The PhD of Krishna Bulusu was part of this project.

2011-2014 **PHC-Utique-C3 Project**
I contributed to the setting up of the Hubert-Curien Partnerships project (Communications Cognitives et Coopératives dans les réseaux ad-hoc sans fil) between the CEDRIC/LAETITIA team, the signals and systems laboratory of CentraleSupélec, the higher school of communications of Tunis (SUP'COM) and the national school of engineers of Tunis (ENIT). This project focuses on cognitive and cooperative communications in ad-hoc wireless networks. One aspect of this project was to study the impact of power amplifier non-linearities on multi-carrier systems (OFDM and FBMC-OQAM). The PhD of Hanen Bouhadda was carried out within the framework of this collaborative project.

1.5.3 National projects

2021-2024 **ANR MESANGES Project**
The MESANGES (Metasurface-based Electronically Steerable Antenna arrays for Next Generation EHF Systems) ANR project focuses on the use of mmWave frequencies for 5G+/6G/Wi-Fi systems. Our partners in this project are Orange, IEMN, CEA-Leti and INSA-IETR. More specifically, most of the partner's efforts will be made on demonstrating the benefits of coupling smart metasurface-based electronically steerable antenna arrays with dedicated hybrid multi-user beamforming algorithms. At CNAM, we will study beamforming solutions for the steering of the transmit and reflect arrays for both single and multi-user cases. I will participate to the supervision of the PhD student that will be recruited to work on these tasks.

2015-2019 **ANR WONG5 Project**[4]
I contributed to the setup and management of this ANR project. The objectives of the WONG5 project (Waveforms MOdels for Machine Type Communication inteGrating 5G Networks) are the study and proposal of the best suited waveform for the physical layer of Critical Machine Type Communication (C- MTC). Our partners in this project were THALES, CEA-Leti and CentraleSupélec-Rennes. My contributions to this project were as follows:

- Joint administrative and technical coordination of the project with Pr. Daniel ROVIRAS,
- Comparative study of more than fifteen post-OFDM waveform in a C-MTC context, in terms of complexity, frequency localization, spectral efficiency, latency, etc,
- Improvement of the energy efficiency of the best suited waveforms to C-MTC systems, by reducing the PAPR,

[3] https://www.ict-emphatic.eu/Europeanproject
[4] www.wong5.fr

- Development of a testbed, based on software defined radio, to select the best suited waveform for C-MTC systems.

During this project, I have co-supervised two postdoctoral researchers and four master students.

2014-2017 **ANR ACCENT5 Project**[5]
This ANR project (Advanced Waveforms, MAC Design and Dynamic Radio Resource Allocation for Device-to-Device in 5G Wireless Networks) focuses on the study of advanced waveforms for Device-to-Device (D2D) communications in 5G networks. CNAM was part of this project with THALES, CentraleSupélec-Rennes and Teamcast. I worked on workpackage 2 of this project for improving D2D Green aspects. More precisely, my contribution to this project was on the optimization of power amplifier performance for FBMC-OQAM waveforms. The optimization of power amplifier efficiency was carried out by reducing the FBMC-OQAM PAPR and/or linearizing the power amplifier characteristics. These studies were carried in the framework of Krishna's Bulusu PhD.

1.5.4 Projects submitted but not accepted for funding

Because PhD and Postdoctoral researchers are mostly funded by collaborative projects, since my arrival in CNAM, I had a great activity in proposing new academic and industrial projects. In addition to the above projects accepted and funded by national and international organizations, many proposals were prepared and submitted but not accepted. Among the collaborative submitted projects I will point out:

Oct. 2020 **MIMOSA:** (Multiple Input Multiple Output networks with diStributed Antennas), with CentraleSupelec-Rennes, Sequans and CEA-Leti (ANR project).

Oct. 2020 **ARoFOAV:** ARchitectures optiques intégrées robustes à des Formes d'Ondes AVancées, with CEA-Leti (ANR project).

Oct. 2018 **EC-RAN4IoT:** Efficient C-RAN dynamic architectures for IoT systems, with IRISA, Nokia and CEA-Leti (ANR project).

May. 2018 **RIMOW:** Rf Impairments Mitigation techniques for post-OFDM Waveforms, in collaboration with Mahindra-Ecole Centrale engineering school in India (CEFIPRA project).

Apr. 2017 **OPTIMUM:** OPTImisation de formes d'onde MUlti-porteuses en présence d'imperfections RF dans un contexte MIMO et Massive MIMO, with SUP'COM-Tunis and CentraleSupelec-Rennes (PHC-Utique project).

Feb. 2015 **SPECMORE:** SPectrum Efficiency and Coexistence for MObile Radio Emergency systems, with eleven European partners (CELTIC-PLUS European project).

May. 2014 **FUI PHYLAP:** PHYsical LAyer for Professional mobile radiocommunications, with Thales, Sequans, Silicom, LS telcom, Siradel and Télécom ParisTech (FUI project).

Feb. 2013 **OFLER:** OQAM-FBMC widely LinEar Receiver and time reversal, with Thales, INSA IETR and Silicom (ANR project).

Mar. 2012 **TRIoMPH:** TRIals of Multicarrier advanced PHysical layers for cognitive radio, in collaboration with thirteen European partners (FP7-STREP European project).

[5] https://anr.fr/Project-ANR-14-CE28-0026

1.6 Supervision

Postdoctoral researchers	PhD students	Master students
2	6	10

1.6.1 Postdoctoral researchers

Jan. 2018 - Oct. 2018 **Rafik Zayani**

Within the framework of the WONG5 project, I supervised Dr. Rafik Zayani who was in charge of realizing a testbed to compare the performance of the selected post-OFDM waveforms against users asynchronism, frequency offset and power amplifier nonlinearities. The proposed testbed was based on reconfigurable platforms (USRP NI-USRP-2942R device). The work carried out was highlighted by one journal paper and one conference paper.

Oct. 2016 - Sept. 2017 **Yahia Medjahdi**

I supervised Dr. Yahia Medjahdi who carried an exhaustive and comparative study of different waveforms candidates for C-MTC communications. This work was done within the framework of the WONG5 project. We carried out a critical study of fifteen post-OFDM waveforms based on different criterion, such as frequency localization, robustness to time asynchronism, frequency offset, complexity, latency, spectral efficiency, and sensitivity to power amplifier effects. This research has resulted in two journal papers and six conference papers.

1.6.2 PhD students

Since Jan. 2019 **Meryem Benosman**

- *Title:* **Optimization of the energy efficiency of post-OFDM waveforms, in the presence of power amplifiers, by reduction of the PAPR and digital pre-distortion**.
- *Supervision rate:* 40%.
- *Defense date:* scheduled for January 2022.
- *Co-supervised with:* Tlemcen university, Algeria.
- *Funded by:* PHC-Tassili ATOME5+ project.
- *Publications:* 1 conference paper.

Since Oct. 2017 **Khaled Tahkoubit**

- *Title:* **Study and techniques for reducing imperfections in the RF chain for post 5G multi-carrier waveforms**.
- *Supervision rate:* 60%.
- *Defense date:* scheduled for November 2021.
- *Co-supervised with:* Oran university, Algeria.
- *Funded by:* Algerian government.
- *Publications:* 1 journal paper, 2 conference papers.

Since Oct. 2018 **Xinying Cheng**

- *Title:* **Energy Efficiency enhancement for massive MIMO-OFDM systems with RF impairments**.
- *Supervision rate:* 40%.
- *Defense date:* October 11^{th}, 2021.

- *Committee:* Reviewers: Pr. Martine LIENARD (Lille University) and Pr. Luc DENEIRE (Côte d'Azur University). Examiners: Pr. Yves LOUET (CentraleSupélec) and Pr. Mohamed Slim ALOUINI (King Abdullah University of Science and Technology). Supervisors : Pr. Daniel Roviras (CNAM), Dr. Hmaied Shaiek (CNAM) and Dr. Rafik Zayani (ISI-Tunis).
- *Funded by:* French ministerial grant.
- *Publications:* 2 journal papers.

2015-2019 **Hayfa Fhima**

- *Title:* **Contributions of Widely Linear filtering to multi-carrier modulations based on filter banks (FBMC-OQAM)**.
- *Supervision rate:* 40%.
- *Defense date:* December 12^{th}, 2019.
- *Committee:* Reviewers: Pr. Tahar Ezzedine (INSAT) and Pr. Raoof Kosai (ENSIM). Examiners: Pr. Geneviève Baudoin (ESIEE) and Pr. Jamel Belhadj Taher (ENISO). Supervisors : Pr. Daniel Roviras (CNAM), Pr. Ridha Bouallegue (Supcom), Dr. Hmaied Shaiek (CNAM) and Dr. Rafik Zayani (ISI-Tunis).
- *Co-supervised with:* SUP'COM, Tunisia.
- *Funded by:* Tunisian government and WONG5 ANR project.
- *Publications:* 1 journal paper, 4 conference papers.
- *Actual position:* Associate professor at ISIT'COM, Hammem Sousse, Tunisia.

2013-2016 **Krishna Bulusu**

- *Title:* **Performance analysis and PAPR reduction techniques for Filter Bank based Multi-Carrier systems (FBMC-OQAM) with Non Linear Power Amplifiers**.
- *Supervision rate:* 60%.
- *Defense date:* April 29^{th}, 2016.
- *Committee:* Reviewers: Pr. Geneviève Baudoin (ESIEE) and Pr. Yves Louet (CentraleSupélec). Examiners: Ing. Laurent Martinod (CASSIDIAN), Pr. Jean-François Hélard (INSA-Rennes) and Dr. Rafik Zayani (ISI-Tunis). Supervisors: Pr. Daniel Roviras (CNAM) and Dr. Hmaied Shaiek (CNAM).
- *Funded by:* EMPhAtiC European project ICT $N°318362$ and ACCENT5 ANR project.
- *Publications:* 1 book chapter, 1 patent, 2 journal papers, 6 conference papers.
- *Actual position:* Associate professor at Mahindra-Ecole Centrale, Hayderabad, India.

2013-2016 **Hanen Bouhadda**

- *Title:* **Study of the impacts of non-linearities in FBMC-OQAM systems**.
- *Supervision rate:* 40%.
- *Defense date:* March 22^{nd}, 2016.
- *Committee:* Reviewers: Pr. Noureddine Hamdi (INSAT) and Pr. Raoof Kosai (ENSIM). Examiners: Pr. Geneviève Baudoin (ESIEE) and Pr. Ammar Bouallegue (ENIT). Supervisors: Pr. Daniel Roviras (CNAM), Pr. Ridha Bouallegue (Supcom), Dr. Hmaied Shaiek (CNAM) and Dr. Rafik Zayani (ISI-Tunis).
- *Co-supervised with:* SUP'COM school, Tunisia.
- *Funded by:* PHC-Utique C3 project.
- *Publications:* 1 journal paper, 4 conference papers.
- *Actual position:* Associate professor at SUP'COM Tunis.

1.6.3 Master students

Feb. 2021 **Khaled Ramdani**

- *Title:* **Study and implementation of auto-encoders for OFDM system in the presence of power amplifiers**.
- *Supervision rate:* 50%.
- *Funded by:* Algerian government.

Sept. 2019 **Xu Ouyang**

- *Title:* **Performance of CP-OFDM and WOLA-OFDM waveforms in 5G context with different numerologies**.
- *Supervision rate:* 100%.
- *Funded by:* WONG5 project.

Sept. 2018 **Xinying Cheng**

- *Title:* **Experimental testbed for post-OFDM Waveforms Performance**.
- *Supervision rate:* 50%.
- *Funded by:* WONG5 project.
- *Publications:* 1 journal paper, 1 conference paper.

Sept. 2018 **Xiotian Fu**

- *Title:* **Mitigating nonlinearity effects on post-OFDM waveforms caused by power amplifier**.
- *Supervision rate:* 50%.
- *Funded by:* WONG5 project.
- *Publications:* 1 journal paper, 1 conference paper.

Sept. 2017 **Yassmine Ben Afia**

- *Title:* **Joint PAPR reduction and linearization for post-OFDM waveforms**.
- *Supervision rate:* 50%.
- *Funded by:* CEDRIC laboratory.

Sept. 2017 **Khaled Tani**

- *Title:* **Post-OFDM waveform PAPR reduction, by SLM and TR methods**.
- *Supervision rate:* 50%.
- *Funded by:* Algerian government.
- *Publication:* 1 conference paper.

Sept. 2013 **Xueying Zhang**

- *Title:* **Application of Widely Linear processing techniques on Filter Bank based Multi-Carrier (FBMC) modulation**.
- *Supervision rate:* 50%.
- *Funded by:* CEDRIC laboratory.

Sept. 2012 **Saidou Sall**

- *Title:* **Performance of multi-carrier communications (OFDM/FBMC-OQAM) with nonlinear amplifiers in cognitive radio**.
- *Supervision rate:* 50%.
- *Funded by:* CEDRIC laboratory.
- *Publication:* 1 conference paper.

Jan. 2009 **Oussema Lengliz**

- *Title:* **Virtual bass synthesis**.
- *Supervision rate:* 100%.
- *Funded by:* ENIT-TELECOM Bretagne-Cabasse.

Jan. 2008 **Khaled Lakhdahar**

- *Title:* **Automatic room acoustic transfer function correction**.
- *Supervision rate:* 100%.
- *Funded by:* ENIT-TELECOM Bretagne-Cabasse.
- *Publication:* 1 conference paper.

1.7 Publications

Book chapters	Journal papers	Conference papers	Patents	Deliverables
1	17	35	3	8

1.7.1 Book chapter

[B1] K. Bulusu, **H. Shaiek**, D. Roviras, R. Zayani, and M. Renfors. "Power Amplifier Effects and Peak-to-Average Power Ratio Mitigation". Book title: "Orthogonal Waveforms and Filter Banks for Future Communications Systems". July 2017, Academic Press, Elsevier, pp. 451-480, (isbn: 978-0-12-810384-5).

1.7.2 Journal papers

[J17] K. Bulusu, **H. Shaiek**, and D. Roviras. "HPA Linearization for Next Generation Broadcasting Systems with Fast Convergence-Digital Predistortion". Accepted in IEEE Transactions on Broadcasting, pp. 1-9, April 2021. **[IF: 3.42]**.
[J16] H. Fhima, R. Zayani, **H. Shaiek**, D. Roviras, B. S. Cheng, and R Bouallegue. "Comparison of Linear, Widely Linear and Fresh Equalizers for FBMC-OQAM Systems with Different Numerologies". Wireless Pers Commun, June 2020. (doi: /10.1007/s11277-020-07615-5). **[IF: 1.06]**.
[J15] X. Cheng, R. Zayani, **H. Shaiek**, and D. Roviras. "Analysis and Cancellation of Mixed-Numerologies Interference for Massive MIMO-OFDM UL". IEEE Wireless Communications Letters, vol. 9(4), pp. 470-474, January 2020. (doi : 10.1109/LWC.2019.2959526). **[IF: 4.66]**.
[J14] **H. Shaiek**, R. Zayani, Y. Medjahdi, and D. Roviras. "Analytical Analysis of SER for Beyond 5G Post-OFDM Waveforms in Presence of High-Power Amplifiers". IEEE Access, vol. 7, pp. 29441-29452, 2019. (doi : 10.1109/ACCESS.2019.2900977) **[IF: 3.75]**.
[J13] X. Cheng, R. Zayani, **H. Shaiek**, and D. Roviras. "Inter-Numerology Interference Analysis and Cancellation for Massive MIMO-OFDM Downlink Systems". IEEE Access, vol. 7, pp. 177164-177176, 2019. (doi : 10.1109/ACCESS.2019.2957194). **[IF: 3.75]**.
[J12] R. Zayani, **H. Shaiek**, and D. Roviras. "PAPR-Aware Massive MIMO-OFDM Downlink". IEEE Access 2019, vol. 7, pp. 25474-25484, 2019. (doi : 10.1109/ACCESS.2019.2900128). **[IF: 3.75]**.
[J11] K. Tahkoubit, A. P. Adda, **H. Shaiek**, and D. Roviras. "Iterative Dichotomy PAPR Reduction Method for Multicarrier Waveforms". IEEE Communications Letters, pp. 2073-2076, 2019. (doi:

10.1109/LCOMM.2019.2935439). **[IF: 4.66]**.
[J10] R. Zayani, **H. Shaiek**, and D. Roviras. "Efficient Precoding for Massive MIMO Downlink Under PA Nonlinearities". IEEE Communications Letters, pp. 1611-1615, 2019. (doi :10.1109/LCOMM.2019.2924001). **[IF: 4.66]**.
[J9] R. Zayani, **H. Shaiek**, and D. Roviras. "Ping-Pong Joint Optimization of PAPR Reduction and HPA Linearization in OFDM Systems". IEEE Transactions on Broadcasting, pp. 1-8, 2019, (doi:10.1109/TBC.2018.2855664). **[IF: 3.42]**.
[J8] R. Zayani, **H. Shaiek**, X. Cheng, X. Fu, C. Alexandre, and D. Roviras. "Experimental Testbed of post-OFDM Waveforms Toward Future Wireless Networks". IEEE Access, vol. 6(1), pp. 1-17, 2018, (doi:10.1109/ACCESS.2018.2879375). **[IF: 3.75]**.
[J7] Y. Medjahdi, S. Traverso, R. Gerzaguet, **H. Shaiek**, R. Zayani, D. David , R. Zakaria, J. B Doré, M. Ben Mabrouk, D. Le Ruyet, Y. Loüet, and D. Roviras. "On the Road to 5G: Comparative Study of Physical Layer in MTC Context". IEEE Access, vol. 5(1), pp. 26556 - 26581, 2017, (doi:10.1109/ACCESS.2017.2774002). **[IF: 3.75]**.
[J6] R. Zayani, **H. Shaiek**, D. Roviras, and Y. Medjahdi. "BER analysis of FBMC-OQAM systems with Phase Estimation Error". IET Communications, vol. 11(15), pp. 2269-2273, 2017. (10.1049/iet-com.2017.0646). **[IF: 1.67]**.
[J5] K. Bulusu, **H. Shaiek**, and D. Roviras. "Reducing the PAPR in FBMC-OQAM systems with Low Latency Trellis-based SLM Technique". EURASIP Journal on Advances in Signal Processing, pp. 1-18, 2016, (doi:10.1186/s13634-016-0429-9). **[IF: 1.14]**.
[J4] K. Bulusu, M. Renfors, J. Yli-Kaakinen, **H. Shaiek**, and D. Roviras. "Enhanced Multicarrier Techniques for Narrowband and Broadband PMR Coexistence". Transactions on Emerging Telecommunications Technologies, pp. 1-14, 2016, (doi:10.1002/ett.3056). **[IF: 1.60]**.
[J3] R. Zayani, **H. Shaiek**, D. Roviras, and Y. Medjahdi. "Closed-form BER expression for (QAM or OQAM) based OFDM system with HPA nonlinearity over Rayleigh fading channel". IEEE Wireless Communications Letters, pp. 1-4, 2015, (doi:10.1109/LWC.2014.2365023). **[IF: 4.66]**.
[J2] H. Bouhadda, **H. Shaiek**, D. Roviras, R. Zayani, Y. Medjahdi, and R. Bouallegue. "Theoretical analysis of BER performance of non-linearly amplified FBMC/OQAM and OFDM signals". EURASIP Journal on Advances in Signal Processing, pp. 1-16, 2014, (doi:10.1186/1687-6180-2014-60). **[IF: 1.14]**.
[J1] **H. Shaiek** and J. M. Boucher. "Optimizing the Directivity of Multiway Loudspeaker Systems". EURASIP Journal on Audio, Speech, and Music Processing. pp. 1-11, 2010 (doi :10.1155/2010/928439). **[IF: 1.29]**.

1.7.3 Conference papers

[C35] M. Benosman, **H. Shaiek**, Y. Bendimerad, R. Zayani, D. Roviras, and F. Bendimerad. "Low Complexity Neural Network based digital predistortion for Memory Power Amplifiers". In MSPN, Virtual, October 2020.
[C34] K. Tahkoubit, **H. Shaiek**, A. P. Adda, and D. Roviras. "Energy efficiency comparison of Outphasing and IDP techniques with non-linear power amplifiers". In IEEE CommNet, Virtual, September 2020.
[C33] K. Tahkoubit, A. P. Adda, **H. Shaiek** and D. Roviras. "PAPR reduction of BF-OFDM waveform using DFT-Spread technique". In IEEE ISWCS, Oulu, Finland, August 2019.
[C32] K. Bulusu, S. Maddila, **H. Shaiek**, and D. Roviras. "HPA Linearization for FBMC-OQAM Signals with Fast Convergence-Digital Predistortion". In IEEE ISWCS, Oulu, Finland, August 2019.
[C31] H. Fhima, **H. Shaiek**, R. Zayani, D. Roviras, B. Sens Chang, and R. Bouallegue. "Analysis of Widely Linear Equalization over Frequency Selective Channels with Multiple Interferences". In IEEE WiMOB, Limassol, Cyprus, October 2018.
[C30] Y. Medjahdi, Y. Loüet, D. Roviras, S. Traverso, R. Gerzaguet, **H. Shaiek**, R. Zayani, D. Demmer, R. Zakaria, J. Doré, M. Ben Mabrouk, and D. Le Ruyet. "Impact of selective channels on post-OFDM waveforms for 5G Machine Type Communications". In IEEE ISWCS, Portugal, Lisbon, August 2018.
[C29] Y. Loüet, D. Roviras, **H. Shaiek**, and R. Zayani. "Global power amplifier efficiency evaluation with PAPR reduction method for post-OFDM waveforms". In IEEE ISWCS, Lisbon, Portugal, August 2018.

[C28] R. Zayani, **H. Shaiek**, C. Alexandre, X. Cheng, X. Fu, and D. Roviras. "A Testbed for experimental performance evaluation of Multicarrier Waveforms in presence of RF PA". In IEEE ISWCS, Lisbon, Portugal, August 2018.
[C27] H. Fhima, B. Sens Chang, R. Zayani, **H. Shaiek**, D. Roviras, and R. Bouallegue. "Performance of Linear and Widely Linear Equalizers for FBMC/OQAM modulation". In IEEE ICT, Saint-Malo, France, June 2018.
[C26] K. Tani, Y. Medjahdi, **H. Shaiek**, R. Zayani, and D. Roviras. "PAPR reduction of post-OFDM waveforms contenders for 5G and Beyond using SLM and TR algorithms". In IEEE ICT, Saint-Malo, France, June 2018.
[C25] Y. Medjahdi, **H. Shaiek**, D. Roviras, Y. Loüet, and B. Mouna. "Non linear power amplifier effects on post-OFDM waveforms". In URSI AT-RASC, Spain, May 2018.
[C24] B. Sens Chang, C. Da Rocha, H. Fhima, R. Zayani, **H. Shaiek**, and D. Roviras. "On the Performance of a Widely Linear SC-FDE System Under Multiple Independent Interferences". In IEEE PIMRC, Montreal, Canada, October 2017.
[C23] Y. Medjahdi, D. David , R. Zayani, J. B. Doré, **H. Shaiek**, and D. Roviras. "Comparison of Promising Candidate Waveforms for 5G: WOLA-OFDM Versus BF-OFDM". In IEEE ISWCS, Bologna, Italy, August 2017.
[C22] H. Fhima, R. Zayani, **H. Shaiek**, D. Roviras, and B. Sens Chang. "Widely Linear Equalizer Performance with Multiple Independent Interferences". Greece, In IEEE ISCC, July 2017.
[C21] Y. Medjahdi, R. Zayani, **H. Shaiek**, and D. Roviras. "WOLA processing: a useful tool for windowed waveforms in 5G with relaxed synchronicity". In IEEE ICC International Workshop on the Main Trends in 5G Networks (MT5Gnet), Paris, France, May 2017.
[C20] R. Zayani, Y. Medjahdi, **H. Shaiek**, and D. Roviras. "WOLA-OFDM: a potential candidate for asynchronous 5G". In IEEE GLOBECOM, Washigton, USA, December 2016.
[C19] S. Bulusu, **H. Shaiek**, and D. Roviras. "PA Linearization of FBMC-OQAM Signals with Overlapped Recursive Error Correcting Predistortion". In IEEE ISWCS, Poznan, Poland, September 2016.
[C18] S. Bulusu, **H. Shaiek**, and D. Roviras. "Impact of HPA Non-linearity on Coexistence of FBMC-OQAM Systems with PMR/PPDR Systems". In IEEE VTC-Spring, Nanjing, China, May 2016.
[C17] H. Bouhadda, R. Zayani, **H. Shaiek**, D. Roviras, and R. Bouallegue. "Iterative receiver cancellation of nonlinear power amplifier distortion in FBMC/OQAM system". In IEEE Wimob, Abu Dhabi, EAU, October 2015.
[C16] S. Bulusu, **H. Shaiek**, and D. Roviras. "Reduction of PAPR of FBMC-OQAM Signals by Dispersive Tone Reservation Technique". In IEEE ISWCS, Brussels, Belgium, August 2015.
[C15] K. Bulusu, **H. Shaiek**, and D. Roviras. "Potency of Trellis-based SLM over symbol-by-symbol approach in reducing PAPR for FBMC-OQAM Signals". In IEEE ICC, London, UK, June 2015.
[C14] H. Bouhadda, R. Zayani, **H. Shaiek**, D. Roviras, and R. Bouallegue. "Receiver Technique for Detection and Correction of Nonlinear High Power Amplifier Distortion Errors in OFDM systems". In IEEE VTC-Spring, Glasgow, Scotland, May 2015.
[C13] K. Bulusu, **H. Shaiek**, and D. Roviras. "Prediction of Spectral Regrowth for FBMC-OQAM system using Cumulants". In IEEE Wimob, Larnaca, Cyprus, October 2014.
[C12] K. Bulusu, **H. Shaiek**, D. Roviras, and R. Zayani. "PAPR Reduction for FBMC-OQAM Systems using Dispersive SLM Technique". In IEEE ISWCS, Barcelona, Spain, August 2014.
[C11] H. Bouhadda, **H. Shaiek**, R. Zayani , Y. Medjahdi, D. Roviras, and R. Bouallegue. "Sensitivity analysis of FBMC signals to Non Linear phase distortion". In IEEE ICC-NSW, Sydney Australia, June 2014.
[C10] R. Zayani, Y. Medjahdi , H. Bouhadda, **H. Shaiek**. D. Roviras, and R. Bouallegue. "Adaptive Predistortion techniques for non-linearly amplified FBMC-OQAM signals". In IEEE VTC-Spring, Seoul, Korea, May 2014.
[C9] S. Sall, **H. Shaiek**, D. Roviras, and Y. Medjahdi. "Prediction of the nonlinear spectral regrowth in FBMC systems for cognitive radio context". In IEEE ISWCS 2013, Ilmenau, Germany, August 2013.
[C8] Y. Medjahdi, D. Le Ruyet, D. Roviras, **H. Shaiek**, and R. Zakaria. "On the Impact of the Prototype Filter on FBMC Sensitivity to Time Asynchronism". In IEEE ISWCS 2012, Paris, France, August 2012.
[C7] R. Nicol, **H. Shaiek**, and P. Rueff. "Objective and subjective assessment of various headphones for

spatial audio rendering". In Proceedings of Forum Acusticum 2011, Aalborg, Denmark, June 2011.
[C6] K. Lakhdhar, **H. Shaiek**, M. Jaidane, and J. M. Boucher. "Iterative equalization of room transfer function using biquadratic filters". In IEEE I2MTC, Singapore, May 2009.
[C5] G. Ndo, **H. Shaiek**, M. Jaidane, and J. M. Boucher. "An hybrid approach of low frequency room equalization: notch filters based on common acoustical pole modeling". In EUSIPCO, Poznan, Poland, September 2007.
[C4] **H. Shaiek**, B. Debail, Y. Kerneis, J. M. Boucher, and P. Y. Diquelou. "An optimized full-bandwidth 20Hz-20kHz digitally controlled co-axial source". Proceedings of the 121^{th} convention of the Audio Engineering Society, AES, preprint $n°6813$, San Francisco, USA, October 2006.
[C3] **H. Shaiek**, J. M. Boucher, B. Debail, and Y. Kerneis. "Design and real-time implementation of a digital filter bank dedicated to co-axial loudspeaker systems". In IEEE 3^{rd} ISIVC, Hammamet, Tunisia, September 2006.
[C2] **H. Shaiek**, B. Debail, J. M. Boucher, Y. Kerneis, and P. Y. Diquelou. "Enhanced control of sound field radiated by co-axial loudspeaker systems using digital signal processing techniques". Proceedings of the 120^{th} convention of the Audio Engineering Society, AES preprint $n°6723$, Paris, France, May 2006.
[C1] B. Debail and **H. Shaiek**. "Radiated sound field analysis of loudspeaker systems: discrete geometrical distribution of circular membranes versus co-incident annular rings". Proceedings of the 119^{th} convention of the Audio Engineering Society, AES preprint $n°6583$, New York, USA, October 2006.

1.7.4 Patents

[P3] R. Zayani, **H. Shaiek**, D. Roviras, and K. Bulusu. "Method for conditioning a signal for amplification thereof, method for amplification, associated conditioning device and amplification device". PCT/FR2017/052845, October 2017.
[P2] P. Y. Diquelou, D. Kerneis, and **H. Shaiek**. "Method for developing correction filters for correcting the acoustic modes of a room". WO2012045927, October 2012.
[P1] **H. Shaiek**, B. Debail, and J. M. Boucher. "Activation signal filtering device for e.g. professional listening system, has digital filtering unit with channel separation unit under constraint, where separation unit has separator filters covering frequency band between channels". FR20060004533, May 2006.

1.7.5 Deliverables

[D8] R. Zayani, **H. Shaiek**, D. Roviras, C. Alexandre, and S. Traverso. "Experimental testbed of post-OFDM Waveforms". WONG5 Document Number D5.3, October 2019.
[D7] S. Traverso, R. Zayani, **H. Shaiek**, C. Alexandre, and D. Roviras. "Software Defined Radio demonstrator specifications". WONG5 Document Number D5.2, January 2019.
[D6] Y. Louet, A. Nafkha, **H. Shaiek**, R. Roviras and R. Zayani. "Overall power budget", WONG5 Document Number D3.3, May 2018.
[D5] Y. Louet, **H. Shaiek**, D Roviras, Y. Medjahdi, R. Zayani, and M. B. Mabrouk. "New methods to enhance the energy efficiency". WONG5 Document Number D3.2, October 2017.
[D4] **H. Shaiek**, D. Roviras, Y. Medjahdi, R. Zayani, M. Ben Mabrouk, and Y. Louet. "Performance of the candidate waveforms in the presence of power amplifier". WONG5 Document Number D3.1, April 2017.
[D3] Y. Medjahdi, S. Traverso, J-B. Doré, **H. Shaiek**, D. Roviras, R. Gerzaguet, R. Zayani, D. Demmer, P. Chevalier, Y. Louet, M. Ben Mabrouk, R. Zakaria, and D. Le Ruyet. "Critical and comparative study of waveforms in C-MTC context". WONG5 Document Number D2.1, January 2017.
[D2] M. Pischella, **H. Shaiek**, A. Cipriano, K. Bulusu, D. Le Ruyet, C. Bader, and O. Rousset. "Energy-efficient power controls and interference mitigation (first issue)". ACCENT5 Document Number D2.1, January 2016.
[D1] **H. Shaiek**, D. Roviras, K. Bulusu, M. Renfors, L. Martinod, M. Narandzic, L. Marijanovic, and S. Tomic. "Reduction of PAPR and non linearities effects". EMPhAtiC Document Number D3.3, September 2014.

1.7.6 White papers

[W1] M. Renfors, L. G. Baltar, N. Bartzoudis, D. Gregoratti, E. Kofidis, L. Martinod, A. Myrvoll, S. Nedic, D. Petrov, D. Raki, V. Ringset, and **H. Shaiek**, "Flexible and Spectrally Localized Waveform Processing for Next Generation Wireless Communications". White paper of the 3^{rd} work package of FP7 EMPHATIC project, April 2015.

1.7.7 PhD dissertations

[PHD1] **H. Shaiek**. "Optimizing wide band co-axial loudspeaker systems using digital signal processing techniques". TELECOM Bretagne, Brest, France, July 2007.

1.8 Scientific outreach

1.8.1 Collaborations

Since 2012, I participated to several research projects, which have enabled me to diversify my scientific collaborations with French and international partners.

Since Sept. 2011 — **Innov'Com laboratory, SUP'COM, Tunisia**.
This collaboration started in May 2011, with the setting up of the PHC-Utique C3 project, which made it possible to fund the stays in France of Hanen Bouhadda, of which I was the PhD co-supervisor. As part of this collaboration, Dr. Rafik Zayani: member of the Innov'Com laboratory of the SUP'COM school in Tunis, was invited to CNAM in 2013 and 2015, for a period of 6 months and we worked on the characterization and correction of non-linearities introduced by power amplifiers in FBMC-OQAM systems. Between April 2015 and January 2016, I coordinated, with the help of several members of the CEDRIC and Innov'Com laboratories, the organization of the ISW-5G winter school. In 2016, we started a second thesis jointly supervised by the two laboratories: thesis of Hayfa Fhima, on the application of Widely-linear filtering to quasi-rectilinear modulations of the FBMC-OQAM type.

2014-2016 — **Tampere University of Technology, Finland**.
As part of the European EMPhAtiC project, I worked closely with the team of Pr. Markku Renfors from Tampere University of Technology (TUT) on the reduction of PAPR and the effects of nonlinearities for FBMC-OQAM systems. I oversaw the 3.3 deliverable of this project. We continued this collaboration with a publication in Transactions on Emerging Telecommunications Technology, on the coexistence of narrowband PMR systems with FBMC-OQAM based broadband systems. This collaboration was crowned with the editing of Chapter 13 of the book "Orthogonal Waveforms and Filter Banks for Future Communications Systems", entitled "Power Amplifier Effects and Peak-to-Average Power Ratio Mitigation". In January 2016, I invited Pr. Marrku Renfors at ISW-5G Winter School.

2017-2019 — **Federal University of Technology Paraná, Curitiba, Brazil**.
Dr. Bruno Sens Chang: Associate Professor at the Federal University of Technology Paraná, Curitiba in Brazil is a former PhD student of the LAETITIA team. Dr. Sens Chang's thesis focused on the proposal of new precoding and equalization techniques for FBMC-OQAM system. I worked with Dr Chang, as part of Hayfa Fhima's PhD, to propose equalization structures suited to rectilinear or quasi-rectilinear signals such as OQAM signals. I invited Dr. Sens Chang for two months (February and March 2018), where we worked jointly on writing a paper to ICT'2018 conference.

Since Jan. 2018 — **Telecommunications laboratory of Tlemcen University, Algeria**.
I contributed to the elaboration of partnership projects, for funding the stays of PhD students in joint supervision with the university of Tlemcen. In January 2018, we won a PHC funded project named "Optimization of the energy efficiency of 5G Multi-carrier waveforms (ATOME5+). This collaboration started in January 2019, with the PhD of Meryem Benosman. I am co-supervising this PhD dealing with the application of AI-based techniques to reduce PAPR and correct RF impairments.

2016-2018 — **CentraleSupélec/IETR, Rennes**.

- I worked with Pr. Carlos BADER and several partners of the EMPhAtiC FP7 and ACCENT5 ANR projects on the writing of deliverables. Specifically, we co-worked on the study of candidate waveforms for 5G and beyond wireless communications in terms of coexistence capabilities.
- I worked with Pr. Yves Louet as part of task 3 of the ANR WONG5 project, on techniques for improving the energy efficiency of OFDM and post-OFDM waveforms. Within the framework of deliverable 3.3 of this project, we established a realistic power budget of a transmitter by taking into account OFDM and post-OFDM waveforms, PAPR reduction techniques complexities and realistic power amplifier DC power.

2016-2018 — **CEA-Leti, Grenoble**.
This collaboration began with the ANR WONG5 project in October 2015. I contributed to the critical comparative analysis of candidate waveforms for C-MTC communications. At CNAM, we worked on the implementation of many waveforms (CP-OFDM, WOLA-OFDM, UF-OFDM, FBMC-OQAM, FBMC-QAM, FFT-FBMC, WCP-COQAM) which were compared to the waveform proposed by CEA-Leti: the BF-OFDM. The comparison concerned several metrics, among which I can cite: the PSD, the complexity, the latency, the robustness against timing-offset and frequency-offset. In November 2020, I contributed, with Dr. Jean-Baptiste Doré and Dr. David Demmer, to the proposal of an ANR project for investigating the design of multi-user precoding schemes with partial channel state information (CSI) in cell free MIMO systems.

2016-2018 — **Thales Communications and Security (TCS), Gennevilliers**.
This collaboration, with Dr. Sylvain Traverso began in January 2016 and focused on a comparative analysis of candidate post-OFDM waveforms for C-MTC. TCS contributed to the implementation of the waveforms: f-OFDM, N-Continous OFDM and FMT. Then, we compared these waveforms with those studied by CNAM and also by the other partners involved in the ANR WONG5 project.

Since Sept. 2017 — **University of Science and Technology, Oran, Algeria**.
Since July 2017, Khaled Tahkoubit: PhD student from the university of sciences and technologies of Oran, contacted us to work together on proposing new techniques for reducing the RF impairments for 5G and beyond systems. We also had the opportunity to welcome his PhD supervisor, Pr. Ali Pacha, in our research laboratory. We then decided to begin a co-supervision of Khaled Tahkoubit's PhD. The defense of this thesis is scheduled in November 2021.

Since Sept. 2018 — **Mahindra-Ecole Centrale, Haydarabad, India**.
Dr. Krishna Bulusu: my second PhD student, joined Mahindra-Ecole Centrale engineering school in Hayderabad, India in September 2017, as an associate professor. He contacted us in January 2018, with a view to submitting a Franco-Indian partnership project, within the framework of the CEFIPRA program. The collaboration with Dr. Krishna Bulusu continued with further work on fast convergence PA linearization algorithms for FBMC-OQAM signals.

1.8.2 Distinctions

Since Sept. 2017 Doctoral supervision and research grant: Prime d'Encadrement Doctoral et de Recherche (PEDR), since September 2017.

Dec. 2006 Second intellectual property awards winner (organized by "la compagnie nationale des conseils en propriété industrielle"), for the project "Four-way coaxial loudspeaker driven by active digital signal processor", December 2016, Paris.

1.8.3 Reviewing activities

- **Journals:** IEEE Transactions on Signal Processing, IEEE Transactions on Vehicular Technology, IEEE Wireless Communication Letters, IEEE Communication Letters, IEEE Access, International Journal of Distributed Sensor Networks, Physical Communications.
- **Conferences:** IEEE VTC-Spring, IEEE ICC, IEEE ICCE and IEEE ISWCS, IEEE WCNC, IEEE PIMRC, ICT.
- **Technical Program Committee in conferences:**
  - IEEE IWCMC 2021,
  - ICT 2018-2020,
  - IEEE ICC 2017,
  - IEEE ISWCS 2012, 2016-2021,
  - IEEE VTC-Spring 2020.
- **Session chair:**
  - IEEE ISWCS 2014, Barcelona,
  - IEEE ISWCS 2016, Poznan,

1.8.4 Organization of scientific events

- I am a research topic editor of "Waveform Design for Beyond 5G Networks" in Frontiers in Communications and Networks Journal. The call was announced in October 2020 and the submission deadline is scheduled for June 22^{nd} 2021. https://www.frontiersin.org/research-topics/16638/waveform-design-for-beyond-5g-networks,
- I organized, with Pr. Daniel Roviras, a special session on Post-OFDM waveforms for 5G radio access technology. This special session was organized within the framework of the ISWCS 2017 conference in Bologna, http://iswcs2017.radionetworksgroup.org/.
- I organized, with Pr. Daniel Roviras, within the framework of the IEEE ISWCS 2016 conference in Poznań, http://iswcs2016.radiokomunikacja.edu.pl/ a special session on PAPR reduction and power amplifier pre-distortion for post-OFDM waveforms to be adopted for beyond 5G context.
- I organized, as general co-chair: ISW-5G http://www.supcom.mincom.tn/isw5g2016/: a winter school on post- waveforms OFDM for 5G. This school took place in Tunis from January 21^{st} to 22^{nd}, 2016 (150 participants).
- I was part of the organizing committee of the IEEE ISWCS 2012 conference https://web1.see.asso.fr/iswcs2012/images/call_for_paper_ISWCS2012_v5.pdf. This conference was organized by the CEDRIC/LAETITIA team from August 28^{th} to 31^{st}, 2012 at CNAM (320 participants).

1.8.5 Seminars

- "On the efficiency of post-OFDM waveforms in the presence of power amplifiers", university of Tlemcen, November 2019.
- "Presentation of WONG5 project", DGA-MI seminar on data processing and communications of drone systems, Bruz, May 2016.

1.8.6 Participation to PhD dissertation committees

I participated, as a co-supervisor, to the following PhD dissertation committees:

- **Hayfa Fhima:** in December 2019, "Contributions of Widely Linear filtering to multi-carrier modulations based on filter banks (FBMC-OQAM)".
- **Krishna Bulusu:** in April 2016, "Performance analysis and PAPR reduction techniques for Filter Bank based Multi-Carrier systems (FBMC-OQAM) with Non Linear Power Amplifiers".
- **Hanen Bouhadda:** in March 2016, "Study of the impacts of non-linearities in FBMC-OQAM systems".

1.8.7 Membership in selection committees

- In April 2021 and May 2020, I was part of the selection committees for a research and teaching assistant positions (ATER) in electronics and telecommunications at CNAM.
- In April 2014, I was a member of the selection committee for the recruitment of an associate professor in Communication, Electronics and Instrumentation at the University of Le Mans.

1.9 Teaching activities

1.9.1 Teaching activities at CNAM

Description of the provided teaching: At CNAM, I give courses ranging from the first year Bachelor (1^{st} year of Diplôme Universitaire de Technologies) to the last year of Master degrees. The provided teaching are courses, tutorials, practical works and tutored projects in electronics, signal processing and digital communications. Most of these courses are given in French and part of them are given in English. Part of these courses are also available online with video resources on Moodle. The students concerned belong to the following fields:

- Master's degree in radiocommunication techniques,
- Master's degree in mobile telecommunications systems,
- Master's degree in sciences, technologies, health with specialization in networks and telecommunications,
- Engineering degree in electronic systems, telecommunications, and computer science,
- Engineering degree in electronic systems and railway signaling,
- Bachelor's degree in telecommunications, in partnership with DongGuan University of Technology (DGUT),
- Bachelor's degree in electrical engineering and computer science.

Tab. 1.1 summarizes the teaching activities carried out at CNAM, since February 2011.

My average teaching load is about 245 hours/year, corresponding to 33% of classes, 38% of tutorials and 29% of labs and projects.

Topic	Language	Level	Classes	Tutorials	Projects
Advanced digital communications	FR	Master's	$55h$	$48h$	$30h$
Advanced techniques in analog and digital electronics	FR	Master's	–	–	$143h$
Analog signal processing	FR	B.Sc.	$120h$	$170h$	$77h$
Digital signal processing	FR+ENG	Master's	$193h$	$135h$	$90h$
Electronics	FR	B.Sc.	$216h$	$333h$	$89h$
Introduction to signal processing	FR	B.Sc.	$81h$	$85h$	$95h$
Microcontrollers	FR+ENG	B.Sc.	$186h$	$206h$	$222h$

Table 1.1: Summary of my teaching activities at CNAM.

Advanced digital communications This course focuses on mobile radio channels with a study of the main models used to characterize large scale and small-scale fading effects. Much of the course is dedicated to modeling mobile radio channels and studying fading laws such as Rayleigh, Rice and Nakagami. Theoretical analysis of the performance over Rayleigh fading channel with diversity is also carried.

Advances techniques in analog and digital electronics I am the coordinator of this teaching unit, which is based on labs and projects. Several topics are addressed in this unit. Of these subjects, I quote: (1) General study of transmission lines, crosstalk. (2) Spectral analysis with analog and digital approaches. (3) Channel coding. (4) Digital modulations. (5) Real-time digital filtering with DSP TMS320C6713. (6) Huffman codes. (7) Blind synchronization. (8) Implementation of OFDM waveform on MATLAB and on Software Defined Radio (SDR) platforms.

Analog signal processing Representation and signals classification based on energy and power is firstly introduced. Fourier transform, convolution, correlation are also studied. The emphasis is putted on duality between time and frequency domains. Filtering of analog signals is also hightailed, with demonstration examples.

Digital signal processing This course is an introduction to stationary random discrete signals. The concepts of autocorrelation/intercorrelation and power spectral density are introduced. Applications such as linear prediction, system identification, systems equalization are discussed. Then, an overview on gradient type algorithms is made.

Electronics This course is divided into two parts: the first one is related to digital electronics. However, the second one focusses on analog signals. The topics introduced in the first part are: combinatorial logic, sequential logic, temporal characteristics, study of medium integration circuits (counters and shift registers). The second part of the course introduces the basic concepts of electricity and fundamental theorems/methods for circuit analysis: Kirchhoff's laws, Thévnin's and Norton's theorems. Then, an analysis of 1^{st} and 2^{nd} order filters, based on elementary dipoles and operational amplifiers, using Bode diagrams is performed.

Introduction to signal processing Introduction to signal acquisition scheme, with an overview on Analog to Digital Converter (ADC), Digital to Analog Converter (DAC), sampling theorem, quantization noise, linear time invariant systems, digital convolution, Discrete Fourier Transform (DFT), Fast Fourier Transform (FFT), Finite Impulse Response (FIR) filters and Infinite Impulse Response (IIR) filters.

Micro-controllers The course starts with an introduction to the general organization of a microprocessor system architecture and internal operation (main buses, UALs, registers, memories, etc.). The practical work is based on the STM32F429 (ARM Cortex-M4) microcontroller. The evaluation board used is the Nucleo-144. This platform integrates some peripherals (push buttons, LEDs) as well as Arduino Uno and STMicroelectronics Morpho connectors.

Teaching related responsibilities: Since my arrival at CNAM, I have been responsible for the following teaching units:

- ELE008: Introduction to microcontrollers. I was actively involved in the modernization of this course, which was based on a 16-bit microcontroller: the 68HCS12 from Freescale. The new version of this course, proposed since September 2019, uses the STM32F429 (ARM Cortex-M4) microcontroller. The latter is equipped with a lot of features, in terms of input and output, and especially in terms of the variety of available evaluation platforms.
- ELE109: Advanced techniques in analog and digital electronics. I am responsible for the scientific coordination of this labs based unit, involving many colleagues from the electrical engineering department. I have actively participated in the evolution of the content of this unit intended for master's students.

1.9.2 Teaching activities outside CNAM

ENSTA-ParisTech: Since 2013, I have been involved, with Pr. Michel Terré, to taught a signal processing course for first year engineering students at ENSTA-ParisTech. Each year, I give 22 hours of tutorials and labs on: sampling, introduction to random signal processing, Fourier transform, FIR/IIR filtering and linear prediction.

ISEP: Since September 2017, I have been managing the "Signal acquisition and processing" course, intended for third-year engineering students in Wireless systems at ISEP. This course is taught in English for a volume equal to 45 hours/year. Topics covered in this course range from signal sampling to analysis of the correlation of stationary random signals, including Fourier transform and filtering. Particular emphasis is placed on the supervision and monitoring of students in tutored project mode.

ESIEE-Paris: Since April 2017, I have been responsible for the course entitled "Mathematical tools for signal processing", intended for students in the first year, specializing in telecommunications and networks at ESIEE-Paris. This course represents 30 hours of lessons, tutorials, and practical work. The main objective of this teaching unit is to introduce the tools and methods of analysis and processing of deterministic continuous-time and discrete-time signals.

CentraleSupélec: Since November 2018, I have been involved in a training session given by CentraleSupélec Paris, entitled digital signal processing: methods and techniques. This training is offered twice a year for experienced engineers working in electronics and data processing. My contribution lasts 1.5 hour for introducing adaptive filters, with a focus on the stochastic gradient algorithm (LMS) and the recursive least square algorithm (RLS).

1.9.3 Massive Online Open Access Course

In January 2015, I proposed, in collaboration with Pr. Daniel Roviras, the first session of a Massive Online Open Access Course (MOOC) on "introduction to signal processing" https://www.fun-mooc.fr/courses/CNAM/01008S02/session02/about. This MOOC is intended for students who wish to have an overview of graduate studies in the field of signal processing. This MOOC lasts six weeks. Each week consists of 5 to 6 video sequences followed by quizzes which allow learners to evaluate their achievements. At the end of each week, as well as at the end of the course, a graded assessment tests are offered. For

Session	Period	Participants
2015	from January 17^{th} to February 27^{th}	3388
2016	from February 15^{th} to March 27^{th}	4446
2017	from May 2^{nd} to June 12^{th}	4256
2018	from April 24^{th} to June 4^{th}	4004
Total		16294

Table 1.2: Information about the different MOOC sessions.

each week discussions are open on a dedicated forum. The weekly feedbacks and the main questions asked on the forums are addressed during a live hangout session.

Starting from an introduction to linear systems and filtering, we present time and frequency representation of signals with Fourier transform. Spectral analysis is introduced together with random signals. Next, we come to digital signal processing and its applications.

This MOOC was offered in four sessions, between January 2015 and June 2018. Tab. 1.2 summarizes some information about this MOOC. Based on data extracted from FUN[6] platform, it appeared that 40% of the participants to this MOOC are master 1 or 2 students, 20% are preparing Bachelor degrees and 10% are PhD students.

1.9.4 Teaching materials

Since 2011, I have been strongly involved in the educational life of the electrical engineering department at CNAM. I managed the development of two teaching units "ELE109: Advanced techniques in analog and digital electronics" and "ELE008: Introduction to microcontrollers", of which I am the manager and scientific coordinator. I have also prepared and edited materials, for courses, tutorials and practical works corresponding to the following topics:

- Advanced techniques in analog and digital electronics,
- Analog signal processing,
- Digital signal processing,
- Electronics,
- Introduction to signal processing,
- Microcontrollers.

1.9.5 Projects supervision and apprentices monitoring

Third-year engineering students in telecommunications and railway signaling at CNAM, prepare tutored projects for the study and development of prototypes meeting given specifications. These specifications are drawn up by the students and validated by the supervising teacher, who follows them up through progress meetings. Between 2017 and 2019, I followed two groups of engineering students from the previously mentioned CNAM engineering specializations.

Much of my teaching at CNAM is aimed at dual education system, combining apprenticeships in a company and vocational education at CNAM. This status requires the designation of a referent teacher who monitors the student's education, upon entering CNAM and until obtaining his diploma. The role of the referent teacher is to ensure the smooth running of the student's training, both academically and in terms of the adequacy between the missions carried out in this company and the diploma objectives. Since 2011, I follow an average of eight apprentices per year, between engineering and bachelor's degrees.

[6] https://www.fun-mooc.fr/fr/

1.10 Administrative responsibilities

Since Sept. 2019 I oversee CNAM professional bachelor's degree in sciences, technologies, health with a specialization in home automation and smart objects. Among my different tasks, I supervise the academic evolution of the syllabus, I preside the diplomas committees and I am the corresponding professor for the certification with French ministry of education (AERES).

Since Sept. 2019 I oversee CNAM degree in mechatronics, in agreement with the university of Poitiers. Among my different tasks, I supervise the academic evolution of the syllabus with my colleagues from the university of Poitiers, I preside the diplomas committees and I am the corresponding professor for the certification with the engineer title commission (CTI).

Since Sept. 2020 I oversee CNAM engineering degree in automation and robotics, with specializing in mechatronics. Among my different tasks, I supervise the academic evolution of the syllabus, I preside all national examinations (admission to the engineering school, diplomas committees) and I am the corresponding professor for the certification with the engineer title commission (CTI).

1.11 Elective mandates

Since May 2018 Elected member of the scientific council of the electrical engineering department.

Since Jan. 2018 Elected member of the scientific council of the CEDRIC laboratory.

Part II

Part II: Research activities and prospects

Chapter 2

Overview of my research activities

2.1 Introduction

In this chapter, I will give an overview of my research activities, before and after being associate professor. The first part will be dedicated to the research activities carried, between 2003 and 2010, as PhD student and as a research engineer in the field of acoustics and audio signal processing. The main contributions achieved, as well as related publications, made during this period will be presented.

The second part of this chapter will focus on all the research activities carried as associate professor at CNAM since February 2011. A general context of my research studies will be first introduced. Then, I will present the four topics over which I have been working during this decade. These topics are: (1) Comparative study of post-OFDM MWFs for 5G and beyond systems, (2) Theoretical analysis of IB and OOB PA distortions, (3) Proposal of signal processing and hybrid techniques to enhance PA efficiency and (4) Enhancement of the energy efficiency of OFDM based Massive-MIMO networks with mixed numerology. For each research topic, I will present the projects under which the work has been carried, along with the different collaborations carried out. I will also give an overview on the main achievements and related publications.

It's important to underline here that scientific and technical contributions for each of the previously mentioned research topics will be detailed in chapters 3, 4, 5 and 6.

2.2 PhD related research activities

2.2.1 Context

From October 2003 to July 2007, I prepared my PhD thesis with the Signal and Communications Department of TELECOM Bretagne, in collaboration with Cabasse Acoustic Center. This thesis dealt with the optimization of high-end multi-way loudspeaker systems radiation by using dedicated digital signal processing techniques. From April 2007 to February 2009, I worked as research engineer with Canon Inc. group. A summary of the scientific contributions achieved during the two periods is summarized in the following subsections.

2.2.2 Contributions

Free space optimization of the sound field radiated by a multi-way loudspeaker system: To reach this objective, we combined Cabasse knowhow in terms of electro-acoustical conception and advances in digital filtering applied to audio. Indeed, with more than 50 years' experience, Cabasse *R&D* engineers proposed in 2005, the first full range coaxial loudspeaker in the word. This system can reproduce the entire audio band extending from 20 Hz to 20 kHz with a well-controlled directivity. We have first studied the theoretical and measured sound field radiated by this loudspeaker system, with respect to a classical one, whose radiating surfaces are spatially spread-distributed. For this study, I have considered the two acoustic systems, given by Fig. 2.1. Each system is made up of three piston-like radiating surfaces embedded in an infinite flat baffle. System 1 is a source consisting of three coaxially mounted loudspeakers. System 2 is a source consisting of three radiating surfaces, which are spatially spread-distributed. The near fields radiated by the two acoustic systems at the level of two crossover frequencies: $f_1 = 800\ Hz$ and $f_2 = 4000\ Hz$, are given by Fig. 2.2. In the case of system 1 and for $f_1 = 800\ Hz$, the radiated waves are quasi-spherical with a decrease in sound pressure in $1/r$. At $f_2 = 4000\ Hz$, this system becomes more directional in its main axis while keeping a homogeneous

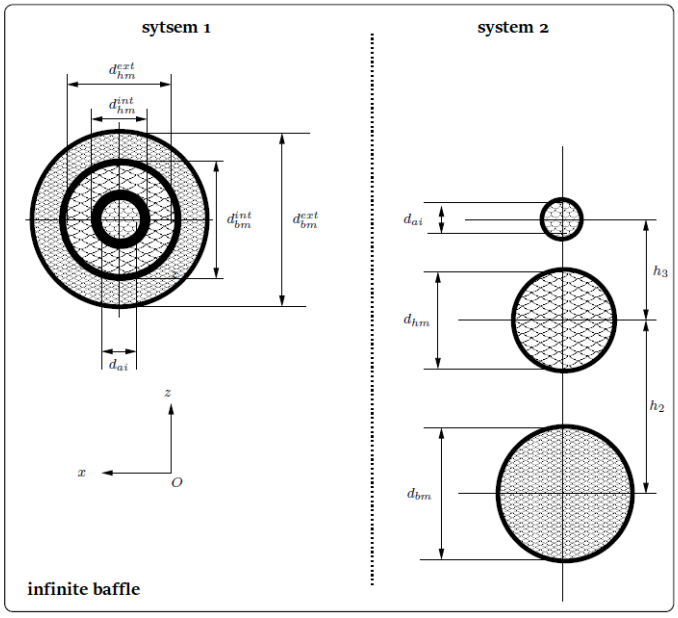

Figure 2.1: Three-way loudspeaker system.

radiation even in very close field ($r \leq 0.5m$). On the other hand, system 2 presents an asymmetric radiation with marked interference zones. The radiated field irregularities are more important in the near field region between 0.5 m and 1 m, where a shifting of 15 cm of the receiver can cause a variation of 25 dB in the amplitude of the radiated field. The accuracy of this theoretical study has been validated through measurements on real systems and published in a conference paper [7]. The reference coaxial loudspeaker system proposed by Cabasse still suffers from residual problems, such as imperfect phase alignment, frequency bands overlapping and non-flat on-axis frequency response. One of the main contributions of my PhD was to propose a dedicated digital filter bank to correct the residual imperfections of the coaxial loudspeaker system and enhance its performances in order to approach as well as possible the theoretical point source. The system model of the digitally controlled multi-way loudspeaker is given by Fig. 2.3.

The originality of the digital filter bank I developed, and validated on real systems, is that it ensures an enhanced control of the system directivity making it possible to correct possible radiation shifts over transducers' frequency overlap bands. The proposed algorithm is based on a complex weighting of the

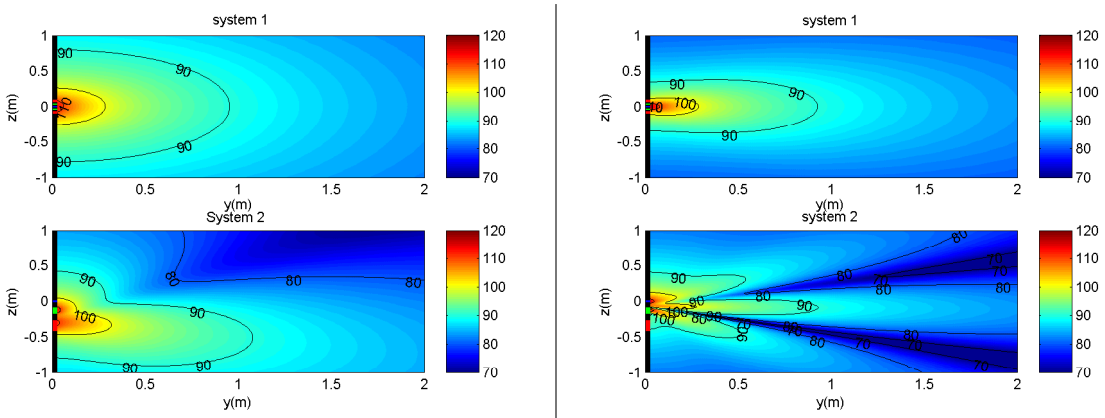

(a) $f_1 = 800\ Hz$. *(b)* $f_2 = 4000\ Hz$.

Figure 2.2: Fields radiated by the two models of acoustic systems.

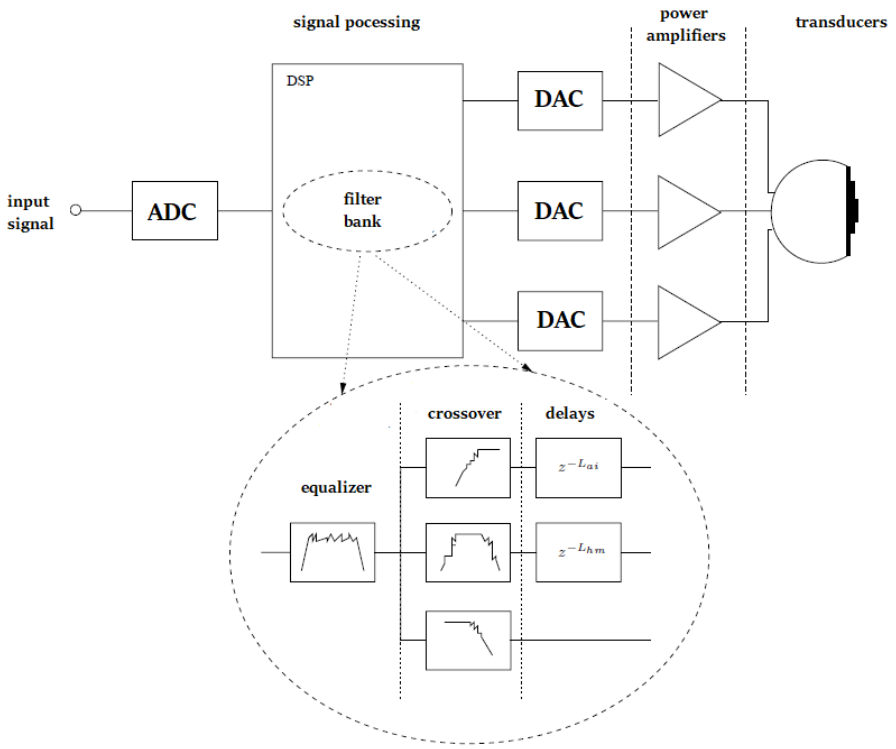

Figure 2.3: Digitally controlled co-axial loudspeaker system.

crossover frequency responses, to reach a given target in terms of radiation pattern or directivity index. The proposed algorithm was first patented [8] and then published in a conference and a journal papers [9, 10].

By comparing the radiation diagrams of Figs. 2.4 (a) and 2.4 (b), we note that the crossover filter optimization makes it possible to ensure a more homogeneous and progressive directivity.

Optimization of the sound field radiated by a multi-way loudspeaker system in a listening room: The second part of the optimization procedure is to enhance the sound field radiated by the multi-way loudspeaker system is related to the transfer brought by the listening room: equalization of the Room Transfer Functions (RTFs). Indeed, many researchers were concerned with the correction of multiple room reflections and acoustic reverberation. However, no universal solution has been adopted. In the context of my PhD the considered acoustic sources stimulate the very low frequencies room modes. I decided, first, to work on the design of adequate digital filters to compensate for room mode, in the low frequency part of the audio spectrum. This choice is based on the fact that the resonant modes of a listening room are well localized in low frequencies. The identification and correction of these modes, in a privileged listening area in the room, would therefore allow a significant improvement in the quality of the reproduced sound. The experimental protocol used for the measurement of RTF is given by Fig. 2.5. The proposed solution is a multiple-point low frequency compensation technique of the room modes. This approach consists in averaging the RTFs measured at different listening positions and to systematically detect the room modes, to finally correct them using cascaded second-order notch filters. After fixing the total number of resonances to be corrected P, each resonance i is controlled by a biquadratic cell $C^i(z)$. The equalizer $C(z)$ is so the cascade of P biquadratic cell: $C(z) = \prod_{i=1}^{P} C^i(z)$. where $C^i(z)$ is given by:

$$C^i(z) = \frac{b_0^i + b_1^i z^{-1} + b_2^i z^{-2}}{1 + a_1^i z^{-1} + a_2^i z^{-2}}. \tag{2.1}$$

The design of these filters is based on the method proposed by S. White [11], allowing to establish direct relations between a given room mode parameter and the transfer function coefficients a_i and b_j,

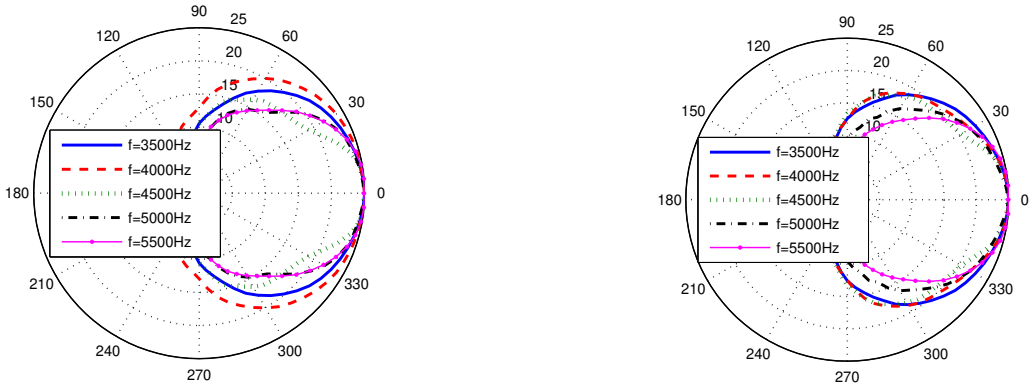

(a) Without optimization. *(b) With optimization.*

Figure 2.4: Directivity characteristics of the co-axial loudspeaker system after crossover filters optimization.

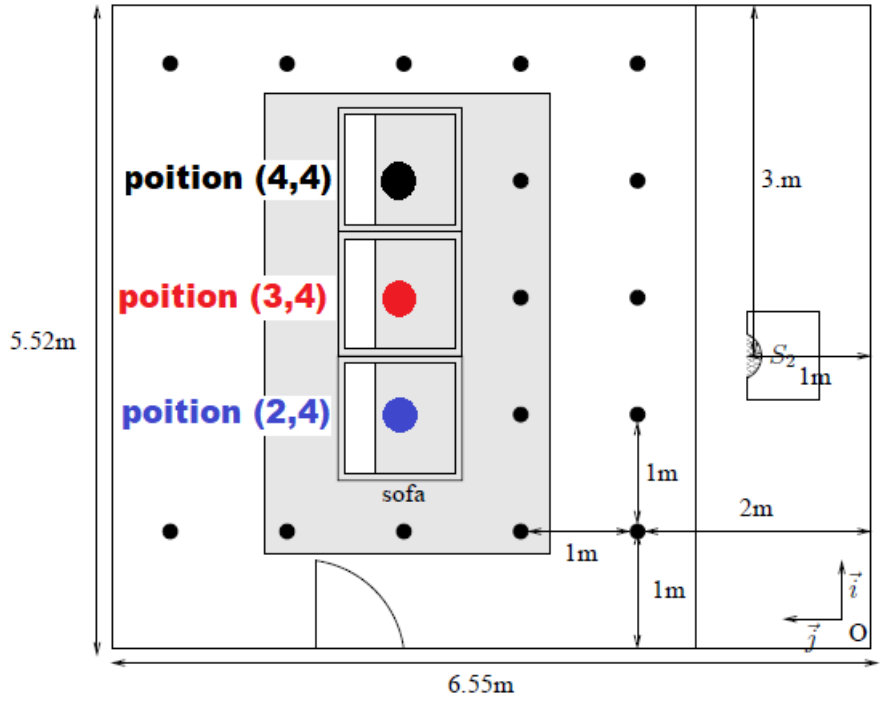

Figure 2.5: Experimental protocol for RTF measurements using a subwoofer with pass-band [20 Hz, 200 Hz].

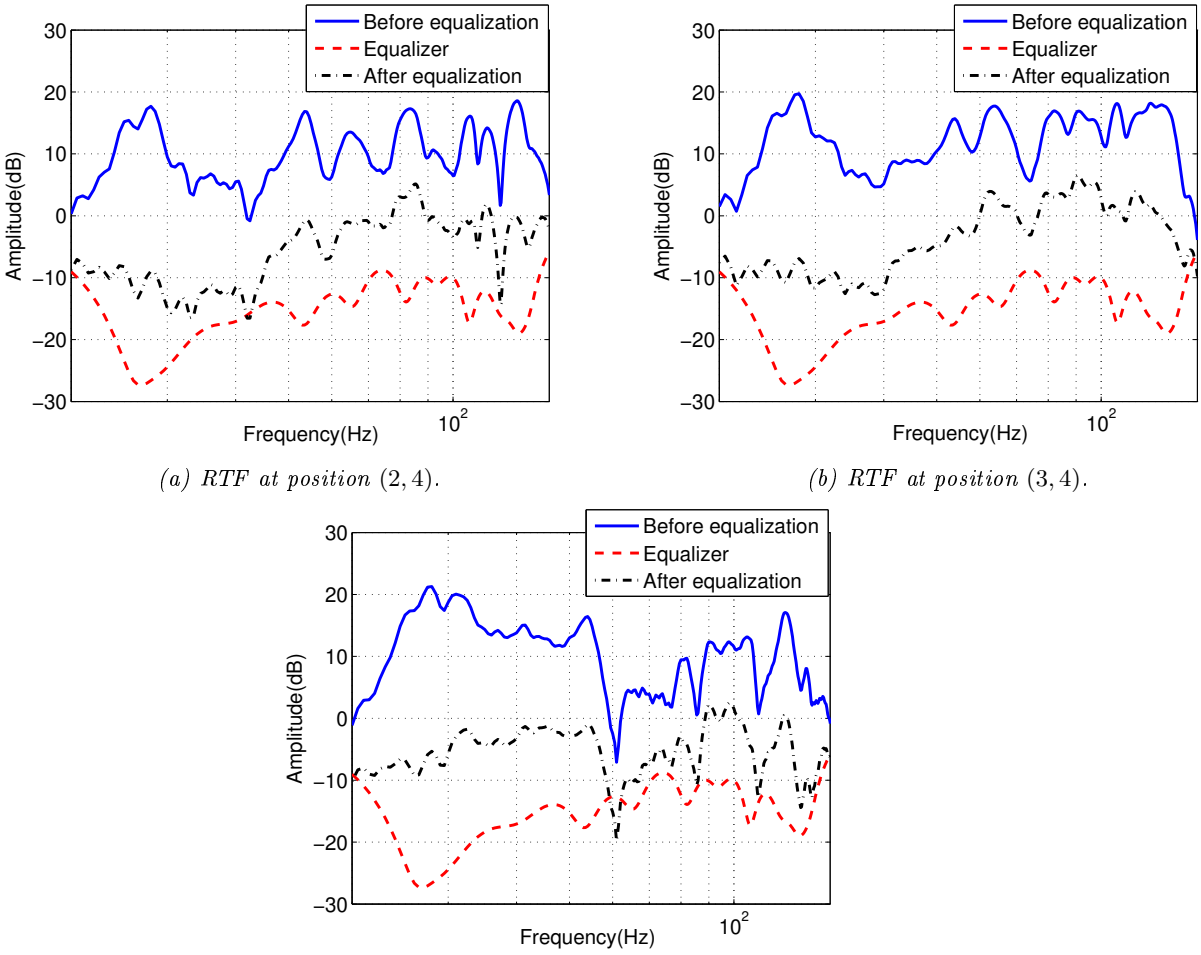

(a) RTF at position $(2, 4)$.

(b) RTF at position $(3, 4)$.

(c) RTF at position $(4, 4)$.

Figure 2.6: Multi-point low frequency equalization of RTF based on automated design of notch filters ($P = 11$).

($i = 1..2$ and $j = 0..2$) of a biquadratic cell. The originality of the proposed method, for multi-point RTF equalization, is that it allows an automated design of digital cascaded notch filters giving the possibility to correct the peaks that are common to all the room responses measured over a given listening area. From Fig. 2.6, we can see the results of an example compensating for the effects of room modes at the three selected positions on the sofa shown in Fig. 2.5. Indeed, the cascade of biquadratic cells reduces on average the gains of the resonant peaks common to the different positions over the selected listening zone. The results corresponding to the proposed algorithms where published in two conference papers [12, 13].

Implementation on DSP and evaluations tests: The goal being to lead to an industrial model, I carried out subjective tests to evaluate the proposed digital filtering over Cabasse coaxial loudspeakers. I started by characterizing the dispersion at the level of the loudspeaker's responses. Then, I implemented on a DSP [1] (Analog Devices DSP, ADSP-21369) all the digital filtering algorithms proposed (delays, crossover, equalization and enhanced directivity control). Finally, I carried out blind subjective evaluation tests to access the advantages of coupling the coaxial loudspeaker with the proposed digital processing proposed. This work was published in two conference papers [14, 15]. Then, I focused on the validation of an automatic room acoustic transfer function correction algorithm. A subjective evaluation

[1] Digital Signal Processor

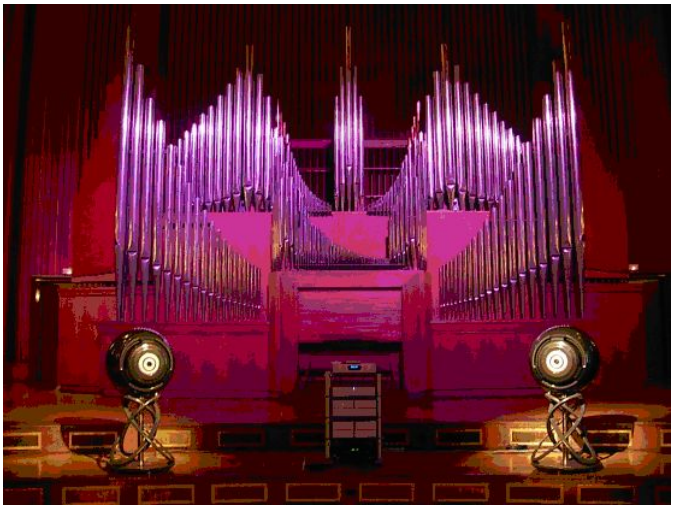

Figure 2.7: La Sphère prototype exhibited in Radio France studio 103.

of this algorithm, under different listening conditions and configurations, made it possible to confirm the robustness of the proposed method, patented in October 2012 [16]. Fig. 2.7 shows the prototype of "La Sphère": the first full range and digitally controlled coaxial loudspeaker system exhibited in Radio France studio 103.

2.3 Research activities at CNAM

2.3.1 Context

Each generation of mobile communication system has had great social and economic impacts on peoples and societies. Particularly, it is expected that the new generation: 5G, will increase actual users experience, in terms of data rates, reliability and 0s-like latency, to connect anyone/anything anywhere and at any time. This motivated researchers and telecommunications manufacturers, all over the word, during the last decade to intensify their research & development activities on 5G system. Preliminary studies, carried-out during the exploratory research phase of 5G (2012-2015), announced a peak data rate of 20 $Gbps$, corresponding to two order increase with respect to the existing LTE networks [17]. However, 5G is not only a technology that would provide enhanced Mobile Broad Band (eMBB) communications to increase the data rate. Indeed, we expect from 5G to serve new use cases such as machine-type communication (MTC), exhibiting different operating requirements in terms of availability, reliability, latency, throughput, and devices density. One of the first contributions on 5G wireless networks requirements [17], classified MTC applications into two main categories: massive MTC (mMTC) and mission critical MTC (cMTC). mMTC, also labeled as Internet of Things (IoT), exhibits high devices densities (1 $Mdevice/km^2$), short transmitted packets and high energy constraints (long battery life). As applications related to mMTC, we can cite sensors and actuators deployment in smart homes and smart cities over a wide area for surveillance and area-covering measurements. In the other side cMTC principally concern communications between machines involved in applications like Industrial manufacturing processes, observation of critical environments, remote medical surgery and vehicle-to-vehicle/infrastructure (V2X)... In cMTC context, latency, reliability, and high data rates are prominent. The maximum latencies targeted, in the cMTC scenario, is of the order of a millisecond. Fig. 2.8, gives an overview of the different scenarios and some applications envisaged in the context of 5G. From this figure, we can see that 5G will be designed to support diverse services with different data traffic profiles: throughput, latency and density of connected devices. One of the major challenges of 5G was the introduction of a New Radio (NR) access technology, which offers the flexibility needed to support these very different types of services. From another side, due to permanent debates on climate change, every emerging technology, including

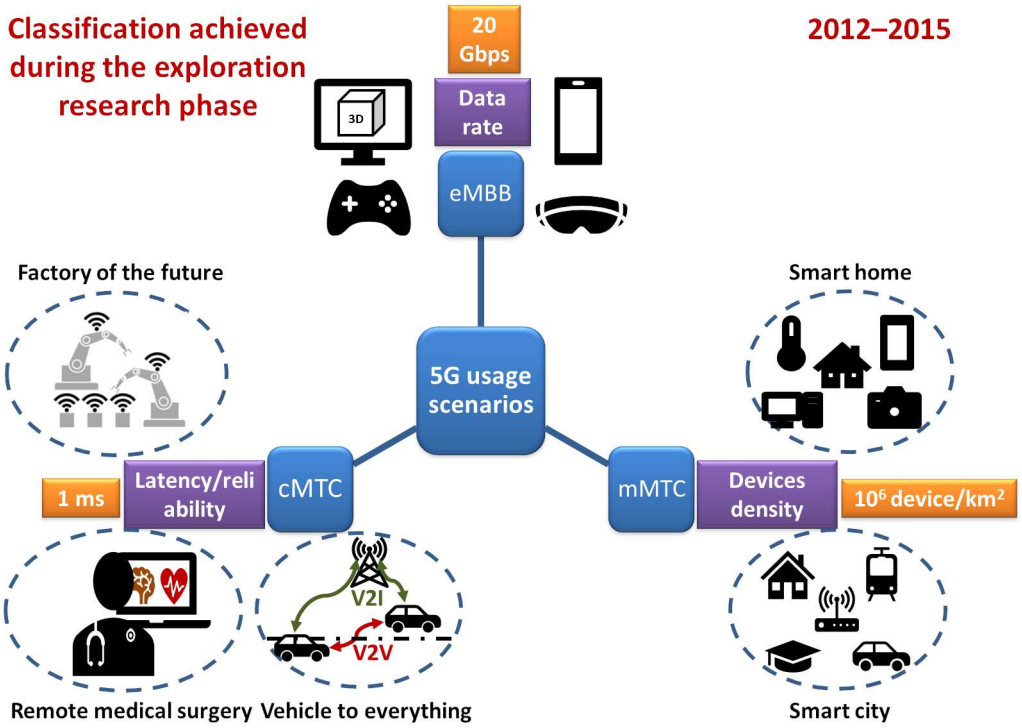

Figure 2.8: Scenarios and applications considered in the context of 5G during the exploratory phase.

5G, is scrupulously evaluated on its carbon footprint. As part of the information and communication technologies (ICT), 5G should keep mastered energy consumption. In 2018 the ICT sector's carbon footprint was evaluated to be 730 $Mt\ CO_2$-equivalents or 1.4% of overall global emissions, and the sector uses 800 TWh or 3.6% of the worldwide global electricity [18]. By 2025 these emissions are expected to triple with the deployment of 5G networks, if no serious efforts are made to reduce this footprint [19]. A significant part of these emissions, about the half, is attributed to user's devices whereas the sixth is dedicated to fixed and mobiles network infrastructures [20]. By user's devices, we mean older phones, fixed cordless phones mobile phones, smartphones, tablets Routers, modems, CPE (customer premises equipment), desktop and laptop, PCs, public displays, connected devices, (IoT)... Device's densification, emphasized by 5G use cases, should not increase drastically the total energy consumption. From the infrastructure side, the highest power consumer is the base station (BS), for which the radiated power is function of devices density in the covered area. BS can account for approximately $50-80\%$ of total energy consumption, with $\sim 60\%$ of them reserved to the power amplifier (PA) [21]. International Telecommunication Union (ITU) has been leading international efforts to enable mobile broadband communications (3G, 4G and now 5G). In January 2012, ITU defined the 4G wireless cellular technology: International Mobile Telecommunications (IMT)-Advanced and this is now being deployed worldwide. This technology uses Orthogonal Frequency Division Multiplexing (OFDM) Multicarrier Waveform (MWF) for downlink (DL) communications. OFDM has demonstrated its supremacy for high data rate transmissions over frequency selective channels at low implementation cost. However, for uplink (UL), a single carrier Discrete Fourier Transform (DFT) pre-coded OFDM waveform has been adopted. The main reason behind the use of a single carrier waveform for UL is that OFDM modulated time domain signal exhibits high fluctuations in terms of instantaneous power, with respect to the average one. The high Peak to Average Power Ratio (PAPR) of OFDM signals, make them very sensitive to PA nonlinear (NL) behavior. Indeed, PA is a crucial component of the transmitter, which input-output behavior is commonly defined by the Amplitude Modulation to Amplitude Modulation (AM/AM) and Amplitude Modulation to Phase Modulation (AM/PM) conversion characteristics. These characteristics are always nonlinear, in the vicinity of the saturation region, where PA efficiency is maximized. The standardization of 5G NR started in

2016. The first release appeared in December 2017 [22] and confirmed the appearance of specific features compared to previous releases. An important feature of 5G NR is that this technology will support scalable numerologies to cover different use case requirements [23]. Indeed, 5G will offer three main use cases: eMMB, mMTC and cMTC (labeled rather as Ultra Reliable and Low Latency services in release 15). Additionally, 5G should came with cost-effective deployment topologies, ranging from macro cells to small cells across sub 6 GHz and mmWave ($\sim 52.6\ GHz$) spectrum. Another important feature of 5G NR is that it will exploit the full potential of Multiple Input Multiple Output (MIMO) antenna technology. Particularly, in 5G NR the number of antenna elements integrating BS units may reaches hundreds, while being higher compared to the number of user's devices. This concept is defined as Massive MIMO [2]. With massive MIMO and the large number of BS active antenna elements we can address simultaneously many users through beamforming, achieving thus higher throughput for the system. The beams directivities are adapted to users' needs and allows to limit emissions in directions where there is no need for communications.

As highlighted previously, several areas of research emerged during the exploratory and experimental research phases on 5G. Those related to the definition and development of 5G NR were of great interest to me and were well in line with the research activities carried out within the LAETITIA team of the CEDRIC laboratory. This team has strong expertise in the field of advanced MWFs and particularly on Filter Bank Multi-Carrier (FBMC) systems. Members of the LAETIITIA team had strongly contributed to the European FP7 PHYDYAS project [3], involving 13 partners and led by Pr. Maurice Bellanger. The research activities that I have developed since my arrival at CNAM are centered around the following four axes:

- **Advanced post-OFDM MWFs for 5G and beyond systems:** One of the first questions raised during the exploratory research phase of the 5G systems was: shall we maintain OFDM as the MWF for 5G NR? Otherwise, which MWF, among those proposed in the literature, would better meet the requirements of 5G use cases? This question motivated us to carry out, within the framework of the WONG5 project, an exhaustive comparative study of the most promising MWFs suited for cMTC/URLLC use case. Several Key Performance Indicators (KPIs) have been considered to compare the selected MWFs: frequency localization, spectral efficiency, End-to-End Physical layer latency, robustness to time and frequency synchronization errors, power fluctuation and transceiver complexity. Among all the MWFs candidate for 5G NR, FBMC-OQAM: the best frequency localized one is characterized by real domain orthogonality, that could be lost under frequency selective channels. In this context and based on the cyclo-stationarity of the OQAM signal, we have proposed advanced equalization structures based on Widely linear and Frequency Shift (FRESH) processing, that have been applied to a FBMC-OQAM system using different 5G numerologies.

- **In-band and Out-of-Band distortions analysis:** The primary source of Radio Frequency (RF) imperfections in a transceiver is the NL PA. For MWFs based transmissions, such as those candidates to reach the requirements of 5G use cases, the envelope of the signal to be amplified is far from being constant, presaging significant non-linear distortions, if the PA is operated at low input Back Off (IBO) (i.e. close to its saturation region). We characterized analytically, for different types of memoryless PA (models or measured), and for different MWFs, the IB distortions in terms of bit error rate or symbol error rate. For the characterization of OOB emissions, we proposed analytical prediction of spectral regrowth based on cumulants.

- **PA efficiency enhancement solutions for 5G and beyond MWFs:** OFDM, as well as most MWFs candidate for 5G NR, exhibit high PAPR exceeding 10 dB. This property implies, to reduce the distortions induced by the PA, to work at large IBO values. However, this scenario is not attractive in terms of energy efficiency. Different approaches can be proposed to improve the energy efficiency. The first proposed solutions are based on digital signal processing (DSP) algorithms to reduce the PAPR and to compensate for the NL PA characteristics by using Digital

[2] also known as large-scale antenna systems, very large MIMO, hyper MIMO, full-dimension MIMO or ARGOS
[3] http://www.ict-phydyas.org/

Pre-distortion (DPD). These processing are offered either separately or jointly. A significant effort has been put on MWFs with specific signal structures, such as FBMC-OQAM. Another solution that we have proposed is based on an hybrid approach which consists of modifying the architecture of the RF transmitter by splitting the MWF time domain signal into several (2 or more) low PAPR sub-signals which can be amplified via PAs at higher efficiency.

- **Enhanced energy efficient Massive MIMO networks with mixed numerology and RF impairments:** The diverse use cases requirements is an important challenge for the 5G NR, where the coupling of OFDM-based massive MIMO and mixed numerologies can be envisaged. We have investigated the use of spatial multiplexing of users with different numerologies and sharing the same bandwidth. We have also analyzed the Inter-Numerology Interference (INI) and derived the theoretical expressions for DL and UL scenarios, along with corresponding cancellation schemes. As last contribution in this direction, we considered energy-efficient DL transmission in OFDM based massive MIMO in presence of PA. We designed a low complexity transmission scheme taking into consideration massive MIMO precoding, PAPR reduction and DPD.

In what follows, I will give a summary of my scientific contributions presenting the context where results have been obtained (international or national projects) and the researchers involved in the publications (other collaborating laboratories and industrials, supervised postdoctoral researchers, PhD, and master students). A detailed presentation of the scientific contributions will be given in chapters 3, 4, 5 and 6.

2.3.2 MWFs for 5G and beyond systems

The strong constraint on the latency of cMTC systems requires minimizing network access times by allowing asynchronous communications between users. The same problem can also be found for mMTC applications, were the transmitted/received data packet sizes are usually quite small. The overhead associated with orthogonal transmission, in terms of time alignment signaling becomes so very large, when large numbers of devices are connected. In [24] it has been demonstrated that OFDM is not adapted for asynchronous communications. Another drawback of OFDM is the spectral efficiency loss inherent to the Cyclic Prefix (CP) insertion. My first research focus, carried out within the framework of the WONG5 project, concentrated on the study of post-OFDM MWFs, that would better meet the requirements of 5G cMTC/URLLC use case. This project involved CNAM, CEA-leti, THALES and CentraleSupélec. Beyond the relaxation of the constraint on time synchronisation, other criteria must be considered during the comparative study of post-OFDM MWFs. As Key Performance Indicators (KPIs), chosen with the WONG5 project partners, we considered: Power Spectral Density (PSD) localization, Spectral Efficiency (SE), End-to-End Physical layer latency, PAPR, transceiver complexity, adaptability to MIMO transmissions and performances over frequency-selective and/or time varying channels. Fig. 2.9 gives an overview on this research activity.

Several post-OFDM MWFs have been intensively studied in the literature in the last decade. Those considered for comparison by WONG5 project were:

- **WOLA-OFDM:** for Weighted Overlap and Add OFDM [25],
- **UF-OFDM:** for Universal Filtered OFDM (or also UFMC) [26],
- **f-OFDM:** for filtered OFDM [27],
- **N-Continous OFDM:** [28],
- **FMT:** for Filtered MultiTone [29],
- **FBMC-OQAM:** for Filter Bank MultiCarrier with Offset Quadrature Amplitude Modulation [30, 31],
- **WCP-COQAM:** for Windowed Cyclic Prefix-based Circular-OQAM [32],
- **FBMC-QAM:** for Filter Bank MultiCarrier with Quadrature Amplitude Modulation [33, 34],

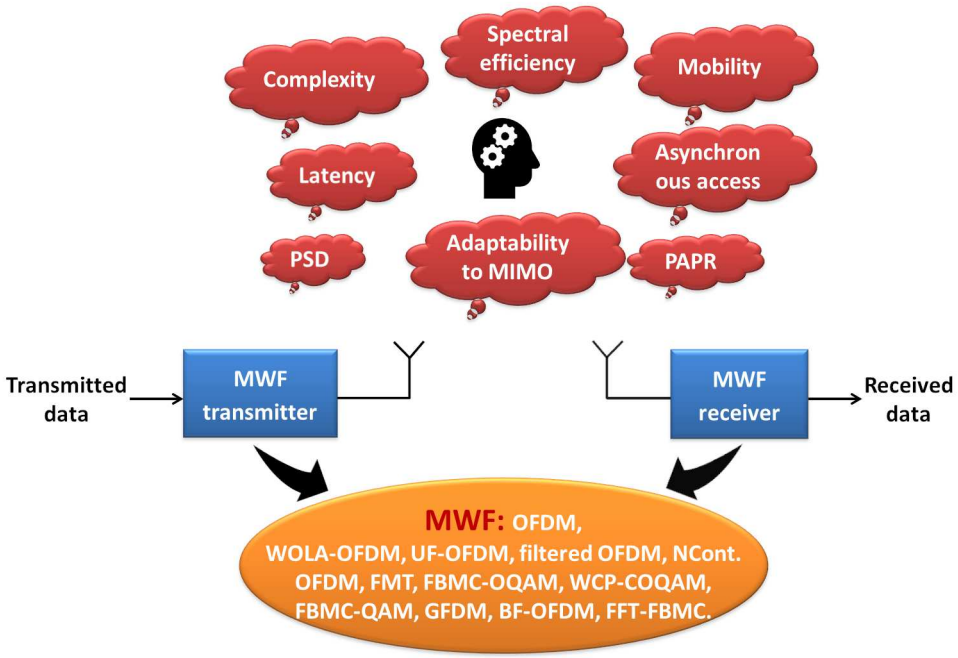

Figure 2.9: Comparative study of OFDM and post-OFDM MWFs for 5G and beyond systems.

- **GFDM:** for Generalized Frequency Division Multiplexing [35],
- **FFT-FBMC:** for Fast Fourier Transform FBMC [36],
- **BF-OFDM:** for Block-Filtered OFDM [37].

To meet the 5G requirements, each of these MWFs try to provide solutions to the limitations of CP-OFDM, via windowing and/or filtering at the transmitter (Tx) and/or receiver (Rx), where the filtering could be done at subcarrier level or at resource block (RB) level.

The study of the above-mentioned waveforms, considering CP-OFDM as a basis for comparison, was distributed among the various partners of the WONG5 project. At CNAM, we were in charge of the study of CP-OFDM, WOLA-OFDM, UFMC, FMT, FBMC-OQAM, FBMC-QAM and WCP-COQAM.

As first contribution, we have demonstrated that WOLA-OFDM provides better PSD localization than classical CP-OFDM, thanks to the smooth time domain windowing applied at the transmitter side. Additionally, the receiver side windowing, leaded to reduced users' interference in an asynchronous context. This work, co supervised with Pr. Daniel Roviras and achieved by a postdoctoral researcher under my responsibility: Dr. Rafik Zayani, was published in a conference paper [38]. Inspired from [32], we extended the previous contribution, during Yahia Medjahdi's post-doc, to combine WOLA processing and circular pulse shaping filter. The proposed MWF called WOLA based circular offset quadrature amplitude modulation (WOLA-COQAM) has shown improved robustness, compared to classical WOLA-OFDM, against time synchronization errors. This contribution has been published in a conference paper [39].

The other MWFs: UFMC, FMT, FBMC-OQAM, FBMC-QAM and WCP-COQAM were studied as part of Dr. Yahia Medjahdi's post-doc, which I supervised with Pr. Daniel Roviras. The investigated MWFs have been classified based on their orthogonality criterion, which is a very important feature when adapting them to MIMO communications. The performances of these MWFs, and those studied by the others WONG5 project partners, have been deeply analyzed in a review journal paper [40] and a conference paper [39]. The main conclusions of this exhaustive comparative study are the following:

- **PSD localization:** windowed/filtered MWFs offered better frequency localization than CP-OFDM. The best frequency localization was achieved by FBMC-OQAM, thanks to the steep slopes of its prototype filter,

- **Spectral efficiency:** in short bursts case, all MWFs gave almost the same spectral efficiency, except FBMC-OQAM, FMT and FBMC-QAM, due to long prototype filters. With long bursts scenario, all the MWFs share the same spectral efficiency,

- **Latency:** for very short bursts, CP-OFDM-inspired MWFs generated the lowest latencies compared to the other MWFs requiring filtering operation. In the case of very long bursts, MWFs using CP or zero padding (ZP) gave higher latencies due to the number of CP/ZP added to the transmitted signal,

- **Robustness against time and frequency synchronization errors:** thanks to their well-frequency localized transmit/receive filters, FMT, FBMC-OQAM, FFT-FBMC, FBMC-QAM and f-OFDM provided good performances compared to CP-OFDM,

- **Complexity:** Regarding the transmitter: CP-OFDM and WOLA-OFDM achieved the lowest complexities. However, N-continuous OFDM and UFMC required huge computational resources reaching up to 200 times CP-OFDM complexity. At the receiver side, WOLA-OFDM, N-continuous OFDM and BF-OFDM receivers showed a complexity like the CP-OFDM one,

- **PAPR:** as time domain signals, at the output of all the considered MWFs, have complex Gaussian distribution, we have confirmed quite same PAPR for all the MWFs,

- **Adaptability to MIMO:** The investigated MWFs have been classified based on their ability to keep the orthogonality: (1) in the complex domain (e.g. most of the OFDM-inspired MWFs), (2) in the real domain (OQAM based techniques) and (3) non-orthogonal MWFs (like GFDM and FBMC-QAM). Among these three groups, the first one is directly adaptable to MIMO transmissions.

For the performance of the studied MWFs over frequency-selective and time-varying channels, we have considered, for WONG5 project scenario, the E model of the HIPERLAN/2 channel [41]. This channel model is designed for the 5 GHz band, for typical large open space outdoor environments and with Non-LOS (NLOS). From this study, it appeared that UF-OFDM is very sensitive to channel delay spread, whereas all other MWFs are much more robust. If for low mobility case (5 km/h), all MWFs have the same performance, at 150 km/h, WOLA-COQAM, FFT-FBMC and BF-OFDM experience an error floor ten times greater than the one obtained with the other MWFs. These results have been published in a conference paper [42].

Among the MWFs candidate for 5G NR, we have clearly identified FBMC-OQAM as the MWF exhibiting the best frequency localization, thanks to its prototype filter [43], providing then the best performance in supporting asynchronous users access. However, the use of the OQAM modulation, break the orthogonality under frequency selective channels. As part of Hayfa Fhima's PhD, I have been interested on the study and implementation of advanced equalization schemes applied to FBMC-OQAM. As OQAM is known to be a cyclo-stationary (CS) and non-second order circular (NSOC) modulation, it was relevant to study advanced equalization techniques based on widely linear and Fresh approaches [44]. We developed three minimum mean squared error (MMSE) based equalizing structures: a linear equalizer (LE), a widely linear equalizer (WLE) and a widely linear FRESH equalizer (WL FRESH). For the proposed equalizers, both symbol-spaced (SSE) and fractionally spaced (FSE) processing have been evaluated, in synchronous DL/UL and asynchronous UL scenarios, with mixed numerologies transmissions. The results showed the supremacy of the proposed WL FRESH equalizer to suppress INI and inter symbol interferences (ISI) over frequency selective channels. The work carried out within the framework of this thesis was highlighted by a journal paper [45] and four conference papers [46, 47, 48, 49].

More insights on the contributions related to the study of post-OFDM MWFs, for 5G and beyond systems, will be given in chapter 3.

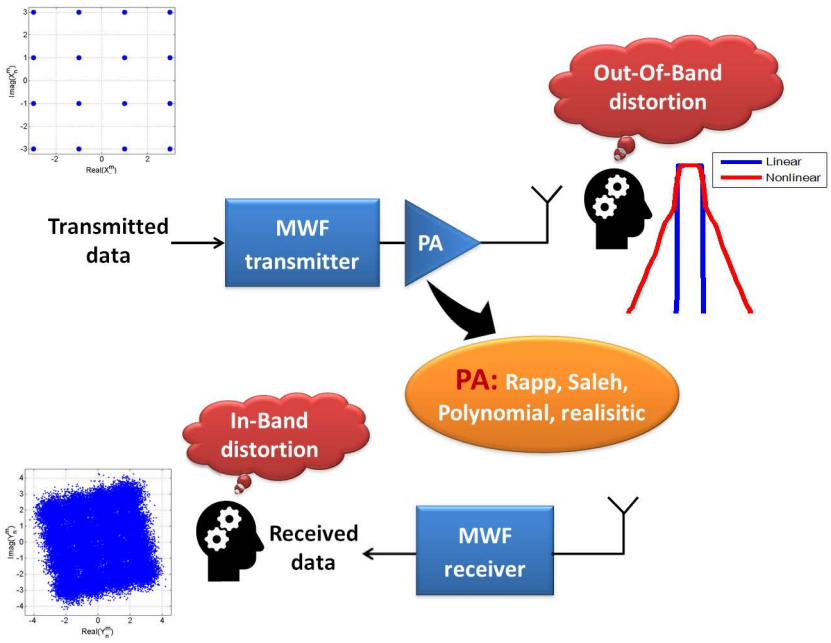

Figure 2.10: In-band and Out-of-Band nonlinear PA effects analysis.

2.3.3 Power amplifier distortions analysis

MWFs are suffering from a major drawback related to their high PAPR. The PAPR measures the variation of the instantaneous power compared to the mean power of the transmitted multicarrier signal. Low values of PAPR correspond to a transmitted signal which power is always very close to its mean power, while high PAPR values indicate that the instantaneous power can be very high compared to the mean. The distribution of the transmitted power is not very important as far as linear systems are used in the transmission chain. Unfortunately, some elements of the chain are nonlinear (NL). In particular, the power (PA) has a NL behavior. This device can be quasi linear for a certain part of the input powers and NL for high input powers. Furthermore, the output power of a PA is limited to a saturation power. For small input powers, the PA is operated in its quasi-linear region and the high PAPR of the multicarrier signal will not have any influence on the transmitted signal. Nevertheless, this situation has a high cost in terms of energy efficiency. Especially, for mobile applications with batteries, it is thus necessary to increase the power efficiency. Real PA communications systems will then be operated as close as possible to the saturation power to increase the power efficiency. By doing that, two negative effects will appear:

- **Out-Of-Band (OOB) distortions:** the output signal spectrum will be broadened compared to the input one. This is also known as spectral regrowth,
- **In-Band (IB) distortions:** the transmitted signal will be distorted causing transmission errors.

From what has been said previously, it appears clearly that the performances of CP-OFDM and post-OFDM waveforms are strongly affected by PA, especially if energy efficiency optimization is targeted. This observation motivated us to develop deep studies of the two types of distortions induced by memoryless PA. These studies were carried out in terms of theoretical analysis of IB and OOB distortions and completed by simulations, using modelled or real PA. Fig. 2.10 illustrates the scenario and the context of the studies envisaged within the framework of this research axis.

In-Band distortions analysis

With all the advantages shown by the FBMC-OQAM MWF, we were interested within the framework of Hanen Bouhadda's PhD, in the analytical characterization of the IB distortions undergone by this MWF

over Additive White Gaussian Noise (AWGN) and flat fading Rayleigh channels. As a first contribution, we proposed a theoretical approach to evaluate the Bit Error Rate (BER) performance for FBMC-OQAM as well as CP-OFDM MWFs in presence of Saleh PA model, exhibiting both AM/AM and AM/PM conversion characteristics. The proposed approach is based on Bussgang's theorem [50], for modelling the IB distortion as a complex gain and an uncorrelated additive noise. Through this study, we have demonstrated a very important feature of FBMC-OQAM. Indeed, when only the amplitude of the modulated signals is distorted by the PA, FBMC-OQAM exhibited the same performance, in terms of BER, as CP-OFDM. However, FBMC-OQAM is shown to be more sensitive to phase distortions than CP-OFDM. This sensitivity is related to the intrinsic interference term introduced by this modulation. This finding have been published in a conference paper [51].

For FBMC-OQAM, as well as any other MWFs, we carried analytical study of the BER, in presence of memoryless PA. This study required theoretical expressions of the complex gain and the variance of the NL distortion noise term computed by Busgang theorem. For simple PA models, such as the Soft Envelope Limiter (SEL), Dardari et al. [52] proposed analytical expressions to compute these parameters. However, for other PA, such as Rapp, Saleh, or polynomial models, or for real measured PA, BER derivation was generally intractable. Another original contribution we proposed in this direction is the proposal of a generalized method based on a polynomial fitting of the PA characteristics allowing to compute theoretical expressions of the BER for any PA model or measurement. The proposed approach has been applied to CP-OFDM and FBMC-OQAM MWFs for Additive White Gaussian Noise (AWGN) and Rayleigh channels and the obtained results have been published in a journal paper [53]. For Rayleigh flat fading channels, the BER analytical expressions developed in [53], for CP-OFDM and FBMC-OQAM MWFs, required numerical integration. We investigated, in the journal paper [54], closed form expressions of the BER for both MWFs and showed that FBMC-OQAM signal has the same sensitivity to the PA nonlinearity as the CP-OFDM signal when the channel is perfectly equalized.

The work proposed in [53], has been extended, within the framework of the WOWG5 project, to study the Symbol Error Rate (SER) of other MWFs. The considered post-OFDM MWFs are: WOLA-OFDM, UFMC, f-OFDM and FBMC-OQAM. Two PA models have been considered in this work: (1) a 4 GHz long term evolution (LTE) user equipment PA provided by [55] and modeled using a polynomial model [56], (2) a Rapp model. With this study, we developed a universal approach to compute theoretically the SER for any measured or modelled memoryless PA and for each MWF. Theoretical results validate the simulated ones and show that PA distortions strongly affect the performance of the studied MWFs. It was shown that the selected MWFs almost perform as the classical CP-OFDM when PA is operated near its saturation region. These results were part of deliverable [57] of WONG5 project and have been published in a journal paper [58].

Out-Of-Band distortions analysis

Within the framework of the FP7 EMPHAtiC project, we have been interested on the prediction the spectral regrowth of CP-OFDM and FBMC-OQAM MWFs. Theoretical studies, using Price theorem and cumulants, have been conducted to predict theoretically the PSD at the output of different PA models.

From the comparative analysis of CP-OFDM and post-OFDM MWFs [40], we have shown that FBMC-OQAM exhibits the best frequency localization. This advantage is maintained if the PA is linear. However, when the PA is operated near to its saturation region, there will be a spectrum regrowth and the advantage of this MWF, compared to CP-OFDM, will be reduced. In this case, it can be useful to predict the spectral regrowth induced by the NL PA to have a quite reliant information about the unused sub-carriers.

Two popular methods are commonly used for the prediction of the spectral regrowth of MWFs in presence of NL-PA: The first method is based on Price's theorem [59] and the second one is based on cumulants [60]. These methods are based on deriving a closed form expression for the auto-covariance function of the PA output, whose Fourier Transform (FT) yields the output PSD. With Price theorem, the estimation of the PSD regrowth is generally based on a (Solid State Power amplifier) SSPA model approached by a given order polynomial model [61]. This latter can fail in predicting accurately the PSD regrowth, especially at the vicinity of the PA saturation region. During the master training of Saidou

SALL, we proposed a suitable polynomial modelling for the PA conversion characteristics, to obtain a more reliable analytical estimation of the spectral regrowth of FBMC-OQAM. These results have been published on a conference paper [62].

However, Price theorem is generally applied to memoryless PA models, exhibiting only AM/AM distortion. Also, it involves intensive integral calculus for high polynomial orders which will impact the closed-form expression derivation. For these reasons, we have switched to methods based on cumulants [60]. Within the first part of Krishna Bulusu's PhD, we have extended the work proposed by Zhou et. al [63] to predict the spectral regrowth of FBMC-OQAM signals by using cumulants. In this work, we considered memoryless PA models exhibiting both AM/AM and AM/PM conversion characteristics and fitted with polynomial function. Simulation carried for FBMC-OQAM confirmed the good accuracy of the derived closed form expressions of the predicted PSD. We also demonstrated that the Non-linearity order and the IBO play vital role in spectral regrowth prediction accuracy. These results have been published in a conference paper [64].

It's worth to point that the approaches used for the prediction of the spectral regrowth for CP-OFDM and FBMC-OQAM can be applied to most of the post-OFDM MWFs candidate for 5G. Indeed, provided that the PA input signal can be viewed as complex Gaussian, prediction of the spectral regrowth, using Price theorem or cumulants, remains valid.

The scientific contributions related to this research topic will be given in chapter 4.

2.3.4 Enhanced PA efficiency for 5G and beyond MWFs

According to several studies [17, 19], the ICT sector accounts for nearly 3% of the worldwide energy consumption. For mobile communications systems, the power consumption helps to define the battery life. From the base station side, the estimated consumed power is about 80% of the total energy of cellular infrastructure [21]. In fact, in today's macro base stations, the PA efficiency plays a key role in the energy efficiency of the whole transmitter chain as this device is the most power-consuming component. From another side, CP-OFDM as well as most of the MWFs candidate for 5G and beyond systems suffer from high PAPR. If the PA is operated in its quasi-linear region, the high PAPR of the multicarrier signal will not have any influence on the quality of the transmission. Nevertheless, this situation has a high cost in terms of energy efficiency, especially for mobile applications with batteries. In order to increase power efficiency, PA should be operated as close as possible to its saturation region, but this would introduce broadening of the amplified signal spectrum, as well as distortion over the transmitted signal itself. Many solutions have been proposed to increase the efficiency of PA in 4G-5G networks. These solutions can be broadly classified into three categories:

- **Signal processing-based approaches:** These solutions do not require any change in the transmitter architecture. The PA efficiency is increased with the help of PAPR reduction techniques and/or linearization techniques. These processing can be also cascaded to get an enhanced control of the PA efficiency. Otherwise, PAPR reduction and PA linearization can be designed to work jointly by seeing the two pre-processing as signal adding techniques. In few words, all the techniques, related to this approach, intend to reduce the IBO by making the PA operating as close as possible to its saturation region.

- **Modified architecture transmitter-based approaches:** They aim at modifying the transmitter architecture. Several solutions can be used: envelope tracking, Doherty amplifiers, Kahn techniques, parallel architectures, linear amplification with nonlinear component (LINC) also known as Out phasing technique.

- **Network based approaches:** The power efficiency is increased while using smaller cells and massive MIMO technology. Adding to this, the idea to reduce the power amplifier activation as well as on/off techniques. In this way the operating point of the power amplifier can be updated according to the load of the cell (night and day traffic changes).

Increasing the PA efficiency could also be a mix of all the aforementioned techniques. In [65], the authors combined envelope tracking, PAPR reduction and on/off techniques for multi-carrier based transmissions.

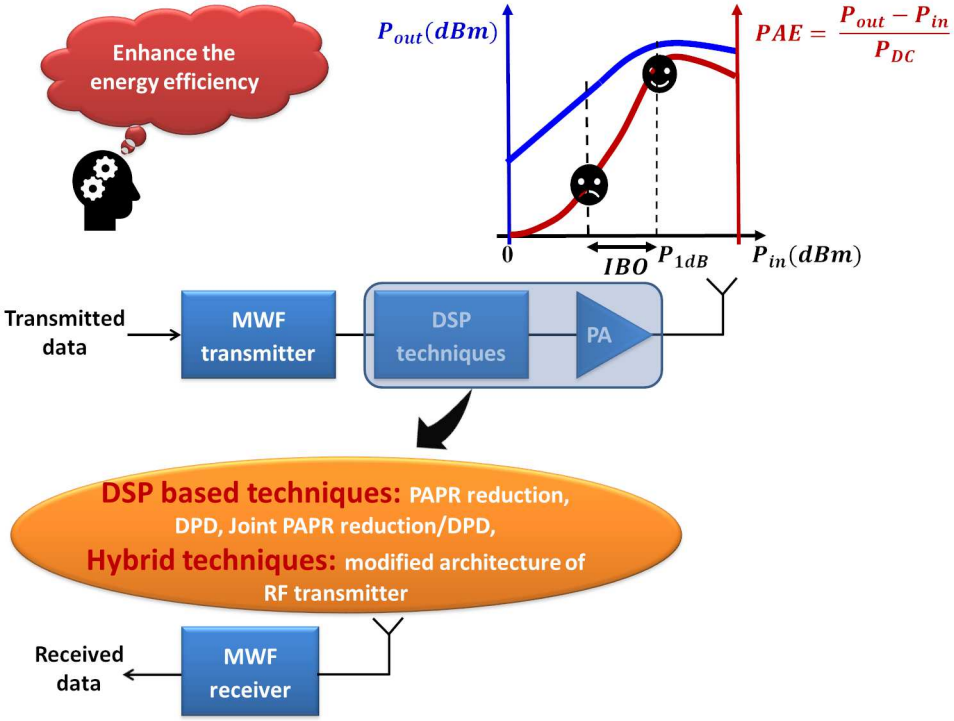

Figure 2.11: Energy efficient transmitters for 5G MWFs.

A third topic of my research activities, focused on studying and proposing different solutions to enhance PA efficiency in 5G context, by using either signal processing-based solutions or modified architecture-based ones. An illustration of this research topic is given in Fig. 2.11. Regarding network-based approaches and particularly those based on massive MIMO technology, some contributions will be presented in the next section.

2.3.4.1 Signal processing-based solutions

The classification of post-OFDM MWFs candidates for 5G NR, can be based on the way in which the sub-carriers are filtered at the modulator level: filtering by sub-carrier or by group of sub-carriers. Depending on the spectral localization of the analysis filter, the length of the impulse response may spread out causing an overlap between the symbols. This phenomenon must be considered in the pre-processing algorithms such as those dedicated to the reduction of the PAPR or to the DPD.

FBMC-OQAM case

Being a MWF technique, FBMC-OQAM suffers from high PAPR and its good frequency localization property is no longer valid in real communication systems and in presence of NL PAs. As a consequence, spectral regrowth may appear over the amplified signal, hampering much of its attractive appeal to be the ideal candidate for 5G NR. As part of the FP7 European project EMPHAtiC, the ANR project ACCENT5 and the PHC-C3 project, we have focused on improving the energy efficiency of FBMC-OQAM transceivers by reducing the PAPR and designing dedicated DPD schemes.

PAPR reduction techniques for FBMC-OQAM: Classical probabilistic schemes proposed for CP-OFDM systems cannot be directly applied to FBMC-OQAM. By taking overlapping signal structure of FBMC-OQAM into account, we have initially proposed a Dispersive SeLective Mapping (DSLM) scheme [66], which is essentially a symbol by-symbol approach. However, DSLM leaded to a sub-optimal performance w.r.t the classical SLM scheme applied to CP-OFDM as the peak reduction we may obtain for the current symbol, can possibly be destroyed by the future symbol. We have improved this technique

by using a trellis-based scheme involving, for the optimization of the PAPR, more than one symbol at a time. The proposed algorithms named Trellis base SLM (TSLM) scheme have been published in a journal and a conference papers [67, 68].

We have then proposed a third solution for reducing the PAPR of FBMC-OQAM signals, named as Dispersive Tone Reservation (DTR). This algorithm has been published in a conference paper [69].

PA linearization techniques for FBMC-OQAM: In the case of pre-distortion, we have demonstrated the need to consider the overlapping nature of FBMC-OQAM symbols. A novel DPD technique, named Overlapped Recursive Error Correcting (OREC) DPD has been proposed for FBMC-OQAM [70].

The OREC-DPD algorithm relies on a constant convergence rate, thereby, leading to slow convergence. Recently, we have enhanced this algorithm to a very fast converging one [71, 72] requiring few iterations.

Co-existence capabilities of a FBMC-OQAM system working with NL PA: One of the main objectives of the FP7 European EMPHAtiC project was to investigate the coexistence of narrow band and broadband systems for Professional Mobile Radio (PMR) communication systems like Public Protection and Disaster Relief (PPDR). In [73], it has been shown that classical CP-OFDM based LTE system needs sufficient guard-band or additional filtering in order to coexist in a PMR band, even without considering the RF impairments of the transmitter. In practice, it is imperative to consider the RF impairments especially those related to NL PA. During Krishna's Bulusu PhD, we investigated the coexistence of narrow band and broadband PMR systems that can support asynchronism, have low latency and are able to be operated with NL devices. We demonstrated that a LTE-like FBMC-OQAM broadband system working with NL PA devices can still co-exist with legacy PMR systems with high energy efficiency, when proper PA linearization techniques are applied jointly with PAPR reduction methods. This work was carried out jointly with Pr. Markku Renfors from Tampere University of Technology (Finland). The obtained results have been published in a journal paper [67] and then completed by a conference paper [74].

All of the contributions made to characterize and mitigate the IB and OOB effects of NL PA on FBMC-OQAM as well as the associated techniques to improve the efficiency of PAs were published in chapter 13 of the book [75]. I managed the coordination of this work, carried out jointly with colleagues from Tampere University of Technology.

Case of other MWFs: WOLA-OFDM, UF-OFDM, F-OFDM and BF-OFDM

PAPR reduction techniques: Within the framework of the WONG5 ANR project, we have focused on applying PAPR reduction techniques for many MWFs candidate for 5G NR. As stated before, all the time domain signals generated with most post-OFDM modulations exhibit high PAPR levels, like those observed with regular CP-OFDM signal. There are many PAPR reduction techniques whose performance could be very different depending on several criteria: complexity, receiver modification (known as downward compatibility), IB distortions, OOB regrowth, etc. We focused on PAPR reduction techniques like: TR, SLM, pre-coding and applied them to CP-OFDM, WOLA-OFDM, UF-OFDM, f-OFDM and BF-OFDM.

For WOLA-OFDM, UF-OFDM and f-OFDM, the application of SLM and TR techniques were straightforward. The evaluation of the PAPR reduction techniques was performed considering the PAPR reduction gain and the complexity of the algorithms. Through this evaluation, we demonstrated that: (1) for all the considered post-OFDM MWFs, both SLM and TR remain as efficient as in CP-OFDM. (2) for UF-OFDM, both algorithms require huge complexity resources. These results give rise to a conference paper publication [76].

Within the framework of the 3^{rd} work package of WONG5 project, I carried, jointly with colleagues from CentraleSupélec Rennes, a study to estimate the overall power budget of transmitters integrating PA DC power and consumption related to the PAPR reduction algorithms. The considered MWFs were: CP-OFDM, WOLA-OFDM, f-OFDM and BF-OFDM, while the PAPR reduction method is the SLM one. The obtained results have been published in a conference paper [77].

As part of Khaled Tahkoubit's PhD we have adapted a DFT spreading technique, used for CP-OFDM, to BF-OFDM for UL transmissions. We have shown that SC-FDMA and DFT spread BF-OFDM achieve quite same PAPR reduction performance of around 2 dB. This contribution has been published in a conference paper [78].

Testbed for demonstrating post-OFDM MWFs capabilities in cMTC context: The selection of the best post-OFDM adapted for cMTC scenario, has been carried out during the WONG5 project. Regarding sub-band filtering-based MWFs: f-OFDM and BF-OFDM won the race, where UF-OFDM lost it due to its important implementation complexity. In another hand WOLA-OFDM is also an interesting candidate for 5G cMTC applications thanks to its reduced complexity and good performance regarding the targeted KPIs.

We developed at CNAM a Software Defined Radio (SDR) testbed to demonstrate, in real world, the feasibility of the proposed DSP algorithms proposed to enhance the energy efficiency of the proposed transceivers based on selected MWFs, while taking CP-OFDM as basis of comparison. This work, co-supervised with Pr. Daniel Roviras and Dr. Christophe Alexandre, has been carried by a postdoctoral researcher: Dr. Rafik Zayani and two master students: Mrs. Xinying Cheng and Mrs. Xiaotian Fu.

Through this testbed, we have confirmed the supremacy of WOLA-OFDM and BF-OFDM in improving the energy efficiency and the robustness to asynchronism. The PA efficiency enhancement relied on PAPR reduction and DPD algorithms to operate the device at low IBO values. Furthermore, the developed testbed has been dedicated to evaluating the capability of the selected MWFs in handling multi-user signals when there is imperfect synchronization in time domain. A detailed description of the proposed testbed along with a selection of some obtained results have been published in a conference paper [79] and a journal paper [80].

Joint PAPR reduction & DPD

Conventionally, PAPR reduction and DPD techniques are optimized separately and applied independently. Some studies focused on their association aiming at avoiding mutual effects. Among the proposed solutions, we can cite [81, 82]. From another side, the work carried during Krishna Bulusu's PhD showed the feasibility to view the DPD as an adding signal technique. This statement is also true for some PAPR reduction techniques such as clipping and TR. Thereby, an interesting idea has been raised saying that both PAPR reduction and DPD can be combined and made through a unique adding signal operation. This means that both processing can be done at one stretch by adding a signal, which not only reduces PAPR but also linearizes the PA, which yields to a joint optimization of the two processing.

With Dr. Rafik Zayani, we took up this idea and apply it to CP-OFDM. We proposed a new technique called "Ping-Pong Joint Optimization" (P2JO) to optimize jointly PAPR reduction and predistortion for CP-OFDM signals. The proposed approach synthesizes, iteratively, one correction signal for reducing the PAPR and linearizing the PA conversion characteristics to reach a given performance in terms of Mean Square Error (MSE). We have shown that the proposed solution allows a better trade-off between PA efficiency and linearity, compared to classical combinations of the two-processing. As the idea seemed very interesting to us, we started by patenting it via a European patent [83]. We published then the proposed algorithm and the related results in a journal article [84].

2.3.4.2 Modified architecture transmitter-based approaches

The algorithmic solutions proposed previously, to improve the energy efficiency of MWFs-based transceivers, would not require a modification of the architecture of the RF chain. These solutions aim to reduce fluctuations in peak signal power and/or linearize the conversion characteristics of the PA. Another approach, to enhance PA efficiency, would rather consist in changing the design of the RF chain. This can be done by amplifying the multi-carrier signal via several PAs, ensuring at least equal performance to classical schemes, but with lower overall power consumption. This is the key idea, for example, for the LINC technique. As part of Khaled Tahkoubit's thesis, we focused on answering this question: how could we break down a signal with a strong PAPR, coming from a given MWF, into signals with weaker PAPR, so that they can be amplified with better power efficiency? This reflection led us to propose a new method called Iterative Dichotomy PAPR (IDP) reduction. The proposed IDP algorithm is based on decomposing the MWF signal into a sum of M ($M \geq 2$) signals having constant envelope and a residual error signal carrying all the original signal peaks. A judiciously weighted version of the residual signal is then added to each of the M constant envelope signals to give a lowered PAPR signal that could be amplified by M PA, at better efficiency. We have carried out theoretical analysis for computing the

M signals and confirmed their validity by simulation results. The first part of this study concentrated on a second order decomposition of CP-OFDM signal ($M = 2$). At this order, a PAPR gain of 2.2 dB was achieved by the IDP algorithm compared to classical CP-OFDM transmitter. These results have been published in a journal paper [85].

As the transmitter architecture related to the IDP method is very similar to that of the LINC (also known as Out Phasing in the literature) one, we have compared the performances of these techniques. The comparison has been done following the three main points: (1) comparing the output power for the same DC consumed power and the same BER performance, (2) studying the influence of timing errors in the combination process and (3) examining the effect of a mismatch between the PAs conversion characteristics. The results of this comparative study have been published in a conference paper [86]. We have recently generalized the results published in [85] to any dichotomy order. These results were submitted to IEEE Transactions on Wireless Communications.

In chapter 5, I will present some of the results related to the enhancements of MWFs based transceivers in presence of NL PAs.

2.3.5 Massive MIMO networks with mixed numerology and nonlinear PAs

3GPP consortium converged, in December 2017 [22], towards the requirements of NR: defined as the new radio interface for 5G systems. As expected, NR will enable new use cases, improve data rates, reduce latency, improve coverage capacity and reliability. These requirements should be fulfilled with enhanced network energy efficiency, while allowing to enlarge the sub-6GHz spectrum to mmWave. Among the prominent technologies proposed to reach the 5G NR requirements, Massive MIMO and mixed numerology have been retained to support various configurations on top of OFDM waveform.

The major innovation of release 15 of 3GPP with respect to former standards is the support of various numerologies [23] which allows scalable Sub Carrier Spacing (SCS) and symbol duration. By doing so, challenges of 5G can be properly addressed. Indeed, shortening symbols reduces the latency required for some URLLC/cMTC. Moreover, enlarging the SCS increases the robustness against the Doppler effect occurring in mobility scenarios.

Massive MIMO is an emerging technology that uses many antennas at the BS serving many tens of terminals in the same frequency resources. Massive MIMO relies on spatial multiplexing with high number of antennas helping to focus energy into ever smaller regions of space. This beamforming brings huge improvements in throughput and radiated energy efficiency.

As the power of the signal to be transmitted by each individual antenna is sufficiently reduced, massive MIMO includes extensive use of inexpensive low-power components. PA with very relaxed linearity requirements will necessitate PAPR reduction and/or predistortion signaling, which can exploit the massive MIMO system extra degrees of freedom, equal to the difference between the number of BS antennas and the number of user's terminals.

As part of Xinying Cheng's PhD, I have been interested, since October 2018, in the study of two issues linked to massive-MIMO systems. The first one is related to the interference caused by users using different numerologies and the other one concerns energy efficiency with emitters architectures with joint MIMO precoding, PAPR reduction and DPD. A simplified illustration of these research topics is given by Fig. 2.12.

2.3.5.1 Analysis and cancellation of mixed-numerologies interference for massive MIMO-OFDM

The extremely diverse service requirements are an important challenge for the upcoming 5G wireless communication technologies, where OFDM-based massive MIMO and mixed numerologies transmission are proposed as solutions. During the first year of Xinying Cheng's PhD we have introduced a new transceiver for massive MIMO-OFDM DL systems where we have investigated the use of spatial multiplexing of users, sharing the same bandwidth, whose associated numerologies are different. We first introduced a precoding design that aims to manage the mixed numerologies spectrum sharing (SS) transmission. Then, we analyzed the Inter Numerology Interference (INI) and derived the theoretical expressions in massive MIMO-OFDM DL. We demonstrated that by using the proposed precoding scheme and considering two

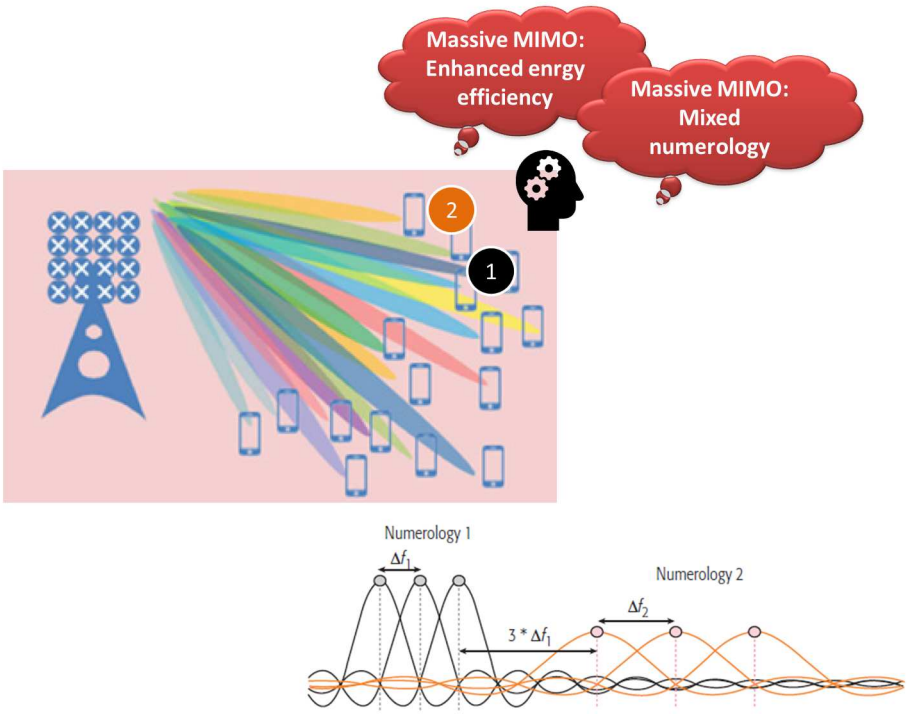

Figure 2.12: Massive MIMO - mixed numerology and enhanced energy efficiency.

groups of users with two different numerologies, INI appears only in frequency selective channels. Besides, the transmission of users using numerology with large SCS always achieves the best quality, only users using the numerology with small SCS suffer from INI. Based on the derived closed-form INI expressions, we have proposed an INI mitigation/cancellation procedure. The INI analysis and cancellation scheme, for massive MIMO-OFDM DL, have been published in a journal paper [87]. The work proposed in [87] has been extended to UL transmissions supporting different services and using different numerologies, while sharing the same frequency band. As for the DL scenario, we have first derived theoretical expressions of the INI and validated them by simulations. Then, based on this theoretical analysis, we proposed an INI cancellation scheme which can suppress the INI at the BS side without increasing the transmitter's complexity. These results have been published in a journal paper [88].

2.3.5.2 Enhanced energy efficiency of Massive-MIMO system

As said previously, the use of massive MIMO would significantly improve the energy efficiency of the 5G network, thanks to spatial multiplexing gain. However, the signals at the output of the multiuser (MU) precoder in single carrier or multi carrier mode exhibit high PAPR. From another side, the use of extensive and inexpensive low-power PA, could dramatically impacts the overall system performance if nothing is done to reduce the PAPR and/or increase the PA linearity region. During the second year of Xinying Cheng's PhD, we have been interested on this topic. We have designed an OFDM massive MIMO transceiver, taking into consideration MU precoding, PAPR reduction and DPD, with special care to the required computational complexity. The proposed precoder is solution of a convex optimization problem solved via steepest gradient descent (GD) approach. The proposed algorithm is compared to other equivalent transmission schemes, including different combinations of MU precoding, PAPR reduction and DPD processing. The main conclusion of this work is that the proposed transmission scheme provides low computational complexity than the other existing schemes while closely approaching their performance. A journal paper describing the proposed algorithm and its comparison with the existing solutions have been submitted to IEEE Transactions on Vehicular Technology.

The scientific contributions corresponding to this last research topic will be presented in chapter 6.

2.4 Conclusion

This chapter presented an overview of all my research activities. After a quick look to the main contributions made between 2003 and 2009 in the field of acoustics and digital audio processing, I introduced the general context of my activities at CNAM. Then, I presented the four research topics developed as associate professor at CNAM, as well as the contributions and collaborations developed since 2011. As the research axes are now clearly identified and introduced, the main related scientific contributions will be developed in chapters 3, 4, 5 and 6.

Chapter 3

MWF for 5G and beyond systems

3.1 Introduction

URLLC communications require minimizing network access times by allowing possible asynchronous communications between users. Indeed, the overhead required by orthogonal transmission to ensure synchronization becomes large and brings large latencies concerning network access. Beyond the relaxation of the constraint on the time asynchronism, other criteria must be considered during the comparative study of post-OFDM MWFs. As Key Performance Indicators (KPIs), we can consider: Power Spectral Density (PSD) localization, Spectral Efficiency (SE), End-to-End Physical layer latency, PAPR, transceiver complexity, adaptability to MIMO transmissions and performances over frequency-selective and/or time varying channels.

Among the studied MWFs, FBMC-OQAM was shown to be very attractive regarding frequency localization and robustness to users asynchronism. However, the high level of intrinsic interference makes it very sensitive to channel selectivity. This raised the need for advanced equalization techniques, exploiting the statistical properties of OQAM signals.

Between 2015 and 2019, I have been interested, within the framework of the WONG5 ANR project, on the study and comparison of post-OFDM MWFs, that would better meet the requirements of 5G cMTC/URLLC use case. This project involved CNAM, CEA-leti, THALES and CentraleSupélec. The results presented in this chapter have been carried with two post-doctoral researchers: Dr. Yahia Medjahdi and Dr. Rafik Zayani and a PhD student: Mrs. Hayfa Fhima.

3.2 Post-OFDM MWFs

3.2.1 MWFs classification

Before presenting the different MWF candidates for the physical layer of the future 5G URLLC applications, it should be interesting to classify them based on some crucial aspects. A possible classification of these MWFs can be achieved with respect to the orthogonality criterion. A given MWF is orthogonal when the transmitted symbols are separable at the receiver after propagation over distortion free channels. Based on this definition, we can distinguish three categories:

- Orthogonality in the complex domain $\mathbb{C}$: were complex-valued data symbols are transmitted every symbol period T with a subcarrier spacing F, where the symbol density $TF \geq 1$,
- Orthogonality in the real domain $\mathbb{R}$: due to the use of time-frequency well-localized prototype function, the orthogonality is restricted to $\mathbb{R}$ by transmitting real-valued data symbols [89]. To maintain the symbol density at $TF = 1$, two real-valued symbols are transmitted per unit time-frequency lattice area. In such a case, we find offset-QAM (OQAM)-based MWFs,
- Non-orthogonality: the concept of transmitting real data instead of complex one, makes more complex the MIMO adaptation of the OQAM based techniques due to the high level of inherent interference brought by the prototype filter. Other solutions have been proposed to optimize the prototype filter response and transmitting complex QAM symbols rather than real ones. In this category we can cite FBMC-QAM and GFDM proposals.

In addition to the orthogonality-based classification, MWF can be clustered by considering the possible usage of filtering/windowing at transmitter (Tx) and/or receiver (Rx) and the granularity: subcarrier

MWFs	Orthogonality	Filtering granularity	Guard interval
CP-OFDM	$\mathbb{C}$	n/a	CP
WOLA-OFDM	$\mathbb{C}$	n/a	CP
UF-OFDM	$\mathbb{C}$	RB	ZP
f-OFDM	$\mathbb{C}$	sub-band	CP
N-Cont.-OFDM	$\mathbb{C}$	n/a	CP
FMT	$\mathbb{C}$	subcarrier	n/a
FFT-FBMC	$\mathbb{C}$	RB	CP
BF-OFDM	$\mathbb{C}$	RB	CP
FBMC-OQAM	$\mathbb{R}$	subcarrier	n/a
Lapped-OFDM	$\mathbb{R}$	subcarrier	n/a
WCP-COQAM	$\mathbb{R}$	subcarrier	CP
WOLA-COQAM	$\mathbb{R}$	subcarrier	CP
FBMC-QAM	Non Orthogonal	subcarrier	n/a
GFDM	Non Orthogonal	subcarrier	CP

Table 3.1: MWFs classification.

wise vs resource block (RB) wise. Another classification can be based on wether a given MWF uses or not cyclic extensions to absorb filters transient response and/or channel delay spread. In Tab. 3.1, I give different possibilities to classify the MWFs that will be studied and compared in this chapter.

CP-OFDM and Filtered/windowed MWFs which are orthogonal in the complex domain (WOLA-OFDM, UF-OFDM, N-Continuous OFDM, FMT, BF-OFDM, FFT-FBMC) are in fact orthogonal only for propagation channels which are not too frequency selective. For such MWFs, the use of MIMO technology is straightforward. However, filtered MWFs which are not orthogonal in the complex domain (FBMC-OQAM, Lapped-OFDM, WCP-COQAM, WOLA-COQAM, FBMC-QAM, GFDM) generate both ISI and ICI at reception. These interferences explain the strong performance degradation of most of the standard MIMO schemes used for CP-OFDM, even for propagation channels which are relatively weakly frequency selective. For this reason, advanced MIMO schemes, aiming at mitigating the effects of ISI and ICI, are required for non-complex orthogonal filtered MWFs.

3.2.2 MWFs description

CP-OFDM CP-OFDM is widely used in several wireless standards (e.g., IEEE 802.11 and 3GPP-LTE). It consists of splitting up a stream of complex symbols at high-rate into several lower-rate streams transmitted on a set of orthogonal subcarriers which are implemented using the inverse fast Fourier transform (IFFT). The CP-OFDM receiver can be implemented using the fast Fourier transform (FFT). In order to keep the orthogonality between subcarriers, a cyclic prefix (CP) is usually inserted. Therefore, after the FFT operation, the channel equalization becomes trivial through a single coefficient per subcarrier. This modulation is used for 4G/LTE system and it is also the one chosen for 5G NR. In the following, this MWF will be considered as basis of comparison.

WOLA-OFDM To maintain the benefits of CP-OFDM while reducing the Out-Of-Band (OOB) emissions, straightforward enhancements can be made to smooth the time-domain discontinuities between adjacent symbols. This approach named WOLA-OFDM have been introduced by Qualcomm [25].

In WOLA-OFDM Tx, the soft edges are added to the cyclic extensions of a given symbol by a time domain windowing. More specifically, the windowing operation can be performed on both the original CP and the newly added cyclic suffix as depicted by Fig. 3.1 (a). To create this latter, we copy and append the first W_{Tx} samples of a given symbol to its end. Adjacent symbols could overlap with each other in the edge transition regions, which leads to a similar overhead as in the CP-OFDM.

In addition to the transmit windowing, an advanced receive windowing is applied to suppress the asynchronous inter-user interference (i.e., adjacent non-orthogonal signals). In the first step, the receiver takes $N_s + 2W_{\mathrm{Rx}}$ samples ($N_s = N_{\mathrm{FFT}}$ denotes the FFT size), which correspond to the samples of one

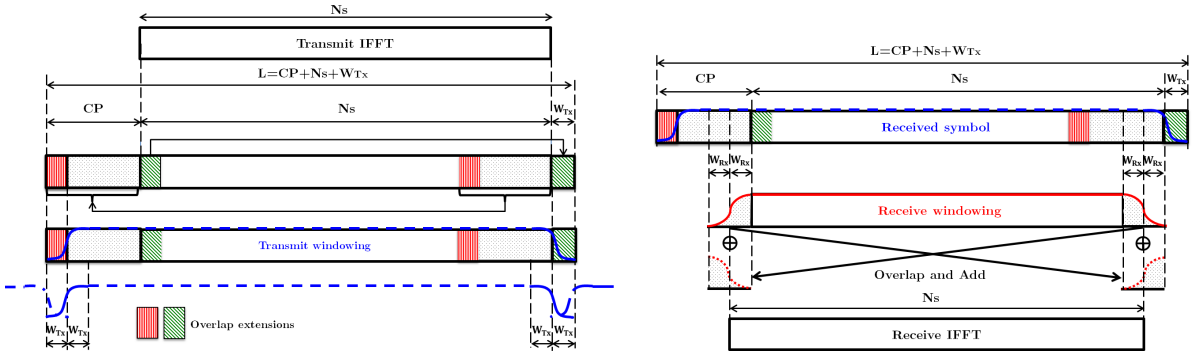

(a) Tx. (b) Rx.

Figure 3.1: WOLA processing.

WOLA-OFDM symbol. Then, these samples are windowed. In the second step, an Overlap and Add processing is applied to create the useful N_s samples from the $N_s + 2W_{\text{Rx}}$ ones, as depicted by 3.1 (b).

This MWF has been studied and implemented at CNAM, during the postdoctoral stay of Dr. Rafik Zayani. The performance of this MWF in asynchronous conditions has been published in a well cited conference paper [38].

UF-OFDM UF-OFDM has been proposed by Alcatel-Lucent Bell Laboratories [26], and it is also referred to UFMC in the literature [90]. UF-OFDM is a combination of ZP-OFDM (traditional CP-OFDM where the CP is replaced by a Zero Padding (ZP) [91]) and filtered-OFDM which will be presented in the next paragraph: each OFDM symbol at the output of the IFFT is filtered and the ZP is used to absorb the filter transient response. When the channel is perfect, UF-OFDM holds the orthogonality of the subcarriers. Nevertheless, the orthogonality is no longer sustained as the time spreading of the channel increases. At the reception, the multiuser interferences coming from time and frequency asynchronism are first reduced by applying a window on the received UF-OFDM block symbols [92]. Finally, a FFT of size two times greater than the IFFT used at the transmitter is applied to the received UF-OFDM block symbols and only even subcarrier indexes are kept. With Dr. Yahia Medjahdi, we have studied and implemented this MWF.

Filtered-OFDM f-OFDM was proposed as a 5G candidate at the 3GPP RAN1 workgroup [93]. At the transmitter side, the poor OOB radiation of traditional CP-OFDM is improved thanks to a filter applied to the CP-OFDM symbol. At the receiver side, the interferences coming from time and frequency asynchronous adjacent users are reduced using a similar filter at the input of a CP-OFDM receiver. The filtering process required by f-OFDM generates inter block interferences, but if the filter is properly designed the impact of these interferences on the link performance are negligible [93]. It must be noted that the ramp-up and the ramp down generated by the filter increase the burst length and consequently the latency, reducing so the spectral efficiency.

N-continous OFDM The N-continuous OFDM scheme has been introduced in [28]. The idea of this MWF consists in creating consecutive adjacent CP-OFDM symbols which are continuous in the time domain to improve the poor OOB radiation of traditional CP-OFDM. The construction of OFDM symbols will render the transmitted signal and its first N derivatives continuous using a precoding matrix which is placed between the symbol mapping and the IFFT. One advantage of N-continuous OFDM scheme is to have traditional CP-OFDM as its core MWF at both transmitter and receiver sides. Nevertheless, in its basic form, this scheme requires the transmission of side information (precoding matrix) to the receiver to recover the data. A solution to cope with this problem has been proposed in [94] and consists in using a systematic precoding matrix.

FMT FMT is a multicarrier modulation technique that has been specifically developed for DSL applications [29]. In FMT, a conventional method of frequency division multiplexing is used, i.e., the

subcarrier bands are not overlapping. Each subcarrier is a traditional single carrier modulation filtered with square-root Nyquist filter. This filter limits the effective transmission bandwidth of each band to $B = (1+\alpha) \cdot D_s$, where D_s is the symbol rate and α is the roll off factor, which should be judiciously chosen to avoid large square root Nyquist filter length which drastically increases the latency and the overhead. Some recent works have proposed new filters [95] in order to cope as much as possible with this problem providing a good compromise between OOB radiation and group delay.

FBMC-OQAM & Lapped-OFDM One of the drawbacks of the CP-OFDM and some of the windowing/filtering-based OFDM MWFs previously introduced is the loss of spectral efficiency due to the use of CP or specific guard band. This leads to a symbol density greater than 1. Thus, to avoid this drawback, we have to choose a MWF with symbol density of one. However, it is theoretically proven, based on the Balian Low theorem [89], that it is not possible to fulfill simultaneously (1) a prototype filter which is well-localized in both time and frequency domain, (2) the transmission of data symbols satisfying complex orthogonality and (3) a symbol density equal to 1. To achieve these objectives, we can restrict the orthogonality condition to the real domain. In this case and over a distortion-free propagation channel, it is possible to recover the data at the receiver side when real-valued (or purely imaginary) Pulse Amplitude Modulation (PAM) is used instead of Quadrature Amplitude Modulation (QAM). With this solution and to maintain a symbol density equal to 1, we should transmit two real-valued symbols per unit area of the time-frequency lattice. One of the pioneering solutions, fulfilling the Balian Low theorem, and called FBMC-OQAM (FBMC based on transmitting Offset-QAM symbols), was proposed by Saltzberg [89] in the mid-1960s.

The key-idea of FBMC-OQAM is to use well-frequency localized prototype filters, providing thus improved adjacent channel leakage performance compared to CP-OFDM. To ensure orthogonality between adjacent symbols and adjacent subcarriers, while keeping maximum spectral efficiency, Nyquist constraints on the prototype filter combined with OQAM are used, bringing so the orthogonality from the complex domain to the real one. Indeed, in OQAM, the in-phase and the quadrature components of a given QAM symbol are time staggered by half a symbol period. The duration of the prototype filters is usually a multiple of the FFT size (KN_{fft}), where K is called the overlapping factor and N_{FFT} the total number of subcarriers. With Dr. Yahia Medjahdi, we considered two prototype filters: (1) FBMC-OQAM based on the most used PHYDYAS filter [96] with $K = 4$ and (2) Lapped-OFDM using the sine prototype filter with $K = 2$ [31].

The baseband of the FBMC-OQAM transmitted signal can be defined as follows [51] :

$$x(t) = \sum_{m=0}^{N_{FFT}-1} \sum_{n=-\infty}^{+\infty} a_{m,n} h(t - nT/2) e^{j\frac{2\pi}{T}mt} e^{j\varphi_{m,n}}, \tag{3.1}$$

where $h(t)$ is the prototype filter impulse response, $a_{m,n}$ are real-valued symbols and $\varphi_{m,n}$ is a phase term equal to $\frac{\pi}{2}(m+n) - \pi mn$.

Considering the shifted versions of $h(t)$ in time and frequency noted: $\gamma_{m,n}(t) = h(t - nT/2)e^{j\frac{2\pi}{T}mt}e^{j\varphi_{m,n}}$, in a distortion-free noise-less channel, the demodulated signal y_{m_0,n_0} at time instant n_0 and subcarrier m_0 is given by:

$$\begin{aligned} y_{m_0,n_0} &= \langle x(t), \gamma_{m_0,n_0}(t) \rangle = \int_{-\infty}^{+\infty} i(t) \gamma^*_{m_0,n_0}(t) dt = \sum_{n=-\infty}^{+\infty} \sum_{m=0}^{N_{FFT}-1} a_{m,n} \int_{-\infty}^{+\infty} \gamma_{m,n}(t) \gamma^*_{m_0,n_0}(t) dt \\ &= a_{m_0,n_0} + \sum_{m \neq m_0} \sum_{n \neq n_0} a_{m,n} \underbrace{\int_{-\infty}^{+\infty} \gamma_{m,n}(t) \gamma^*_{m_0,n_0}(t) dt}_{\Psi_{m_0,n_0}} = a_{m_0,n_0} + j u_{m_0,n_0}, \end{aligned} \tag{3.2}$$

where $\gamma^*_{m_0,n_0}(t)$ is the complex conjugate of $\gamma_{m_0,n_0}(t)$ and $\langle ., . \rangle$ stands for the inner product.

According to [97], the prototype filter is designed such that the intrinsic interference term is orthogonal to the useful symbol i.e. is purely imaginary. Considering the PHYDYAS prototype filter proposed in [97],

	n_0-3	n_0-2	n_0-1	n_0	n_0+1	n_0+2	n_0+3
m_0-1	$0.043j$	$0.125j$	$0.206j$	$0.239j$	$0.206j$	$0.125j$	$0.043j$
m_0	$-0.067j$	0	$-0.564j$	1	$0.564j$	0	$0.067j$
m_0+1	$0.043j$	$-0.125j$	$0.206j$	$-0.239j$	$-0.206j$	$-0.125j$	$0.043j$

Table 3.2: Transmultiplexer impulse response.

the coefficients Ψ_{m_0,n_0} are given in table 3.2. Consequently, a perfect reconstruction of the transmitted real symbols $a_{m,n}$ is obtained by taking the real part (OQAM decision) of the demodulated signal y_{m_0,n_0}.

WCP-COQAM and WOLA-COQAM Despite the various advantages of FBMC-OQAM systems, the long prototype filters could be questionable for URLLC communications [98]. Besides, FBMC-OQAM signals are not suitable to short packet transmission due to long ramp-up/down of the prototype filter leading thus to a non-negligible loss in spectral efficiency. In order to overcome this situation, burst truncation can reduce this loss but it has detrimental effects like additional interference and significant OOB radiation [99]. Circular convolution with time-windowing was proposed in [33], [32] to remove the overhead signal while maintaining smooth transition at the burst edges. This solution is known as Windowed Cyclic Prefix-based Circular-OQAM (WCP-COQAM). In order to avoid multipath channel interference, a CP can easily be inserted since COQAM corresponds to a block transform [32]. Thanks to circular convolution, the continuity of CP-COQAM signal is maintained inside a given CP-COQAM block. However, since signal discontinuities can be observed between different CP-COQAM blocks, there is no remarkable difference between the CP-COQAM spectrum and CP-OFDM one [100]. Note that this behavior is independent of how well is localized the prototype filter frequency response. At the receiver side, the CP is removed, windowed samples are compensated and the receive circular convolution is applied afterwards. The OQAM decision is then made to recover the desired useful data symbols.

In [38], we compared WOLA-OFDM and UF-OFDM in relaxed synchronization scenario. The obtained results show that WOLA-OFDM outperforms UF-OFDM in various asynchronous configurations. Motivated by this result, we investigated, during the postdoctoral stay of Dr. Yahia Medjahdi, the effectiveness of WOLA processing on WCP-COQAM. The modified MWF is called WOLA-COQAM, where the WOLA transmitter performs a time domain windowing to produce soft edges at the beginning and the end of the original transmitted block, which length is cyclically extended from $N_s = KN_{\text{FFT}}$ samples to $N_s + CP + W_{Tx}$ (see Fig. 3.1 (a)). In addition to the transmit windowing, the WOLA processing is also applied at the receiver side in order to enhance asynchronous inter-user interference suppression, as illustrated in Fig. 3.1 (b). Note that the applied receive window is independent of the transmit one and its length is equal to $N_s + 2W_{Rx}$. This windowing is followed by Overlap and Add processing which minimizes the effects of windowing on the useful data.

FFT-FBMC In order to overcome the FBMC-OQAM intrinsic interference issue, a precoded FBMC scheme has been proposed in [101, 36]. This scheme proceeds by precoding the data in a subcarrier-wise manner using an IFFT. In FFT-FBMC proposal, blocks of $N/2$ data complex symbols in each subcarrier k go through a N-IFFT operation. The $N/2$ data symbols are alternately fed to the first and last $N/2$ bins of the N-IFFT. When the subcarrier index k is odd (resp. even), the symbols are fed to the first (resp. last) $N/2$ bins. After that, the N-IFFT outputs are extended with a CP of size L, and fed to the FBMC modulator of M carriers.

Thus, the interference coming from others subcarrier is removed by a simple equalization thanks to the subcarrier-wise IFFT/FFT precoding/decoding and CP insertion. Whereas the interference coming from the adjacent carriers can be avoided by a special data transmission strategy and a good frequency-localized prototype filter. Fig. 3.2 (a) depicts the scheme of the FFT-FBMC Tx proposed in [101].

At the output of the FBMC demodulator, the serial symbols in each subcarrier q are reshaped into blocks of size $N + L$ to only keep N symbols in each block. This operation is referred to as "S/P + CP removal" in Fig. 3.2 (b) . After that, N symbols of each block are fed to a N-FFT whose only $N/2$

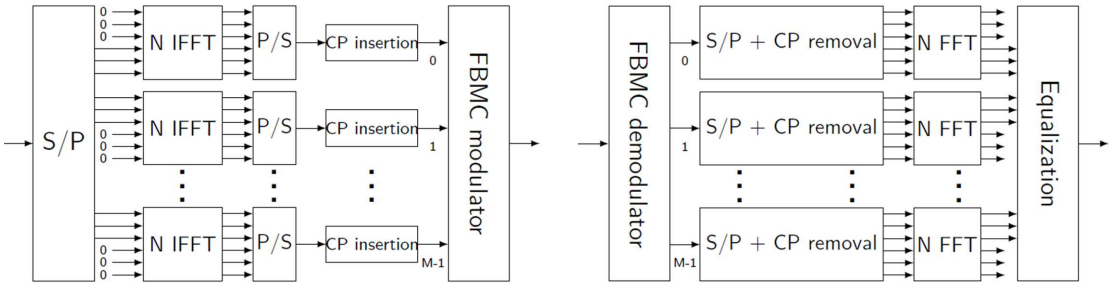

(a) Tx. (b) Rx.

Figure 3.2: FFT-FBMC transeiver.

output symbols are kept for detection. Again, the first $N/2$ output symbols are kept when the subcarrier index q is odd, and the last $N/2$ symbols are kept when q is even.

The intercarrier interference is avoided thanks to the $N/2$ zeros inserted in the N-IFFT in each sub-band, ensuring the orthogonality in the complex domain [102] and the efficiency of single-tap equalization [103].

BF-OFDM Block-Filtered OFDM (BF-OFDM) is another precoded filter-bank multi-carrier modulation that has been introduced by CEA-leti [104, 37]. The precoding scheme is performed by means of CP-OFDM modulators (of size N) and the filtering operation is applied with a Poly Phase network (PPN) (of size M) as for FFT-FBMC. However, the main difference with respect to this latter is the insertion of a filter pre-distortion stage at the transmitter side. The extra stage aims at compensating the distortion induced by the filter to flatten the transmitted signal spectrum inside the carrier bandwidth. As a consequence, no filtering stage is required at the receiver side to properly recover the signal and the receiver scheme can be reduced to a simple $\frac{MN}{2}$-FFT preceded by a CP removal.

FBMC-QAM FBMC-OQAM uses a per-subcarrier filtering, reducing thus OOB emission and providing more flexibility to meet 5G NR requirements. Such enhancements are at the price of orthogonality condition that only holds in the real domain and is no longer valid in the presence of realistic channels. Indeed, the self-interference inherent to OQAM-based schemes is a major problem when considering MIMO schemes [105], [106]. Some solution schemes were proposed based on iterative interference estimation and cancellation. However, such solutions are limited by error propagation induced by the residual interference since the interference power is as strong as the useful signal power [30], [107]. In order to overcome this problem, it has been demonstrated, in [108] and [109], that the interference power must be small and should be kept under a certain threshold, in order to counteract the error propagation phenomenon and consequently make more efficient the interference cancellation scheme. In order to achieve this objective and reduce the interference level, the authors in [107] proposed the use of QAM modulation, instead of OQAM one, in FBMC systems. Actually, a significant part of self-interference is avoided by only transmitting QAM symbols every signalling period $nT, n \in \mathbb{Z}$. Such a combination is called FBMC-QAM systems. In order to improve the performance of FBMC-QAM symbols, new prototype filters have been designed, optimizing simultaneously spectrum localization, self-interference level, and overall spectral efficiency [34].

GFDM Generalized Frequency Division Multiplexing (GFDM) is a MWF performing a time-frequency filtering over a data block [35]. This MWF is therefore flexible but also non-orthogonal. A data block corresponds to the set of symbols transmitted over a group of N_{FFT} consecutive subcarriers over N_B time slots and thus is composed of $N_{FFT} \times N_B$ symbols. The sub-carrier wise filtering is performed by means of circular convolution. However, as the symbols overlap in both time and frequency, interference (inter and intra data blocks) is generated. It is worth noticing that inter data block interference can be avoided by proper dimensioning of the CP.

In the literature two receiver schemes have prevailed: the Matched Filter (MF) and the ZF architectures [110]. With the MF approach, the received blocks are filtered by the transmission matched

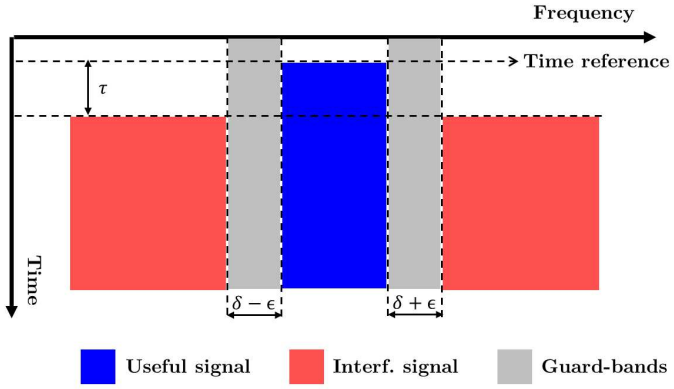

Figure 3.3: Coexistence scenario: two asynchronous users with τ [s] TO, ε [kHz] CFO and free guard-bands of δ $[kHz]$.

filters. This scheme provides low complexity but poor performance due to ISI. When it comes to the ZF approach, the signal is demodulated with the Moore pseudo-inverse of the transmitter matrix. This scheme suffers from noise enhancement and the provided performance depends on the properties of the transmitter matrix [111].

3.3 MWFs comparison

In this section, I will present a comparison of the MWFs introduced previously. The studies, carried under my supervision, have been achieved during the postdoctoral stay of Dr. Yahia Medjahdi.

I would like to stress that the results presented in this section are a selection of the work published in the review paper [40]. Also, to simplify the presentation, some results corresponding for example to the comparison of MWFs in terms of PAPR and robustness over frequency selective channels will not be developed in this section. Interested readers may refer to [40, 42], for a more detailed description of the results presented here.

3.3.1 Comparison scenario

Except for BF-OFDM and FFT-FBMC, the total number of active sub-carriers for all the other MWFs is equal to 1024 and the corresponding Sub Carrier Spacing (SCS) is equal to 15 kHz. Among these waveforms, the size of the guard interval for those using a CP is $N_{CP} = 72$, corresponding to a maximum delay spread of 4.68 μs. For BF-OFDM and FFT-FBMC, we considered 64 carriers, with an SCS equal to 180 kHz (1 LTE-RB bandwidth.). The number of active subcarriers has been set at $N/2 = 32$. For these two waveforms, we have considered a CP of size $N_{CP} = 4$.

The comparison scenario, depicted in Fig. 3.3, corresponds to two coexisting users sharing the available frequency band, where the blue colored area and the red colored one correspond to the time/frequency resources allocated to the user of interest (UI) and to the interfering one, respectively. The useful signal occupies 3 LTE RB corresponding to 540 kHz, while the interfering bandwidth is equal to 1.62 MHz (i.e., 9 LTE-RB) equally portioned on the two sides of the useful signal. A guard-band of δ kHz, illustrated by the gray colored area, is separating the frequency bands of both users.

The receiver of interest is assumed to be perfectly synchronized, in both time and frequency domains (i.e. neither Timing Offset (TO) nor Carrier Frequency Offset (CFO) are considered), and is located at equal distance from both transmitters[1]. However, as illustrated in Fig. 3.3, a time/frequency synchronization misalignment (τ and ε denote timing and carrier frequency offsets, respectively) can occur between the receiver of interest and the interfering user. Note that we consider a TO distributed between $-T/2$ and $+T/2$, where T is the OFDM symbol duration ($T = 66.66$ μs). Due to this synchronization mismatch, the receiver of interest potentially suffers from the interference inducing thus performance

[1] Note that in this work, we assumed the same transmit power per subcarrier for both useful and interfering users

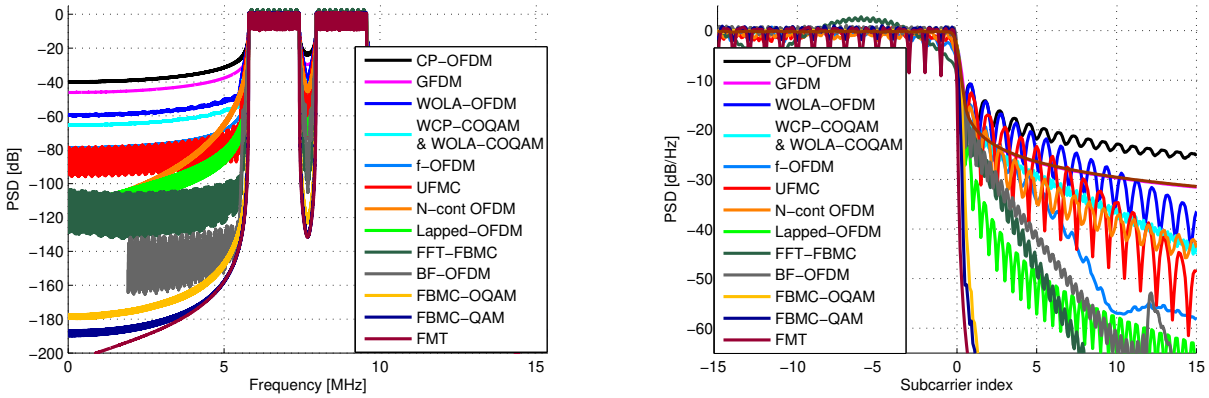

Figure 3.4: Interference users PSD comparison.

degradation. To highlight the impact of this interference, we consider perfect and noiseless channels between both transmitters on one side and the victim receiver on the other side.

3.3.2 Power Spectral Density

It is well established that traditional CP-OFDM has poor frequency domain localization. In LTE, 10% of the system bandwidth is used for guard bands. These large guard bands located at both edges of the spectrum are necessary to reach enough attenuation to meet LTE spectrum mask requirement. It is expected that 5G and beyond systems use more efficiently the allocated bandwidth and improve the overall spectral efficiency of the system. Thus, good, or excellent spectral containment will be a key parameter for future 5G and beyond MWF in order to support neighboring signals.

We present in Fig. 3.4 the PSD comparison of the considered MWFs. We choose to plot only the contribution of the interference users (IUs) so that we can observe at the same time the level of OOB emission and the level of emission within a spectral hole corresponding to the UI. As expected, the worst PSD performance is given by CP-OFDM MWF. The far-end PSD is dominated by the MWFs adopting subcarrier wise filtering, namely Lapped-OFDM, FBMC-QAM, FBMC-OQAM and FMT. BF-OFDM and FFT-FBMC provide also excellent PSD performances thanks to the use of the filter bank approach in the signal construction. N-continuous OFDM has a relatively slow decaying but provides good far-end PSD. UF-OFDM and f-OFDM apply their filter to a group of subcarriers, and we can observe that their performances are in the same order of magnitude. WCP-COQAM and WOLA-COQAM present moderate far-end PSD performance due to time domain transition between successive blocks. The time domain windowing applied by WOLA-OFDM improves by about 20 dB the spectral containment of CP-OFDM, but its far-end PSD performance remains moderate. Like WCP-COQAM and WOLA-COQAM, GFDM is not very well localized in the frequency domain due to the block construction of GFDM signal generating time domain transitions between blocks.

3.3.3 Spectral efficiency and latency

Spectral efficiency (SE), given in bits/s/Hz, is a key parameter for high data rate systems since it gives a clear idea of the achievable data rates for a given bandwidth. In Tab. 3.3, we present the SE according to the number of transmitted parallel vector symbols S, and also its asymptotic version called Asymptotic Spectral Efficiency (ASE) where S tends toward infinity. The required number of parallel vectors is different for each MWF and depends on the number of complex QAM symbols N_{QAM} to be transmitted, but also on the way a block symbol is built. S is given by:

WF	Spectral Efficiency	Asymptotic Spectral Efficiency	End-to-End Physical layer latency
CP-OFDM	$\frac{N_{\text{FFT}}}{N_{\text{FFT}}+N_{CP}}$	$\frac{N_{\text{FFT}}}{N_{\text{FFT}}+N_{CP}}$	$S \times \frac{N_{\text{FFT}}+N_{CP}}{F_s}$
WOLA-OFDM	$\frac{S\times N_{\text{FFT}}}{S\times(N_{\text{FFT}}+N_{CP})+W_{\text{Tx}}}$	$\frac{N_{\text{FFT}}}{N_{\text{FFT}}+N_{CP}}$	$\frac{S\times(N_{\text{FFT}}+N_{CP})+W_{\text{Tx}}}{F_s}$
UF-OFDM	$\frac{N_{\text{FFT}}}{N_{\text{FFT}}+ZP}$	$\frac{N_{\text{FFT}}}{N_{\text{FFT}}+ZP}$	$S \times \frac{N_{\text{FFT}}+L_{\text{ZP UF-OFDM}}}{F_s}$
f-OFDM	$\frac{S\times N_{\text{FFT}}}{S\times(N_{\text{FFT}}+N_{CP})+L_{\text{Trunc}}}$	$\frac{N_{\text{FFT}}}{N_{\text{FFT}}+N_{CP}}$	$\frac{S\times(N_{\text{FFT}}+N_{CP})+L_{\text{Trunc}}}{F_s}$
N-Cont OFDM	$\frac{N_{\text{FFT}}}{N_{\text{FFT}}+N_{CP}}$	$\frac{N_{\text{FFT}}}{N_{\text{FFT}}+N_{CP}}$	$S \times \frac{N_{\text{FFT}}+N_{CP}}{F_s}$
FMT	$\frac{S}{(S+K-1)(1+\alpha)}$	$\frac{1}{1+\alpha}$	$\frac{(S-1+K)N_{\text{FFT}}}{F_s}$
FFT-FBMC	$\frac{S\times\frac{N}{2}}{K+\frac{1}{2}[S\times(N+N_{CP})-1]}$	$\frac{N}{N+N_{CP}}$	$\frac{M\times\frac{N}{2}\times S+M\times\frac{N_{CP}}{2}\times(S-1)+\left[(N_{CP}-3)\times\frac{M}{4}+K\times\frac{M}{2}\right]}{F_s}$
BF-OFDM	$\frac{S\times\frac{N}{2}}{K+\frac{1}{2}[S\times(N+N_{CP})-1]}$	$\frac{N}{N+N_{CP}}$	$\frac{\frac{M}{2}\left[S\times N+N_{CP}(S-1)+\frac{N_{CP}-3}{2}+K\right]}{F_s}$
FBMC-OQAM	$\frac{S}{S+K-1/2}$	1	$N_{\text{FFT}}\frac{S-\frac{1}{2}+K}{F_s}$
Lapped-OFDM	$\frac{S}{S+3/2}$	1	$\frac{S+\frac{3}{2}}{F_s}$
WCP-COQAM	$\frac{KN_{\text{FFT}}}{KN_{\text{FFT}}+N_{CP}}$	$\frac{KN_{\text{FFT}}}{KN_{\text{FFT}}+N_{CP}}$	$S \times \frac{KN_{\text{FFT}}+N_{CP}}{F_s}$
WOLA-COQAM	$\frac{S\times K\times N_{\text{FFT}}}{S\times(K\times N_{\text{FFT}}+N_{CP})+W_{\text{Tx}}}$	$\frac{K\times N_{\text{FFT}}}{K\times N_{\text{FFT}}+N_{CP}}$	$\frac{S\times(K\times N_{\text{FFT}}+N_{CP})+W_{\text{Tx}}}{F_s}$
FBMC-QAM	$\frac{S}{S+K-1}$	1	$N_{\text{FFT}}\frac{S-1+K}{F_s}$
GFDM	$\frac{N_B\times N_{\text{FFT}}}{N_B\times N_{\text{FFT}}+N_{CP}}$	$\frac{N_B\times N_{\text{FFT}}}{N_B\times N_{\text{FFT}}+N_{CP}}$	$S\frac{N_B\times N_{\text{FFT}}+N_{CP}}{F_s}$

Table 3.3: Spectral efficiency and End-to-End Physical layer latency comparisons.

$$S = \begin{cases} \lceil \frac{N_{QAM}}{K\times N_{FFT}} \rceil & \text{for WCP-OQAM and WOLA-COQAM} \\ \lceil \frac{N_{QAM}}{N_B\times N_{FFT}} \rceil & \text{for GFDM} \\ \lceil \frac{N_{QAM}}{M\times\frac{N}{2}} \rceil & \text{for FFT-FBMC and BF-OFDM} \\ \lceil \frac{N_{QAM}}{N_{FFT}} \rceil & \text{otherwise} \end{cases} \tag{3.3}$$

where $\lceil . \rceil$ refers to the ceiling operation, N_B is the number of time slots (for GFDM), N_{FFT} is the total number of subcarriers for all the MWFs excepting FFT-OFDM and BF-OFDM. For these last ones, N and M are respectively the number of used subcarriers and the number of active carriers. We can observe that for small values of S, the MWFs which have their filter applied to each subcarrier have a spectral efficiency penalty due to their longer impulse response. This is especially true for FMT since the overlap factor K is usually much longer: for instance, we usually consider $K = 16$ for a roll off factor of 0.25, instead of $K = 2$ for Lapped-OFDM or $K = 4$ for FBMC-OQAM and FBMC-QAM. All the MWFs which require a guard interval (CP or ZP) suffer from the fact that this guard interval does not transmit any useful information. When S tends toward infinity, only FBMC derivatives (Lapped-OFDM, FBMC-OQAM and QAM) achieve full capacity, i.e., $ASE = 1$.

The latency of a MWF is a crucial key parameter in URLLC communications. In our analysis, we use the End-to-End (E2E) physical layer latency criterion defined as the time delay from which the forward error correction is capable to decode the bits corresponding to the N_{QAM} transmitted symbols. E2E latency comparison is provided by table 3.3. In this table, F_s is the sampling frequency equal to 15.36 MHz for all the MWFs, excepting FFT-FBMC and BF-OFDM, for which the sampling frequency is equal to 11.52 MHz. In order to better assess the performance of the other MWFs, we present in Fig. 3.5 the E2E with respect to traditional CP-OFDM scheme. In this figure, we can observe that the large group delay of the FMT prototype filter and the loss of spectral efficiency due to the roll off factor drastically increases the latency of FMT scheme. All other MWFs latencies are in the same order of magnitude as CP-OFDM. We can also observe that for small N_{QAM} values, the latency of WOLA-OFDM is very similar to the one of CP-OFDM while MWFs with long impulse response filters suffer and yield to higher latencies. When N_{QAM} increases, FBMC based MWFs become a little bit better than OFDM.

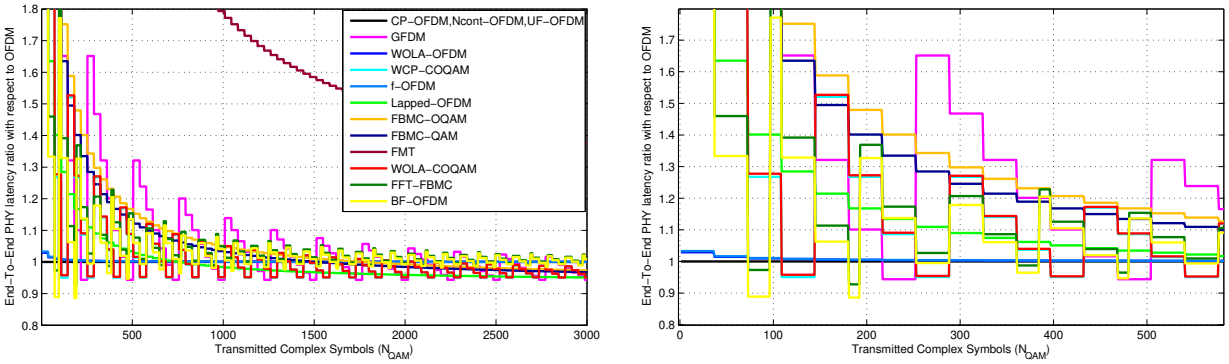

Figure 3.5: End-to-End Physical layer latency ratio with respect to traditional CP-OFDM scheme for a user which used 3 RB.

3.3.4 Influence of timing offset

In this section, we discuss the performance of the considered MWFs in multi-user asynchronous access in time. The asynchronous interference impact on the performance of the various MWF schemes will be assessed using the normalized mean square error (MSE) on the decoded symbols (of the UI) in ideal noiseless channel. Per-subcarrier MSE can provide a meaningful information about the distribution of asynchronous interference across useful subcarriers. Two cases of guard-bands are examined: $\delta = 0$ and 75 kHz.

To distinguish the degradation induced by timing synchronization errors from the one caused by CFO, we consider in this section that there is no CFO between the interfering signal and the useful one. The timing misalignment τ varies from $-T/2 = -33.33$ μs to $T/2 = 33.33$ μs. The per-subcarrier MSEs of MWFs are depicted in Fig. 3.6. In CP-OFDM case, we can see that the orthogonality between subcarriers is maintained if the delay error τ does not exceed the CP duration. When τ is outside the CP interval, the orthogonality is no longer ensured. This loss of orthogonality gives rise to a strong level of asynchronous interference even when increasing the guard band. Such a behavior is due to the poor frequency localization of the rectangular transmit/receive OFDM filters.

For WOLA-OFDM, we can see that the interference level in the middle of the bandwidth becomes lower (approx. -35 dB) compared to CP-OFDM scheme. We can also see that blue colored area (MSE less than -30 dB) becomes larger when increasing the guard band. This can be explained by the fact that WOLA processing applied at the receiver is able to suppress inter-user interference as well.

Thanks to the per-RB filtering, the UF-OFDM scheme shows better performance compared to CP-OFDM. Indeed, thanks to additional windowing at the receiver side, UF-OFDM offers interesting gain when the TO is outside the ZP region. Like WOLA-OFDM, the ZP region offering the lowest MSE is significantly reduced in UF-OFDM because the ZP length is originally used to absorb the transmit filter response. Furthermore, when increasing the spectral distance of the victim subcarrier from the interfering ones, the interference level decay is more important compared to CP-OFDM but less significant when compared to WOLA-OFDM.

In f-OFDM scheme, since filtering is applied at both transmitter and receiver sides, the inner subcarriers are more protected compared to the previous schemes. In fact, the long filters used in this MWF offers a better frequency localization of the transmitted signals and a better protection against inter-user interference compared to WOLA-OFDM and UF-OFDM.

Concerning N-cont. OFDM, one can see that the MSE is close to that of UF-OFDM when TO exceeds the CP region. Inside this region, the orthogonality between subcarriers is maintained as in CP-OFDM case leading thus to the absence of asynchronous interference.

In FMT case, we can observe that there is no (or negligible) asynchronous interference. Such a result is due to no (or negligible) interaction between subcarriers. Indeed, each FMT subcarrier can be seen as a traditional single carrier modulation which respects the Nyquist criteria thanks to the long transmit/receive FMT filters. Note that this excellent robustness against asynchronous interference is

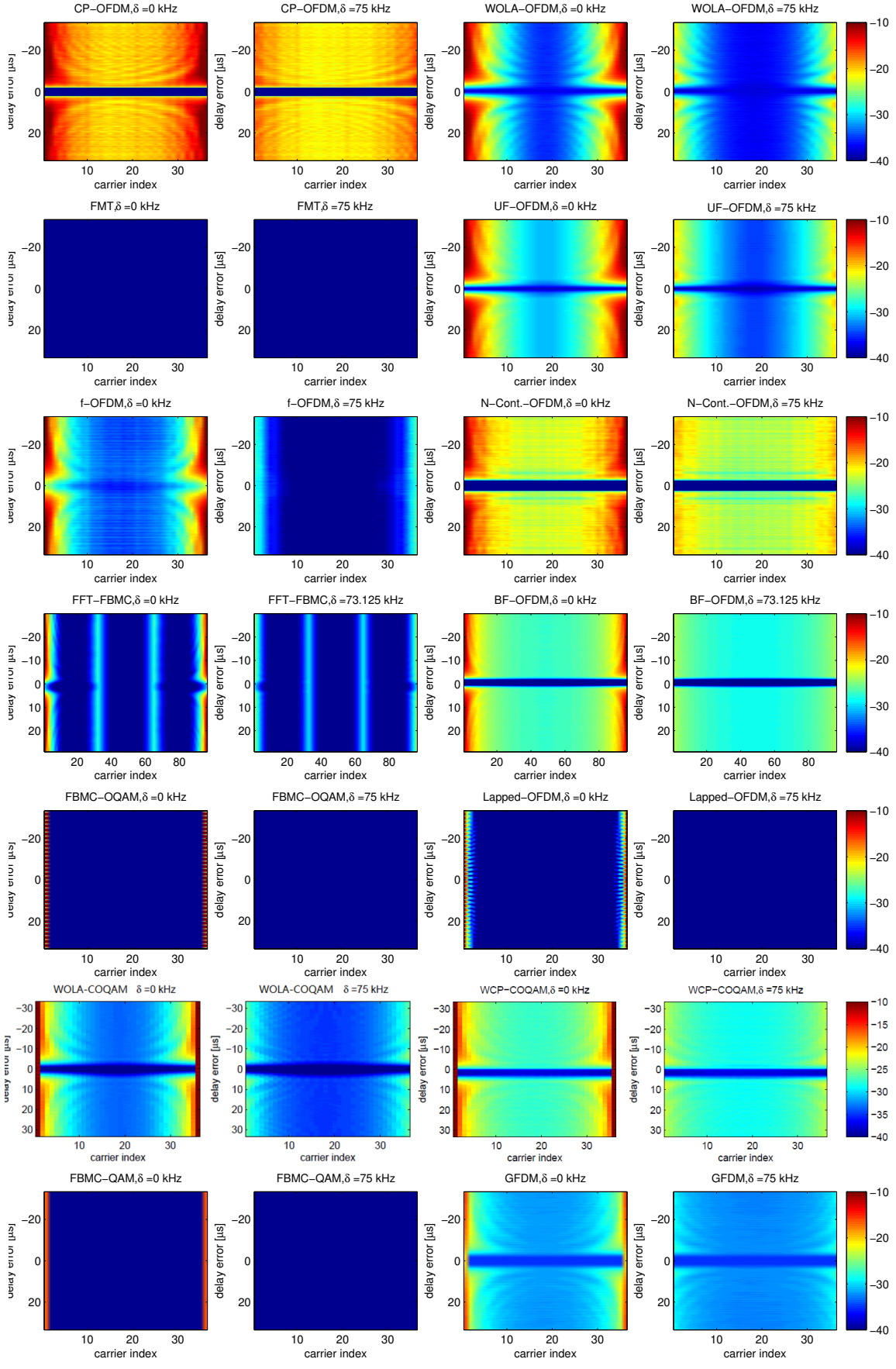

Figure 3.6: Per-subcarrier NMSE against TO, $\delta = 0$ and 75kHz (73.125 kHz for FFT-FBMC and BF-OFDM.)

obtained to the detriment of latency which is very high in such a case (see section 3.3.3).

Regarding FFT-FBMC case, one can observe that the MSE is almost between $-30\ dB$ and $-38\ dB$ except two regions:

- Inner subcarrier located at the edges of the useful RBs frequency bands, where the MSE is about $-28\ dB$. Such a result can be explained by the fact that subcarrier gain at the RB edges is slightly lower than the gain of subcarriers located at the middle of the RB.
- Edge subcarriers (in the vicinity of interfering subcarriers), where the MSE varies from more than $-10\ dB$ when $\delta = 0\ Hz$ to $-30\ dB$ when $\delta = 75\ kHz$. As in filter-bank MWFs the edge subcarriers are highly impacted by interference, but this distortion is spread over more than one subcarrier because of the non-uniform gain over RB subcarriers.

Although the fact that BF-OFDM transmitter is like FFT-FBMC one, the performances are not the same. Indeed, BF-OFDM MSE is higher than FFT-FBMC one when the timing errors are outside the CP region. This is a direct consequence of the BF-OFDM receiver which is no more than the classical CP-OFDM receiver (i.e a simple FFT). However, the FFT-FBMC receiver is more efficient in asynchronous case thanks to the filtering performed by the analysis filter-bank.

For FBMC-OQAM (using PHYDYAS prototype filter bank) and Lapped-OFDM, we can observe that a very small number of edge subcarriers are affected by interference thanks to the good spectral containment of FBMC-OQAM and Lapped-OFDM signals. Such a behavior is directly linked to the design of the prototype filter which is a key-property of FBMC based MWFs. Indeed, FBMC prototype filters are commonly designed in order to minimize the interaction between subcarriers (e.g. in PHYDYAS case, a subcarrier overlaps at most with a single subcarrier on each side). When increasing the guard-band size, FBMC can reach the FMT performance by offering a MSE below $-40\ dB$ for the entire useful frequency band.

For WCP-COQAM, the windowing protection against asynchronous inter-user interference is less efficient compared to filtering one. This explains the poor WCP-COQAM performance in fully asynchronous case compared to FBMC-OQAM and Lapped-OFDM. By applying WOLA processing to WCP-COQAM, we can see significant improvement in terms of normalized MSE. Indeed, lower interference level in the middle of the bandwidth is achieved by WOLA-COQAM. This can be explained by the fact that the WOLA processing applied at the receiver is able to reduce inter-user interference as well.

Since FBMC-QAM and GFDM are non-orthogonal MWFs, they suffer from a high level of self-interference which makes us unable to distinguish the asynchronous interference from the self-distortion. To overcome this limitation, we introduced interference cancellation schemes for both MWFs. With interference cancellation, the performances of FBMC-QAM are almost like FBMC-OQAM where only a single subcarrier at each edge is impacted by the asynchronous interference. Such a result is due to the well-frequency localization of Samsung-Type-I prototype filter where a given subcarrier only interacts with its immediate adjacent subcarriers. Inserting a guard-band $\delta > 15kHz$ ($75\ kHz$ in this case) makes all useful subcarriers free from asynchronous interference. Regarding GFDM, one can see that asynchronous interference is more important on the edges of the useful frequency band. Thanks to transmit/receive filtering, the asynchronous interference decay becomes important when increasing the spectral distance between UI and IU. Moreover, we can observe that the best performance is obtained when the TO is inside the CP interval except for the edge subcarriers when $\delta = 0\ Hz$.

It should be mentioned that the scenario considered is a noiseless case. These results are so a bound on the achievable performance. The interference cancellation scheme will suffer from noise and performance will be worst in case of Additive White Gaussian Noise (AWGN) channel.

3.3.5 Influence of carrier frequency offset

In this section, we assume that both users (UI and IU) are perfectly synchronized in time domain ($\tau = 0$) but there is an offset between their respective carrier frequencies. The objective here is to examine the impact of CFO-induced inter-user interference on the performances of the various MWFs. The CFO ε considered here varies from $-1.5\ kHz$ to $+1.5\ kHz$. No guard-band is considered between the UI subcarriers and the IU ones $\delta = 0\ Hz$.

In Fig. 3.7, we have the per-subcarrier MSE of the studied MWFs. In CP-OFDM and N-cont. OFDM cases, the edges subcarriers are more sensitive to CFO compared to inner ones. In fact, the MSE at the edges becomes important even for negligible CFO (from 150 Hz) while inner subcarriers keep best performances (MSE< -30 dB) even when $\varepsilon = 1.5$ kHz.

When it comes to WOLA-OFDM, UF-OFDM and f-OFDM, the same behavior can be reported. Indeed, except the sensitivity of a few number of edge subcarriers to CFO when there is no guard-band, WOLA-OFDM and UF-OFDM provide good performance with a MSE below -35 dB for any subcarrier/CFO point.

In FMT case, the best performance is achieved where a negligible MSE (dark-blue color: MSE less than -40 dB) is shown for all useful subcarriers. This can be explained by the fact that the FMT prototype filter is extremely well frequency localized.

For FFT-FBMC, the MSE at the edges of each RB is about -30 dB, whereas it is less than -35 dB in the other subcarriers. As we have previously explained, this phenomenon is due to the filter shape in frequency domain. It is also worth noticing that except in each subcarrier edges the MSE is almost invariant with respect to CFO. In BF-OFDM case, the MSE is below -30 dB in a larger region around the 0 Hz CFO.

As previously discussed, the robustness against time asynchronism of OQAM-based MWFs is ensured thanks to transmit/receive filtering that limits the interaction between a given subcarrier and its neighborhood. Indeed, one can see that, like timing asynchronism, only a small number of subcarriers are suffering from asynchronous inter-user interference (e.g., one subcarrier on each side in FBMC-OQAM case).

Due to the block-based structure which is built-in property of WCP-COQAM and WOLA-COQAM signals, these schemes are more sensitive to CFO-induced inter-user interference compared to FBMC-OQAM and Lapped-OFDM systems. In fact, one can observe that the asynchronous interference caused by IU is more important, impacting thus a higher number of useful subcarriers compared to other OQAM-based MWFs. Moreover, this interference is slowly decreasing w.r.t. to the spectral distance between a given victim subcarrier and the interfering signal.

As stated in the previous section, the performance of both FBMC-QAM and GFDM, have been implemented with interference cancellation based-receivers. In FBMC-QAM, since the considered CFO does not exceed the subcarrier spacing (i.e., $|\varepsilon_{max}| = 1.5$ kHz), we can see that except the two subcarriers of the edges, the rest of useful subcarriers are completely protected against the asynchronous interference (it becomes almost negligible compared to the residual self-interference). In GFDM case, the asynchronous interference affects more than one subcarrier at each edge, but the subcarriers located at the middle remain almost free of asynchronous interference.

3.3.6 Complexity

This section aims at estimating the complexity of the transmitter and receiver schemes for the considered MWFs. The complexity will be assessed by counting the number of real multiplications per unit of time to perform both the modulation and demodulation process. It has been preferred to assess the number of multiplications per unit of time to compare as fairly as possible the schemes that do not share the same sampling frequency (FFT-FBMC and BF-OFDM). To do so, a burst of S symbol vectors (as defined in equation (3.3)) is considered. For the schemes that exhibit symbol overlapping, the complexity will be benchmarked when S tends to infinity. In this analysis, we will assume that one complex multiplication can be carried out with three real multiplications [112]. Moreover, the Cooley-Tukey implementation will be considered for the FFT implementation. The relative complexities of the different transmission and reception schemes, with respect to that of CP-OFDM, are given in Tab. 3.4.

Due to its precoding stage, N-Cont. OFDM is the most complex waveform with more than 205 times of the CP-OFDM complexity. Moreover, we can observe that waveforms relying on time convolution (UF-OFDM, f-OFDM) require higher computation resources for the transmitter scheme than the others. Note that, WOLA-COQAM, WCP-COQAM and GFDM are also more computation hungry.

On the contrary, waveforms based on polyphase network (FMT, FBMC-QAM, Lapped-OFDM and FBMC-QAM) provide an efficient hardware implementation. FFT-FBMC and BF-OFDM are more

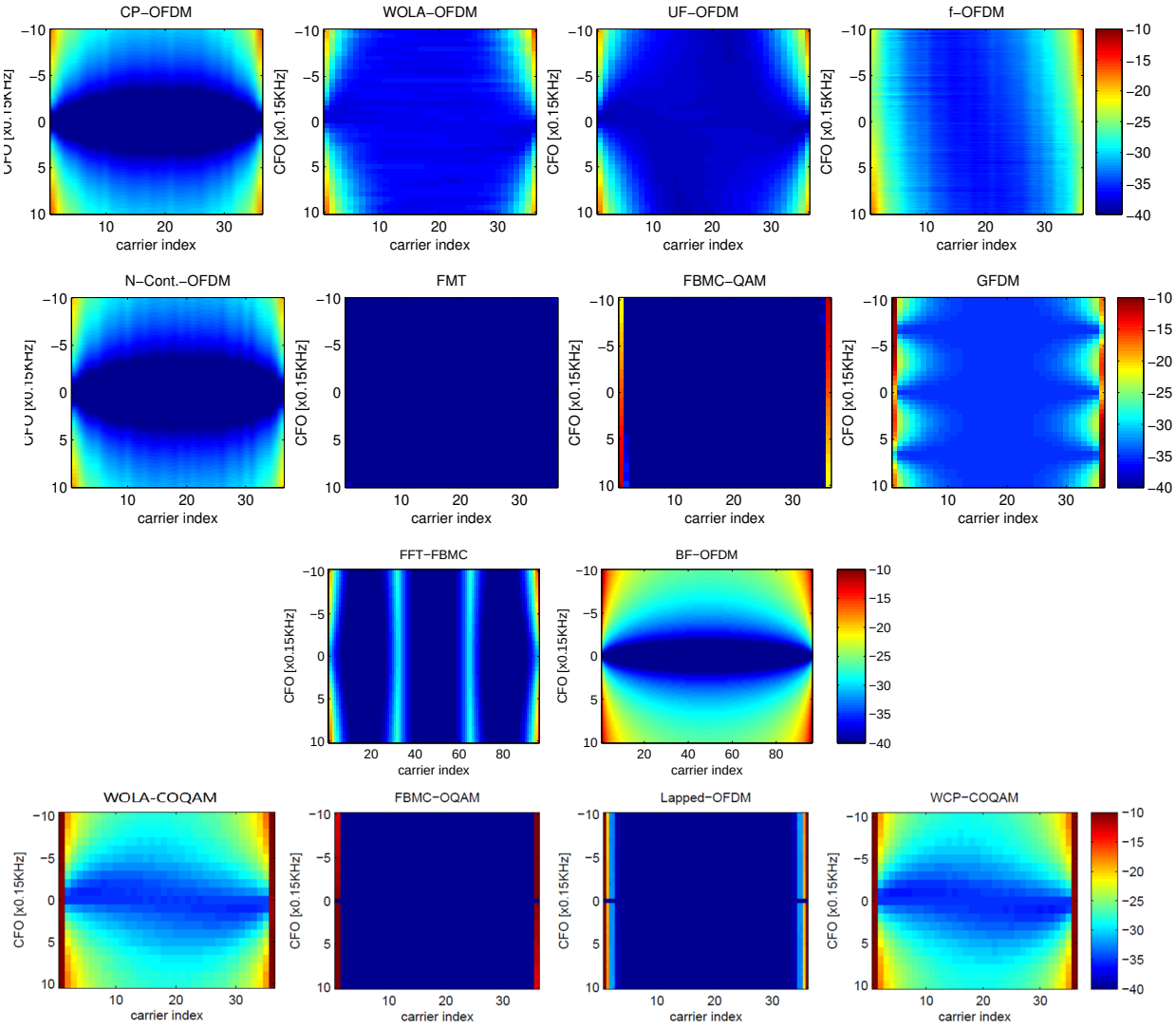

Figure 3.7: Per-subcarrier NMSE against CFO, $\delta = 0\ kHz$.

complex because of their precoding stage. As expected, the OFDM and the WOLA-OFDM are the least complex.

When it comes to the receiver schemes, waveforms relying on a simple FFT (OFDM, BF-OFDM, UF-OFDM, N-cont. OFDM) with an eventual light receiver processing (WOLA-OFDM) perform well. UF-OFDM is slightly more complex because of its double size FFT while BF-OFDM is slightly more efficient thanks to its longer sampling period. Polyphase-network based receivers still perform well while the f-OFDM is still the more complex because of the time-convolution. WOLA-COQAM, WCP-COQAM and GFDM receivers are highly complex respectively because the oversampled-FFT and the interference cancellation stage.

3.3.7 Evaluation and discussions

In this section, I will evaluate and discuss the simulation results obtained previously. It is not straightforward to rank the different criteria that have been analyzed in the light of a URLLC communications. In this scenario, some criteria are of prime importance such as: latency, asynchronous capabilities, reliability, energy efficiency and spectral efficiency. Therefore, to give an overview on all of the considered MWFs, we introduce in Fig. 3.8 a radar plot where each corner corresponds to a given criterion. The criteria, taken for comparison, are summarized in table 3.5. From Fig. 3.8, one can notice that some

MWFs	Tx			Rx
	5RBs	25RBs	50RBs	
CP-OFDM	1.00	1.00	1.00	1.00
WOLA-OFDM	1.01	1.01	1.01	1.01
UF-OFDM	25.80	131.01	263.93	2.21
f-OFDM	37.85	37.85	37.85	37.85
N-Cont.-OFDM	205.80	205.80	205.80	1.00
FMT	3.35	3.35	3.35	3.35
FFT-FBMC	1.81	2.10	2.46	1.81
BF-OFDM	1.82	2.16	2.58	0.84
FBMC-OQAM	3.28	3.28	3.28	3.28
Lapped-OFDM	2.71	2.71	2.71	2.71
WCP-COQAM	3.29	3.29	3.29	17.41
WOLA-COQAM	6.46	6.46	6.46	2.46
FBMC-QAM	2.14	2.14	2.14	2.14
GFDM	3.28	3.28	3.28	9.03

Table 3.4: Tx/Rx complexity normalized with respect to OFDM.

Criterion	Specification
PSD	spectral distance of $\delta = 75\ kHz$
SE (short bursts)	a burst size = single multicarrier block
SE (long bursts)	a burst size = high number of multicarrier blocks
Latency (short bursts)	same as SE (short bursts)
Latency (long bursts)	same as SE (long bursts)
Robustness to timing offset	guard-band $\delta = 75\ kHz$
Transmitter complexity (Narrow-Band case)	5 RBs are used
Transmitter complexity (Broad-Band case)	50 RBs are used
Receiver complexity	-

Table 3.5: Comparison criteria specification

MWFs with complex orthogonality such as WOLA-OFDM, UF-OFDM and f-OFDM have the CP-OFDM latency level, a more or less moderated added complexity and good performance concerning TOs. For MWFs with real orthogonality and filtering applied at subcarrier level, the FBMC-OQAM, in comparison with CP-OFDM, exhibits higher latency, better performance concerning TO and higher complexity. Nevertheless, COQAM bases MWFs have poor performance concerning TO. Finally, for MWFs without orthogonality, the FBMC-QAM has higher latency, better TO performance and higher complexity than CP-OFDM. Differently, the GFDM has a very high complexity at the receiver side if interference cancellation is considered and poor performance in terms of TO.

3.4 Advanced equalization structures for FBMC-OQAM

3.4.1 Context and motivation

As discussed in the previous section, FBMC-OQAM showed some interesting features. This MWF has the best frequency localization, providing then the best performance in supporting asynchronous access while ensuring high spectrum efficiency. However, FBMC-OQAM loses rapidly its good properties under frequency selective channels and requires advanced equalization techniques [75].

Since FBMC-OQAM system employs OQAM, which is a non-second order circular modulation (NSOC) of quasi-rectilinear (QR) type, classical linear equalization [44] is not an optimal solution to

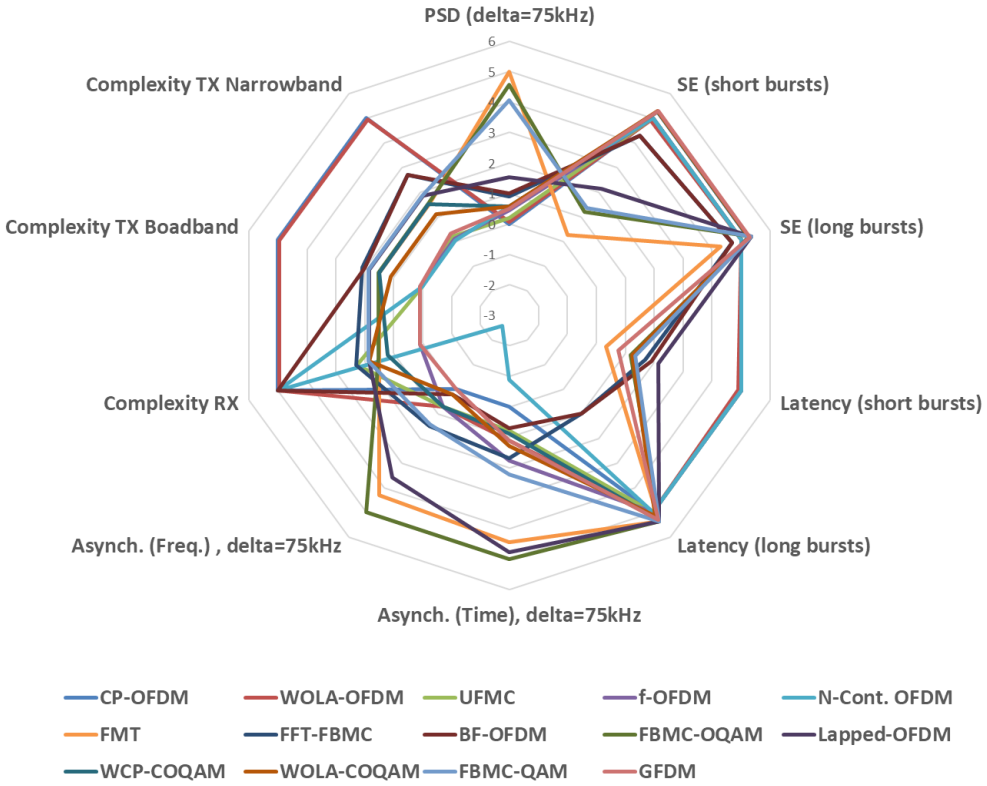

Figure 3.8: Performance overview.

recover efficiently the transmitted data. Indeed, in [113], authors demonstrated that for OQAM based MWFs, widely linear equalization (WLE) outperforms classical linear equalization (LE). Furthermore, FBMC-OQAM signal is also considered to be cyclo-stationary [114, 115], for which frequency shift filtering (Fresh) processing [116, 117, 118] has demonstrated its outstanding performance, with regards to LE and WLE approaches.

Motivated by the performance provided by FBMC-OQAM in asynchronous transmissions and the capability of WLE and WL Fresh equalizers in dealing with frequency selective channels when considering NSOC and cyclo stationary (CS) signals [116, 117, 119], we have focused, within the Hayfa Fhima's PhD, on the design of new WL based equalization schemes for FBMC-OQAM.

3.4.2 Equalization structures

We consider the system model given in Fig. 3.3 with two users: a UI transmitting over frequency selective channels, is interfered by an IU which is located at δ Hz guard band from the UI. Both users don't use the same numerology, i.e., different parameter settings for the MWF, such as SCS, symbol duration and CP length, as defined in [23].

From Tab. 3.2, we can notice that, for a given FBMC-OQAM subcarrier, the main interferences come from the couple of the immediately adjacent sub-carriers. Additionally, the OQAM modulation can be seen as the transmission of two M-PAM (pulse amplitude modulation) streams on the same sub-carrier. Hence, and without loss of generality, a given sub-carrier of an FBMC-OQAM transmission can be seen as the equivalent model shown in Fig. 3.9. In this figure, $x(n)$ is the useful signal and $i(n)$ is the interfering one. $p_1(m)$ and $p_2(m)$ are the prototype filters impulse responses. The signal at the matched filter output is down sampled with factor P to allow symbol spaced equalization (SSE) (for $P = 1$) or fractionally spaced equalization (FSE) (for $P > 1$). We denote $y_p(l)$ as the equalizer input signal. L_e is the equalizer length ($L_e = L_S$ for SSE and $L_e = P.L_s$ for FSE) and $\gamma_p(l)$ is the equalizer output with P times the symbol rate. Finally, we consider the vector $\boldsymbol{y_p}(l)$ of length L_e, defined as

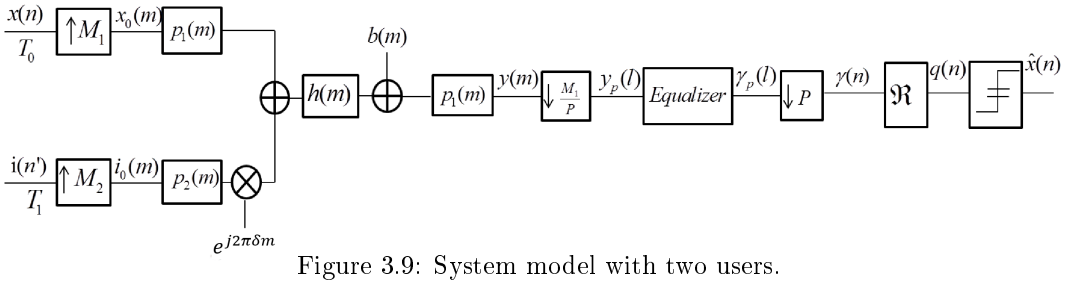

Figure 3.9: System model with two users.

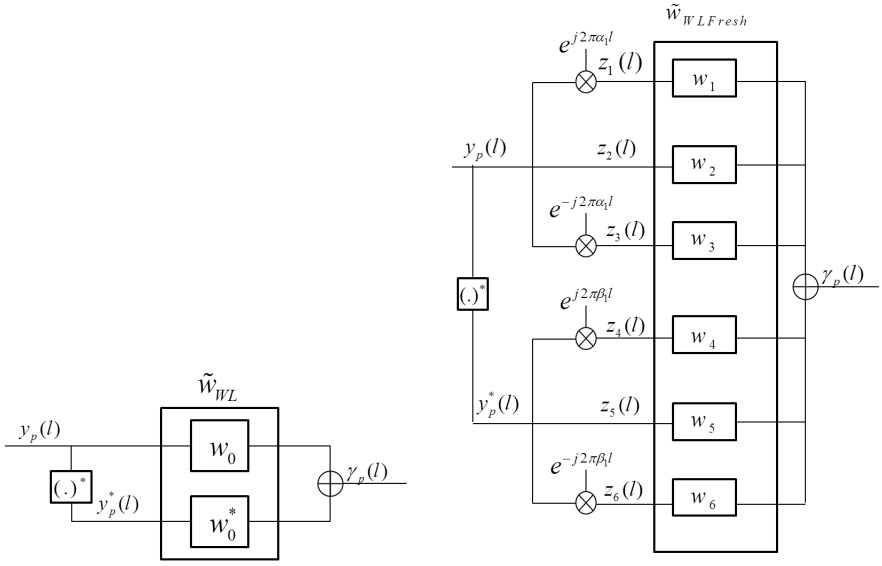

(a) Widely linear. (b) Widely linear Fresh.

Figure 3.10: Equalization schemes.

$\boldsymbol{y_p}(l) = [y_p(lT_0), y_p(lT_0 - T_e), ..., y_p(lT_0 - (L_e - 1)T_e)]^T$. Note that T_0 is equal to half the symbol period for the OQAM signal of the UI and T_1 as equal to half the symbol period related to the OQAM signal of the IU.

Linear Equalization "LE"

The classical LE uses only the information carried by the auto-correlation matrix of the signal $y_p(l)$. Hence, the LE is a vector $\in \mathbb{C}^{1\times L_e}$ where the coefficients are given by [120]:

$$\boldsymbol{w_{LE}} = \boldsymbol{r}_{x\boldsymbol{y_p}} \boldsymbol{R}_{\boldsymbol{y_p}}^{-1}, \tag{3.4}$$

where $\boldsymbol{r}_{x\boldsymbol{y_p}} = \mathbb{E}[x(n)\boldsymbol{y_p^H}(l)]$ is a vector $\in \mathbb{C}^{1\times L_e}$ which represents the inter-correlation vector between the transmitted symbol and the equalizer input samples. $\boldsymbol{R}_{\boldsymbol{y_p}} = \mathbb{E}[\boldsymbol{y_p}(l)\boldsymbol{y_p^H}(l)]$ represents the auto-correlation matrix $\in \mathbb{C}^{L_e\times L_e}$ of the equalizer input signal.

Widely Linear Equalization "WLE"

In WL processing [121] the equalizer uses the information contained in the second order properties of the signal, i.e the information carried by both the auto-correlation and pseudo-autocorrelation matrix. Let us consider $\tilde{\boldsymbol{y}}_{\boldsymbol{p}}(l) = [\boldsymbol{y_p^T}(l), \boldsymbol{y_p^*}(l)]^T$ to be a vector of length $2L_e$, which represents the WL equalizer input. The scheme of the WL processing is given by Fig. 3.10 (a). The number of the WLE input branches are doubled, compared to the classical linear processing. Over each branch, the signal and its conjugate

version, will be followed by a sub-equalizer having the same number of taps as the LE (i.e., L_e). The WL equalizer $\in \mathbb{C}^{1\times 2L_e}$, is given by

$$\tilde{\boldsymbol{w}}_{\boldsymbol{WL}} = \boldsymbol{r}_{x\tilde{\boldsymbol{y}}_{\boldsymbol{p}}} \boldsymbol{R}^{-1}_{\tilde{\boldsymbol{y}}_{\boldsymbol{p}}}, \tag{3.5}$$

where $\boldsymbol{r}_{x\tilde{\boldsymbol{y}}_{\boldsymbol{p}}}$ is a vector $\in \mathbb{C}^{1\times 2L_e}$ and represents the inter-correlation vector between the transmitted symbol and the equalizer input in its widely linear version (i.e.: $\tilde{\boldsymbol{y}}_{\boldsymbol{p}}(l)$). Besides, $\boldsymbol{R}_{\tilde{\boldsymbol{y}}_{\boldsymbol{p}}}$ is the auto-correlation matrix $\in \mathbb{C}^{2L_e\times 2L_e}$ of the signal $\tilde{\boldsymbol{y}}_{\boldsymbol{p}}(l)$. This matrix can be represented by:

$$\boldsymbol{R}_{\tilde{\boldsymbol{y}}_{\boldsymbol{p}}} = \mathbb{E}[\tilde{\boldsymbol{y}}_{\boldsymbol{p}}(l)\tilde{\boldsymbol{y}}^{\boldsymbol{H}}_{\boldsymbol{p}}(l)] = \begin{bmatrix} \boldsymbol{R}_{\boldsymbol{y}_{\boldsymbol{p}}} & \boldsymbol{C}_{\boldsymbol{y}_{\boldsymbol{p}}} \\ \boldsymbol{C}^{*}_{\boldsymbol{y}_{\boldsymbol{p}}} & \boldsymbol{R}^{*}_{\boldsymbol{y}_{\boldsymbol{p}}} \end{bmatrix}, \tag{3.6}$$

where $\boldsymbol{C}_{\boldsymbol{y}_{\boldsymbol{p}}} = \mathbb{E}[\boldsymbol{y}_{\boldsymbol{p}}(l)\boldsymbol{y}^{\boldsymbol{T}}_{\boldsymbol{p}}(l)]$ represents the pseudo-autocorrelation matrix ($\in \mathbb{C}^{L_e\times L_e}$) of the signal $\boldsymbol{y}_{\boldsymbol{p}}$.

Widely Linear Fresh Equalization "WL Fresh"

When the NSOC signal is stationary, there is no correlation between the spectral components of the signal [122]. This is because the whole information is carried by the auto-correlation and the pseudo-autocorrelation matrices. However, when the NSOC signal is non-stationary, this is no longer true. In particular, when the signal is characterized as cyclo-stationary [116, 117, 114, 115], there is correlation between the spectral components of the signal. Moreover, the auto-correlation and the pseudo-autocorrelation functions of the interferer signal, composed by the IU signal plus the noise and called $I(l)$, are periodic functions of time [117]. Hence, they can be represented as Fourier series expansions, given as follows

$$\boldsymbol{R}_I(t,\xi) = \sum_{\alpha_i} \boldsymbol{R}^{\alpha_i}_I(\xi) e^{j2\pi\alpha_i t}, \tag{3.7}$$

$$\boldsymbol{C}_I(t,\xi) = \sum_{\beta_i} \boldsymbol{C}^{\beta_i}_I(\xi) e^{j2\pi\beta_i t}. \tag{3.8}$$

where $\boldsymbol{R}^{\alpha_i}_I(\xi)$ and $\boldsymbol{C}^{\beta_i}_I(\xi)$ are defined, respectively, as the non-conjugate and conjugate cyclic correlation functions. Likewise, α_i and β_i are called the Second Order (SO) non conjugate and conjugate cyclic frequencies of the IU signal. For OQAM signal, the SO non conjugate and conjugate cyclic frequencies are given as follows [44]:

$$\begin{cases} \alpha_i = \dfrac{i}{T_1} & \text{for } i \in \mathbb{Z}, \\ \beta_i = \pm 2\delta + \dfrac{i}{T_1} & \text{for } i \in \mathbb{Z}, \end{cases}$$

where δ stands for the guard band between the UI and the IU.

The WLE exploits only the information contained in the couple $(\alpha_i, \beta_i) = (0, 0)$, for any value of i. For OQAM signals, the most two energetic conjugate cyclic frequencies are $\beta_0 = 2\delta$ and $\beta_1 = 2\delta - \dfrac{1}{T_1}$, [116, 117]. Hence, if $\delta \neq \dfrac{i}{2T_1}$, the WLE gives poor performance and becomes equivalent to the LE if there is no energy at the null conjugate cyclic frequency. To better consider the cyclo-stationarity of the signal, another structure of equalizer has been introduced, which exploits better the correlation between the spectral components of the signal. This structure is called Frequency Shift (Fresh) [117] equalizer. Without loss of generality, we will limit the WL Fresh equalizer to the use of only one set of couple of cyclic frequencies $(\pm\alpha_1, \pm\beta_1)$, which correspond to the most energetic ones. The structure of the used WL Fresh equalizer is given in Fig. 3.10 (b). With the use of the cyclic frequencies in addition to the null couple $(\alpha_i = 0, \beta_i = 0)$, the Fresh equalizer has 6 branches, resulting to an equalizer with 6 times more taps than the classical one.

Let us consider the observation vector $\tilde{\boldsymbol{z}}_{\boldsymbol{p}}(l) = [\boldsymbol{z}^{\boldsymbol{T}}_{\boldsymbol{1}}(l), \boldsymbol{z}^{\boldsymbol{T}}_{\boldsymbol{2}}(l), \boldsymbol{z}^{\boldsymbol{T}}_{\boldsymbol{3}}(l), \boldsymbol{z}^{\boldsymbol{T}}_{\boldsymbol{4}}(l), \boldsymbol{z}^{\boldsymbol{T}}_{\boldsymbol{5}}(l), \boldsymbol{z}^{\boldsymbol{T}}_{\boldsymbol{6}}(l)]^T$, where $\boldsymbol{z}_{\boldsymbol{i}}(l) = [z_i(lT_0), z_i(lT_0 - T_e), ..., z_i(lT_0 - (L_e - 1)T_e)]^T$, for $i = 1, .., 6$. $z_i(l), i \in \{1, 3\}$ is the frequency shifted version of the received signal $y_p(l)$; this shift is done via the use of the cyclic frequencies $+\alpha_1, 0$ and $-\alpha_1$, respectively. Likewise, $z_i(l), i \in \{4, 6\}$ represents the frequency shifted version of the received signal

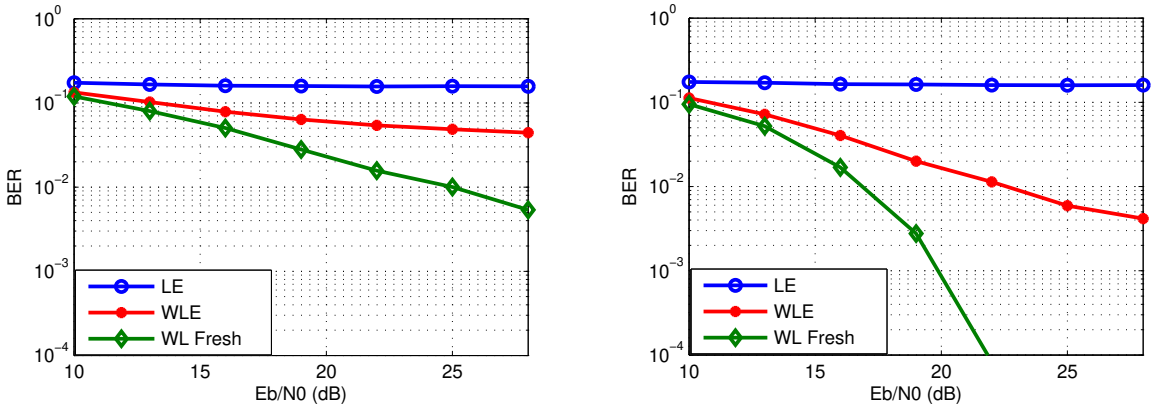

(a) SSE. (b) FSE with P=8.

Figure 3.11: BER performance over a frequency selective channel.

complex conjugate $y_p^*(l)$ and that is done by the use of the conjugate cyclic frequencies $+\beta_1, 0$ and $-\beta_1$. Therefore, the WL Fresh equalizer is given by the following expression

$$\tilde{\boldsymbol{w}}_{\boldsymbol{WLFresh}} = \boldsymbol{r}_{x\tilde{\boldsymbol{z}}_{\boldsymbol{p}}} \boldsymbol{R}_{\tilde{\boldsymbol{z}}_{\boldsymbol{p}}}^{-\mathbf{1}}, \tag{3.9}$$

where $\boldsymbol{r}_{x\tilde{\boldsymbol{z}}_{\boldsymbol{p}}}$ is a vector $\in \mathbb{C}^{1\times 6L_e}$ and represents the inter-correlation vector between the transmitted symbols and the equalizer input in its Fresh version (i.e., $\tilde{\boldsymbol{z}}_{\boldsymbol{p}}(l)$). Besides, $\boldsymbol{R}_{\tilde{\boldsymbol{z}}_{\boldsymbol{p}}} = \mathbb{E}[\tilde{\boldsymbol{z}}_{\boldsymbol{p}}(l)\tilde{\boldsymbol{z}}_{\boldsymbol{p}}^{\boldsymbol{H}}(l)]$ is a matrix $\in \mathbb{C}^{6L_e\times 6L_e}$, and it is defined as the auto-correlation matrix of the signal $\tilde{\boldsymbol{z}}_{\boldsymbol{p}}(l)$.

3.4.3 Performance analysis

In this section, we evaluate the performance of the previously described equalization schemes (LE, WLE and WL Fresh) for a FBMC-OQAM system in different scenarios: UL/DL, synchronous/asynchronous and with mixed numerologies transmissions. We assume that UI and IU are using different numerologies with symbol duration ratios equal to a power of 2, $T_1 = 2^a T_0$, where a is positive integer.

The UI and IU use different numerologies, with respectively $M_1 = 64$ and $M_2 = 2 \times M_1 = 128$ subcarriers and transmitting 64−OQAM symbols. We recall that τ is the time shift describing the asynchronism between the UI and IU. δ denotes the guard band between the two users. When using the WL Fresh equalizer, the SO non conjugate and conjugate cyclic frequencies used are given by: $\alpha_1 = \frac{1}{T_1}$ and $\beta_1 = 2\delta + \frac{1}{T_1}$. For both scenarios: DL and UL, we activate only 5 SCs for the UI (using numerology 1) and 8 SCs for the IU (using numerology 2).

DL case In this scenario, we assume a perfect synchronization between UI and IU ($\tau = 0$). The guard band δ is chosen to be equal to one UI sub-carrier spacing ($\delta = \frac{1}{M_1}$). Since only the SCs in the edge of the band are affected, we have focused on the impact of one edge IU subcarrier on the BER over the neighboring UI subcarrier, with δ equal to one UI sub-carrier spacing. The channel is a frequency selective 8 taps finite impulse response (FIR) filter whose coefficients are randomly chosen. The BER performance of the SSE equalizers as well as the FSE equalizers are presented in Fig. 3.11. It is clear from this figure that the WL Fresh equalizer out-performs both the LE and WLE, whereas the worst behavior is provided by the LE. This is true for both SSE and FSE cases. Eventually, when P increases, the WLE and WL Fresh equalizers performance increase, and the WL Fresh gives always the best performance.

UL case For this case, users are not necessarily synchronous in time. Thus, we will study the impact of this asynchronism as well as the guard band on the system performance for LE, WLE and WL Fresh equalizers in their FSE version with $P = 8$.

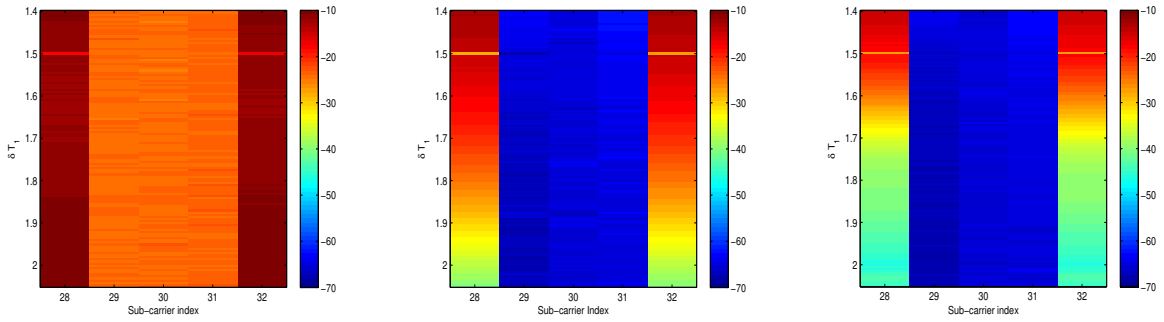

(a) LE. (b) WLE. (c) WL Fresh.

Figure 3.12: MSE performances for synchronous UI and IU.

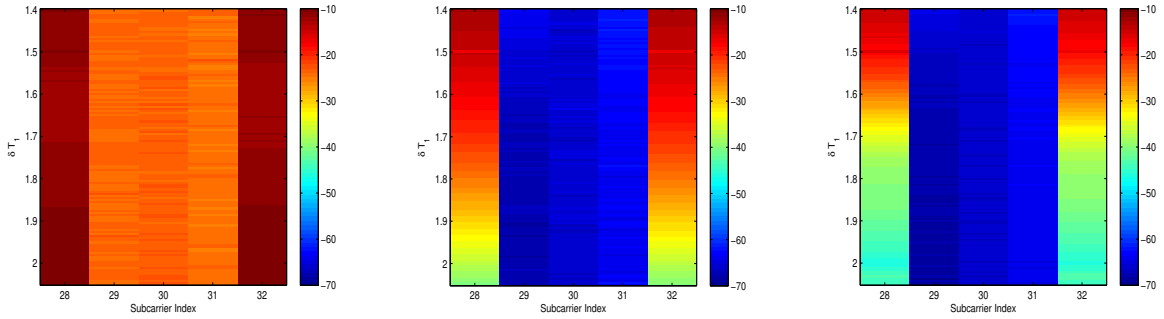

(a) LE. (b) WLE. (c) WL Fresh.

Figure 3.13: MSE performances for asynchronous UI and IU ($\tau = \frac{T_1}{2}$).

The per-subcarrier MSE performance, when the two users are synchronous, is given by (Fig. 3.12). Whereas, Fig. 3.13 depicts the performance when the UI and IU are transmitting asynchronously. In the two contexts, an ideal channel is considered to see the impact of mixed numerologies on the different equalizer behaviors.

From Figs. 3.12 and 3.13, we can deduce that for all equalizer cases, all the SCs are affected by the interferer. This remark remains true regardless the guard interval δ size as well as the asynchronism time. Moreover, the WLE and the WL Fresh provide the same MSE performance when considering the SCs in the middle of UI bandwidth. When focusing on the SCs in the edge, we can see from the color degradation that the LE gives the worst performance in the two scenarios when compared to the WLE and WL Fresh.

Furthermore, an interesting and new finding can be deduced from Fig. 3.12: when the UI and IU are synchronous. In this scenario, we can note a notch when the $\delta = \frac{3}{2T_1}$, where the performance of WLE and WL Fresh equalizers are very close. This can be explained by the fact that when $\delta = \frac{3}{2T_1}$, the conjugate cyclic frequency β_3 is null and since the WLE uses the information contained in all $(\beta_i = 0, i \in \mathbb{Z})$, the WLE gives the same performance as the WL Fresh. Besides, when the guard band is out of the notch, the WL Fresh outperforms the WL equalizer over the edge SC. It is noticeable that when the guard band δ is large, the two users are sufficiently spaced in the frequency domain, meaning while, the IU does not impact the UI anymore, so, the two widely linear equalizers give the same performance. This remains valid in the two contexts (synchronous as well as for the asynchronous cases).

3.5 Conclusion

In this chapter, I presented the activities carried out as part of a first line of research developed since my arrival at CNAM. This axis focuses on the study and proposal of MWFs adapted to cMTC/URLLC communications. Most of this work was carried out as part of the ANR WONG5 project leaded by CNAM between 2015 and 2019. This work has been carried out while keeping a watch on the recommendations of the standardization bodies for 5G, particularly in terms of MWFs candidates for 5G NR and of requirements for URLLC transmissions.

The CP-OFDM, which was chosen for 5G NR, did not however seem to us to be the best MWFs in view of the studies that we carried out. Indeed, this MWF has significant limitations in terms of frequency localization and spectral efficiency. In my opinion, other MWFs such as WOLA-OFDM, f-OFDM or BF-OFDM seemed more efficient for a cMTC scenario. Beyond these complex orthogonal waveforms, we have taken a particular interest in the FBMC-OQAM which presented an excellent frequency localization thanks to a very selective filtering at sub-carrier level. However, the real domain orthogonality of this MWF made it very sensitive to the effects of frequency selective channels. In this sense, we have developed advanced equalization techniques exploiting the higher order statistical properties of OQAM signals.

It should be noted that all the work carried out within the framework of this chapter is done using perfect RF equipments (RF impairments induced by power amplifiers). The aim of the next chapter will be to study the impact of non-linear power amplifiers on the performance of a selection of MWFs introduced in this chapter.

Chapter 4

PA distortions analysis

4.1 Introduction

Despite the discussed advantages of the MWFs presented in chapter 3, they may lose rapidly their good properties when non-linear (NL) radio frequency (RF) power amplifiers (PAs) are used. Indeed, as these MWFs suffer from high Peak to Average Power Ratio (PAPR) of the modulated signal, amplifying them at sufficient PA efficiency may induce undesirable effects.

The PA nonlinearities phenomena lead to in-band performance degradation and spectral regrowth causing adjacent channel interference. PA harmful effects may appear for both UL and DL transmissions. From another side, memory effects in PAs can introduce asymmetry in sidebands Adjacent Channel Leakage Ratio (ACLR) [123, 124, 125].

In this regard, we have been interested on analytical characterization of the in-band (IB) and Out-of-Band (OOB) non-linear distortions, induced by memoryless PAs, on the performance of some post-OFDM MWFs. In particular, we focused, within the Hanen Bouhadda's PhD, on the NL PA effects on system BER and SER performance over AWGN and Rayleigh channels. The originality of this work, carried within the FP7 EMPhAtiC project and continued during the WONG5 project, is the proposal of a universal approach to make this analysis feasible for any measured or modelled memoryless PA and for many MWFs candidate for 5G NR. Regarding OOB effects, we have applied some approaches proposed in the literature: Price theorem and cumulants, in order to predict the spectral regrowth induced by any memoryless PA exhibiting both amplitude and phase distortions.

The objectives of this second research axis developed at CNAM was the study of the effects of PA impairments. Two PhD students: Hanen Bouhadda and Krishna Bulusu, co-supervised with Pr. Daniel Roviras, contributed strongly to the results presented in this chapter.

In a first section of this chapter, I will present the context and objectives of the carried studies. In a second section, I will describe the PA characteristics and models that are used in the following. Next, section 4.4 is devoted to the analysis of in-band effects while section 4.5 is devoted to OOB effects and spectral regrowth analysis.

4.2 Context and motivation

MWFs suffer from a major drawback related to their high PAPR. To characterize power fluctuations, the Complementary Cumulative Distribution Function (CCDF) of the PAPR is a widely used performance criterion. The CCDF of the PAPR is defined as the probability that the PAPR per block of consecutive symbols exceeds a given level P_0:

$$\mathrm{CCDF}(P_0) = \mathrm{Prob}\left[PAPR\left(i\right) > P_0\right], \tag{4.1}$$

where $PAPR(i) = \frac{\max\left[|x(n)|^2\right]}{E\left[|x(n)|^2\right]}$, i is a the block index, $x(n)$ is the time domain signal for block number i with $n = [0; N_{\mathrm{Block}} - 1]$, N_{Block} is the considered block size[1].

The CCDF of the PAPR of some of the MWFs described in chapter 3 are presented in Fig. 4.1, for a block size $N_{\mathrm{Block}} = 1024$. We can observe, from this figure, that all MWFs have almost equivalent PAPR performances.

The distribution of the transmitted power given by the CCDF of the PAPR is not very important as far as linear systems are used in the transmission chain. Unfortunately, some elements of the chain are

[1] Note that for CP-OFDM, $N_{\mathrm{Block}} = N_{\mathrm{FFT}}$

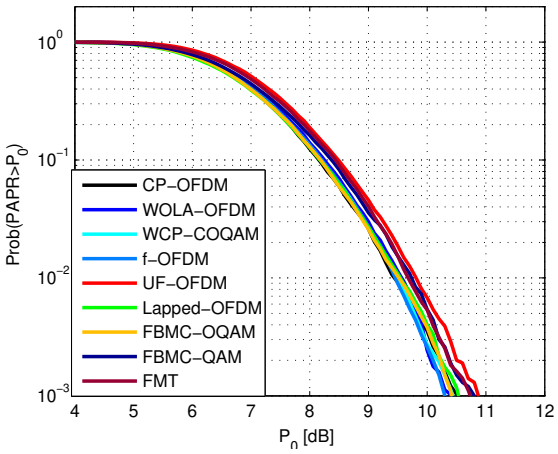

Figure 4.1: CCDF of the PAPR of some MWFs calculated over a block length of 1024 samples.

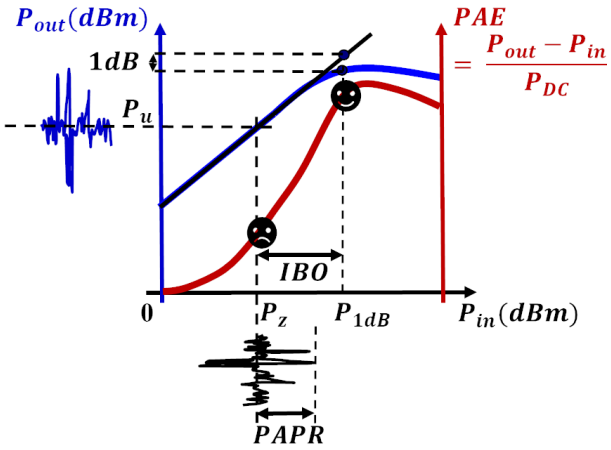

Figure 4.2: PA nonlinear behavior.

NL, among them the PA was shown to be the most problematic. Indeed, PA at the emitter side can be quasi linear for a certain part of the input powers P_{in} (see Fig. 4.2) and NL for input powers which are close to the $1dB$ compression point (P_{1dB}). Furthermore, the output power P_{out}, of a PA saturates for high values of the input power.

If the input power is always far from P_{1dB}, the PA is operated in its quasi linear region and the high PAPR of the MWF signal will not have any influence on the quality of the transmission. This scenario is illustrated in Fig. 4.2 by an input signal with a large IBO. Nevertheless, this situation has a high cost in terms of energy efficiency. The concept of energy efficiency can be understood by defining the power added efficiency (PAE) of a PA, as the ratio between the RF added power and the consumed one.

$$PAE = \frac{P_{out} - P_{in}}{P_{DC}}, \tag{4.2}$$

where P_{DC} is the power consumed by the PA.

Operating a PA with a very low mean input power gives a low mean output power compared to the consumed power P_{DC}. Especially, for mobile applications with batteries it is necessary to increase the power efficiency and operate the PA as close as possible to its saturation region. By doing that, two negative effects (distortions) will appear: (1) distortions will occur in the transmitted signal causing transmission errors, (2) output signal spectrum will be broadened compared to the input one. Within the framework of this research axis, I focused on the following two topics.

1. Firstly, I have focused on the study of the IB distortions induced by NL PAs. In this part, I investigated the SER/BER performance of some MWF based transmissions when memoryless NL PA are used. Theoretical and experimental analysis will be carried to show a very good agreement between theory and simulations for a selection of MWFs operating with some modelled or measured PAs.

2. Secondly, I have been concentrated on the prediction of the OOB spectral regrowth induced by NL memoryless PA. A theoretical study using Price theorem and cumulants will be presented to compute theoretically the spectral regrowth of a post-OFDM MWF signal when amplified by NL PAs.

4.3 PA models and characteristics

Fig. 4.3, shows a generic transmission scheme of MWFs in presence of a NL PA.

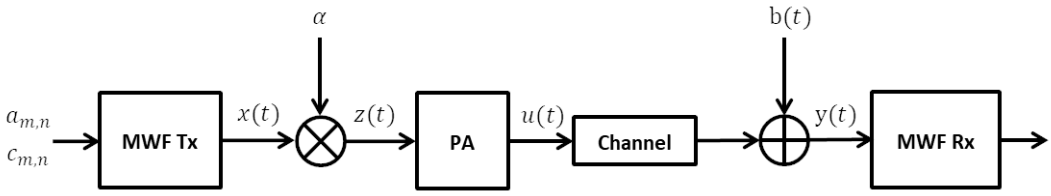

Figure 4.3: Basic system model for MWF transceiver.

In Fig. 4.3, the M-array QAM or OQAM symbols ($c_{m,n}$ or $a_{m,n}$) are modulated by a MWF and amplified before transmission over a given channel. Before amplifying the signal $x(t)$, it is necessary to scale it by a real positive gain α to ensure a given IBO[2]. For a given mean power: $P_x = \mathbb{E}\left[|x(t)|^2\right]$, the gain α needed to ensure a signal $z(t)$, with a given IBO value is

$$\alpha = \sqrt{\frac{P_{1\text{dB}}}{10^{\frac{IBO}{10}} P_{\text{x}}}}. \tag{4.3}$$

The $1dB$ compression point refers to the input power level where the transfer characteristics of the amplifier have dropped by 1 dB from the ideal linear characteristics.

The complex envelope $z(t)$ of the signal at the input of the PA can be written as

$$z(t) = \rho(t)e^{j\varphi(t)}, \tag{4.4}$$

where: $\rho(t)$ is the input signal modulus, and $\varphi(t)$ is the input signal phase.

Broadly, the nonlinear PA models can be classified into two categories: memoryless nonlinear models and nonlinear models with memory. Memoryless PA are characterized by AM/AM (amplitude to amplitude) and AM/PM (amplitude to phase) conversions. Nonlinear models with memory aim also to capture the effects that are manifested not only by the instantaneous input signal magnitude but also the frequency dependent characteristics of the signal envelope e.g., making AM/AM and AM/PM functions non-static and depend on the past input signal. Memory effects in PAs are attributed to various sources, thermal and electric [123, 124]. These effects are more important in high power PAs, but also appear as the signal bandwidth is increased. The studies presented in this chapter were carried out with PAs without memory. The extension to PAs with memory is a possible prospect with the ever-increasing bands of transmitted signals.

In our study, we assumed that the PA frequency response is constant over the useful signal frequency band, which allows neglecting the memory effects of the PA. Thus, any change in the signal input occurs instantaneously at the output. As a general formulation, the amplified signal $u(t)$ can be written as

$$u(t) = F_a(\rho(t))e^{j(F_p(\rho(t))+\varphi(t))} = S(\rho(t))e^{j\varphi(t)}, \tag{4.5}$$

where: $F_a(\rho(t))$ and $F_p(\rho(t))$ are respectively the AM/AM and AM/PM characteristics of the PA. $S(\rho(t)) = F_a(\rho(t))e^{jF_p(\rho(t))}$ is called the complex soft envelope of the amplified signal $u(t)$.

Many memoryless PA models have been proposed and studied in literature. Among them we can cite the following models

- The Soft Envelop Limiter (SEL), used for modeling a PA with a perfect linearization system. The global transfer function can be described by the following AM/AM and AM/PM functions

$$\begin{aligned} F_a(\rho(t)) &= \begin{cases} \rho(t), \rho(t) \leq v_{sat}, \\ v_{sat}, \rho(t) > v_{sat}, \end{cases} \\ F_p(\rho(t)) &= 0, \end{aligned} \tag{4.6}$$

  where v_{sat} is the PA input saturation level.

[2]IBO is computed from the $1dB$ compression point.

- The Rapp model, commonly used for modeling Solid State Power Amplifiers (SSPA), exhibits only AM/AM conversion [126]. It can be expressed as

$$\begin{aligned} F_a(\rho(t)) &= \frac{G_0\rho(t)}{(1+(\frac{G_0\rho(t)}{v_{\text{sat}}})^{2p})^{\frac{1}{2p}}}, \\ F_p(\rho(t)) &= 0, \end{aligned} \tag{4.7}$$

  where G_0 is the linear gain and p is a smoothness positive factor that controls the transition from the linear region to the saturation region. When $p \to \infty$, the Rapp model converges towards a SEL model.

- The Saleh model, generally used for modeling Travelling Wave Tube Amplifiers (TWTA) [127]. According to this model, the AM/AM and AM/PM conversion characteristics can be expressed as follows

$$F_a(\rho(t)) = v_{sat}^2 \frac{\rho(t)}{\rho(t)^2+v_{sat}^2}, \tag{4.8}$$

$$F_p(\rho(t)) = \phi_0 \frac{\rho(t)^2}{\rho(t)^2+v_{sat}^2}, \tag{4.9}$$

  where ϕ_0 controls the maximum phase distortion introduced by this PA model.

- The polynomial model, widely used for purpose of theoretical analysis. The complex soft envelope of the signal at the output of this PA model can be written as

$$S(\rho(t)) = F_a(\rho(t))e^{jF_p(\rho(t))} = \sum_{l=1}^{L} a_l \rho(t)^l, \tag{4.10}$$

  where L is the polynomial order, and a_l are the complex coefficients of the polynomial function.

4.4 In band distortions analysis

4.4.1 Nonlinear distortion modeling

When considering a large number of subcarriers, due to central limit theorem, the PA input signal $z(t)$ is assumed to be a zero mean, complex Gaussian random process. According to the Bussgang theorem [128], the NL PA output $u(t)$ is related to the input $z(t)$ by the following equation

$$u(t) = Kz(t) + d(t), \tag{4.11}$$

where $d(t)$ is a zero-mean noise, which is uncorrelated with $z(t)$ and K is a complex gain with modulus $|K|$ and phase ϕ_K.

According to [129], K can be computed analytically by

$$K = \frac{1}{2}\mathbb{E}\left[\frac{\partial S(\rho(t))}{\partial \rho(t)} + \frac{S(\rho(t))}{\rho(t)}\right], \tag{4.12}$$

where $\mathbb{E}$ is the expectation operator. We recall that $S(\rho) = F_a(\rho(t))\exp(jF_p(\rho(t)))$ is the complex soft envelop of the amplified signal $u(t)$.

The variance σ_d^2 of the NL noise $d(t)$ is given by the following equation

$$\sigma_d^2 = \mathbb{E}(|d(t)|^2) = \mathbb{E}\left(|S(\rho(t))|^2\right) - |K|^2\,\mathbb{E}(\rho(t)^2). \tag{4.13}$$

Analytical computation of K and σ_d^2

The analytical computation of the NL distortion parameters K and σ_d^2 depends on the complexity of the expression of $S(\rho(t))$. Indeed and based on equations (4.12) and (4.13), the authors in [129] computed analytically K and σ_d^2 in the case of the SEL PA model. In this case, K and σ_d^2 are expressed as

$$K = (1 - e^{-\frac{v_{\text{sat}}^2}{\sigma_z^2}}) + \frac{1}{2}\sqrt{\pi \frac{v_{\text{sat}}^2}{\sigma_z^2}}\text{erfc}\left(\sqrt{\frac{v_{\text{sat}}^2}{\sigma_z^2}}\right). \tag{4.14}$$

$$\sigma_d^2 = \sigma_z^2(1 - e^{-\frac{v_{\text{sat}}^2}{\sigma_z^2}} - K^2), \tag{4.15}$$

where σ_z^2 is the variance of the PA signal input.

Nevertheless, for more complicated expressions of $S(\rho(t))$, such as Rapp, Saleh or measured memoryless PA models, the derivation of analytical expressions for the parameters K and σ_d^2 is generally intractable. In order to simplify the computation and obtain analytical expressions for these parameters, we proposed a polynomial decomposition of $S(\rho(t))$. By doing this, we can analytically compute the NL distortion parameters of equations (4.12) and (4.13) for any memoryless PA conversion characteristics after polynomial fitting.

Proposed method

The approach proposed, during the Hanen Bouhadda's PhD, aims to approximate the PA conversion characteristics by a polynomial model as given by equation (4.10).

In classical polynomial models existing in literature, only odd coefficients are generally used for fitting the AM/AM curve [63]. In order to better fit the complex soft envelope $S(\rho(t))$ of the amplified signal, we have chosen to use a full rank order polynomial with odd and even coefficients.

Using a polynomial decomposition of $S(\rho(t))$, the computation of K and σ_d^2 given by equations (4.12) and (4.13) can be done, giving closed form analytical expressions. This will be achieved by the computation of the expectation of a power of Rayleigh random variable, $\mathbb{E}[\rho(t)^l]$, where, $l = 1.....L$. By combining equations (4.12) and (4.10), we can write

$$K = \frac{1}{2}\sum_{l=1}^{L}(l+1)a_l\mathbb{E}\left[\rho(t)^{l-1}\right]. \tag{4.16}$$

The variance σ_d^2 of the NL noise distortion $d(t)$, given in equation (4.13), becomes

$$\sigma_d^2 = \sum_{l=1}^{L}|a_l|^2\,\mathbb{E}\left[\rho(t)^{2l}\right] + 2\sum_{n,l=1,n\neq l}^{L}\Re[a_n a_l]\mathbb{E}\left[\rho(t)^{n+l}\right] - |K|^2\,\mathbb{E}\left[\rho(t)^2\right], \tag{4.17}$$

where $\Re[.]$ stands for the real part.

The above theoretical expressions of K and σ_d^2 involve the computation of the expectation of $\rho(t)^l$ (l is a positive integer). This expectation is equivalent to calculate the l^{th} derivation of the Moment Generating Function (MGF). We can write $\mathbb{E}[\rho(t)^l]$ as

$$\mathbb{E}[\rho(t)^l] = \left.\frac{\partial^l M(t)}{\partial t^l}\right|_{t=0} \tag{4.18}$$

where l is a positive integer, and $M(t)$ is the MGF: $M(t) = e^{\rho t}$.

A generic expression for the computation of $\mathbb{E}[\rho(t)^l]$ is given in [130]. It is expressed as follows

- For odd values of l, we have

$$\mathbb{E}\left[\rho(t)^l\right] = \left.\frac{\partial^l M(t)}{\partial t^l}\right|_{t=0} = \sqrt{\frac{\pi}{2}}\sigma_z^l\prod_{i=0}^{\frac{l-1}{2}}(2i+1). \tag{4.19}$$

IBO (dB)	ϕ_0 (eq 4.9)	Simulation K (eq 4.12)	Simulation σ_d^2 (eq 4.13)	Theoretical K (eq 4.21)	Theoretical σ_d^2 (eq 4.22)
Rapp					
4	-	0.7699	4.4759×10^{-3}	0.7690	4.4431×10^{-3}
6	-	0.8307	1.8950×10^{-3}	0.8297	1.8722×10^{-3}
8	-	0.8798	7.0742×10^{-4}	0.8785	7.0583×10^{-4}
Saleh					
4	0	0.6042	1.0330×10^{-2}	0.6036	1.0317×10^{-2}
6	0	0.6976	4.9589×10^{-3}	0.6969	4.9654×10^{-3}
8	0	0.7784	2.1228×10^{-3}	0.7775	2.1030×10^{-3}
4	$\pi/6$	$0.5917 + 0.1106j$	1.1339×10^{-2}	$0.5904 + 0.1068j$	1.1271×10^{-2}
6	$\pi/6$	$0.6887 + 0.0995j$	5.5901×10^{-3}	$0.6870 + 0.0948j$	5.5812×10^{-3}
8	$\pi/6$	$0.7727 + 0.0830j$	2.4194×10^{-3}	$0.7727 + 0.0830j$	2.4345×10^{-3}

Table 4.1: Comparison between numerical and theoretical values of $\boldsymbol{K}$ and $\boldsymbol{\sigma_d^2}$

.

- For even values of l, we have

$$\mathbb{E}\left[\rho(t)^l\right] = \left.\frac{\partial^l M(t)}{\partial t^l}\right|_{t=0} = (\sqrt{2}\sigma_z)^l(\frac{l}{2})!, \tag{4.20}$$

where ! stands for the factorial operator.

Using equations (4.16), (4.19), and (4.20), we obtain finally the generic expression for computing the complex gain K as

$$K = a_1 + \sqrt{\frac{\pi}{8}} \sum_{l=2,\ l\ even}^{L} (l+1)a_l\sigma_z^{l-1} \prod_{i=0}^{\frac{l-2}{2}}(2i+1) + \frac{1}{2} \sum_{l=3,\ l\ odd}^{L} (l+1)a_l(\sqrt{2}\sigma_z)^{l-1}(\frac{l-1}{2})!, \tag{4.21}$$

where: $\sigma_z = \sqrt{P_z} = \sqrt{\alpha^2 P_x} = \sqrt{\frac{P_{1\text{dB}}}{10^{\frac{IBO}{10}}}}$ is the standard deviation of the PA input signal.

The analytical expression of variance σ_d^2 of the NL noise $d(t)$ is given by

$$\begin{aligned}\sigma_d^2 = &\sum_{l=1}^{L} |a_l|^2 2^l \sigma_z^{2l} l! - 2|K|^2\sigma_z^2 + \sqrt{\frac{4\pi}{2}} \sum_{l,n=1,l\neq n,\ (l+n)\ odd}^{L} \Re[a_l a_n^*]\sigma_z^{l+n} \prod_{i=0}^{\frac{l+n-1}{2}}(2i+1) \\ &+ 2 \sum_{l,n=1,l\neq n,\ (l+n)\ even}^{L} \Re[a_l a_n^*](\sqrt{2}\sigma_z)^{l+n}(\frac{l+n}{2})!.\end{aligned} \tag{4.22}$$

We should note that both K and σ_d^2 are function of the signal IBO through σ_z^2 that is given by $\sigma_z^2 = \frac{P_{1dB}}{10^{IBO/10}}$.

Validation of the analytical expressions of K and σ_d^2

In order to validate our analytical analysis of K and σ_d^2 (equations (4.21) and (4.22), at first, we will compute by simulation the values of K and σ_d^2 obtained, respectively, by equations (4.12) and (4.13) for a given PA model (Rapp and Saleh). After approximation of each PA model with the polynomial model of order $L = 10$, the parameters K and σ_d^2 can be theoretically computed based on equations (4.21) and (4.22). Tab. 4.1, which is extracted from [53], compares the simulated and theoretically computed values for different PA models and different scenarios. The results are given for 10^6 4QAM symbols modulated over 64 subcarriers. For the Saleh model, we have $v_{\text{sat}} = 1\ V$, and for the Rapp one, we used the same saturation voltage with $p = 1$ and $G_0 = 1$ (equation (4.7)).

According to table 4.1, we observe, with a polynomial approximation of order $L = 10$, a very good agreement between simulation and theoretical results for both K and σ_d^2, for both Rapp and Saleh PA models.

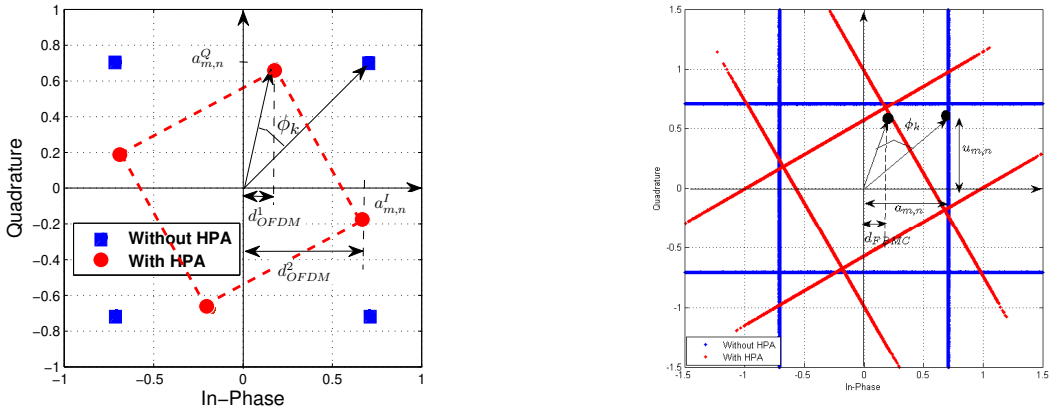

(a) CP-OFDM. (b) FBMC-OQAM.

Figure 4.4: Example of 4QAM constellation before and after PA.

4.4.2 Sensitivity analysis of OQAM based MWFs to phase errors

This study was carried during Hanen Bouhadda's PhD, where the main objective was to characterize and compensate the IB distortions induced by NL PA over FBMC-OQAM signals. As a first part of studies, we have been interested on the sensitivity of QAM and OQAM based MWF in the case where there is a phase offset at the receiving side or, equivalently, the NL PA complex gain K is not properly corrected at the receiver side. In this case the received signal after PA and channel filtering can be expressed as

$$y(t) = z(t) * [Kh_c(t)] + d(t) * h_c(t) + b(t), \tag{4.23}$$

where $h_c(t)$ is the channel impulse response and $*$ stands for the convolution product operator. We remind here that K is a complex gain that will be written $|K|\, e^{j\phi_K}$.

When considering CP-OFDM, an illustrative example of the output 4QAM constellation after PA is presented in Fig. 4.4 (a).

Let d_{OFDM} be the distance projected on real axis of the received signal points affected by the phase rotation induced by the PA complex gain K. This distance is equal to

$$d_{OFDM} = \mathrm{Re}\big((a^I_{m,n} + ja^Q_{m,n})\,|K|\, e^{j\phi_K}, \tag{4.24}$$

where $a^I_{m,n}$ and $a^Q_{m,n}$ denote respectively the in-phase and the quadrature components of the transmitted complex symbol. Depending on the sign of $a^Q_{m,n}$, the decision distance is rather d^1_{OFDM} $(a^I_{m,n} > 0)$ or d^2_{OFDM} $(a^I_{m,n} < 0)$.

As explained in section 3.2.2, FBMC-OQAM exhibits high intrinsic interference. Indeed, for this MWF, the transmission of a real symbol at time n_0 and on subcarrier m_0 generates a pure imaginary intrinsic interference u_{m_0,n_0} (equation (3.2)). However, in the presence of a phase offset (ϕ_K, this interference is no longer imaginary. Consequently, by taking the real part of the received signal, we obtain a part of the useful signal distorted by the interference signal (u_{m_0,n_0}). Fig. 4.4 (b) shows the 4QAM constellation affected by the PA complex gain and the distance representation in the FBMC-OQAM case. We note that this constellation is considered before the OQAM demodulation. The FBMC-OQAM distance d_{FBMC} is given by

$$d_{FBMC} = |K|(a_{m_0,n_0}\cos(\phi_K) - u_{m_0,n_0}\sin(\phi_K)), \tag{4.25}$$

where u_{m_0,n_0} is given by equation (3.2) and it corresponds to all possible combinations of adjacent symbols.

If no correction is made at the receiver side for the complex gain K, the 4QAM BER of CP-OFDM over AWGN channel is defined by

$$BER^{OFDM}_{4QAM} = \frac{1}{2}\,\mathrm{erfc}\left(\frac{d^1_{OFDM}}{2(\sigma_b^2+\sigma_d^2)}\right) + \frac{1}{2}\,\mathrm{erfc}\left(\frac{d^2_{OFDM}}{2\sqrt{(\sigma_b^2+\sigma_d^2)}}\right), \tag{4.26}$$

where $erfc(.)$ represents the Gauss complementary error function and σ_b^2 is the variance of white Gaussian noise.

For the FBMC-OQAM case, the decision distance d_{FBMC} can take a set of values corresponding to all possible values of u_{m_0,n_0}. We have then

$$BER_{4QAM}^{FBMC} = \sum_{u_{m_0,n_0}} P(u_{m_0,n_0}) \text{erfc}\left(\frac{d_{FBMC}}{2\sqrt{(\sigma_b^2+\sigma_d^2)}}\right), \tag{4.27}$$

where $P(u_{m_0,n_0})$ is the distribution probability of u_{m_0,n_0}.

In the case where we assume a perfect estimation of the NL distortion parameter K (K is jointly estimated with the channel response), we do the correction and the decision distances $d_{OFDM}^1 = d_{OFDM}^2 = d_{FBMC} = 1$. In this case BER_{4QAM}^{OFDM} and BER_{4QAM}^{FBMC} given by equations (4.26) and (4.27) are identical and are given by

$$BER_{4QAM}^{OFDM} = BER_{4QAM}^{FBMC} = \text{erfc}\left(\frac{|K|}{2\sqrt{(\sigma_b^2+\sigma_d^2)}}\right). \tag{4.28}$$

Using equation (4.26) and equation (4.27), we compare theoretical and simulation results for both CP-OFDM and FBMC-OQAM systems when a Saleh PA model is used. Fig. 4.5 depicts the CP-OFDM and FBMC-OQAM BER performance considering an IBO of $6dB$ and a 4QAM modulation scheme. Four scenarios are investigated: a) The linear case (no PA). b) Only the AM/AM characteristic of Saleh PA model is considered (i.e, $\phi_0 = 0$ of equation (4.9)), c) Both AM/AM and AM/PM conversion characteristics are considered (with $\phi_0 = \pi/3$) without complex gain correction at the receiver side, d) Both AM/AM and AM/PM conversion characteristics are considered (with $\phi_0 = \pi/3$) with phase error correction. This figure shows that the analytical and simulation results are in good mach in the different scenarios. It can also be noted that in the cases b) [$\phi_0 = 0$ (K is a real gain)] and d) [$\phi_0 = \frac{\pi}{3}$ (with correction of the NL factor K)], FBMC-OQAM and CP-OFDM reach the same BER performance and that theoretical result of equation (4.28) is in very good agreement with simulation results. Difference between cases b) and d) is only related to the increase of the NL noise variance σ_d^2 when AM/PM conversion is considered with $\phi_0 = \frac{\pi}{3}$. For case c), a significant degradation is present for FBMC-OQAM system compared to CP-OFDM. Even if this case is not very realistic (we have said earlier that correction of the complex gain K will be made jointly with the equalization process), it shows that FBMC-OQAM is more sensitive to phase estimation errors than CP-OFDM. This is mainly due to the distribution of the intrinsic interference in this MWF.

In [131], we have extended this work to the case where a phase estimation error occurred during the channel estimation process. The analysis carried in this paper proposed a BER analytical expressions for OQAM based MWF in AWGN and Raleigh flat fading channels. The analysis are based on approximating the intrinsic interference of OQAM MWF with a Gaussian probability distribution. For interested readers please refer to this paper to get more information about the proposed analysis.

4.4.3 SER analysis of MWFs in presence of realistic NL PAs

We used the method proposed in section 4.4.1 to compute theoretically the gain K and σ_d^2 to evaluate the symbol error rate (SER) of some MWF candidate for 5G NR. This analysis will be done for two PA models: PA1 and PA2, which will be described briefly here after.

PA1: Polynomial model

This model is based on a measured commercial 4 GHz long term evolution (LTE) user equipment PA provided by [55], exhibiting both AM/AM and AM/PM distortions. The measured AM/AM and AM/PM curves of this PA model are approximated using a full rank 9^{th} order ($L = 9$ in equation (4.10)) polynomial model.

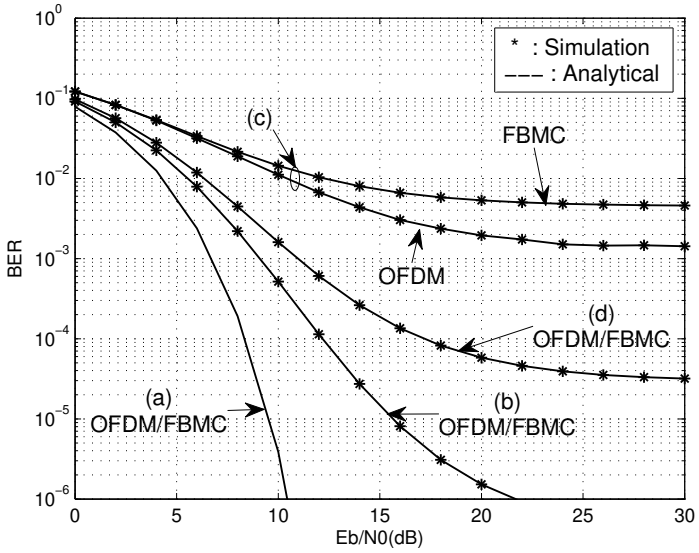

Figure 4.5: CP-OFDM and FBMC-OQAM performance comparison, 4QAM, 64 subcarriers, Saleh's PA model.

PA2: Rapp model

The second power amplifier model PA2, is based on a Rapp model and exhibits only amplitude distortion. The AM/AM conversion function: $F_a(\cdot)$, of the Rapp model is given by equation (4.7). As expected from a Rapp model, PA2 AM/AM conversion characteristic shows a linear performance for low amplitudes of the input signal. The parameters G_0 and v_{sat}, are computed to make the linear gain of this PA model equal to that of PA1. The knee factor p is chosen to be equal to 1.1 to have a different $1dB$ compression point from that of PA2 model. For purpose of theoretical analysis of PA2 effects on transmitted signals, the AM/AM characteristic of this PA model is approximated with a full rank polynomial model of order $L = 15$. The conversion characteristics of the two PA models are depicted by Fig. 4.6.

Case of AWGN channel

According to equation (4.23) and to the system model shown in Fig. 4.3, we can write the received signal $y(t)$, in presence of AWGN channel, and after perfect compensation of the complex gain K at the receiver side as follows

$$y(t) = \alpha x(t) + \frac{d(t) + b(t)}{K} \tag{4.29}$$

From equation (4.29), it is straightforward to write, that, over AWGN channel, the SER of MQAM modulated symbols for any MWF [132], as:

$$SER_{MQAM}^{AWGN} = 2(1 - \frac{1}{\sqrt{M}})erfc\left(\sqrt{\frac{3\alpha^2 |K|^2 log_2(M)}{2(M-1)(\sigma_d^2 + \sigma_b^2)}}\right), \tag{4.30}$$

where $\sigma_b^2 = \sigma_u^2/(log_2(M).E_b/N_0)$ is the thermal noise variance corresponding to E_b/N_0 and σ_u^2 is the variance of the PA output signal.

From equation (4.3), it can be seen that IBO coefficient α depends on the considered MWF scheme. Indeed, the average power of the transmitted signal $x(t)$: P_x can be influenced by the windowing and/or the filtering processes used in the MWF transceiver. In [58], we developed deep analysis on how we can compute theoretically IBO coefficients for some post-OFDM MWF with respect to CP-OFDM one.

Fig. 4.7 (a) presents the SER of the selected MWFs for the 3GPP PA model (PA1) with an IBO equal to $4dB$ and a 16QAM modulation. We recall that this PA model exhibits both AM/AM and AM/PM

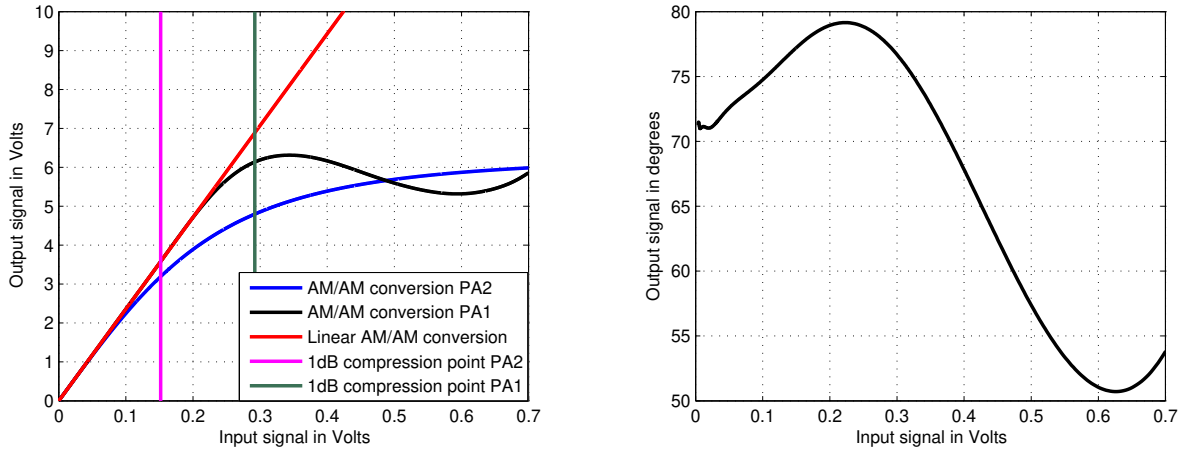

(a) AM/AM. (b) AM/PM (for PA1 only).

Figure 4.6: Conversion characteristics of PA1 and PA2.

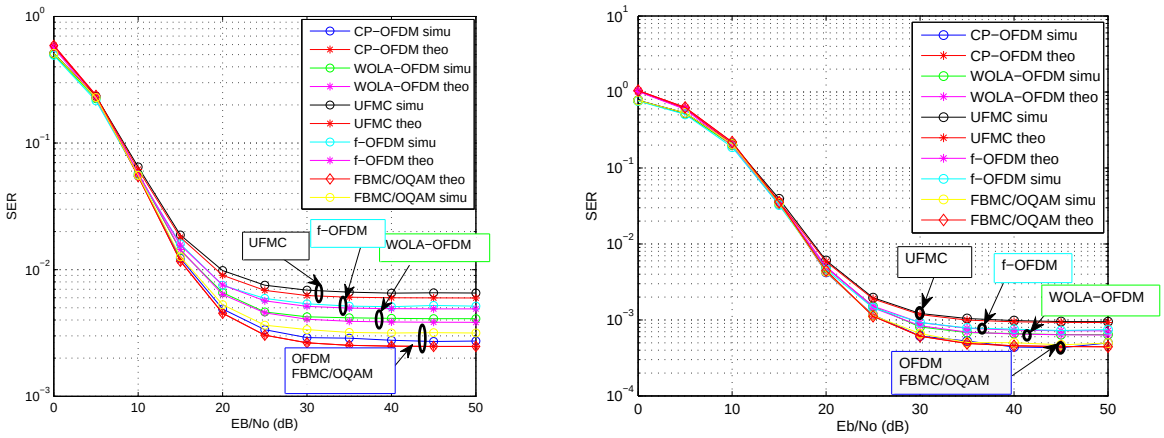

(a) PA1 (16QAM). (b) PA2 (64QAM).

Figure 4.7: SER performance of several MWFs, IBO=4dB.

distortion. As in the case of PA2, FBMC/OQAM and CP-OFDM show the same performance. However, WOLA-OFDM, UFMC and f-OFDM have lower performances than CP-OFDM. This behavior can be explained by the fact that the IBO coefficient α is impacted by the windowing/filtering operations related to these MWFs. However, the mean power of signals at the output of CP-OFDM and FBMC-OQAM modulators are the same.

Fig. 4.7 (b) presents the SER of the selected MWFs for the Rapp model PA (PA2) with an IBO equal to $4dB$ and a 64QAM modulation. As noticed for PA1, FBMC/OQAM and CP-OFDM have the same performance. WOLA-OFDM, UFMC and f-OFDM have lower performances than CP-OFDM as explained before.

Case of Rayleigh fading channel

In [54], we analyzed the effect of nonlinearities, with emphasis on amplitude and phase distortions, on the performance degradation of MWFs over frequency-flat Rayleigh fading channel. We derived a closed-form BER expression for M-array (QAM or OQAM) based OFDM system, which is valid for any PA model, even for real measured one.

We assume a slowly varying flat fading Rayleigh channel with a coherence time larger than the

symbol duration. The channel response $h_c = \nu e^{j\psi}$ is characterised by a Rayleigh distributed gain ν and a uniformly distributed phase $\psi \in [0, 2\pi]$. Assuming a perfect knowledge of the channel state information (CSI) and the complex gain K at the receiver, the ZF equalized signal is given by

$$\frac{h_c^*}{|h_c|^2 K} y(t) = z(t) + \frac{d(t)}{K} + \frac{h_c^*}{|h_c|^2 K} b(t) \tag{4.31}$$

The signal model of equation (4.31) is valid for both QAM and OQAM signals. For a given average power P_u at the PA output, the instantaneous Signal to Noise Ratio (SNR) of the detected signal can be derived as

$$\gamma = \frac{|K|^2 \nu^2 \sigma_z^2}{\nu^2 {\sigma_d}^2 + {\sigma_b}^2} \tag{4.32}$$

In [54], we developed a closed-form BER expression of uncoded (QAM or OQAM) based OFDM over quasi-static frequency-flat Rayleigh channel. This BER is given by the following equation

$$\begin{aligned} BER &= a\Big(1 - \frac{2}{\sqrt{\pi}} \sum_{n=0}^{+\infty} \sum_{k=0}^{+\infty} \frac{(-1)^{k+n}}{k!n!(2n+1)} \Big(\frac{\sigma_b^2}{\Gamma}\Big)^{k+1} \Big(\frac{1}{\sigma_d^2}\Big)^{n+k+3/2} \frac{(b|K|^2\sigma_x^2)^{n+1/2}}{k+n+3/2} \\ &\times \ {}_2F_1(k+2, n+k+3/2; n+k+5/2; 1)\Big) \end{aligned} \tag{4.33}$$

where $\Gamma = E[\nu^2]$ is the average fading power, ${}_2F_1(.,.;.;.)$ denotes the Hypergeometric function and (a,b) are modulation-specific constants with $a = \frac{2\sqrt{M}-1}{\sqrt{M} log_2(M)}$ and $b = \frac{3log_2(M)}{M-1}$ for MQAM.

To find the number of terms required in the infinite series of equation (4.33), we have checked many values of n and k and have verified their tightness with the simulations for different values of M. For all the results shown in Fig. 4.8, the infinite series have been truncated to $n = 10$ and $k = 50$ terms with negligible loss in precision.

We considered FBMC-OQAM and CP-OFDM systems with $N_{FFT} = 64$ subcarriers. For the PA model, we consider the Saleh's one operating at an IBO $= 6\ dB$ with a nominal phase distortion $\phi_0 = \pi/3$. With these PA model parameters, the nonlinear parameters K and σ_d^2 are respectively equal to $0.6624 + 0.1954j$ and 0.0074. It should be interesting to underline that this study is valid for any memoryless PA model because gain K and σ_d^2 can be computed for any PA using equations (4.21) and (4.22).

Fig. 4.8 shows an evaluation of the closed form BER quasi-static frequency-flat Rayleigh fading channel. For each value of M, we can see a very good agreement between the Monte-Carlo simulation results and those obtained analytically by using equation (4.33). We can also underline, for a given value of M, the perfect matching between the BER achieved by the FBMC-OQAM system and the CP-OFDM based one.

4.5 Out of band distortions analysis

The frequency localization of most MWFs is compromised when realistic RF impairments are taken into account [133]. When a signal with time-varying envelope passes through a NL PA, spectral regrowth appears at the PA output. Spectral regrowth causes adjacent channel interference, which is very tightly controlled by regulatory bodies for many over-the-air applications. Prediction of spectral regrowth for a prescribed level of PA non-linearity can be very helpful for designing communication systems. Given the PA conversion characteristics, it is desirable to be capable to predict theoretically, whether the PA can be used to amplify certain types of signals. Through polynomial model of PA, we can derive a closed-form expression for the output auto-covariance function, whose Fourier transform (FT) yields to the PSD, for any stationary input.

There are two popular methods for spectral regrowth analysis, where we can derive a closed-form expression for the auto-covariance function of the PA output. The first method is based on Price's theorem [134] and the later one is based on cumulants [123]. In a scenario where AM/PM conversion is to be considered, it becomes complicated to predict the PSD using the Price theorem. Additionally,

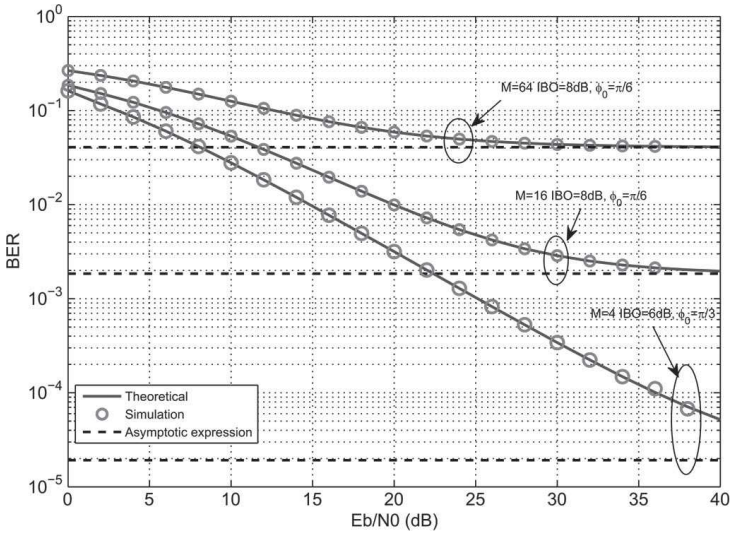

Figure 4.8: BER vs E_b/N_0 for M-ary (QAM or OQAM) based OFDM, $N_{FFT} = 64$, Saleh PA model.

the computation of integration variables required by this method becomes complicated when high order polynomial PA models are used. Due to these two reasons, the cumulant-based method becomes more adequate for PSD prediction.

We recall that $z(t) = \rho(t)e^{j\varphi(t)}$ and $u(t)$ are the base-band equivalent for the PA input and output signals respectively (Fig. 4.3). For any measured or modeled PA, we can approximate its input output conversion characteristics by a NL polynomial as

$$u(t) = z(t)\sum_{l=0}^{L} a_{2l+1}\rho(t)^{2l} = \left[\sum_{l=0}^{L} a_{2l+1}\rho(t)^{2l+1}\right] e^{j\varphi(t)}, \tag{4.34}$$

where, $2L+1$ is the order of the polynomial model and a_{2l+1} are the complex coefficients of the polynomial model.

In equation (4.34), only the odd order harmonics are taken into account by the polynomial fitting process [135]. In [136], this approximation was compared to full ranking polynomial and the conclusion is that both approaches give the same performance in terms of base-band modeling of PA nonlinearity.

As a first contribution, we proposed in [62], the prediction of the spectral regrowth of OQAM based MWF with Rapp PA model and using Price theorem. Then, during the Krishna Bulusu's PhD, we extended our analysis to any measured or modelled PA, using cumulants [64]. I want to underline that the analysis presented here after are not restricted to CP-OFDM and FBMC-OQAM. Indeed, the proposed methods (based on Price theorem and on cumulants) remain valid provided that the signal at the output of the MWF Tx is Gaussian.

4.5.1 Prediction of spectral regrowth with Price theorem

Using the AM/AM odd order polynomial model with real coefficient, the soft complex envelope of the amplified signal (see equation (4.34)) can be written as following

$$S(\rho(t)) = \sum_{l=0}^{L} a_{2l+1}\rho(t)^{2l+1}. \tag{4.35}$$

The analytical estimation of the PSD re-growth, based on Price's theorem, which is applicable to any memoryless nonlinearity is presented in [134]. This theorem is summarized by the following formula

$$\frac{\partial^n R_u}{\partial R_z^n} = \mathbb{E}\left\{S^n(\rho(t)).S^n(\rho(t-\tau))\right\}, \tag{4.36}$$

where n is the order of the derivative. R_z and R_u are respectively the cross-correlation functions of the PA input and output signals.

The derivation of equation (4.36), determines the relationship between R_u and R_z which can be written as

$$R_u(\tau) = \sum_{l=0}^{L} \eta_{2l+1} R_z(\tau)^{2l+1}, \tag{4.37}$$

where η_{2l+1} are integration coefficients which are function of both the polynomial fitting coefficients (a_{2l+1} with $l = 1..L$) and σ_z^2, which is the variance of the signal at the PA input. For more details about the way to compute the integration coefficients η_{2l+1}, please refer to [62].

By applying FT to equation (4.37), we can deduce the estimated PSD of the output signal $\Gamma_u(f)$ given by

$$\Gamma_u(f) = \sum_{l=0}^{L} \eta_{2l+1} \underbrace{\Gamma_z(f) * ... * \Gamma_z(f)}_{2l+1}, \tag{4.38}$$

where $*$ denotes the convolution product and $\Gamma_z(f)$ the PSD of the PA input signal $z(t)$.

To validate the accuracy of the spectral re-growth prediction given by equation (4.38), we will use a polynomial fitting of Rapp PA model. For this model we used a saturation voltage $v_{sat} = 1\ V$ and a knee factor $p = 2.25$, according to measurements corresponding to a real WIMAX amplifier used in PHYDYAS European Project [137].

Two scenarios will be examined. In the first one, a single user is occupying a given number of sub-carriers. The second scenario correspond to a fragmented spectrum between 3 users. The FBMC-OQAM system transmits signals over 1024 sub-carriers. The modulated signals are gain-scaled to achieve a suitable IBO for the signals at the input of users PAs.

Fig. 4.9 (a) gives the results concerning the PSD of the signal at the output of the Rapp model approximated by 3^{rd} and 5^{th} order odd coefficients. The IBO is fixed $1dB$ in this first scenario. As shown in Fig. 4.9 (a), the 5^{th} order polynomial PA model is able to estimate the spectral re-growth of the amplified signal with a higher accuracy. It is straightforward that increasing the polynomial order model of the AM/AM characteristic, leads to a more accurate PSD estimation of the non-linearly amplified signals.

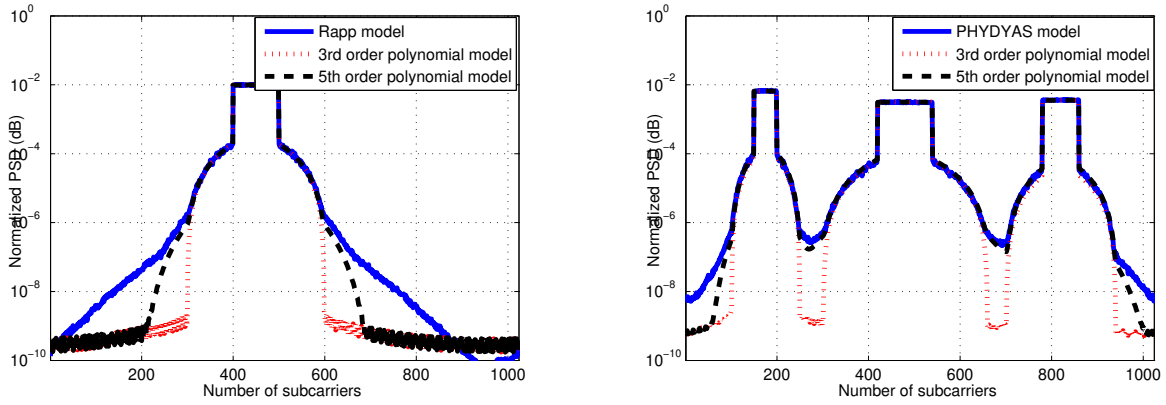

(a) Single user case.

(b) Multi user case.

Figure 4.9: Spectral regrowth prediction using Price theorem with polynomial models of order 3 and 5.

In a second scenario, we study the impact of the polynomial model order on the estimation of the PSD re-growth in the case where three users are operating on closely spaced sub-bands. The three users have different bandwidths and are amplified with the same PA model, but at different IBO values

- User 1: 120 subcarriers with $IBO = 1dB$,
- User 2: 50 subcarriers with $IBO = 2dB$,

- User 3: 80 subcarriers with $IBO = 3dB$.

We can see from Fig. 4.9 (b) that the estimated PSD at the output of a 5^{th} order polynomial fits well the simulated PSD corresponding to Rapp model. Indeed, a gap of about $25dB$, between the PSD estimated by a 3^{rd} order polynomial and the simulated one, is observed at the overlapping bands between the users. In the case where the estimation of the PSD is based on the use of a polynomial model of order 3, we could see free bands between the three operating users, which is not really the case. For FBMC-OQAM, as for any other MWF systems, it is more appropriate to increase the polynomial model approximation for the PA characteristic. This leads to more accurate analytical estimation of the spectral re-growth of the nonlinearly amplified signals, but at an extent of augmented complexity related to the computation of the integration parameters η_{2l+1} required by equation (4.38).

4.5.2 Prediction of spectral regrowth with cumulants

Price theorem involves integral calculus. It may sometime involve difficulty in determining the integration constant which will impact the closed-form expression derivation. Additionally, in a scenario where AM/PM conversion is to be considered, it becomes complicated to predict the PSD using the Price theorem. Due to these two reasons, the cumulant-based method seems to be more adequate for PSD prediction [123]. We carried this study during the Krishna Bulusu's PhD and within the framework of the FP7 EMPhAtiC project.

Because of their interesting properties, cumulants are used as an alternative to the moments of a distribution. Cumulants were first introduced by Thorvald N. Thiele, who called them as *semi-invariants* [138]. They were first called *cumulants* in a paper by Ronald Fisher and John Wishart [139]. The n^{th} order cumulant of a random variable z is defined as

$$c_{nz} = \frac{\partial^n}{\partial t^n} C(t)\bigg|_{t=0}, \tag{4.39}$$

where $C(t)$ is the cumulant generating function given by the logarithm of the MGF $M(t) = \mathbb{E}(e^{tz})$.

$$C(t) = ln(\mathbb{E}(e^{tz})) = \sum_{n=1}^{\infty} c_{nz} \frac{t^n}{n!}. \tag{4.40}$$

For high number of sub-carriers, we can assume most of MWFs signals to be Gaussian process as evident from Central limit theorem. If $z(t)$ is zero-mean, Gaussian and i.i.d, the auto-covariance function of the PA output $u(t)$ is the same as its auto-correlation function: $c_{2u}(\tau)$. Closed form expression of this function can be derived by using Cumulants. According to [123], the auto-correlation function for a $(2L+1)^{th}$ polynomial order nonlinearity is given as

$$c_{2u}(\tau) = \sum_{m=0}^{L} \xi_{2l+1} |c_{2z}(\tau)|^{2l} c_{2z}(\tau), \tag{4.41}$$

where $c_{2z}(\tau)$ is the auto-correlation function of the PA input signal and ξ_{2l+1} are constant coefficients given by

$$\xi_{2l+1} = \frac{1}{l+1} \left| \sum_{k=l}^{L} a_{2k+1} \binom{k}{l} (k+1)! [c_{2z}(0)]^{2l} \right|^2, \tag{4.42}$$

where $\binom{n}{m} = \frac{n!}{(n-m)!m!}$, $n \geq m$.

The FT of $c_{2u}(\tau)$, obtained from equation (4.41), yields to the PSD of the amplified signal $\Gamma_u(f)$ and

is given by

$$\begin{aligned}\Gamma_u(f) &= \int_{-\infty}^{+\infty} c_{2u}(\tau)e^{-j2\pi f\tau}d\tau \\ &= \int_{-\infty}^{+\infty}\sum_{l=0}^{L}\xi_{2l+1}|c_{2z}(\tau)|^{2l}c_{2z}(\tau)e^{-j2\pi f\tau}d\tau \\ &= \sum_{l=0}^{L}\xi_{2l+1}\underbrace{\Gamma_z(f)\star\Gamma_z(f)\star\ldots\star\Gamma_z(f)}_{l+1}\star\underbrace{\Gamma_z(-f)\star\Gamma_z(-f)\star\ldots\star\Gamma_z(-f)}_{l},\end{aligned} \tag{4.43}$$

where $\star$ denotes convolution. It has to be noted that, as $\Gamma_z(f)$ is symmetric, i.e. $\Gamma_z(f) = \Gamma_z(-f)$, the $\Gamma_u(f)$ is also symmetric as well.

As from equation (4.38), we call these approachs as spectral prediction, because the knowledge of input PSD $\Gamma_z(f)$ and the polynomial coefficients a_{2l+1} allows the prediction of the $\Gamma_u(f)$.

Note that for many MWF, it is straightforward to have analytical expression of $\Gamma_z(f)$. In [140], you can find those corresponding to CP-OFDM and FBMC-OQAM.

To validate the PSD prediction given by equation (4.43), we carried simulation with a FBMC-OQAM system with 128 SCs. PHYDYAS prototype filter and a Saleh PA model (with $\phi_0 = \pi/3$ and $v_{sat} = 1V$) has been used in the simulations. Fig. 4.10 (a) presents the simulations results with a signal user activating 10 active sub-carriers and operating at an IBO equal to $3dB$. We can observe that the 11^{th} order polynomial approximation gives theoretical result very close to simulated PSD.

In a second scenario, we considered three users operating on closely spaced sub-bands. The three users are amplified at an IBO of $1dB$. The details of active sub-bands for the three users are given below

- User 1: 30^{th} to 39^{th} sub-carrier,
- User 2: 45^{th} to 49^{th} sub-carrier,
- User 2: 52^{nd} to 56^{th} sub-carrier.

Simulation results for PSD prediction when 3 users share neighboring sub-carriers are shown in Fig. 4.10 (b). In this typical scenario, we can notice that despite operating the PA at an $IBO = 1dB$, the prediction of the PSD is well achieved up to $-20dB$, $-25dB$ and $-33dB$ with polynomial fittings of orders 3^{rd}, 7^{th} and 11^{th} respectively. This multiuser scenario confirms that when choosing thinner sub-bands for the different users, and as we are operating the PAs close to their saturation region, we need higher-order polynomial fitting to predict the spectral regrowth accurately.

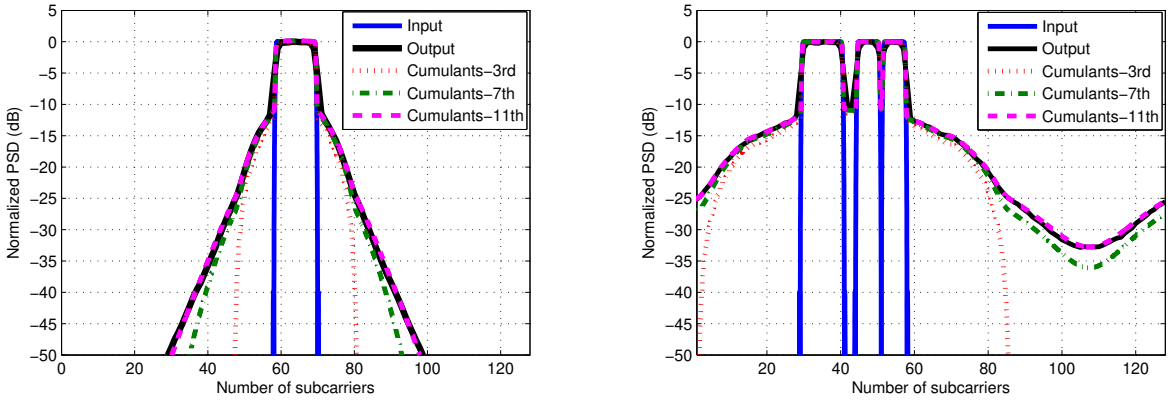

(a) Single user case (IBO=3dB). (b) Multiuser case (IBO=1dB).

Figure 4.10: Spectral regrowth prediction using cumulants with different polynomial model orders.

4.6 Conclusion

In this chapter, I presented a theoretical approach to characterize the IB effects of memoryless NL. Based on Bussgang's theorem, we modeled the in-band distortion by a complex gain and an additive Gaussian noise which is uncorrelated with the signal at the PA input. These distortion parameters can be computed theoretically from polynomial approximation of any memoryless PA conversion characteristics. The developed theoretical performances were found to agree completely with simulations, and FBMC-OQAM, BF-OFDM, WOLA-OFDM and f-OFDM showed quite similar performance with CP-OFDM in terms of BER/SER over AWGN and Rayleigh fading channels.

Polynomial models were also used to characterize the spectral regrowth of the transmitted MWFs introduced by NL PAs with different back-off values. Spectral regrowth prediction for CP-OFDM has been extensively studied in the literature, by using Price's theorem or by cumulants. Here, we have extended the analysis to FBMC-OQAM and we confirm the applicability of the proposed approaches to other MWFs, given that the signals emitted from all MWFs Tx are Gaussian processes.

In-Band distortion level along with prediction of spectral regrowth for a prescribed level of PA non-linearity can be very helpful for designing communication systems. It gives very good understanding about the severity of the PA non-linearity and its impact. Thereby, one can perform PAPR reduction and PA linearization to enhance the system energy efficiency and decrease the spectral regrowth to an acceptable level by regulatory standards. Some contributions on PAPR reduction and PA pre-distortion will be presented in the forthcoming chapter.

Chapter 5

Enhanced PA efficiency for 5G and beyond MWFs

5.1 Introduction

PA linearity and energy efficiency are two vital parameters in the context of signals with strong fluctuations, as it is the case of most of MWF techniques. To get rid of the amplified signal distortion, the PA can be made to operate at high IBO, which leads to very poor energy efficiency. On the other hand, increasing the PA linearity together with PAPR minimization allows to increase power efficiency by increasing the mean power of the input signal very close to input saturation power. Furthermore, if the input signal is always in the linear region of the PA, in-band and OOB effects will be limited.

PAPR reduction and predistortion are pure signal processing techniques, where the MWFs signals is pre-processed before amplification to ensure enhanced energy efficiency. Other approaches can be also envisaged to increase the PA efficiency, among them we can cite those based on modifying transmitter architecture.

As a third research activity axis, I have been interested, in the context of EMPhaTiC European project, Accent5 and WONG5 national projects, on enhancing the energy efficiency of CP-OFDM and some post-OFDM MWFs transceivers by using both signal processing-based techniques as well as modified architecture-based ones. An important part of these studies has been carried with two PhD students: Krishna Bulusu and Khaled Tahkoubit. Also, I have collaborated with many researchers among them, I can cite colleagues from Tampere University of Technology, CentraleSupélec and AIRBUS.

In this chapter, section 5.2 will be devoted to present some signal processing based algorithms and proposed to enhance PA efficiency by reducing the PAPR and/or linearizing PA conversion characteristics. In section 5.3, I will introduce an hybrid approach for enhancing PA efficiency which is based on signal transformation along with modified PA architecture.

5.2 Signal processing based solutions

As explained and studied in the previous chapter, the presence of high peaks causes IB as well as OOB distortions when the MWF signal is passed through a PA, which does not have enough linear range. Looking at Fig. 5.1 (a), we can identify two signal processing approaches for mitigating the NL effects of the PA at the transmitter side:

- We can decrease the distribution of high values of the instantaneous power of the transmitted signal. This is equivalent to lowering the PAPR of $z(t)$, as illustrated in Fig. 5.1 (b),
- We can increase the PA linear range by using PA linearization techniques. This is equivalent to increasing P_z towards v_{sat}^2 (see Fig. 5.1) (b).

In multi-carrier-based communication systems, the PAPR reduction remains to be one of the most crucial issues that need to be solved effectively with a reasonable complexity. Existing popular PAPR schemes for OFDM signals, include clipping [141], Tone Injection (TI) [142], Tone Reservation (TR) [143], Active Constellation Extension (ACE) [144], Partial Transmit Sequence (PTS) [145], Selective Mapping (SLM) [146] and block coding [147]. Comparison of most of these aforesaid schemes can be found in [148] and [149]. In general, PAPR reduction techniques can be broadly classified into three categories namely *clip effect transformations (clipping), block coding techniques and probabilistic approaches.* The

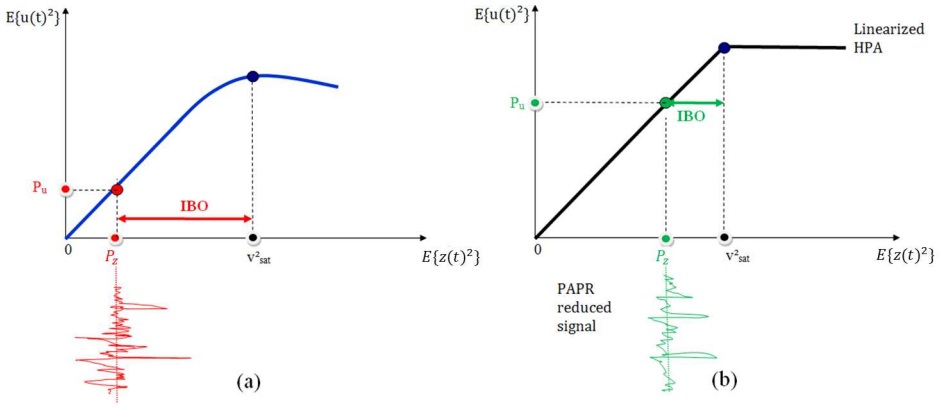

Figure 5.1: Linearized PA and input signal with lowered PAPR.

adaptation of most of the above mentioned PAPR reduction techniques is straightforward to post-OFDM MWF whose signals structures is like that of the CP-OFDM, i.e., no overlapping between symbols. However, this is not valid for filter bank based MWF like FBMC-OQAM, FBMC-QAM or BF-OFDM, where special care should be taken to take into account the overlapping nature of the symbols at the MWF Tx.

From another side, PA linearization aims to mitigate the IB and OOB emissions below the limits determined by standardization and regulatory bodies. These emission limits depend on technologies and standards and can be different between UL and DL. For example the Adjacent Channel Power Ratio (ACPR) limit in LTE uplink transmission is -30 dBc, which is usually obtainable without any PA linearization, while for the downlink it is generally -45 dBc, which usually cannot be met without some kind of PA linearization [75].

PA linearization techniques include feedback linearization, feedforward linearization, RF predistortion, and Digital predistortion (DPD) [150, 151]. Feedback techniques rely on a closed-loop feedback from the PA output to its input to reduce the emissions and are limited in terms of bandwidth. Feedforward linearization is an inherently wide band technique but requires considerable additional RF hardware. The accuracy, flexibility, as well as practical bandwidth of feedforward are all limited by the analog components. RF predistortion is a wide band linearization technique, but its fidelity is rather limited due to the analog implementation. Digital predistortion, on the other hand, is probably the most effective and cost efficient among all linearization techniques. It has the greatest flexibility, reconfigurability, and performance in most cases. Its bandwidth is mostly limited by the digital hardware and will therefore benefit from the scaling of CMOS technology. The focus in the rest of this chapter will be on DPD, while for more information on other linearization techniques, the reader is referred to [150, 151]. In the following, I will present the contributions related to different MWFs, while considering memoryless measured or modelled PAs. The proposed solutions focus either on PAPR reduction, DPD or on a combination of this two processing.

5.2.1 Case of OQAM based MWFs

During the Krishna Bulusu's PhD, I have been working on PAPR reduction and DPD for OQAM based MWF. I will present in the following some of the proposed algorithms.

5.2.1.1 PAPR reduction techniques

Dispersive SLM

Similar to the classical SLM scheme, we proposed a Dispersive SLM (DSLM) algorithm to reduce the PAPR of OQAM based MWFs. With DSLM, each input symbol vector $\mathbf{X}_m$ is phase rotated with U

different input vectors giving $\{\mathbf{X}_m^{(u)}\}_{u=0}^{U-1}$. After MWF modulation, the symbol achieving the least PAPR is selected for transmission.

From Fig. 5.2, it is evident that unlike CP-OFDM, the FBMC-OQAM symbol energy spreads into its succeeding symbol period intervals rather than in its own one, which means that almost all of its energy lies in the two succeeding symbols period intervals rather than its own one. So, to find the optimal rotation for any m^{th} FBMC-OQAM symbol, the overlapping of its previous symbols must be taken into consideration. This is the main idea behind the DSLM algorithm. This algorithm involves the following steps:

Step 1 - Initialization: We generate U phase rotation vectors $\{\boldsymbol{\phi}^{(u)}\}_{u=0}^{U-1}$ of length N_{FFT} and initialize the counter m. As long as the condition $0 \leq m \leq M-1$ (M is the total transmitted FBMC-OQAM symbols.) is satisfied, we perform the following **Steps 2, 3, 4, 5, 6** and **7**.

Step 2 - Phase rotation: The m^{th} input symbol vector $\mathbf{X}_m$ is phase rotated with U different phase rotation vectors $\{\boldsymbol{\phi}^{(u)}\}_{u=0}^{U-1}$, giving $\{\mathbf{X}_m^{(u)}\}_{u=0}^{U-1}$.

Step 3 - FBMC-OQAM modulation: For all patterns of m^{th} input symbol vector, we compute

$$x_m^{(u)}(t) = \underbrace{\sum_{m'=0}^{2m-1}\sum_{n=0}^{N-1} a_{m',n}^{(u_{min}^m)}\gamma_{m',n}(t)}_{overlapping\ past\ symbols} + \underbrace{\sum_{m'=2m}^{2m+1}\sum_{n=0}^{N-1} a_{m',n}^{(u)}\gamma_{m',n}(t)}_{current\ symbol}, \tag{5.1}$$

where $x_m^{(u)}(t) \neq 0$ from $t = [0, (2m+1)\frac{T}{2} + 4T)$, $a_{m',n}^{(u_{min}^m)}$ are OQAM symbols corresponding to previously rotated symbols $\mathbf{X}_m^{(u_{min}^m)}$ and $\gamma_{m,n}(t)$ is the shifted version of the prototype filter impulse response in time and frequency noted (as per equation (3.2)).

Step 4 - Partial PAPR Calculation: Then, we compute the partial PAPR of $x_m^{(u)}(t)$ on a certain interval $T_0 = [mT + T_a, mT + T_b)$, which is any arbitrary interval within the $[mT, mT + 4.5T]$ interval.

$$PAPR_{(T_0)}^{(u)} = \frac{\max_{t\in T_0} |x_m^{(u)}(t)|^2}{\frac{1}{T_0}\int_{T_0} |x_m^{(u)}(t)|^2.dt}, \tag{5.2}$$

where $T_a \geq 0$ and $T_b < 4.5T$. The choice of interval T_0 during this step plays vital role in increasing the peak reduction performance.

Step 5 - Selection: Among $PAPR_{T_0}^{(u)}$, the index u is chosen for the signal with least PAPR as per the below criterion

$$u_{min}^m = \underset{0\leq u\leq U-1}{\arg\min}\left[PAPR_{x_m^{(u)}(t)}\right], mT + T_a \leq t < mT + T_b. \tag{5.3}$$

Step 6 - Updation: We update the current input symbol vector:

$$\mathbf{X}_m^{(u_{min}^m)} = \mathbf{X}_m \,.\, \boldsymbol{\phi}^{(u_{min}^m)}. \tag{5.4}$$

The index u_{min}^m will be stored in a vector $\mathbf{U}_{SI}$ in order to be transmitted as Side Information (SI) for perfect recovery of the signal at the receiver.

Step 7 - Incrementation: Increment the value of m by 1 and go to **Step 2**.

We published this algorithm in the conference paper [66], which is one of the most cited references for reducing the PAPR of FBMC-OQAM signals.

Fig. 5.3 shows the performance of DSLM for different values of U, when the partial PAPR of step 4 is computed over $T_0 = [(m+1)T, (m+3)T)$. From the simulation results, we can notice that the FBMC-OQAM with DSLM is trailing to that of OFDM with SLM in PAPR reduction performance. We can also perceive that the trail gap in terms of PAPR reduction performance, is increasing with the size of U. The reason for sub-optimality is that, in DSLM, the phase rotations of the past symbols are fixed or already chosen since it is based on symbol-by-symbol optimization. Whatever peak reduction we may obtain for the current symbol, can probably be hampered by its immediate next symbol. This motivated us to investigate this sub-optimality and probe for optimal solutions.

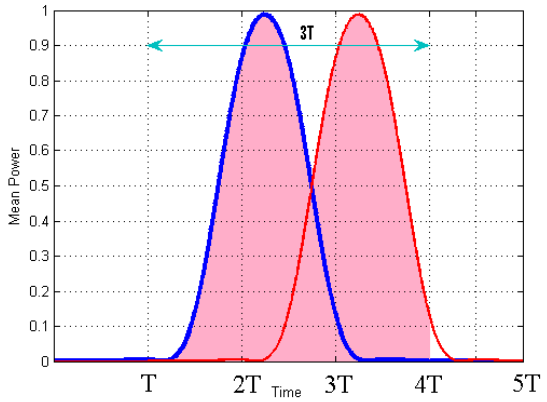

Figure 5.2: Power profile of two FBMC-OQAM symbols in the duration of $[T, 4T]$ w.r.t the current symbol.

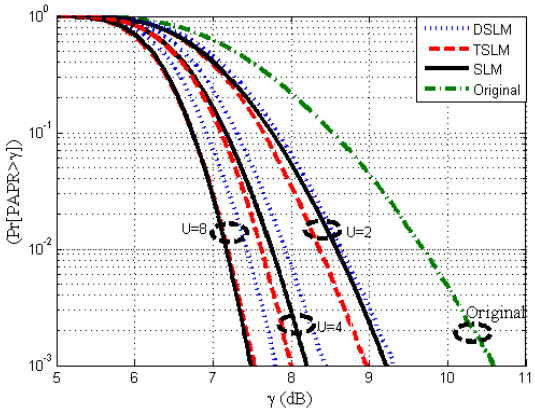

Figure 5.3: CCDF of PAPR for FBMC-OQAM symbols with DSLM and TSLM and OFDM with SLM.

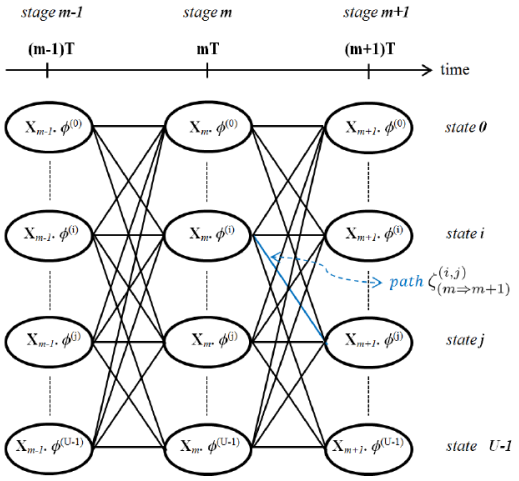

Figure 5.4: Illustration of the trellis diagram between M stages composed of U states.

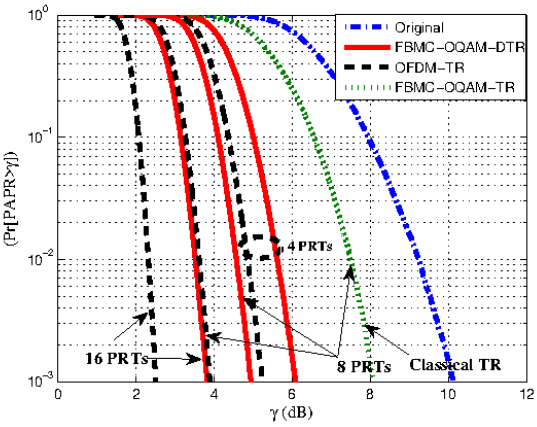

Figure 5.5: CCDF of PAPR plot for FBMC-OQAM symbols with PAPR calculated over $[T, 3T)$ with size of PRT set, $R = \{4,\ 8,\ 16\}$.

Trellis SLM

Optimal approach would be to test all possible phase rotation vectors to find the lowest PAPR in the overall signal composed of M FBMC-OQAM symbols. This would have huge complexity, as there is a need to perform an exhaustive search over U^M possible rotation vectors. A quasi-optimal solution would be a trellis-based dynamic programming, where we perform a trellis-based search to find the optimal phase rotations, considering several successive symbols at a time. This idea gave rise to the Trellis SLM (TSLM) algorithm published in [68, 152].

If we have to transmit M input symbol vectors $\{\mathbf{X}_0, \mathbf{X}_1, \ldots, \mathbf{X}_{M-1}\}$, then we need to find $\mathbf{\Theta}$, which is the optimal set of M different phase rotation vectors that give the best PAPR.

$$\mathbf{\Theta} = \{\boldsymbol{\phi}^{(u^0_{min})}, \boldsymbol{\phi}^{(u^1_{min})}, ..., \boldsymbol{\phi}^{(u^{M-1}_{min})}\}, \tag{5.5}$$

where, $\{u^0_{min}, u^1_{min}, ..., u^{M-1}_{min}\}$ are the indices of optimal phase rotation vectors for the M input symbol vectors, which are to be sent to the receiver as SI. With M FBMC-OQAM symbols and U phase rotation vectors, we need to find the best path in the trellis of Fig. 5.4 that gives the lowest PAPR.

For $0 \leq m \leq M-1$, every m^{th} FBMC-OQAM symbol $x_m(t)$, obtained from modulation of input

symbol vector $\mathbf{X}_m$, is represented as the m^{th} stage in the trellis that will reach at time instant mT. At each stage, there will be U different states, representing the rotated FBMC-OQAM symbols. Among these states, any i^{th} trellis state indicates rotation by phase rotation vector $\boldsymbol{\phi}^{(i)}$. Between every two stages, there exist U^2 number of possible paths. The joint FBMC-OQAM modulation of m^{th} and $(m+1)^{th}$ rotated input symbol vectors $\mathbf{X}_m^{(u)}$ and $\mathbf{X}_{m+1}^{(v)}$ respectively is represented in the trellis by the path $\zeta_{(m\Rightarrow m+1)}^{(u,v)}$ between u^{th} state in m^{th} stage and v^{th} state in $(m+1)^{th}$ stage. For a given arriving state v at stage $m+1$, the survivor state in stage m is the one giving the lowest PAPR. over $T_0 \in [mT+T, mT+4.5T]$. The TSLM algorithm involves the following steps:

Step 1 - Initialization: Firstly, we generate M complex input symbol vectors $\{\mathbf{X}_m\}_{m=0}^{M-1}$ and U phase rotation vectors $\{\boldsymbol{\phi}^{(u)}\}_{u=0}^{U-1}$ of length N_{FFT}. We initialize the counter m ($m=0$) and the state metrics for all states of the first stage ($\Psi_{(u,0)}$ for $u = 0..U-1$). As long as the condition $0 \leq m \leq M-2$ is satisfied, we perform the following **Steps 2, 3, 4, 5** and **6** in a repeated manner.

Step 2 - Phase rotation: Two input symbol vectors $\mathbf{X}_m, \mathbf{X}_{m+1}$ are phase rotated with U different phase rotation vectors $\{\boldsymbol{\phi}^{(u)}\}_{u=0}^{U-1}$ and $\{\boldsymbol{\phi}^{(v)}\}_{v=0}^{U-1}$, giving $\{\mathbf{X}_m^{(u)}\}_{u=0}^{U-1}$ and $\{\mathbf{X}_{m+1}^{(v)}\}_{v=0}^{U-1}$ respectively. The symbols, $a_{m',n}^{(u)}$ and $a_{m',n}^{(v)}$ are chosen from $\mathbf{X}_m^{(u)}$ and $\mathbf{X}_{m+1}^{(v)}$ respectively.

Step 3 - FBMC-OQAM modulation: FBMC-OQAM modulation is done jointly for all combination of the patterns of m^{th} and $(m+1)^{th}$ input symbols, is written by

$$x_m^{(u)}(t) = \sum_{m'=2m}^{2m+1}\sum_{n=0}^{N-1} a_{m',n}^{(u)}\gamma_{m',n}(t), x_{m+1}^{(v)}(t) = \sum_{m'=2m+2}^{2m+3}\sum_{n=0}^{N-1} a_{m',n}^{(v)}\gamma_{m',n}(t), \tag{5.6}$$
$$x_{m,m+1}^{(u,v)}(t) = x_m^{(u)}(t-T) + x_{m+1}^{(v)}(t),\ 0 \leq u,v \leq U-1.$$

Step 4 - Path metric calculation: For each of the U^2 patterns of the modulated FBMC-OQAM signal $x_{m,m+1}^{(u,v)}(t)$, we compute partial PAPR over a duration T_0 as per equation (5.2), where $T_0 \in [mT+T,\ mT+4.5T]$ interval since almost all of the energy of the FBMC-OQAM symbol $x_{m,m+1}^{(u,v)}(t)$, lies within that interval as shown in Fig. 5.2. For the path $\zeta_{(m\Rightarrow m+1)}^{(u,v)}$, we calculate its path metric $\Gamma_{(m,m+1)}^{(u,v)}$ given by:

$$\Gamma_{(m,m+1)}^{(u,v)} = f\big(PAPR_{m,m+1}^{(u,v)}\big) \tag{5.7}$$

where $f(.)$ is any convex function.

Step 5 - Survivor path identification: The states for stage m that are related to the survivor paths leading to stage $m+1$, are stored in a state matrix $\boldsymbol{\lambda}(v,m)$ as given below

$$\boldsymbol{\lambda}(v,m) = \min_{u\in[0,U-1]}\left[\Psi_{(u,m)} + \Gamma_{(m,m+1)}^{(u,v)}\right],\ v = 0,...,U-1. \tag{5.8}$$

Step 6 - State metric updating: The state metric $\Psi_{(v,m+1)}$, for the stage $m+1$, can be updated as follows

$$\Psi_{(v,m+1)} = \Psi_{(\boldsymbol{\lambda}(v,m),m)} + \Gamma_{(m,m+1)}^{(\boldsymbol{\lambda}(v,m),v)},\ v = 0,...,U-1. \tag{5.9}$$

Step 7 - Incrementation: Increment the value of m by 1 and if $0 \leq m \leq M-2$, then go to **Step 2**; Else, for $0 \leq m = M-1$, go to **Steps 8**.

Step 8 - Traceback: Once state metrics for all the M stages has been computed, then identify the state that has the least state metric as shown below

$$\boldsymbol{\Theta}(M-1) = \min_{u\in[0,U-1]}\big[\Psi_{(u,M-1)}\big]. \tag{5.10}$$

Then start tracing back from last stage to the first one in order to find the unique survivor path $\boldsymbol{\Theta}$ by identifying the optimal states at each stage as below

$$\boldsymbol{\Theta}(k) = \boldsymbol{\lambda}(\boldsymbol{\Theta}(k+1),k), \tag{5.11}$$

where, $k = M-2, M-3, ..., 1, 0$. This survivor path $\mathbf{\Theta}$ is the set of optimal phase rotation vectors, that is obtained after solving the optimization problem by dynamic programming (DP) [153], which can help in reducing substantially, the number of paths one need to pick.

The performance of TSLM for a FBMC-OQAM signal with 64 subcarriers and 4QAM modulation is shown in Fig. 5.3 in terms of CCDF plots. We can notice that FBMC-OQAM with TSLM is not only superior to FBMC-OQAM with DSLM scheme in PAPR reduction but also outperforms OFDM with classical SLM. This superior performance implies that when the overlapping nature of the FBMC-OQAM signals is well exploited then it can significantly impact the PAPR reduction and such proper exploitation can be possible with trellis-based approach instead of symbol-by-symbol optimization. Another observation is that the lead gap between CCDF curves of OFDM and FBMC-OQAM gets narrowed as U increases.

Dispersive TR

We have come to conclusion that probabilistic PAPR reduction schemes provide optimal results, with TSLM algorithm. This has prompted us to investigate new category of PAPR reduction techniques. As a next step during the Krishna Bulusu's thesis, we studied an adding signal technique and we have chosen TR. The idea behind TR is to isolate energy used to cancel large peaks to a predefined set of R tones, namely peak reserved tones (PRTs). Such a PRT does not carry any useful information, i.e., PRTs are disjoint from the data tones (DTs). Stated mathematically, the signal corresponding to the m^{th} transmitted symbol will be

$$x_m(t) = d_m(t) + c_m(t), 0 \leq t < \infty, \tag{5.12}$$

where, $c_m(t)$ is the peak cancellation signal and $d_m(t)$ is the data signal (i.e. related to data only). $x_m(t)$ can be represented in frequency domain as $\mathbf{X}$ given by

$$\mathbf{X_m} = \mathbf{D_m} + \mathbf{C_m} \tag{5.13}$$

where the n-th component of the vector $\mathbf{X_m}$ is given by

$$X_{m,n} = \begin{cases} D_{m,n}, & n \in \mathcal{B}^c \\ C_{m,n}, & n \in \mathcal{B} \end{cases} \tag{5.14}$$

where,

- $n = 1..N_{FFT}$ is the subcarrier index,
- $\mathcal{B}$ is the set of PRTs indices, which is of length R,
- $\mathcal{B}^c$ is the complement set of $\mathcal{B}$, containing the DTs indices and is of length $N_{FFT} - R$,
- $D_{m,n}$ is DT set and $D_{m,n} = 0$, for $n \in \mathcal{B}$,
- $C_{m,n}$ is PRT set and $C_{m,n} = 0$, for $n \in \mathcal{B}^c$.

The aim of TR scheme is to compute the optimal values of PRTs subject to

$$c_m(t) = \underset{C_{m,n}}{\arg\min} \underset{n \in \mathcal{B}}{} \Big[PAPR(MOD\{\mathbf{D_m} + \mathbf{C_m}\}) \Big], 0 \leq t < \infty, \tag{5.15}$$

where $\mathcal{MOD}\{.\}$ is a generic modulation operation, corresponding to any MWF.

The optimal $c(t)$ can be obtained by solving equation (5.15) using convex optimization algorithms such as (Quadratically constrained quadratic programs) QCQP [154], (projection onto convex sets) POCS [155], gradient search [154], etc. The QCQP has a computational complexity of $\mathcal{O}(RN_{FFT}^2)$ and yields to the optimal result. The sub-optimal approaches such as POCS and gradient search have a computational complexity of $\mathcal{O}(N_{FFT} \log N_{FFT})$ and $\mathcal{O}(N_{FFT})$ respectively.

For FBMC-OQAM, we have proposed a dispersive version of the TR technique. This algorithm, named dispersive TR (DTR) [69], considers the overlapped past symbols, while calculating signal $c_m(t)$. The idea is closely related to the one used in DSLM and is deeply described in [69].

To analyse the impact of R on the performance of the proposed DTR algorithm, we have considered different scenarios where we have reserved 6.25%, 12.5% and 25% of the total sub-carriers ($N_{FFT} = 64$). We can see from Fig. 5.5 that the exploitation of the overlapping nature of the FBMC-OQAM signals can significantly impact the PAPR reduction. Indeed, the PAPR reduction performance of FBMC-OQAM with classical TR is outperformed by the one with DTR scheme by $3.2dB$, for $R = 8$. Also, in the same figure, we can notice that the CCDF of PAPR for FBMC-OQAM with DTR is closely trailing that of OFDM with classical TR by roughly $1dB$. Another important observation is that, as R increases, the trail gap between CCDF curves of OFDM and FBMC-OQAM is getting increased. The reason for performance lag of DTR scheme is that the PAPR reduction done for the current symbol can be hampered by the future symbols, which is again related to schemes that opt for symbol-by-symbol optimization.

5.2.1.2 PA linearization techniques

PA linearization has seen a large investment of research and development funding in both the industrial and academic sectors. With PA linearization the PA linearity is improved and extended so that the PA can be operated at lower IBO. This means that a lower-power lower-cost linearized PA can be used in place of a higher-power higher-cost one. Furthermore, the linearized PA operates more efficiently since it is operated closer to saturation. Among all linearization techniques, DPD is one of the most cost-effective techniques. A predistorter, which (ideally) has the inverse characteristic of the PA, is used to compensate for the PA non-linearity. The benefits of DPD are even more pronounced for CP-OFDM and post-OFDM MWFs where the PAPR is large. Details about predistortion principle and benefits can be found in [156, 157, 158]. In [159], we proposed an adaptive DPD based on neural networks. Because of the intrinsic interference of FBMC-OQAM system, careful implementation must be done, especially for the phase (AM/PM) correction. This method will not be detailed here and interested readers could refer to the conference paper [159], to get more insights on the proposed method.

In this section, I have chosen to present another DPD technique developed during the Krishna Bulusu's PhD thesis. This method is based on a signal adding approach. Indeed, If the memory effects of the PA are negligible, the predistortion can be seen as a memoryless non-linear function. In such case, it has been shown in [160], that the Bussgang's theorem allows the formulation of predistortion as an adding signal technique for CP-OFDM signals. The idea behind any adding signal DPD technique is that we add a predistortion signal $p(k)$ to the signal $x(k)$ to compensate the PA non-linearity. The predistorted signal $x^{pd}(k)$ can be expressed as

$$x^{pd}(k) = \mathcal{P}\{x(k)\} = x(k) + p(k), \tag{5.16}$$

where $\mathcal{P}\{.\}$ is the predistortion function. The aim of a DPD technique is to obtain a function $\mathcal{P}$ such that

$$\mathcal{A}\{\mathcal{P}\{x(k)\}\} = A_0 x(k), \tag{5.17}$$

where A_0 is a linear gain and $\mathcal{A}\{.\}$ is the PA amplification function.

The proposed DPD technique, to linearize FBMC-OQAM signals is termed as overlapped-recursive error correcting-digital predistortion (OREC-DPD) as it takes into account the overlapping nature of the FBMC-OQAM symbols. The manner in which the overlapping of previous symbols are taken into consideration is similar to that of the proposed PAPR reduction techniques and can be understood from Fig. 5.2. The DPD is done in baseband, which implies that first we model the real PA and then we perform linearization. Illustration of a FBMC-OQAM system along with OREC-DPD scheme is shown in Fig. 5.6. The OREC-DPD algorithm is given below

Step 1: *Step 1a - FBMC-OQAM signal generation* - Firstly, we generate M complex input symbol vectors and oversample them by L times to obtain $\{\widehat{\mathbf{X}}_0, \widehat{\mathbf{X}}_1, ..., \widehat{\mathbf{X}}_{M-1}\}$. Then, for $0 \leq k < (M + 3.5)LN_{FFT} - 1$, we perform discrete-time FBMC-OQAM modulation to obtain the FBMC-OQAM signal $x(k)$.

Step 1b - Predistortion signal initialization - Then, we initialize $m = 0$ and the predistortion signal

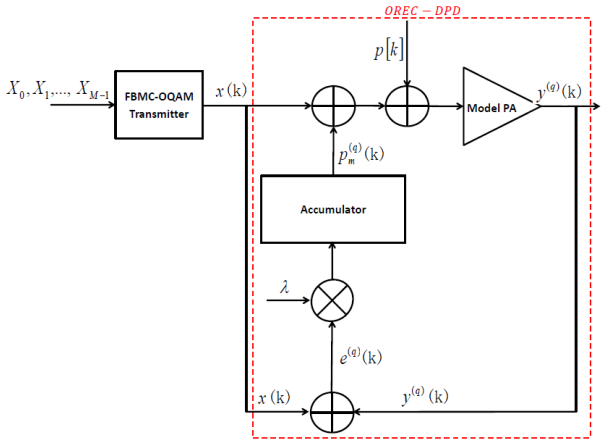

Figure 5.6: Detailed illustration of OREC-DPD block.

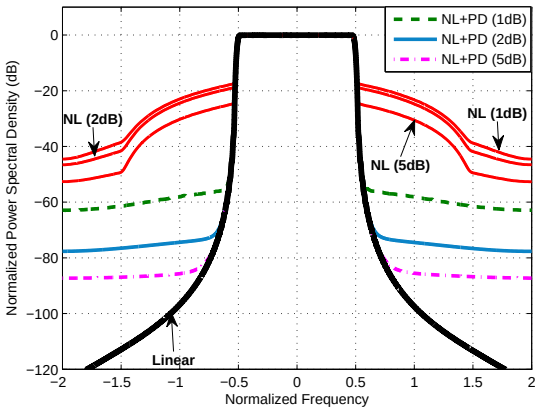

Figure 5.7: Illustration of IBO on OREC-DPD scheme with $p = 2.25$.

$p(k) = 0$

Step 2: For $mLN_{FFT} \leq k < (m+4.5)L_{FFT} - 1$, we initialize iteration counter $q = 1$ and then, initialize the accumulative partial predistortion signal $p_m^{(0)}(k)$ that is related to the m^{th} signal $x_m(k)$ to be zero.

$$p_m^{(0)}(k) = 0, mLN_{FFT} \leq k < (m + 4.5)LN_{FFT} - 1. \tag{5.18}$$

Step 3: Then, we perform the following substeps:

Step 3a - Amplification - The predistortion signal $p(k)$ should be added to the FBMC-OQAM signal $x(k)$ along with the current accumulative predistortion signal up to q^{th} iteration $p_m^{(q)}(k)$ and amplified by the PA model as follows

$$y^{(q)}(k) = \mathcal{A}\Big\{x(k) + p(k) + p_m^{(q)}(k)\Big\}. \tag{5.19}$$

Step 3b - Recursive error computation - The recursive error signal $e^{(q)}(k)$ at iteration q, is the difference between amplified signal $y^{(q)}(k)$ and the input signal $x(k)$

$$e^{(q)}(k) = y^{(q)}(k) - x(k). \tag{5.20}$$

Step 3c - Recursive error correction - The accumulative partial predistortion signal $p_m^{(q)}(k)$, is updated through recursive accumulation as below

$$p_m^{(q)}(k) = p_m^{(q-1)}(k) + \lambda e^{(q)}(k), \tag{5.21}$$

where, λ is the convergence rate.

Step 4: If $q \leq Q$, we increment q and go to **Step 3**. Else, we update the predistortion signal $p(k)$ by accumulating with the partial predistortion signal $p_m^{(Q)}(k)$

$$p(k) = p(k) + p_m^{(Q)}(k). \tag{5.22}$$

Step 5: If $m \leq M - 1$, we increment m and go to **Step 2**. Else, we proceed to next step.

Step 6: Add the obtained predistortion signal $p(k)$ to the FBMC-OQAM signal $x(k)$ to obtain the pre-distorted input signal $x^{pd}(k)$, which shall be fed into the real PA.

$$x^{pd}(k) = x(k) + p(k) \tag{5.23}$$

In the analysis, we considered transmission over 64 sub-carriers, with an oversampling factor $L = 4$. We used a Rapp model with $p = 2.25$ and fixed $\lambda = 0.1$. The impact of IBO on the OREC-DPD scheme

has been simulated for values of $IBO = 1\ dB$, $2\ dB$, $5\ dB$ with $Q = 30$ and presented in Fig. 5.7. It can noticed that there is a spectral de-growth for all the IBO values w.r.t. to the original NL spectral regrowth without any predistortion. This relative decrease is found to be around 18.35 dB, 31.12 dB and 34.62 dB respectively, at normalized frequency of 2.

The OREC-DPD algorithm described here and published in [70], is based on a constant convergence rate λ, thereby, leading to slow convergence. However, there are enhanced methods, in the literature to update λ at each iteration, according to knee factor p and/or IBO values. In [71, 72], we extended this work, where we propose a faster converging DPD technique requiring few iterations compared to OREC-DPD.

5.2.1.3 Co-existence capabilities of a FBMC-OQAM system working with NL PA

Professional mobile radio (PMR) and public protection and disaster relief (PPDR) communications (TETRA, TETRAPOL, TETRA/TEDS [6], APCO 25 in the US and others) are undergoing significant transformation towards supporting broadband data communications services in their future generations. The terrestrial trunked radio (TETRA), as one of the earliest critical communication systems, has evolved from low-speed data in its first release and integrates today the wide band TETRA enhanced data service (TEDS). TEDS supports higher data rates, up to several hundred *kbps*, and fits very well into the existing PMR frequency landscape. However, the real broadband evolution of wireless PMR communications is progressing towards enhanced technical solutions offering high speed data services, while still providing the legacy PMR services. PMR communications must support data-rich broadband services and connect people instantly.

To respond effectively to the wide variety of incidents taking place, professional users demand much faster data and real-time multimedia applications to share, such as video streaming on-the-move, access to remote databases (identity checks, CCTV cameras, etc.), file transfer (maps, pictures, satellite files, etc.), and location-based services.

The new required capacity can be achieved in two complementary ways: by obtaining new frequency bands for PMR/PPDR data services or by fitting a novel broadband data service within the scarcely available spectrum devoted to PMR systems. During the Krishna Bulusu's PhD thesis and within the framework of the EMPhAtiC European project, we focused on the latter approach, which can be seen as a very challenging evolution path, but also the most realistic opportunity to benefit from the advantages of latest developments in MWFs and related signal processing techniques. One of the major issues is being able to introduce new broadband data services within the current frequency allocation, in coexistence with current narrowband PMR/PPDR systems. Having in mind the widely expected dominance of 3GPP long-term evolution (LTE), it is natural to consider the LTE system as a reference basis in the PMR/PPDR system development due to its modularity and wide adoption in the civil world.

In [73], it has been shown that a LTE-like broadband system based on CP-OFDM lacks coexisting capability, even in the absence of RF impairments, because of the high side lobes of this MWF. This implies the need in the context of 5G PMR systems, to probe for new MWFs waveforms that can: 1) support user asynchronism and low latency, 2) permit coexistence with narrowband systems and 3) be capable to be operated with NL devices with high energy efficiency. In this regard, we have made a genuine attempt, to address the hitherto mentioned issues. Although, CP-OFDM have been a natural choice for next generation communications; still it is not considered the optimal MWF technique for PMR coexistence. The principal reason is the lack of sub-channels' spectral confinement, making it especially inapplicable to non-synchronized mobile networks. In this contribution, we investigated the coexistence capabilities of CP-OFDM and FBMC-OQAM systems with a PMR system that operates on licensed narrowband located in PMR UHF bands in Europe and which are around 400 MHz.

The deployed broadband system should satisfy the constraints imposed by the already existing and operational PMR communication devices. The PMR system considered for the analysis is defined by the European Telecommunications Standards Institute (ETSI) TETRA standard [6] which is currently widely used by public safety organizations, both private and governmental, and by around two million of business users over the world. Fig. 5.8, illustrates the considered coexistence scenario where a LTE-like broadband system is deployed between two TEDS systems of 25 kHz bandwidth each. Δf_1 and Δf_2

offset from nominal Rx freq.	blocking level	reception level
50 kHz to 100 kHz	−40 dBm	−81.4 dBc
100 kHz to 200 kHz	−35 dBm	−86.4 dBc
200 kHz to 500 kHz	−30 dBm	−91.4 dBc
> 500 kHz	−25 dBm	−96.4 dBc

Table 5.1: Blocking levels of the 25 kHz-TEDS receiver defined in [6] and reception mask .

refer to the frequency distances between the nearest adjacent interfering broadband LTE system and the nominal carrier frequencies of the existing active narrowband users.

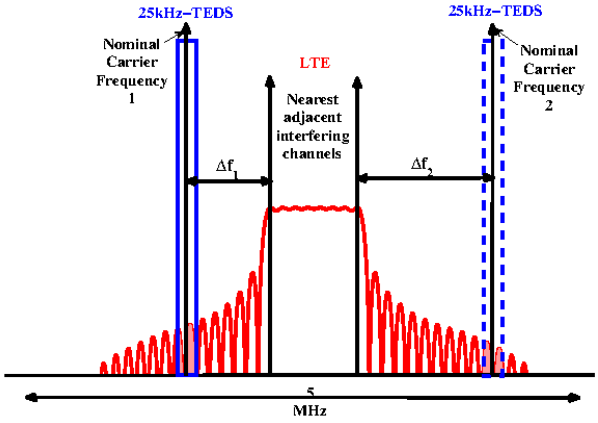

Figure 5.8: LTE broadband in coexistence with narrowband PMR systems.

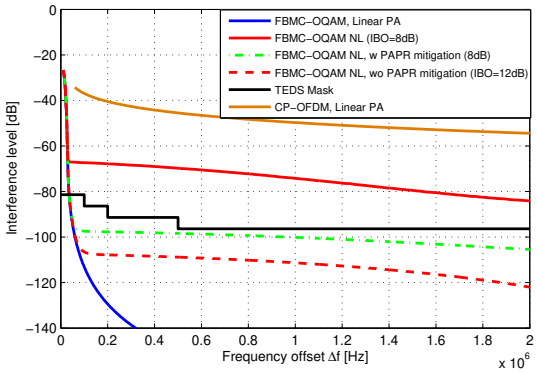

Figure 5.9: Interference plot for 1.4 MHz bandwidth FBMC-OQAM system with SEL PA model and SLM based PAPR mitigation.

To guarantee such cohabitation, the OOB radiation of the deployed LTE system should not exceed the levels defined by the spectrum mask of the TEDS standard. The 25 kHz-TEDS reception mask parameters are depicted in Tab. 5.1.

We have tested the capability of FBMC-OQAM and CP-OFDM to fulfill the TEDS mask, first assuming a linear PA. The PSD of each MWFs is integrated over a 25 kHz bandwidth and compared with the TEDS mask in Fig. 5.9. As demonstrated in [73], we confirmed that with linear PA, only FBMC-OQAM is able to satisfy the TEDS mask.

When using a NL PA, which is operated in its nonlinear region, spectral re-growth increases the interference and endangers the fulfilment of the TEDS mask. We assumed a perfectly linearized PA. The NL PA chosen model is thus a SEL. To respect the TEDS mask, we used PAPR reduction techniques together with adjusted IBOs. Nevertheless, as higher IBO results in energy wastage, increasing IBO to respect the mask is not an optimal approach and PAPR reduction techniques must be jointly applied. In this study, we considered the DSLM technique to reduce the PAPR for FBMC-OQAM. It is clear from Fig. 5.9, that with a symbiotic combination of IBO and U (number of complex vectors used in DSLM algorithm), the interference of FBMC-OQAM fulfils to the TEDS spectrum mask. In the same figure, it can also be seen that as IBO is increased, the interference level is getting decreased. With an IBO = $8dB$ and with a DSLM technique ($U = 8$), the interference level is well reduced below the TEDS spectrum mask. Without PAPR reduction, the input PA signal needs a 12 dB of IBO to fulfil the TEDS spectrum mask.

This work have been jointly carried with two colleagues from Tampere university of Technology and leaded to a joint journal paper in Transactions on Emerging Telecommunications Technologies [67]. A short version of this paper, restricted to CNAM contributions, has been published in a conference paper [74].

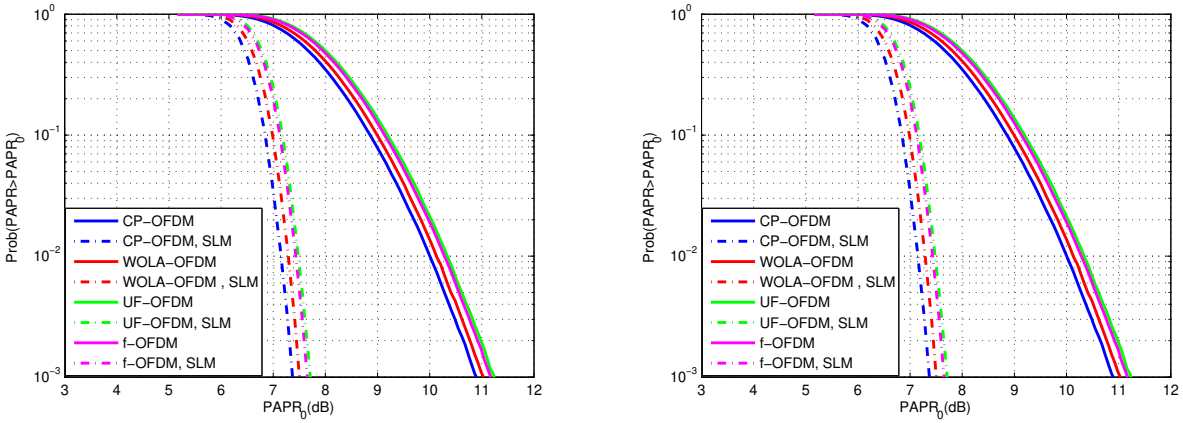

(a) SLM with $U = 16$. (b) TR with 20 iterations and $8,4\%$ of PRT.

Figure 5.10: CCDF of PAPR for CP-OFDM and some post-OFDM MWFs ($N_{FFT} = 256$ and 16QAM).

5.2.2 Case of WOLA-OFDM, UF-OFDM and f-OFDM

As part of the WONG5 national project, we focused on PAPR reduction techniques for OFDM-inspired waveforms: WOLA-OFDM, UF-OFDM and f-OFDM which have almost PAPR levels similar to those observed with CP-OFDM signals. This work has been carried during the Master internship of Khaled Tani. It is worth to mention that, in contrast to CP-OFDM, there are only few works on PAPR reduction in the previously mentioned post-OFDM MWFs. To this end, we have chosen two classical PAPR mitigation techniques: SLM which is a probabilistic method and TR which is an adding signal method.

5.2.2.1 PAPR performances analysis

The PAPR performances for CP-OFDM, WOLA-OFDM, UF-OFDM and f-OFDM are plotted in Fig. 5.10 (a). First, we can see that without PAPR reduction, the three post-OFDM MWFs have PAPRs slightly higher than CP-OFDM one. This difference is related to the fact that the average power of these MWFs, is lower than the CP-OFDM one, due to the windowing and/or filtering applied at the Tx side. A detailed explanation of this problem is given in [40]. Using SLM method, the PAPR decreases by the same amount for all the MWFs.

Fig. 5.10 (b), shows the performance of CP-OFDM, WOLA-OFDM, UF-OFDM and f-OFDM without and with an iteration TR algorithm with a PRT ratio of 8.4%, after a total number of 20 iterations. We can notice that like the SLM case, the PAPR is reduced by the same amount for all MWFs.

5.2.2.2 Complexity analysis and overall power budget

From the performances given in Fig. 5.10, it appears that both PAPR reduction algorithms achieved similar performance for the chosen simulations parameters. However, the energy budget required to achieve that 3.5 dB reduction of the PAPR could be very different between SLM and TR. Also, the implementation cost for each of the considered methods may be very different from one MWF to the other. Thus, we focused on assessing, for each MWF, the complexity of both PAPR reduction techniques, by computing the number of multiplications required to process a complex vector of a size equal to N_{FFT}. The complexity analysis are summarized in Tab. 5.2.

We remind that, for UF-OFDM, the data is processed at the RB level (B active RBs out of all the available ones). For each RB, first there is the predistortion stage with $N'_{FFT} < N_{FFT}$ complex multiplications. Then, there is the transposition to the time domain with only N'_{FFT} active subcarriers out of N_{FFT}. The IFFT is therefore mainly fed by null elements and its complexity can be reduced to $N_{FFT} + \frac{N_{FFT}}{2}\log_2(N'_{FFT})$ complex multiplications. The convolution with the baseband real filter (of length L_{FIR}) adds $M\lfloor\frac{L_{FIR}}{2}\rfloor$ multiplications (neglecting the rise and fall time of the convolution). Finally the up-conversion to the carrier frequencies counts for $(N_{FFT} + L_{FIR} - 1)$ multiplications.

	CP-OFDM	WOLA-OFDM	UF-OFDM	f-OFDM
SLM Per rotated symbol complexity	$2N_{FFT} + \frac{N_{FFT}}{2}\log_2(N_{FFT})$	$2N_{FFT} + \frac{N_{FFT}}{2}\log_2(N_{FFT}) + 4W_{Tx}$	$N_{FFT}(BN'_{FFT} + B(2N_{FFT} + \frac{N_{FFT}}{2}\log_2(N'_{FFT})) + (B+1)(N_{FFT} + L_{FIR} - 1) + BN_{FFT}\lfloor\frac{L_{FIR}}{2}\rfloor)$	$\frac{N_{FFT}}{2}\log_2(N_{FFT}) + (N_{FFT} + N_{CP})\lfloor\frac{L}{2}\rfloor + (2N_{FFT} + N_{CP} + 2L - 2)$
Normalized complexity	1	1,01	242,93	1,67
TR Per iteration complexity	$N_{FFT}.\log_2(N_{FFT})$	$N_{FFT}\log_2(N_{FFT}) + 2W_{Tx} + 2W_{Rx}$	$BN'_{FFT} + B(N_{FFT} + \frac{N_{FFT}}{2}\log_2(N'_{FFT})) + B(N_{FFT} + L_{FIR} - 1) + BN_{FFT}\lfloor\frac{L_{FIR}}{2}\rfloor + N_{FFT}\log_2(2N_{FFT})$	$2(\frac{N_{FFT}}{2}\log_2(N_{FFT}) + (N_{FFT} + N_{CP})\lfloor\frac{L}{2}\rfloor + (N_{FFT} + N_{CP} + L - 1))$
Normalized complexity	1	1,01	180,51	18,90

Table 5.2: Complexity analysis of SLM and TR for different MWFs.

As an illustration of the previous analysis, we computed in Tab. 5.2, the normalized complexity, with respect to CP-OFDM, of the SLM and TR algorithms applied to WOLA-OFDM, UF-OFDM and f-OFDM. This analysis is based on the simulation parameters given in [76] and is obviously independent from the number of complex phase rotation vectors U and the number of iterations K_{iter}. It appears clearly that SLM applied to UF-OFDM exhibits the highest complexity as compared to WOLA-OFDM, which requires mainly the same number of complex multiplications as CP-OFDM. One can so predict that to achieve a given PAPR reduction gain, SLM is almost less complex than TR. Also, the complexity required by UF-OFDM is huge compared to those required by the other MWFs. As a corollary we can disqualify UF-OFDM from a competition to access the overall power budget in which the consumption corresponding to PAPR reduction method is taken into account.

As a second step of our study, we targeted to estimate the power budget of transmission systems based on different MWFs when considering the consumption of (i) the modulation operation (ii) the PAPR reduction method used (in this analysis only SLM will be considered) and (iii) the PA DC power. According to a given IBO and a given value of U, the PAE, given by equation (4.2) can be redefined as:

$$PAE(IBO(U)) = \frac{P_{out}(IBO(U)) - P_{in}(IBO(U))}{P_{DC}(IBO(U)) + P_{SLM}(U)}, \tag{5.24}$$

where P_{in}, P_{out} and P_{DC} are respectively the input, output and DC powers of the PA for a given IBO value. $P_{SLM}(U)$ is the power consumption related to the SLM PAPR reduction algorithm for a given number of rotation vectors U. First, it has to be mentioned that $IBO(U)$ depends on U and decreases with the increase of the PAPR reduction gain given by Fig. 5.10. Besides, the SLM PAPR reduction method consumption was provided by a system generator tool which generates the VHDL code from a high level language of the processing (Matlab). The targeted board was a FPGA board from Xilinx Zedboard (FPGA Zynq-7000 AP SoC XC7Z020-CLG484). The PA used in this study is a typical 1 W, 3 GHz LTE user equipment power amplifier [161]. The AM/AM and AM/PM conversions characteristics of this PA, as well as its DC power are given in [77].

Efficiency results are sketched in Fig. 5.11. It is worth to point that as $CP-OFDM$ and $WOLA-OFDM$ exhibit the same complexity, the corresponding performances are quasi-identical. For each waveform, three initial IBO were considered: 8, 10 and 12 dB. This means that starting from these IBO values, the SLM method was performed (for U = 1, 2, 4, 8, 16 and 32) and the IBO has been decreased in order to achieve the same level of EVM as that obtained with the chain not integrating PAPR reduction. For each value of U, the power consumption of the SLM was evaluated and included based on the expression given in Tab. 6.5. First, as expected the larger the initial IBO value, the lower the efficiency. Second, it appears that efficiencies exhibit a maximum value which refers to the trade-off between the PAPR gain and the complexity of the associated SLM method. This remark holds for all waveforms. Before this maximum (U low), the PAPR gain provides a large PA efficiency versus the complexity of SLM (U less than 10). But after this maximum, even though the PAPR gain is larger, as U increases, the associated SLM complexity and consumption is too large what penalizes the PA efficiency.

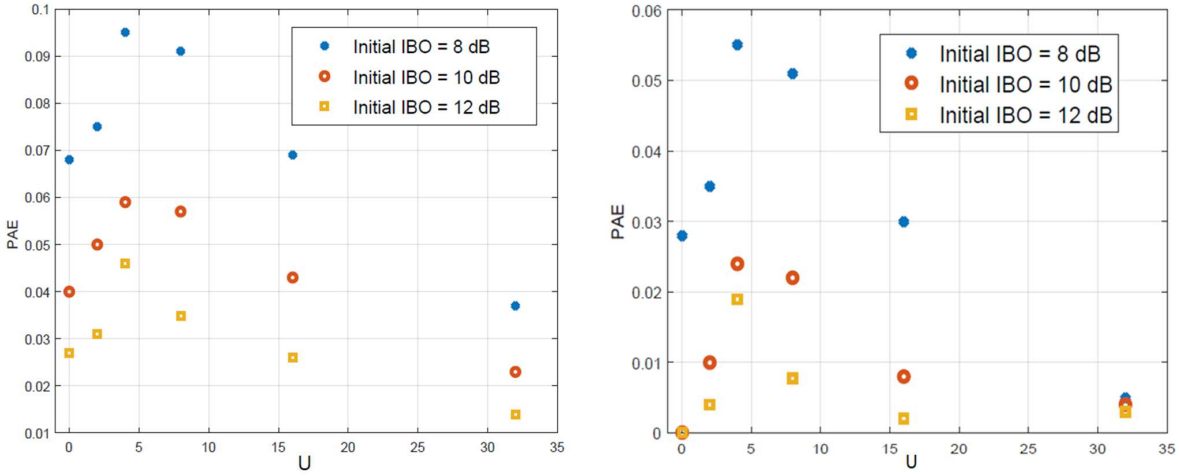

(a) CP-OFDM and WOLA-OFDM. (b) f-OFDM.

Figure 5.11: Global efficiency integrating PAPR reduction.

Efficiency results are very similar between CP-OFDM and WOLA-OFDM as their respective complexities are of same order. The efficiency shows a maximum value of about 10% when the initial IBO is set to 8 dB. For the f-OFDM waveform, the efficiency is less whatever the initial IBO value and the maximum efficiency value is below 6%. For the UF-OFDM waveform, the efficiency results are not relevant at all for the used PA as the values are very low due to the high complexity as seen in Tab. 6.5.

It is important to note that for the 1 W PA considered in this study, the consumption of the FPGA is of the same order of magnitude as the power consumed by the PA, which greatly reduces the PAE. If a PA with higher output power was used, the PAE would be higher with a maximum for values of U greater than those observed in Fig. 5.11.

This work was done, jointly with colleagues from CentraleSupélec and resulted in the publication of a conference paper [77].

5.2.3 Joint PAPR reduction & DPD

Conventionally, PAPR reduction and DPD techniques are optimized separately and applied independently. Some researchers focused on their association aiming at avoiding mutual effects. Among the proposed solutions, we can cite [81, 82]. From another side, the work carried during Krishna Bulusu's PhD showed the feasibility to view the predistortion as an adding signal technique. This statement is also true for some PAPR reduction techniques such as clipping and TR. Thereby, an interesting idea has been raised saying that both PAPR reduction and DPD can be combined and made through a unique adding signal operation. This means that both processing can be done at one stretch by adding a signal, which not only reduces PAPR but also linearizes the PA, which yields to a joint optimization of the two processing. With Dr. Rafik Zayani, we took up this idea and apply it to CP-OFDM. We proposed a new technique called "Ping-Pong Joint Optimization" (P2JO). The proposed approach synthesizes, iteratively, one correction signal for reducing the PAPR reduction and linearizing the PA conversion characteristics to reach a given MSE performance.

The block diagram of P2JO technique is given in Fig. 5.12 and the corresponding algorithm is described in the following

1. Set the minimum EVM^{min}, the reserved tone R, the initial clipping level A_{clip} and the maximal iteration number Max^{Iter}. A_{clip} is closely related with the mean power of the CP-OFDM signal σ_x^2 and the percentage of the Peak Reserved Tones R/N_{FFT}. This threshold is given by $\sqrt{\sigma_x^2 \ln(N_{FFT}/R)}$ [162],

2. Set $i = 0$ and the initial time-domain signal $y^0 = \gamma_0 x$, where x is the original CP-OFDM symbol and γ_0 is a scalar gain to achieve the targeted IBO value,

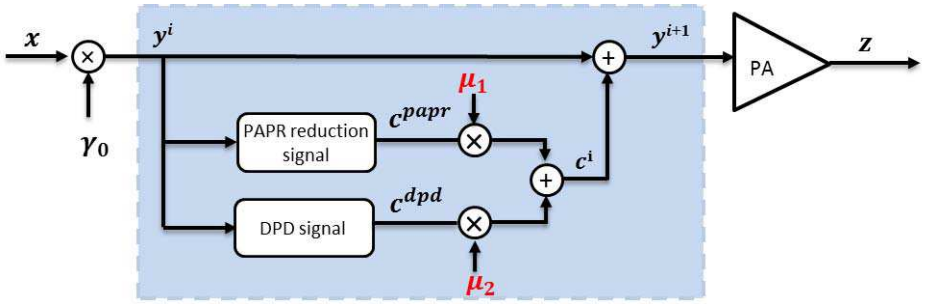

Figure 5.12: Ping-Pong Joint Optimization by adding signal.

3. **TR** : compute the clipping noise $w^i = \bar{y}^i - y^i$ and the peak-cancelling signal $c^{papr,i} = IFFT(S^r FFT(w_i))$, were S^r is an identity matrix of order N_{FFT} with zeros at data positions,
4. **DPD** : compute the predistortion signal $c^{dpd,i} = y^{dpd,i} - y^i$, where $y^{dpd,i}$ is the predistorted version of y^i signal,
5. Update the correction signal $y^{i+1} = y^i + \mu_1 c^{papr,i} + \mu_2 c^{dpd,i}$,
6. Compute the amplified signal $z^{i+1} = \mathcal{A}(y^{i+1})$, where $\mathcal{A}$ is the amplification operation,
7. Calculate $X^{i+1} = S^d FFT(z^{i+1})$ where S^d is an identity matrix of order N_{FFT} with zeros at peak cancelling tones positions,
8. Calculate the error vector magnitude $EVM^{i+1} = \sqrt{\frac{\mathbb{E}\{|X^{i+1}-X^0|^2\}}{\mathbb{E}\{|X^0|^2\}}}$, if $EVM^{min} < EVM^{i+1} < EVM^i$ & $i < Max^{Iter}$, set $i = i+1$ and go to step 3). otherwise, transmit y^{i+1} and go to step 9),
9. End.

In our analysis, we set μ_1 to 1, to keep a maximal performance in terms of power efficiency and push the predistortion to offer its best performance. μ_2 can be modified to clearly evaluate how we can take into consideration the mutual effect between TR PAPR reduction and DPD. It is noteworthy that when $\mu_2 = 1$ the P2JO converges to the same performance obtained by the classical approach, in which we cascade PAPR reduction and DPD. In the following analysis, it's worth to point that "$\mu\%P2JO$" refers to a scenario where $\mu_2 = \mu \times 10^{-2}$. Otherwise, I underline that Output-Back-Off (OBO) is used rather than IBO in the following analysis.

Fig. 5.13 (a) shows BER performance of $1\%P2JO$ and $5\%P2JO$, in presence of Saleh's PA model (equations (4.8) and (4.9)) compared to the classical approach (where PAPR and DPD processing are cascaded without any collaboration). We can see from this figure that with an increase in the number of reserved tones, the capability of the proposed P2JO is improved. Fig. 5.13 (b), shows the OOB emission reduction in the neighbouring channels based on $\mu\%P2JO$, where the proposed algorithm clearly outperforms the classical approach.

The proposed algorithm allows a better trade-off between PA efficiency and linearity while exhibiting reduced implementation complexity, compared to classical cascading of the two-processing. As the idea seemed very interesting to us, we started by patenting it via a European patent [83]. We published then the proposed P2JO algorithm and the related results in the journal article [84]. For detailed description of this algorithms, please refer to [84].

5.2.4 Testbed for demonstrating post-OFDM MWFs capabilities in cMTC context

As an objective of the last task of the WONG5 project, we developed, at CNAM, a software defined radio (SDR) based testbed. We aimed to demonstrate, in real world, the feasibility of some of the DSP based algorithms presented previously to enhance the energy efficiency of a selection of MWFs transceivers in

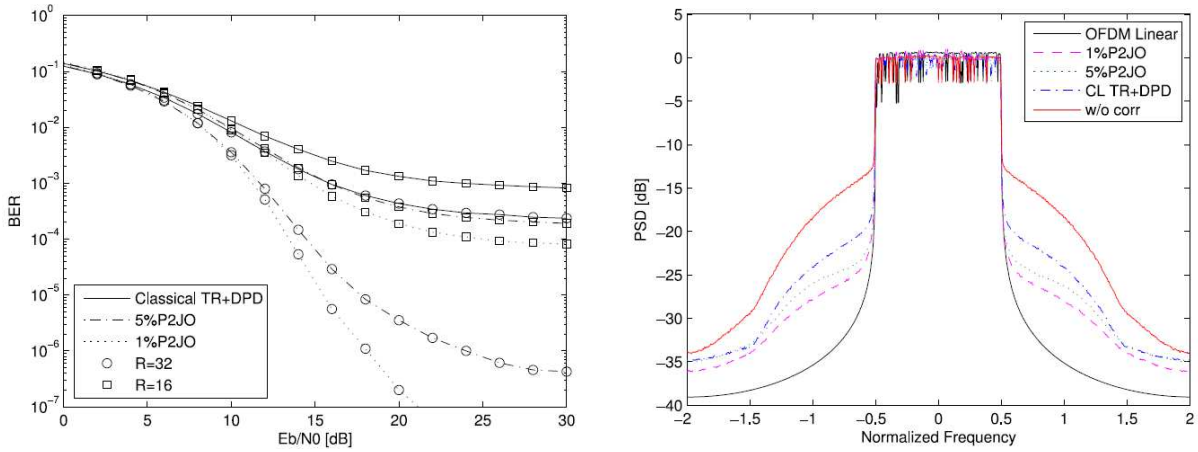

(a) BER. (b) PSD.

Figure 5.13: Performance of an OFDM system with $R = 32, 16$, $16QAM$, $OBO = 3dB$, Saleh PA model.

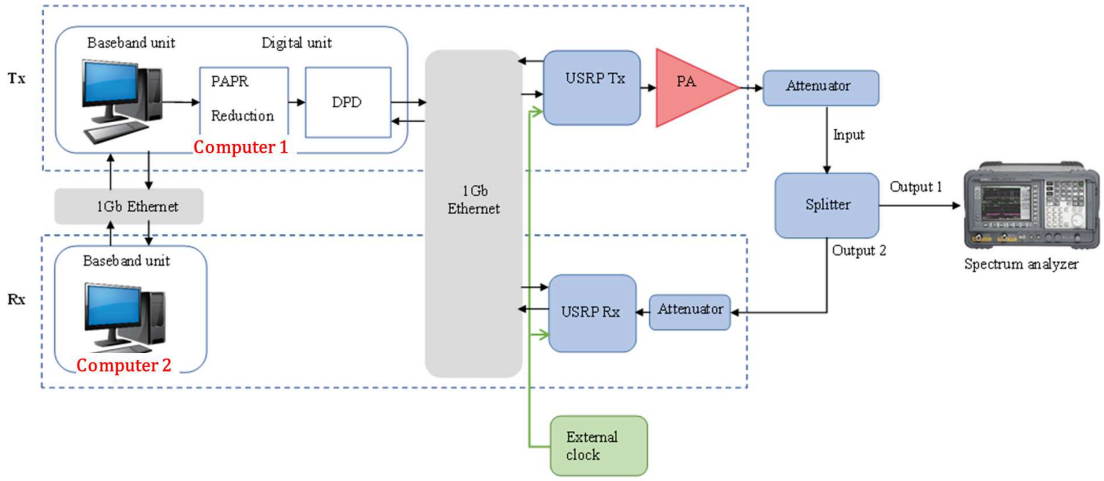

Figure 5.14: Overall architecture of the testbed.

presence of real PA. This work, co-supervised with Pr. Daniel Roviras and Dr. Christophe Alexandre, has been carried by a postdoctoral researcher: Dr. Rafik Zayani and two master students: Xinying Cheng and Xiaotian Fu.

The SDR testbed is realized with two parts, Transmitter (Tx) and Receiver (Rx), to evaluate the performance of several MWFs. The testbed overall architecture is presented in Fig. 5.14. The baseband unit is software-based and implemented using Matlab and it realizes the digital algorithm, e.g., waveform generation, QAM modulation, channel equalization, demodulation, etc. It is worth mentioning that DPD and PAPR reduction methods are also implemented using Matlab.

For SDR hardware, two separate Universal Software Radio Peripherals (USRPs) devices, NI-USRP-2942R are used as transmitter and receiver, integrating digital/RF units. The USRP has tunable carrier frequencies in the range of 400 MHz to 4.4 GHz and tunable transmission rates to 200 $Msps$ [163]. For synchronization of USRP modules, an external clock is used.

In order to ensure a real-time SDR implementation, we have considered two computers. Computer 1 has two solid state disk (SSD), where the first SSD is dedicated to data storage and is shared with computer 2 using a gigabit ethernet switch and the second SSD is dedicated to the operating system. Matlab on computer 1 realizes the digital algorithms and commands the GNU-radio that configures and uploads signal to USRP Tx. Also, a C++ program is implemented in computer 1 to get the received signal from the USRP Rx. This received signal is divided into small packets that will be stored in

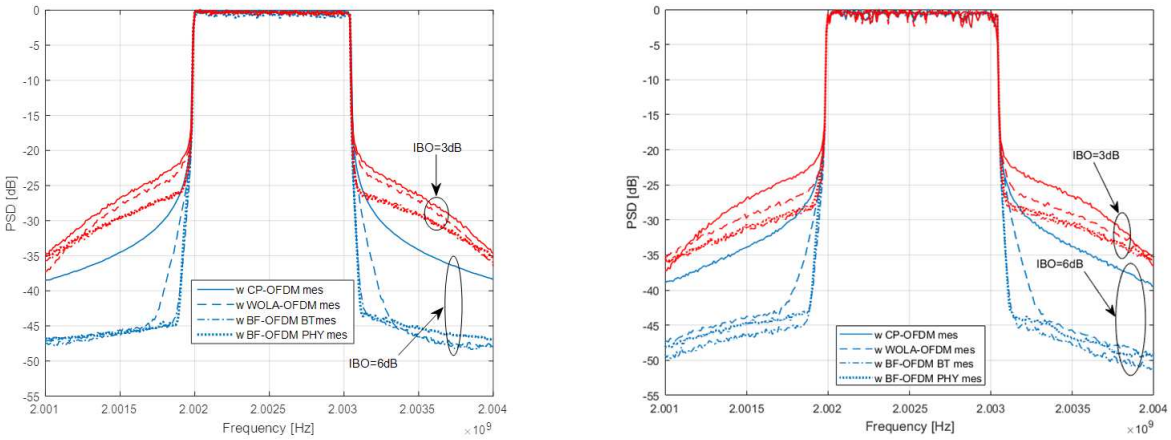

(a) SLM ($U = 8$) and DPD. 8 PRT and DPD.

Figure 5.15: Measured PSD performance of different MWFs.

the shared SSD and will serve for the analyses in the baseband unit. Computer 2 realizes the analysis of received signals. It uses shared received packets and gives some visual performance results such as PSD, constellation, NMSE per subcarrier, average NMSE and BER. Two graphical interfaces have been developed to make the testbed more flexible. On the transmitter side interface, we can choose different configurations, for example, we can select the waveform (CP-OFDM, WOLA-OFDM or BF-OFDM), the input back-off IBO (0, 3, 6, 9 or 12 dB), the PAPR reduction method (TR or SLM), the DPD and we can enable or disable interfering user.

We have used an AWGN channel without any frequency selectivity to clearly see the impact of the RF PA on the performance of the selected MWFs and their robustness to asynchronous transmissions. The PA used is a SSPA PE15A4017 from Pasternack with a bandwidth of 20 MHz to 3 GHz and 27 dB Gain [161].

Using the testbed presented previously, extensive measurements were performed in a realistic laboratory-like environment. For the measurements, two different scenarios were performed to evaluate the performances of the selected MWFs. In scenario 1, the robustness of these MWFs against PA distortions is evaluated when considering DSP based techniques like PAPR reduction and DPD. Scenario 2 is dedicated to evaluating the capability of the selected MWFs to support asynchronous transmissions. The system model used for comparison is the same as that used in section 3.3.1. The User of Interest (UI) occupies 7 RBs, about 1.1 MHz bandwidth from 2.0020 to 2.0031 GHz. As shown by Fig. 3.3, on each side of the Interfering User (IU), there are 7 RBs, occupying 1.1 MHz bandwidth as IU. A guard-band δ is separating the frequency bands of both UI and IU. Also, an offset τ is introduced to create timing asynchronism. For each MWF (CP-OFDM, WOLA-OFDM and BF-OFDM), PAPR reduction is based on SLM or TR algorithms. Whereas, DPD is based on the memoryless polynomial model.

Figs. 5.15 shows measured PSD performance comparison of all MWFs when SLM and TR are, respectively, performed with DPD. We can clearly see the significant gain performed with WOLA-OFDM and BF-OFDM compared to CP-OFDM especially for IBO of 6 dB. We can also note that BF-OFDM outperforms WOLA-OFDM due to the better spectrum containment provided by the sub-band filtering. For an IBO of 6 dB, the CP-OFDM reaches the PSD in the linear case. Nevertheless, because of the rectangular shaping, the PSD localization is poor compared to WOLA-OFDM and BF-OFDM.

In order to study the in-band error with different E_b/N_0 regimes, Fig. 5.16 plots measured BER when PAs are operated at an IBO of 3 and 6 dB . We can note that WOLA-OFDM and BF-OFDM provide almost the same performance compared to the classical CP-OFDM when SLM based PAPR reduction is performed along with DPD. The same behavioural has been noted when TR is used. At an IBO of 6 dB, BER performances provided by all MWFs are very close to the one performed in the linear case.

In scenario 2, as mentioned previously, we evaluate the robustness of the considered MWFs in multi-user asynchronous access. To well assess the performance of these MWFs, we measure the NMSE on the

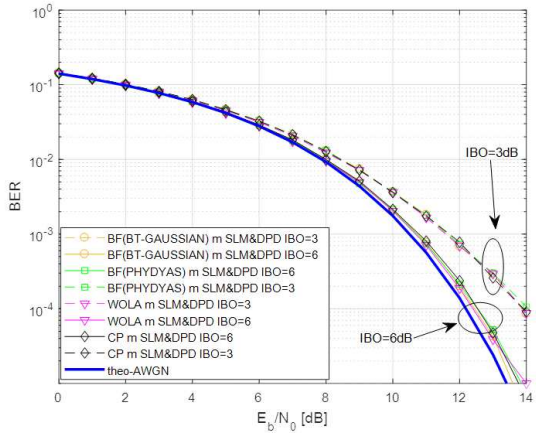

Figure 5.16: BER performance of different MWFs using SLM and DPD, 16QAM.

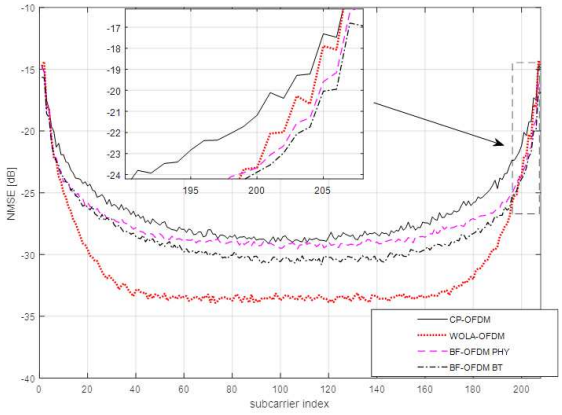

Figure 5.17: NMSE performance of different MWFs when $\tau = 106\ \mu s$ and $\delta = 4,883\ kHz$.

decoded symbols of the user of interest (UI). Per-subcarrier NMSE is assessed in Fig. 5.17, for guard band $\delta = 4,883kHz$ (corresponding to 1 subcarriers spacing) and timing offset $\tau = 106\ \mu s$ (corresponding to 1/2 symbol duration). We can see from Fig. 5.17 that the interference level decreases slowly as the spectral distance between the victim subcarrier and the interferer ones increases. The interference level achieved by WOLA-OFDM in the middle of the bandwidth is lower (approximately $-34\ dB$) compared to CP-OFDM scheme. These good results are related to the WOLA processing applied at the receiver that can suppress inter-user interference resulting from the mismatched FFT capture window.

We move now to BF-OFDM, where additional remarks can be made. Thanks to per-RB filtering, this MWF shows better performance, at the emitter side, compared to CP-OFDM, when both BT-Gaussian and PHYDYAS filters are used. However, the gain of BF-OFDM for the inner subcarriers, located at the middle of the bandwidth, is marginal compared to CP-OFDM. This is a direct consequence of the BF-OFDM receiver which is no more than the classical CP-OFDM receiver (i.e., a simple FFT). Further, at $\tau = 106\ \mu s$, WOLA-OFDM performs better than BF-OFDM, with both prototype filters, as we note a gain of more than 3 dB. From another side, BF-OFDM provides better protection to the edge subcarriers (in the vicinity of interferer subcarriers) compared to both CP-OFDM and WOLA-OFDM. When comparing the two prototype filters considered for BF-OFDM, one can note that a small gain is performed by BT-Gaussian filter compared to the PHYDYAS one. This is directly related to the filter prototype behavioural.

A more detailed description of the proposed testbed along with additional results have been published in the conference paper [79] and the journal paper [80].

5.3 Modified architecture transmitter-based approaches

5G wireless communication systems are expected to support a wide range of services with diverse requirements. One of the main concerns for 5G systems is the improvement of energy efficiency. Furthermore, Multiple-Input Multiple-Output (MIMO) and massive MIMO technologies will be generalized in 5G. Multiplying power amplifiers in MIMO transmitting chains, together with the constraint of an increased energy efficiency and low cost are antagonist constraints. With MIMO transmitters, low-cost PA are needed but could have eventually quite poor properties concerning the linearity.

During Khaled Tahkoubit's PhD, we proposed a hybrid approach for enhancing PA efficiency by modifying its structure. The main idea behind the proposed method is to decompose the multicarrier signal into M signals with much lower PAPR, by using an algorithm called Iterative Dichotomy PAPR (IDP). The M signals are amplified by M PAs, combined with a suitable combiner and then fed to the antenna. When $M = 2$, the IDP technique has an architecture similar to that of linear amplification using nonlinear components (LINC) [164]. In the LINC method, the multicarrier signal is converted into

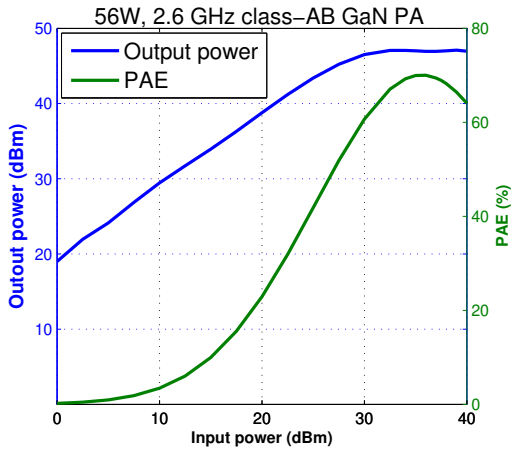

Figure 5.18: Output power and PAE vs. input power of the used PA [1].

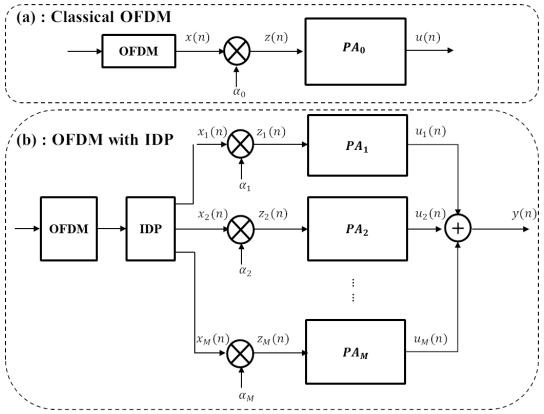

Figure 5.19: OFDM transmitter in presence of PA: (a)-Classical case, (b)-IDP based OFDM.

two signals with null PAPR. These two signals are amplified by two efficient amplifiers in each branch and recombined to form the final amplified signal. Nevertheless, in LINC, the two generated signals before the amplification process have very high power, unlike the IDP method where the power of the two signals to be amplified are much lower.

In this study, we used a realistic PA, which is a 2.6 GHz class-AB based on GaN transistor with a power gain of 19 dB, a maximum output power of 56 W and a maximal power added efficiency (PAE) of 70% [1]. The AM/AM and PAE characteristics of this PA are shown in Fig. 5.18.

5.3.1 Iterative Dichotomy PAPR reduction method (IDP)

The IDP method is downward compatible, i.e., there is no side information to be sent to the receiver. As shown by Fig. 5.19 (b), IDP decomposes the MWF signal $x(n)$ into M sub-signals, $x_m(n), (m = 1, \ldots, M)$. We can write the signal at the output of the IDP processing as follows

$$x(n) = \sum_{m=1}^{M} x_m(n). \tag{5.25}$$

The sub-signals $x_m(n), m = 1, \ldots, M$, are then amplified in each branch by a suitable PA. Before amplification, each sub-signal is scaled by an adequate scalar gain α_m to ensure the targeted IBO_m. As signals $x_m(n)$, have a very low correlation, we can write $P_x = \sum_{m=1}^{M} P_{x_m}$, where P_x is the power of the original signal $x(n)$ and P_{x_m} is the power of the sub-signal $x_m(n)$.

The amplified M sub-signals are recombined by a suitable circuit and the constructed signal is transmitted by the antenna. We assume a perfect synchronized recombination of the M sub-signals at the output of the amplifiers. In addition, if perfect linear amplification was used, the signal $y(n)$ should be equal to an amplified version of $x(n)$.

The general idea of IDP method is to decompose the original signal $x(n)$ as in equation (5.25), where signal $x_m(n)$ is given by

$$x_m(n) = v_m(n) + \frac{R_m}{\sum_{p=1}^{M} R_p} \varepsilon_M(n), \tag{5.26}$$

where $v_m(n)$ is a signal with constant envelope and $\varepsilon_M(n)$ is an error signal. R_m, $m = 1..M$ are real positive scalar compute by algorithm 1.

Each sub-signals $x_m(n)$ is the sum of a constant envelope signal $v_m(n)$ with an additional high PAPR signal. To control the PAPR of the M sub-signals, only a certain percentage of $\varepsilon_M(n)$ is added to $v_m(n)$. This ratio is related to the mean absolute value of $v_m(n)$. By doing so, we ensure that the variable part of

Algorithm 1 IDP Algorithm

1: Initialization : $\varepsilon_0(n) = x(n)$, $m = 0$,
2: $R_{m+1} = E\{|\varepsilon_m(n)|\}$,
3: $v_{m+1}(n) = R_{m+1}.e^{j\varphi_m(n)}$, $\varphi_m(n)$: the phase of $\varepsilon_m(n)$,
4: $\varepsilon_{m+1}(n) = \varepsilon_m(n) - v_{m+1}(n)$,
5: **if** $m < M$ **then**
6: $m = m + 1$, go to 2,
7: **else**
8: Compute $x_m(n)$, $m = 1, ..., M$ following equation (5.26),
9: **end if**

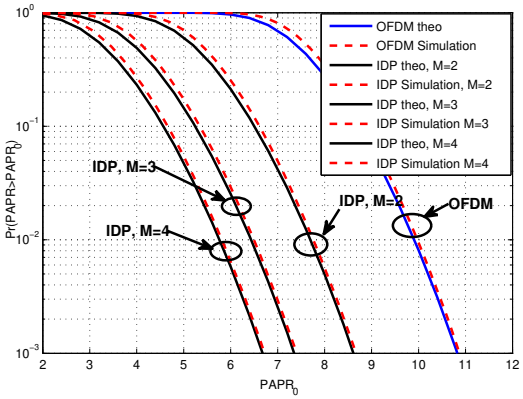

Figure 5.20: CCDF of the PAPR for OFDM and IDP schemes, $16-QAM$, $N_{FFT} = 256$ and $L = 4$.

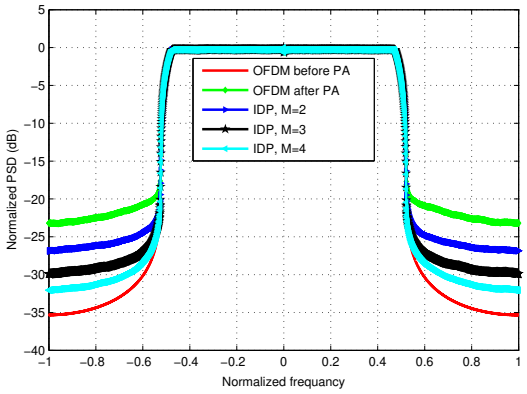

Figure 5.21: PSD before and after PA ($IBO = 3$ dB), for OFDM system and IDP based system for $M = 2, 3, 4$.

the error signal $\varepsilon_M(n)$, to be added to the signal $v_m(n)$, is proportional to its power. The IDP algorithm steps are given in Algorithm 1.

In [85], we proposed a method to compute analytically R_m, for $M = 2$. Recently, we generalized this computation to any order of the dichotomy decomposition M. We also derived relationship between the PAPR of the original signal $x(n)$ and the one of the final signals $x_m(n)$. After straightforward derivations, we obtain

$$PAPR_{x_m} = \frac{P_x}{P_{x_m}} \left[\frac{R_m}{\sum_{p=1}^{M} R_p} \right]^2 PAPR_x. \tag{5.27}$$

For $M = 2$, we have shown, in [85], that the two final signals have quite similar PAPRs equal, approximately to 0.6 times the linear PAPR of the original signal.

The PAPR CCDF of the IDP method with M equal to $2, 3$ and 4 and the original CP-OFDM signal are shown in Fig. 5.20. At $CCDF = 10^{-3}$, the PAPR of the CP-OFDM is about 10.8 dB. At this PAPR CCDF, there is a gain of 2.2 dB, in terms of PAPR, at a dichotomy order $M = 2$. For a higher dichotomy order M, we can reach a gain of $3.4dB$ and $4dB$ with $M = 3$ and $M = 4$, respectively. We can also notice a good agreement between numerical results and theoretical expectations which proves the accuracy of equation (5.27).

As pointed out in chapter 4, the nonlinear amplification causes OOB radiation over adjacent channel. However, the use of IDP technique minimizes this spectral re-growth. In Fig. 5.21, we show the normalized PSD of the input CP-OFDM signal and the output signal in the classical and IDP based configurations of Fig. 5.19 with $IBO = 3$ dB. We can notice the improvement achieved by the IDP method for three dichotomy values: $M = 2, 3, 4$. From this same figure, it can be clearly seen, that performance, in terms of spectral de-growth, increases with the IDP dichotomy order M.

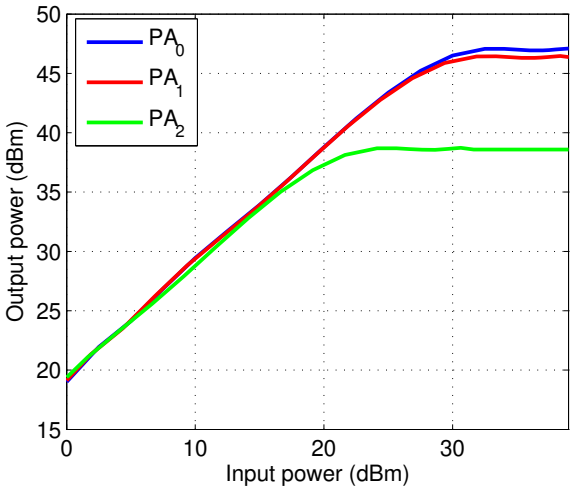

Figure 5.22: Output powers for PAs used by IDP-based and classical OFDM based schemes.

5.3.2 Energy efficiency analysis

We have studied the energy efficiency of the IDP method, by comparing an IDP based OFDM transmitter to a classical one. Fig. 5.19 shows the transmitters corresponding to the classical OFDM scheme (Fig. 5.19 (a)) and the IDP based one (Fig 5.19 (b)).

For the amplification process we use a single power amplifier PA_0 to amplify the CP-OFDM signal $z(n)$., while we use power amplifiers PA_1, PA_2 , ... , PA_M to amplify signals $z_1(n)$, $z_2(n)$, ... , $z_M(n)$, in the IDP based transmitter, as depicted by 5.19 (b). The PA_0 model is based on the 2.6 GHz GaN amplifier characteristics with 19 dB power gain and a PAE up to 70% (Fig 5.18). The other amplifiers used in the IDP based scheme are derived from the PA_0 model by adjusting the power compression points. Because signals, at the output of IDP based and classical OFDM methods, have different powers, the output power curves of the PA_1 and PA_2, used in IDP, are respectively scaled by a factors equal to $P_{x_1}/P_x = 0.8642$ and $P_{x_2}/P_x = 0.1356$. Fig. 5.22 shows the output power characteristics for PA_0, PA_1 and PA_2.

For a given dichotomy order M, all the PA_m, $m = 1..M$ have the same power gain and the same PAE as PA_0. Nevertheless, because input signals $z_m(t)$ have different powers the AM/AM curve of the m^{th} PA are scaled by factors equal to $\sqrt{P_{x_m}/P_x}$ for both input voltage z_n and output voltage u_n. In the following, we give more insights on the approach used to set the parameters of the two schemes of Fig. 5.19, in order to compare their energy efficiency.

From equation (4.2), the consumed DC powers by the classical OFDM and IDP based CP-OFDM schemes are written as

$$P_{DC_{OFDM}} = \frac{P_u - P_z}{PAE}, \tag{5.28}$$

$$P_{DC_{IDP}} = \sum_{m=1}^{M} \frac{P_{u_m} - P_{z_m}}{PAE_m}. \tag{5.29}$$

In order to compare the energy efficiency of the two schemes given by Fig. 5.19, we fixed both consumed DC power and the EVM at the same values and we compare the output signal powers P_y and P_u. To do that, we follow two steps:

1. **[Step 1:]** in order to get the same EVM for signals $u(n)$ and $y(n)$ we fix a common IBO for all power amplifiers PA_0, PA_1 to PA_M. Because the PAPR of $x_m(n)$ signals is lower than the one of the CP-OFDM signal $x(n)$, the expected EVM with IDP method is lower than the EVM of a classical CP-OFDM. Then, we gradually reduce the IBO_m (by increasing α_m) for each PA_m until reaching the same EVM,

IBO for OFDM PA [dB]	3	4	5	6	7	8	9	10
$M = 2$	1.25	1.26	1.27	1.28	1.29	1.30	1.34	1.47
$M = 3$	1.52	1.53	1.54	1.54	1.54	1.54	1.58	1.69
$M = 4$	1.78	1.78	1.79	1.80	1.81	1.82	1.89	2

Table 5.3: Ratio between emitted power for the same DC consumption power and EVM.

2. **[Step 2:]** when both schemes of 5.19 have the same EVM, we enforce a same consumed power P_{DC} for the two schemes and we compare the output powers P_y and P_u.

Tab. 5.3 shows the ratio between the power delivered by the IDP system P_y and the output power of the CP-OFDM system P_u for the same consumed DC power. We can observe from these results that the output power is higher with IDP system. With $M = 2$, the output power P_y is 1.26 times the power P_u, that give an improvement of 26% for $IBO = 3\ dB$. Furthermore, the higher is the dichotomy order M, the higher is the ratio between output powers. For $M = 3$ and $M = 4$ there is an improvement of 53% and 78% at $IBO = 3\ dB$.

To complete this analysis and confirm the advantages of the proposed IDP method, we have compared it, in a conference paper [86], to LINC method. Indeed, both techniques have the same transmitter architecture consisting in the generation of two signals that must be amplified by two PA and then combined for transmission. The comparison has been done following the three main points: (1) comparing the output power for the same DC consumed power and the same BER performance, (2) studying the influence of timing errors in the combination process and (3) analyzing the effect of a mismatch between the amplifiers. Concerning the output emitted power with same DC power and same BER performance, the IDP method outperforms the LINC one, with an emitted power which is twice that of LINC. Concerning timing errors, the two methods are quite impacted. However, the IDP technique is much more tolerant than LINC. Finally, with PA mismatch between the two branches, the IDP method shows low degradations compared to the LINC one.

5.4 Conclusion

In this chapter, I presented some contributions on techniques to improve the energy efficiency of PA in the context of multi-carrier transmissions. Indeed, like CP-OFDM, all the post-OFDM MWFs presented in chapter 3 suffer from high PAPR and are therefore very sensitive to PAs conversion characteristics. Initially, we proposed and adapted probabilistic and signal-adding-based solutions to reduce the PAPR and/or pre-distort the signals to be amplified. The originality of the proposed solutions was based on the fact that they take into account the structures of the signals to be amplified, such as FBMC-OQAM and BF-OFDM, where the overlap between the transmitted symbols must be taken into account in order to achieve acceptable performance. In a second part, I presented an approach to jointly achieve the reduction of PAPR and DPD. This approach, patented in 2017, is based on an iterative and ping-pong synthesis of a single signal that is added to the input of the PA to improve its efficiency and linearity.

Another original contribution that we have proposed consists in posing the problem of improving the energy efficiency of the PA, by modifying the architecture of the latter. This solution is based on splitting the signal to be amplified into several sub-signals with reduced PAPRs and that can be amplified by parallel stages with energy efficient PAs.

In all these contributions, we have kept a close watch on the complexity of the implementation required by the proposed algorithms. This enabled to identify those presenting a real gain in terms of energy efficiency if the corresponding consumption is considered when establishing an overall power budget.

Chapter 6

Massive MIMO networks with mixed numerologies and nonlinear PAs

6.1 Introduction

5G NR requirements should be fulfilled with enhanced network energy efficiency, while allowing to enlarge the sub-6GHz spectrum to mmWaves. Among the prominent technologies proposed to reach the 5G NR requirements, Massive MIMO-OFDM and mixed numerologies have been retained to support various configurations.

The major innovation of release 15 of 3GPP with respect to former standards is the support of various numerologies [23] which allows scalable Sub Carrier Spacing (SCS) and symbol duration. By doing so, challenges of 5G can be properly addressed. Indeed, shortening symbols reduces the latency required for URLLC/cMTC use cases. Moreover, enlarging the SCS increases the robustness against the Doppler effect occurring in mobility scenarios.

Massive MIMO is an emerging technology that uses many antennas at the BS serving many tens of terminals in the same frequency resources. Massive MIMO relies on spatial multiplexing with high number of antennas helping to focus energy into ever smaller regions of space. As the power of the signal to be transmitted by each individual antenna is sufficiently reduced, massive MIMO includes extensive use of inexpensive low-power components. PA with very relaxed linearity requirements will require energy efficiency enhancement solutions, which can exploit the massive MIMO system extra degrees of freedom.

As part of Xinying Cheng's PhD, I have been interested in the study of two issues related to massive-MIMO systems. The first one, which will be presented in section 6.2, is related to the analysis and cancellation of interferences caused by users using different numerologies. In section 6.3, I will present the second topic related to the enhancement of the energy efficiency of dedicated emitters architectures, including joint MIMO precoding, PAPR reduction and DPD.

6.2 Analysis and cancellation of mixed-mumerologies interference for massive MIMO-OFDM

6.2.1 Motivaion

Many studies focused on the analysis of mixed numerologies in SISO, MIMO and OFDM systems. Among these studies, we can cite [165, 166, 167, 168, 169, 170, 171, 172]. In these papers, the approach proposed for supporting diverse services is to introduce flexible numerology allocation over adjacent sub bands. Some recent papers [173] [174] focused on mixed numerologies spectrum sharing (SS). Unlike non-overlapping mixed numerologies systems, it is difficult to prevent interference using windowed/filtered waveforms in mixed numerologies SS systems (i.e., users share the same time/frequency resources). In [174], the authors proposed a new transceiver design for classical MIMO-OFDM using a mixed numerologies SS scheme.

In the first part of Xinying Cheng's PhD, we focused on the use of spatial multiplexing to link users who share the same bandwidth but have different numerologies. We considered a massive MIMO-OFDM system, where we carried, for both DL and UL scenarios, theoretical analysis of internumerology interference (INI) and proposed efficient INI cancellation schemes.

6.2.2 INI theoretical analysis for Massive MIMO-OFDM systems

6.2.2.1 DL scenario

We consider a massive MIMO-OFDM DL scheme with various numerologies. The BS has M_t antennas that serve M_r single-antenna users with different numerologies over a frequency-selective channel, where M_t is far larger than M_r. NUM numerologies, represented by index num, where $num = 1, ..., NUM$, can be used to divide the M_r users into NUM groups. N_{num} and CP_{num} denote the IFFT/FFT size and CP size of group num, respectively. The proposed transceiver can suppress Intra-NI (multi-user interference (MUI) between users using the same numerology) by using several precoders as will be explained later. The BS sends data, over the m_t-th antenna, to the m_r-th user via channel $\sqrt{\alpha_{m_r}}\mathbf{ht}_{m_r,m_t}$, where α_{m_r} is the large-scale fading, $\mathbf{ht}_{m_r,m_t} \in \mathbb{C}^{1\times D}$ is the channel impulse response between transmitting antenna m_t and user m_r, $m_t = 1...M_t$, $m_r = 1...M_r$ and D is the number of channel impulse response taps. For a massive MIMO-OFDM system, the channel frequency response is denoted by $\bar{\mathbf{H}}^{(num)} \in \mathbb{C}^{M_r\times M_t\times N_{num}}$, where

$$\bar{\mathbf{H}}^{(num)}(m_r, m_t, :) = \mathbf{hf}^{(num)}_{m_r,m_t} = FFT(\sqrt{\alpha_{m_r}}\mathbf{ht}_{m_r,m_t}, N_{num}), \tag{6.1}$$

were $FFT(ht_{m_r,m_t}, N_{num})$ represents the channel frequency response corresponding to the impulse response ht_{m_r,m_t} and which is computed with a FFT size equal N_{num}.

For clarity's sake and without loss of generality, we consider two users ($M_r = 2$) using two separate numerologies, as shown in Fig. 6.1. For users 1 and 2, $\mathbf{s}^{(1)}, \mathbf{s}^{(2)} \in \mathbb{C}^{1\times N_1}$ are signals resulting from an M-array QAM. We assume that $N_1 = N \times N_2, CP_1 = N \times CP_2$, where $N = 2^i$ and i is an integer. This generalized synchronized scenario has also been considered in previous works [168] [171]. $\mathbf{x}^{(1)}_{m_t}$ is the modulated OFDM symbol on m_t^{th} transmitting antenna for user 1 and $\mathbf{x}^{(2,n)}_{m_t}$ is user 2's n^{th} modulated OFDM symbol on the m_t^{th} transmitting antenna ($n = 1, ...N$). $\mathbf{x}^{(1)}_{m_t}$ has a total symbol length of N times the symbol length of $\mathbf{x}^{(2,n)}_{m_t}$, and all of the symbols are aligned $x_{mt}(2) = [x_{mt}(2,1), x_{mt}(2,2), ...x_{mt}(2,N)]$.

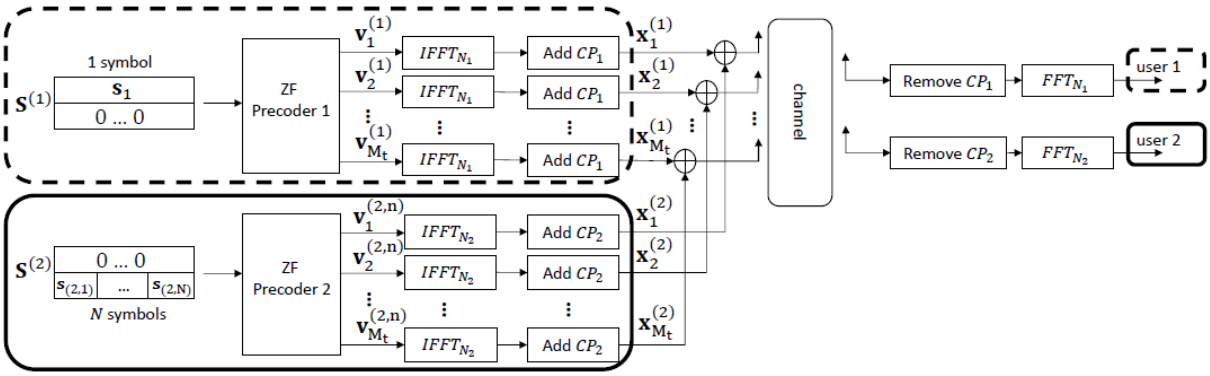

Figure 6.1: System model of the massive MIMO OFDM DL system.

It's worth noting that users in the proposed system share the same bandwidth, resulting in high spectrum performance. Inter-symbol interference (ISI) is avoided at the receiver side if the length of CP_{num} is greater than the length of the multi-path channel.

The analysis of INI between users using different numerologies, we perform in the next paragraphs, is only valid for massive MIMO-OFDM systems, i.e. $M_t \gg M_r$, assuming that the ZF precoders works well and can fully suppress Intra-numerology MUI. In the case of INI between users who use different numerologies, the received symbol after FFT can be written as follows

$$\mathbf{y}_1[n_1] = \mathbf{s}_1[n_1] + \mathbf{ini}^{(2,1)}[n_1] + \mathbf{b}_1[n_1], n_1 = 1, ..., N_1, , \tag{6.2}$$

$$\mathbf{y}_{2,n}[n_2] = \mathbf{s}_{2,n}[n_2] + \mathbf{ini}^{(1,2)}_n[n_2] + \mathbf{b}_{2,n}[n_2], n_2 = 1, ..., N_2., \tag{6.3}$$

where $\mathbf{y}_1$ is the received signal by user 1, $\mathbf{y}_{2,n}$ is the n-th received signal by user 2. $s_1[n_1]$ represents the original symbol on the n_1-th subcarrier with numerology 1 and $\mathbf{s}_{2,n}[n_2]$ is the original symbol of the

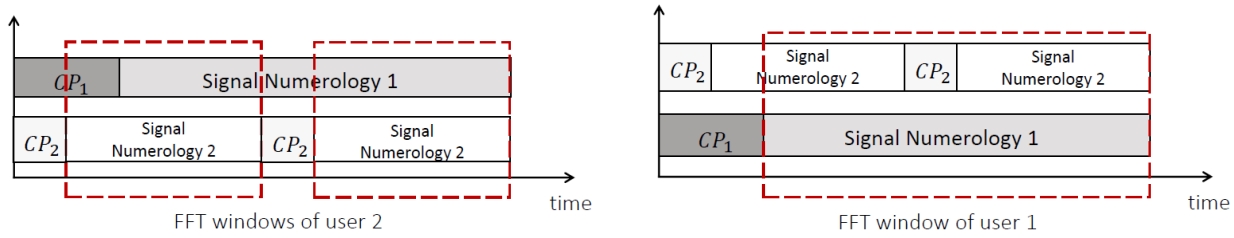

(a) From user 1 to user 2. (b) From user 2 to user 1.

Figure 6.2: FFT windows and INI on the receiver side.

n_2-th subcarrier for n-th symbol with numerology 2. INI from numerology 2 to numerology 1 and INI from numerology 1 to numerology 2 are $\mathbf{ini}^{(2,1)}$ and $\mathbf{ini}_n^{(1,2)}$, respectively. The received noises $\mathbf{b}_1$ and $\mathbf{b}_{2,n}$ are i.i.d circularly-symmetric complex Gaussian distributions with zero-mean and ${\sigma_b}^2$ variance.

INI from numerology 1 with N_1 to numerology 2 with $N_2 = N_1/N$.

In this scenario, we consider that user 2, using numerology 2 with smaller IFFT/FFT size N_2 is interfered by user 1, which is using $N_1 > N_2$. User 2 receives an all-zero signal if only the dash-line block in Fig. 6.1 is enabled. Since the ZF precoder removes all MUI, we only get INI from user 1 due to numerology 1. $\mathbf{ini}_n^{(1,2)}[n_2]$ is derived from the IFFT/FFT window sizes being unequal, as seen in Fig. 6.2 (a).

Based on the analysis carried in, [87], the INI, from numerology 1 to numerology 2, is given by

$$\mathbf{ini}_n^{(1,2)} = \mathbf{G}^{(1)}\mathbf{W}_n^{(1)} \sum_{n_1=1}^{N_1} \sum_{m_t=1}^{M_t} \mathbf{hf}_{2,m_t}^{(1)}[n_1]\mathbf{v}_{m_t}^{(1)}[n_1], \tag{6.4}$$

where $\mathbf{G}^{(1)} = \mathbf{DFT}_{N_2} \in \mathbb{C}^{N_2 \times N_2}$, $\mathbf{hf}_{2,m_t}^{(1)} \in \mathbb{C}^{1 \times N_1}$ is the MIMO channel frequency response between m_t-th transmitting antenna and user 2. $\mathbf{W}_n^{(1)} \in \mathbb{C}^{N_2 \times N_1}$ is the n-th $N_2 \times N_1$ part of matrix $\mathbf{W}^{(1)}$, where $\mathbf{W}^{(1)} \in \mathbb{C}^{N_1 \times N_1}$ is a rotated version of matrix of the inverse discrete Fourier transform (IDFT) [87]. $\mathbf{v}_{m_t}^{(1)} = \left[\mathbf{u}_1^{(1)}[m_t] \dots \mathbf{u}_{N_1}^{(1)}[m_t]\right] \in \mathbb{C}^{1 \times N_1}$ is the reordered version of precoded signals as shown by Fig. 6.1.

Since $\mathbf{H}_{n_{num}}^{(num)} \left(\mathbf{H}_{n_{num}}^{(num)}\right)^{\dagger} = \mathbf{I}_{Mr}$, the ZF precoder given by $\mathbf{P}_{n_{num}}^{(num)} = \mathbf{H}_{n_{num}}^{(num)^H} \left(\mathbf{H}_{n_{num}}^{(num)}\mathbf{H}_{n_{num}}^{(num)^H}\right)^{-1}$ perfectly eliminate all the Intra-NI, which is part of the total MUI. In this case, we can note that $\sum_{m_t=1}^{M_t} \mathbf{hf}_{2,m_t}^{(1)}[n_1]\mathbf{v}_{m_t}^{(1)}[n_1] = 0$, then, we can get $\mathbf{ini}_n^{(1,2)} = 0 \qquad n = 1, ..., N$.

Remark 1: Performance of users using small numerology (IFFT/FFT size) are perfect independently of channel selectivity and power allocation.

As a result, unlike SISO/classical MIMO, where INI exists on small numerology (IFFT/FFT size) [171][173], the INI of users with small IFFT/FFT size is completely suppressed when using the proposed transceiver design for massive MIMO-OFDM.

INI from numerology 2 with N_2 to numerology 1 with $N_1 = N \times N_2$.

In comparison to user 2, user 1's transmission is not properly protected by the ZF precoder, Indeed, when only the solid-line block of 6.1 is enabled, user 1 receives zeros. In this case, where zeros are prepared for user 1, the received signal on user 1 is the INI induced by signal from user 2. This interference comes from N symbols of numerology 2, each of them of length $N_2 = N_1/N$. The INI is induced by an uneven FFT window at the receiver side, as seen in Fig. 6.2 (b) and is given by the sum of INI from each symbol modulated with numerology 2. The total INI, can be expressed as

$$\mathbf{ini}^{(2,1)} = \sum_{n=1}^{N} \mathbf{ini}_n^{(2,1)}, \tag{6.5}$$

where $n = 1, .., N$, $\mathbf{ini}_n^{(2,1)}$ represents the interference from the n-th symbol with numerology 2.

The INI on the n_1-th subcarrier with numerology 1 from the n-th symbol with numerology 2 is given by

$$\mathbf{ini}_n^{(2,1)}[n_1] = \sum_{n_1'=1}^{N_1} \sum_{n_2=1}^{N_2} \mathbf{E}_n(n_1, n_1')\mathbf{Z}(n_1', n_2) \sum_{m_t=1}^{M_t} \mathbf{hf}_{1,m_t}^{(1)}[n_1']\mathbf{v}_{m_t}^{(2,n)}[n_2], \tag{6.6}$$

where

- $n_1 = 1, ..., N_1, n_1' = 1, ..., N_1$, $n_2 = 1, ..., N_2$ and $m_t = 1, ..., M_t$,
- $\mathbf{Z} = \mathbf{G}_2^{(2)}\mathbf{W}_2^{(2)} \in \mathbb{C}^{N_1 \times N_2}$,
- $\mathbf{E}_n \in \mathbb{C}^{N_1 \times N_1} = \begin{cases} \mathbf{G}_1^{(2)}\mathbf{W}_1^{(2)} & for \quad n = 1, \\ \mathbf{G}_2^{(2)}\mathbf{ID}_n^{(2)}\mathbf{W}_3^{(2)} & for \quad n = 2, ..., N. \end{cases}$,
- $\mathbf{G}_1^{(2)} = \begin{bmatrix} \mathbf{0}_{N_1 \times CP_1} & \mathbf{DFT}_{N_1} \end{bmatrix} \in \mathbb{C}^{N_1 \times (N_1 + CP_1)}$, $\mathbf{G}_2^{(2)} = \mathbf{DFT}_{N_1} \in \mathbb{C}^{N_1 \times N_1}$,
- $\mathbf{W}_1^{(2)} = \begin{bmatrix} \mathbf{IDFT}_{N_1} \\ \mathbf{0}_{CP_1 \times N_1} \end{bmatrix} \in \mathbb{C}^{(N_1 + CP_1) \times N_1}$, $\mathbf{W}_3^{(2)} = \mathbf{IDFT}_{N_1} \in \mathbb{C}^{N_1 \times N_1}$,
- $\mathbf{ID}_n^{(2)} = \begin{bmatrix} \mathbf{0}_{T_1 \times (N_1/2)} & \mathbf{0}_{T_1 \times (N_1/2)} \\ \mathbf{I}_{T_2} & \mathbf{0}_{T_2 \times (N_1 - T_2)} \\ \mathbf{0}_{T_3 \times (N_1/2)} & \mathbf{0}_{T_3 \times (N_1/2)} \end{bmatrix} \in \mathbb{C}^{N_1 \times N_1}$,
- $\begin{cases} T_1 = N_1 - (N - n + 1)(N_2 + CP_2), \\ T_2 = \begin{cases} N_2 + CP_2 + D & for \quad n = 2, ..., N-1 \\ N_2 + CP_2 & for \quad n = N, \end{cases} \\ T_3 = \begin{cases} (N-n)(N_2 + CP_2) - D & for \quad n = 2, ..., N-1 \\ (N-n)(N_2 + CP_2) & for \quad n = N. \end{cases} \end{cases}$

Depending on the frequency selectivity of the channel, we can have $\mathbf{hf}_{1,m_t}^{(1)}[n_1] \neq \mathbf{hf}_{1,m_t}^{(2)}[n_2]$, implying that $\mathbf{ini}_n^{(2,1)} \neq 0$.

Impact of the channel response selectivity and N_1/N_2 ratio.

In a constant channel, $\mathbf{ini}_n^{(2,1)}$ is zero due to the channel frequency response characteristic. Indeed, in this case, and regardless the N_1/N_2 ratio, we have $\mathbf{hf}_{1,m_t}^{(1)}[n_1] = \mathbf{hf}_{1,m_t}^{(2)}[n_2]$. Unlike SISO and classical MIMO systems, the proposed massive MIMO scheme provides improved performance in presence of mixed numerologies when the channel is flat. When the channel is frequency-selective, vector $\mathbf{hf}_{1,m_t}^{(1)}$ is the interpolation of vector $\mathbf{hf}_{1,m_t}^{(2)}$. In this case, we can write

$$\mathbf{hf}_{1,m_t}^{(1)}[(n_2 - 1)N + 1] = \mathbf{hf}_{1,m_t}^{(2)}[n_2], \tag{6.7}$$

where $n_2 = 1, ...N_2$.

We can begin by considering the n_2-th subcarrier of the n-th symbol with numerology 2. Its impact on the n_1-th subcarrier with numerology 1 is derived in equation (6.6). According to equation (6.7), the influence of n_2-th subcarrier is zero only when $n_1' = (n_2 - 1)N + 1$, because under this situation, we could obtain $\mathbf{hf}_{1,m_r}^{(1)}[n_1'] = \mathbf{hf}_{1,m_r}^{(2)}[n_2]$. For other values of n_1' ($n_1' \neq (n_2 - 1)N + 1$), the difference between $\mathbf{hf}_{1,m_r}^{(1)}[n_1']$ and $\mathbf{hf}_{1,m_r}^{(2)}[n_2]$ is closely related to the channel selectivity and the difference between N_1 and N_2. Greater selectivity and a larger difference between N_1 and N_2 result in a larger difference in the frequency responses of the two channels, resulting so in higher INI.

Remark 2: In a constant channel, $\mathbf{ini}^{(2,1)}$ is zero due to the channel frequency response characteristic. However this INI is increased by channel selectivity and difference between N_1 and N_2.

Impact of user's power allocation.

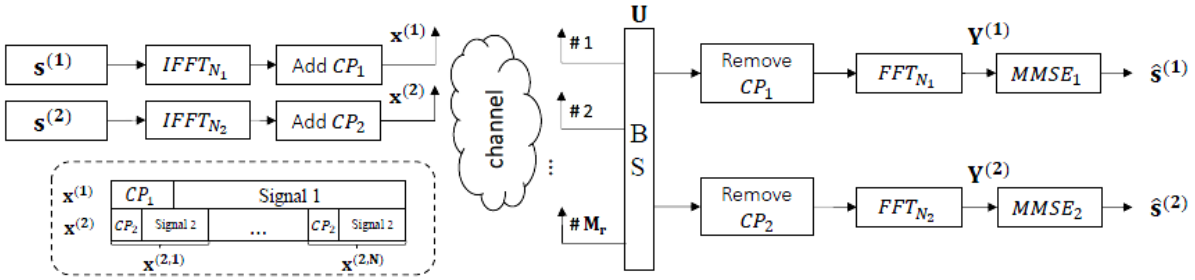

Figure 6.3: System model of the massive MIMO OFDM UL with two different numerologies.

We chose a basic power allocation scheme for users and focused on its impact of INI. We assume that the received signal power by the m_r-th user (p_{m_r}) is proportional to the inverse of its path-loss α_{m_r}. The power allocation for the M_r users is given by

$$\mathbf{P} = \frac{\rho}{M_t}\mathbf{A}^{-1}, \tag{6.8}$$

where ρ is a normalization factor that guarantees that $tr(\mathbf{P}) = P_{Tx}$, with P_{Tx}, being the total emitted power. $\mathbf{P} = Diag(p_1, ..., p_{M_r})$ and $\mathbf{A} = Diag(\alpha_1, ..., \alpha_{m_r})$. Then, as user m_r's large-scale fading increases, the corresponding emitted power increases. In our system, having two users with different path-loss, the generated INI power from user 1 on user 2 ($p^{(1,2)}$) and that from user 2 on user 1 ($p^{(2,1)}$) satisfy

$$\frac{p^{(1,2)}}{p^{(2,1)}} = \frac{\alpha_2}{\alpha_1}. \tag{6.9}$$

As an example, if user 2 is farther away from the BS than user 1, the INI power seen by user 1 is proportional to the power of the signal at the output of the ZF precoder. That is to say, when $\alpha_2 > \alpha_1$, user 1 will suffer from higher INI as a result of user 2's improved transmitting power.

Remark 3: $ini_n^{(2,1)}$ **is directly influenced by power allocated for different users.**

6.2.2.2 UL scenario

In a second step we focused on the UL system. We consider a single-cell massive MIMO-OFDM UL system, where $M_t = 2$ single-antenna users that are using different numerologies N_1 and N_2, transmit signals to a BS equipped with M_r antennas (with $M_t \ll M_r$), over a frequency-selective channel. The system model corresponding to this scenario is given in Fig. 6.3.

As in the UL scenario, we consider a generalized synchronized scenario ($N_1 = N \times N_2, CP_1 = N \times CP_2$, where $N = 2^i$ and i is an integer), at the BS side. For the analysis of INI, we assume a noise free transmission so that the NMSE detection becomes ZF detection. The received signal is separated into two branches and the data stream are then detected through linear processing by two ZF detectors $\bar{\mathbf{P}}^{(1)} \in \mathbb{C}^{2\times M_r \times N_1}$ and $\bar{\mathbf{P}}^{(2)} \in \mathbb{C}^{2\times M_r \times N_2}$. Due to the ZF detection characteristics, the following equations are valid [88]

$$\sum_{m_r=1}^{M_r} \bar{\mathbf{P}}^{(1)}(2, m_r, n_1)\mathbf{hf}_{m_r,1}^{(1)}[n_1]\mathbf{s}^{(1)}[n_1] = 0, \tag{6.10}$$

$$\sum_{m_r=1}^{M_r} \bar{\mathbf{P}}^{(2)}(1, m_r, n_2)\mathbf{hf}_{m_r,2}^{(2)}[n_2]\mathbf{s}^{(2,n)}[n_2] = 0. \tag{6.11}$$

MUI within the same numerology is eliminated by the detection matrices. However, in a mixed-numerologies scheme, INI exists between users sharing the same band.

INI from numerology 1 with N_1 to numerology 2 with $N_2 = N_1/N$.

We assume a noise-free transmission channel and $\mathbf{s}^{(2)} = 0$ to simply focus on the INI caused by user 1. The BS uses $\bar{\mathbf{P}}^{(2)}$ for the detection of user 2's signal and the interference of each subcarrier in n-th symbol can be written as

$$\mathbf{ini}_n^{(1,2)}[n_2] = \sum_{k_2=1}^{N_2}\sum_{n_1=1}^{N_1} \mathbf{G}^{(1)}(n_2,k_2)\mathbf{W}_n^{(1)}(k_2,n_1) \underbrace{\sum_{m_r=1}^{M_r} \bar{\mathbf{P}}^{(2)}(2,m_r,n_2)\mathbf{hf}_{m_r,1}^{(1)}[n_1]\mathbf{s}^{(1)}[n_1]}_{\text{equals to 0 in constant channel (6.10)}}, \tag{6.12}$$

where the matrix definition is the same as equation (6.6).

From equation (6.12), the INI obtained by user 2 is caused by all subcarriers from user 1.

INI from numerology 2 with N_2 to numerology 1 with $N_1 = N \times N_2$.

Similarly, we consider in this scenario $\mathbf{s}^{(1)} = 0$, and a noise-free transmission channel. The BS uses $\bar{\mathbf{P}}^{(1)}$ for the detection of user1's signal and the interference of each subcarrier can be written as

$$\mathbf{ini}^{(2,1)}[n_1] = \sum_{n=1}^{N}\sum_{k_1=1}^{N_1}\sum_{n_2=1}^{N_2} \mathbf{E}_n(n_1,k_1)\mathbf{Z}(k_1,n_2) \underbrace{\sum_{m_r=1}^{M_r} \bar{\mathbf{P}}^{(1)}(1,m_r,n_1)\mathbf{hf}_{m_r,2}^{(1)}[k_1]\mathbf{s}^{(2,n)}[n_2]}_{\text{equals to 0 in constant channel (6.11)}}. \tag{6.13}$$

From (6.13), we can see that $\mathbf{ini}^{(2,1)}[n_1]$ is caused by all subcarriers of user 2.

Impact of the channel response selectivity and N_1/N_2 ratio.

Over flat fading channels, different numerologies between any $m_t = 1...M_t$ transmit antenna and any $m_r = 1...M_r$ receive antenna, give

$$\bar{\mathbf{P}}^{(1)}(m_t,m_r,n_1) = \bar{\mathbf{P}}^{(2)}(m_t,m_r,n_2), \tag{6.14}$$

for all $n_1 = 1...N_1, n_2 = 1...N_2$.

The INI on each subcarrier of user 1 and user 2 is expressed in equations (6.12) and (6.13), respectively. From equation (6.14), in a constant channel, elements in vector $\mathbf{hf}_{m_r,2}^{(1)}$ and vector $\mathbf{hf}_{m_r,2}^{(2)}$ are the same, which will leads to $\bar{\mathbf{P}}^{(1)}(1,m_r,n_1) = \bar{\mathbf{P}}^{(2)}(1,m_r,n_2)$, $\bar{\mathbf{P}}^{(1)}(2,m_r,n_1) = \bar{\mathbf{P}}^{(2)}(2,m_r,n_2)$ for all $n_1 = 1...N_1, n_2 = 1...N_2$. With these substitutions and equations (6.10), (6.11), it is clear that $\mathbf{ini}_n^{(1,2)} = 0$ and $\mathbf{ini}^{(2,1)} = 0$, for $n = 1...N$. As a first conclusion, we can say that over frequency flat channels, the proposed transceiver scheme for massive MIMO-OFDM based mixed numerologies SS UL transmissions does not produce any INI for both user 1 and user 2 (i.e. $\mathbf{ini}_n^{(1,2)} = 0, \quad \mathbf{ini}^{(2,1)} = 0$).

When the channel is frequency-selective, we have

$$\mathbf{hf}_{m_r,m_t}^{(1)}[(n_2-1)N+1] = \mathbf{hf}_{m_r,m_t}^{(2)}[n_2], \tag{6.15}$$

where $n_1 = 1,...N_1, n_2 = 1,...N_2$.

Equation (6.15) shows that there are only a few same-values within the two channel frequency responses for the same time-domain channel between user m_t and receiving antenna m_r. For other values (i.e. $n_1 \neq (n_2-1)N+1$), the difference between $\mathbf{hf}_{m_r,m_t}^{(1)}[n_1]$ and $\mathbf{hf}_{1,m_r}^{(2)}[n_2]$ is closely related to the channel selectivity and to the N_1/N_2 ratio. Greater selectivity and a larger ratio of N_1/N_2 result in a larger difference in the frequency responses of the two channels, inducing higher INI.

Remark 4: Due to the channel frequency response characteristics, in a constant channel, the proposed transceiver scheme for massive MIMO-OFDM based mixed numerologies SS UL transmissions does not produce any INI for both user 1 and user 2 (i.e. $\mathbf{ini}_n^{(1,2)} = 0, \quad \mathbf{ini}^{(2,1)} = 0$). The INIs for both user 1 and user 2 increases with channel selectivity and with N_1/N_2 ratio.

Impact of user's power distribution.

Power allocation strategy has a similar impact as in the DL scenario. For interested reader please refer to [88].

Remark 5: The INIs at user 1 and user 2 are directly affected by the power allocation for different users.

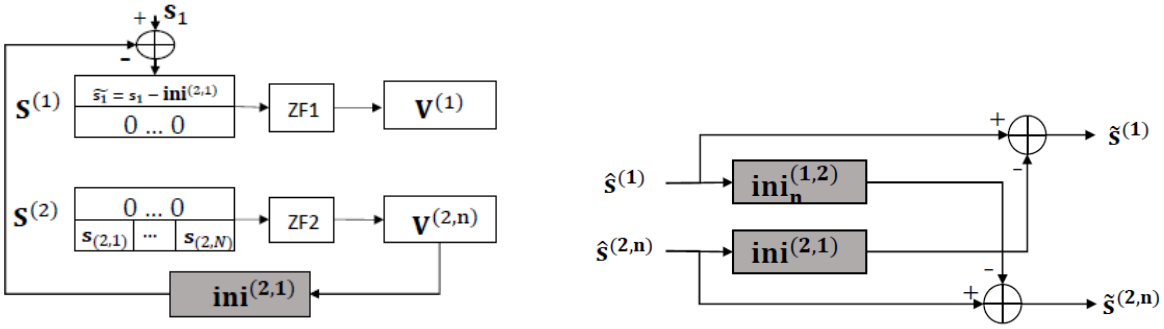

(a) DL. (b) UL.

Figure 6.4: INI cancellation schemes.

6.2.3 INI cancellation schemes

Based on the analytical expressions of INI developed in the previous sections, we will propose here after some INI cancellation schemes for both DL and UL scenarios. The main idea is to reduce the complexity of the single-antenna users by doing all the processing at the BS side.

6.2.3.1 DL INI cancellation

Only numerologies with large IFFT/FFT sizes suffer from INI as compared to numerologies with smaller IFFT/FFT sizes, as seen in section 6.2.2.1. One of the key ideas in massive MIMO DL transmission is to keep all processes at the BS [175], which reduces receiver complexity while maintaining good transmission efficiency. In addition, only the UL transmission estimates channel state in massive MIMO systems. The UL channel estimation is used for precoding in the DL transmission, but discrepancies between the UL and DL channels can be adjusted by a reciprocity adjustment method [176].

On the BS side, Fig. 6.4 (a) indicates the proposed INI cancellation method's scheme. The key concept is to measure the INI from numerology 2 to numerology 1 using knowledge of the MIMO channel response and signals following user 2's precoding. Then, instead of transmitting $\mathbf{s}_1$, we transmit $\widetilde{\mathbf{s}}_1 = \mathbf{s}_1 - \mathbf{ini}^{(2,1)}$. As we demonstrated in section 6.2.2.1, this adjustment does not introduce any INI at user 2, and the proposed transmission scheme perfectly protects the transmission for user 2. The transmit power in INI cancellation is $p_{Tx} = p_u + p_{ini}$, where p_u is the power allocated to users and p_{ini} is the power allocated to INI cancellation. It's worth noting that in equation (6.8), ρ is adjusted to fulfill the constraint imposed by the total transmit power P_{Tx} when taking the p_{ini} into account. According to simulations, the p_{ini} is negligible compared to the power allocated to users (p_u), and it is worth noting that this would result in a minor SNR loss.

6.2.3.2 UL INI cancellation

As analyzed before, in section 6.2.2.2, INIs are created for each user in a frequency-selective channel. With the support of the INI analytical results presented previously, we implement an INI cancellation scheme by performing all processing at the BS side [175]. The full channel state is also calculated on the UL in massive MIMO, which can be used in ZF detection and INI cancellation. The proposed INI cancellation scheme for UL is shown in Fig. 6.4 (b), and it does not add any complexity to the users in this regard. INI is estimated after the symbol estimation, then $\tilde{\mathbf{s}}^{(1)} = \hat{\mathbf{s}}^{(1)} - \mathbf{ini}^{(2,1)}$ and $\tilde{\mathbf{s}}^{(2,n)} = \hat{\mathbf{s}}^{(2,n)} - \mathbf{ini}_n^{(1,2)}$ is applied in order to suppress the INI.

Furthermore, the proposed INI cancellation scheme can be extended to any method that employs more than two numerologies. The INI cancellation can be applied effectively for a given numerology by measuring and extracting the INIs from all other users that use different numerologies. It's worth noting, however, that the proposed INI cancellation approach is just as sensitive to imperfect CSI as ZF detections.

6.2.4 Simulation results

In this section, we will check the accuracy of the derived analytical expressions for INI in a mixed numerologies SS massive MIMO-OFDM scheme. We consider two single-antenna users who use two different numerologies but share the same band in the same cell and the BS is equipped with one hundred antennas. A 16QAM with Gray mapping is considered. Two pairs of numerologies are taken into consideration, with the first pair $N_1 = 1024, N_2 = 512, CP_1 = 72, CP_2 = 36$ and the second pair $N_1 = 1024, N_2 = 256, CP_1 = 72, CP_2 = 18$. The time-domain channel responses $\mathbf{ht}_{mr,mt}[d] = c_d$ have circularly symmetric Gaussian distributed values of zero mean and unit variance, where $d = 1, ..., D$. Four wireless channels are represented by a tap delay line with $D = 1, 2, 8, 18$ taps. It is worth noticing that the CP duration is always adequate to suppress the ISI and ICI induced by the channel.

6.2.4.1 Single user DL scenario

User of Interest	user1 ($N_1 = 1024$)		user2 ($N_2 = 512$)	user2 ($N_2 = 256$)
Interfering User	user2($N_2 = 512$)	user2($N_2 = 256$)	user1($N_1 = 1024$)	
$D = 1$	-300	-300	-300	-300
$D = 2$	-52	-48	-300	-300
$D = 8$	-42	-37	-300	-300
$D = 18$	-38	-33	-300	-300

Table 6.1: NMSE(dB) of user of interest with interfering numerology and different channels for massive MIMO-OFDM DL.

Tab. 6.1 shows the NMSE values in dB for the user of interest, based on the analysis carried in section 6.2.2.1. In this table, we compared different delay spread scenarios with users which are at equal distances from the BS. Tab. 6.1 shows that regardless the N_1/N_2 ratio and the channel selectivity, transmissions for user 2 with small IFFT/FFT size still have the highest quality (NMSE value of about $-300\ dB$). It should be noted that the value of $-300\ dB$ is related to Matlab's floating point precision.

These findings are in full accordance with the study conducted in section 6.2.2.1, which demonstrates that numerology 2 does not suffer from the INI from numerology 1 when the IFFT/FFT size is small. When the N_1/N_2 ratio increases in a frequency-selective channel, user 1 suffers from higher INI coming from numerology 2. User 1's reliability is worse when interference is from $N_2 = 256$ than when interference is from $N_2 = 512$ for the same frequency-selective channel. From another side, when considering the performance of a given pair of N_1 and N_2 under various channel selectivity, we can see that the more selective is the channel, the worse is the user 1 performance.

User of Interest	user 1 ($N_1 = 1024$)			
Interfering User	user 2($N_2 = 512$)		user 2($N_2 = 256$)	
α_1/α_2 (dB)	original (dB)	corrected (dB)	original (dB)	corrected (dB)
20	-22	-300	-18	-300
23	-19	-300	-14	-300
26	-16	-300	-11	-300

Table 6.2: NMSE(dB) of user of interest before and after INI cancellation for massive MIMO-OFDM UL.

The NMSE performances given in Tab. 6.1 assume that the user of interest and the interfering one are located at the same distance for the BS (users with the same path-loss: $\alpha_1/\alpha_2 = 0\ dB$). If we consider a more realistic scenario, we can use equation (6.16) [177] for the LTE path-loss model.

$$\text{Pathloss(dB)} = \alpha = 128.1 + 37.6\log_{10}(d_k) \tag{6.16}$$

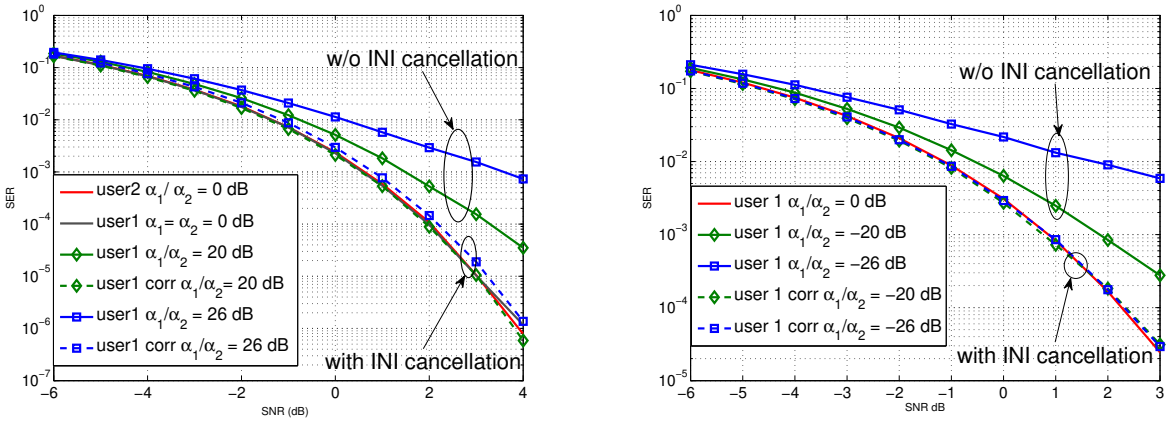

(a) DL with $\alpha_1/\alpha_2 = 0, 20, 23$ and 26 dB

(b) UL with $\alpha_1/\alpha_2 = 0, -20$ and -26 dB..

Figure 6.5: SER performance with and without INI cancellation on user 1.

where d_k is the distance from the BS in km.

User 2 performs better than user 1 regardless the channel selectivity and/or path-loss. For this reason, we will concentrate only on user 1 performance when realistic path-loss is considered. The impact of user's power allocation on system performance is shown in Tab. 6.2, with the number of channel taps $D = 8$.

As the path-loss on user 2 grows, user 1 experiences more INI. When $N_1 = 1024, N_2 = 512$ and $D = 8$, there is a $20dB$ degradation when $\alpha_1/\alpha_2 = 20dB$ compared to $\alpha_1/\alpha_2 = 0dB$. It can also be noticed for Tab. 6.2, that once INI cancellation is applied at the BS side, INI on user 1 falls to $-300dB$ for all path-loss and N_1/N_2 values.

For DL scenario, Fig. 6.5 (a) shows the symbol error rate (SER) vs. $\mathrm{E_b/N_0}$ using $N_1 = 1024, N_2 = 512$ and $D = 18$ to validate the INI analysis on user 1. We can see from this figure that when the path-loss of user 2 increases, user 1's SER suffers significantly. As an example, we can notice at $SER = 10^{-3}$, that there is a SNR loss of $\sim 3\ dB$ when we move from $\alpha_1/\alpha_2 = 0\ dB$ to $\alpha_1/\alpha_2 = 26\ dB$.

6.2.4.2 Single user UL case

User of Interest	user1 ($N_1 = 1024$)		user2($N_2 = 512$)	user2($N_2 = 256$)
Interfering User	user2($N_2 = 512$)	user2($N_2 = 256$)	user1($N_1 = 1024$)	
$D = 1$	-300	-300	-300	-300
$D = 2$	-56	-52	-52	-49
$D = 8$	-47	-45	-44	-40
$D = 18$	-43	-40	-39	-36

Table 6.3: NMSE(dB) of user of interest with interfering numerology and different channels for massive MIMO-OFDM UL.

Tab. 6.3 shows the NMSE values in dB for the user of interest for the UL system described in section 6.2.2.2 under various channel conditions, with $\alpha_1 = \alpha_2$. As expected the results given in Tab. 6.3 show that INIs are increasing with channel selectivity except for the flat fading channel case. These findings are consistent with the analysis presented in section 6.2.2.2, demonstrating that channel selectivity and the increase of N_1/N_2 ratio, raise INIs. For example, under channel $D = 8$, there is 9 dB of degradation on $NMSE$ compared to channel $D = 2$ and 13 dB under channel $D = 18$ for the same pair of numerologies, $N_1 = 1024, N_2 = 512$. Meanwhile, when comparing performance under the same channel selectivity, different pairs of numerologies behave differently, with users suffering more INI as the N_1/N_2 ratio grows.

Similar to the massive MIMO-OFDM DL system, we consider some more realistic scenarios with the LTE path-loss model given by equation (6.16) [177]. The impact of realistic path-loss over system performance is shown in Tab. 6.4, with $D = 8$ as the number of channel taps. As path-loss increases, users experience more INI. When $N_1 = 1024, N_2 = 512$ and $D = 8$, there is a 21 dB degradation on $NMSE$ when $\alpha_1/\alpha_2 = 20$ dB compared to $\alpha_1/\alpha_2 = 0$ dB, and this degradation increases to 28 dB when $\alpha_1/\alpha_2 = 26$ dB. These findings match our study in section 6.2.2.2. It can be also noticed from this table that after the INI cancellation at the BS side, transmission of user 1 and user 2 reached about -70 dB for all path-loss values.

α_1/α_2 (dB)	$NMSE_1$ original (dB)	$NMSE_1$ corrected (dB)	$NMSE_2$ original (dB)	$NMSE_2$ corrected (dB)
0	-47	-70	-44	-69
20	-66	-71	-23	-69
26	-72	-72	-16	-70
-20	-28	-69	-65	-69
-26	-20	-69	-70	-72

Table 6.4: NMSE(dB) values before and after INI cancellation with $N_1 = 1024$, $N_2 = 512$ and $D = 8$ for massive MIMO-OFDM UL.

Using $N_1 = 1024, N_2 = 512, D = 8$ and three separate pairs of locations, Fig. 6.5 (b) shows the SER vs. SNR of different users with/without INI cancellation. We can see that when the path-loss increases, user 1's performance suffers from INI significantly. As noticed in the DL scenario, the SNR loss is ~ 3 dB for $SER = 10^{-2}$, when we move from $\alpha_1/\alpha_2 = 0$ dB to $\alpha_1/\alpha_2 = -26$ dB.

6.2.4.3 Multi-user DL scenario

The simulations carried in the previous sections assume a simple cell including two devices, which are using two different numerologies. In a more realistic scenario, a cell includes many users that can be divided into several groups, each of them is using a given numerology. We will, consider a DL scenario as an example. Users are evenly distributed in the ring around the BS, with inner radius $r_1 = 200$ m and outer radius $r_2 = 1000$ m, as shown in Fig. 6.6 with $M_t = 100$ and $M_r = 30$. The thirty users are divided into three groups: Group 1 includes users 1 to 10, Group 2 includes users 11 to 20, and Group 3 includes users 21 to 30, using three different numerologies of IFFT/FFT sizes equal to 1024, 512, and 256, respectively.

Fig. 6.7 depicts various NMSE values on various UI belonging to various groups. As seen in this figure, certain users have a greater interference than other ones. We can compare the different INI impacts on UI No. 1 from users No. 12 and No. 13, for example, where user No. 1 belongs to group 1 ($N_1 = 1024$) and users No. 12 and 13 belong to group 2 ($N_2 = 512$). The INI generated from user No. 12 to user No. 1 induces a NMSE around -40 dB (blue/green point), while the INI generated from user No. 13 to user No. 1 induces a NMSE around -20 dB. (red point). In this case, it is more important, for user No.1, to cancel the INI generated by user No. 13. To summarize, INI cancellation is interesting, or even important, to use between two users from two different groups who have a significant difference in path-loss.

The work presented in this section have been published in two journal papers [64] and [68] for respectively DL and UL scenarios.

6.3 Enhanced energy efficiency of Massive-MIMO systems

6.3.1 Motivation

As far as a large number of antennas is used at the BS side, massive MIMO precoders exhibit transmit signals with high PAPR, regardless of whether single-carrier or multi-carrier transmission and of whether

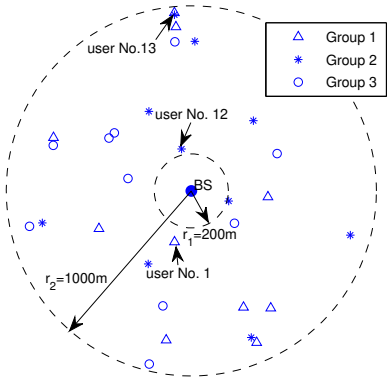

Figure 6.6: User distribution in a ring where BS is in the center.

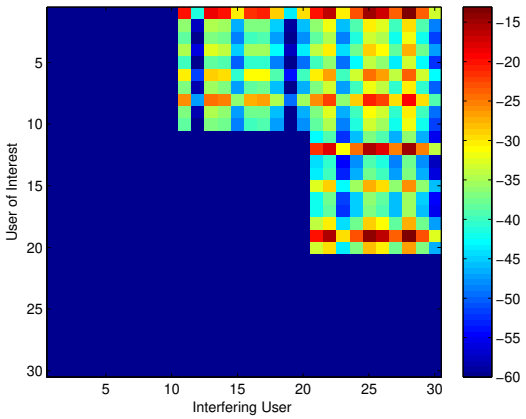

Figure 6.7: NMSE values for different users with different path-loss and channel taps $D = 18$ for massive MIMO-OFDM DL.

a low or a high modulation order is used [178]. As discussed in chapter 4, the non-linearity of RF PA, is the main hardware impairment in the system. The effect of non-linear PA on the energy-efficient design of massive MIMO has been studied in [179] and the spatial characteristic of the non-linear distortion radiated from antenna arrays is shown in [180].

Many research efforts have been recently conducted in multi-user (MU)-MIMO precoding based PAPR reduction. Low-PAPR Tomlinson-Harashima precoding schemes suitable for MU-MISO and MU-MIMO DL were initially described in [181] and [182], respectively. These schemes, however, require specific signal processing at the receiver side (i.e., in the mobile terminal) making them less attractive. Prabhu et al. [183] proposed a peak-clipping scheme for PAPR reduction in OFDM-based massive MIMO where some of the antennas at the BS are reserved to compensate for peak-clipping signals. Another method has been introduced in [184] that aims at reserving some tones to reduce the PAPR in large-scale MU-MIMO-OFDM systems. However, these methods lack efficiency since they sacrifice spectral efficiency by reserving some antennas or some tones, which may be not suitable for future wireless networks.

Recently, some research aimed to jointly perform MU precoding and PAPR reduction for massive MIMO-OFDM, like [185] [186] [187], where algorithm EM-TGM-GAMP, PROXIINF-ADMM and MU-PP-GDm were proposed, respectively. These recent algorithms showed great performance both in MUI and OOB radiation while ensuring acceptable PAPR performance. However, all these solutions, in addition to the fact that they do not consider PA nonlinearities, still have a quite high computational complexity. In [188], we have proposed the MU-PNL-GDm algorithm performing jointly MU precoding, PAPR reduction and digital-predistortion. This algorithm provides good performance, but its complexity is still challenging.

Motivated by all these considerations, we have focused, during Xinying Cheng's PhD, on the development of an efficient DL transmission scheme taking into consideration MU precoding, PAPR reduction and PA linearization. The proposed iterative algorithm, referred to as MU-2P, exploits the high-dimensional degrees of freedom, offered by equipping the BS by many antennas. During the design of this algorithm, we have paid special attention to the computational complexity.

6.3.2 System model

We consider a typical massive MIMO scenario, where the BS is equipped with M_t antennas serving M_r single-antenna users and M_t is significantly larger than M_r. The BS transmits, via the m_t-th antenna, to the m_r-th user over a frequency-selective channel. Here, each antenna is equipped with a PA. The signal vector $\mathbf{s}_n \in \mathbb{C}^{M_r \times 1}$ contains the symbols associated with the n-th OFDM subcarrier for M_r users, where

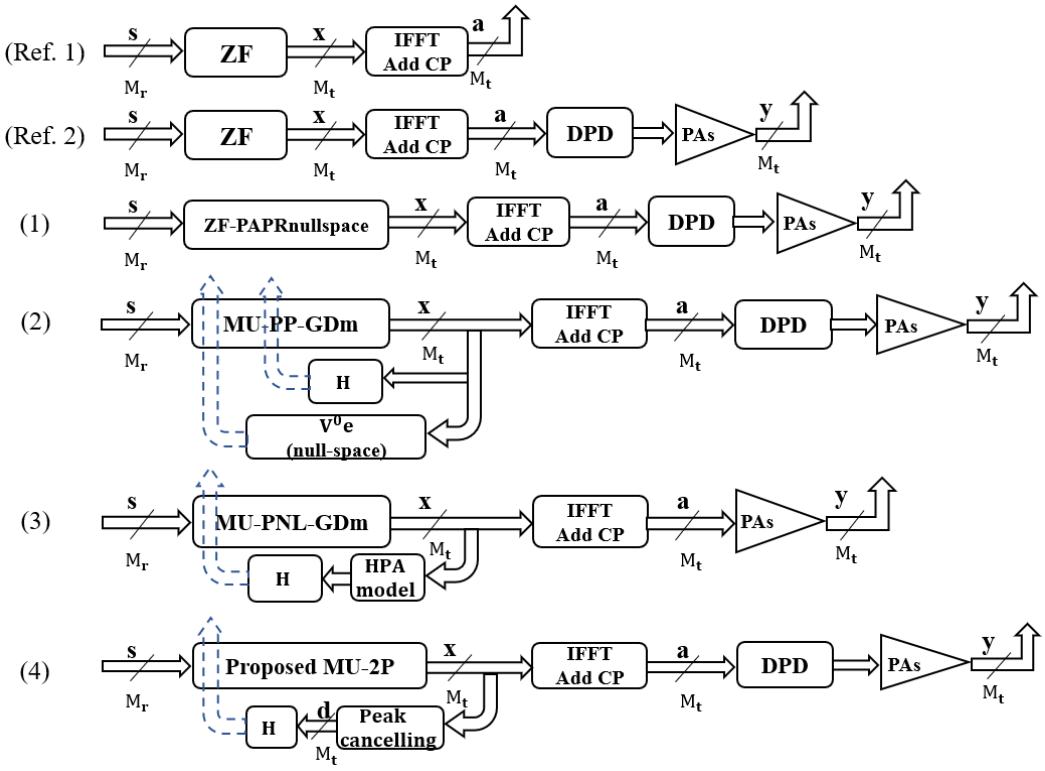

Figure 6.8: Massive MIMO-OFDM schemes.

$n = 1, ..., N$ and it is chosen from a complex-valued constellations. In practice, OFDM systems typically specify certain unused subcarriers, which are used for guard-band (e.g., at both ends of the spectrum). Hence, the set of subcarriers available are divided into two sets χ and χ_c, where the subcarriers in set χ are used for data transmission and the subcarriers in its complementary set χ_c are used for guard band. Moreover, we set $\mathbf{s}_n = \mathbf{0}_{M_r \times 1}$ for $n \in \chi_c$ so that no signal is transmitted on the guard-band.

To suppress the MUI at the receivers, linear precoding scheme is implemented at the BS. Thus, the signal matrices $\mathbf{c}_n \in \mathbb{C}^{M_t \times 1}$ are linearly coded as

$$\mathbf{c}_n = \frac{1}{\sqrt{\zeta_w}} \mathbf{W}_n \mathbf{s}_n, n = 1, ..., N, \tag{6.17}$$

where ζ_w is the power normalization factor designed to obtain an average or instantaneous transmit power equal to σ_s^2 (power of signal s). $\mathbf{W}_n \in \mathbb{C}^{M_t \times M_r}$ and $\mathbf{c}_n \in \mathbb{C}^{M_t \times 1}$ denote respectively the ZF precoding matrices for n-th OFDM subcarrier and the precoded signal on the n-th subcarrier through the M_t antennas.

After precoding, the M_t-dimension vector $\mathbf{c}_n$ is reordered to construct $\mathbf{x}_n$, according to the following mapping

$$\left[\mathbf{x}_1^t \dots \mathbf{x}_{M_t}^t\right] = \left[\mathbf{c}_1 \dots \mathbf{c}_N\right]^T. \tag{6.18}$$

The N-dimensional vector $\mathbf{x}_{m_t}$ denotes the frequency domain signal to be transmitted from m_t-th antenna. Then, the time-domain signal $\mathbf{a}_{m_t}^t$ is obtained by applying an IFFT to $\mathbf{x}_{m_t}$ and a CP is then added to the time-domain samples of each antenna. At the receiver side, assuming that the length of the CP is larger than the length of the multipath channel, ISI and ICI are eliminated.

In this study, we will compare our proposed low complexity algorithm, with two reference schemes noted as (Ref. 1) and (Ref. 2) as well as existing schemes proposed in the literature. Fig. 6.8, depicts the considered schemes along with the proposed one. A brief description of the existing schemes, along with the presentation of the proposed algorithm will be given in the next sections.

For clarity sake and without loss of generality, the input-output relationships of the wireless propagation channel will be written in the frequency domain. Then, the signal received by M_r users at n-th

OFDM subcarrier can be expressed as

$$\mathbf{r}_n = \mathbf{H}_n \mathbf{y}_n + \mathbf{b}_n, \tag{6.19}$$

where $\mathbf{H}_n \in C^{M_r \times M_t}$ is the MIMO channel matrix, $\mathbf{y}_n$ is the transmitted signal and $\mathbf{b}_n$ is the receiver noise whose entries are i.i.d circularly-symmetric complex Gaussian distribution with zero-mean and σ_b^2 variance.

6.3.3 Existing schemes

Schemes (Ref .1) & (Ref. 2)

As shown in Fig. 6.8, there are two reference schemes. (Ref. 1) is the classical ideal massive MIMO-OFDM scheme with ZF precoding and without any PA nonlinearities, which represents the best quality of transmission. On the contrary, (Ref. 2) represents the worst scenario among all the schemes, with only DPD processing before PAs in each branch.

Scheme (1) : ZF precoding and PAPR reduction using null-space + DPD.

The key idea of this scheme is to use ZF precoding method to achieve perfect MUI cancellation and to reduce the PAPR by adding the peak-cancelling signals using the null-space of the channel. The PA nonlinearities are compensated by an external DPD for each PA/antenna. PAPR reduction is achieved by adding peak-canceling signals $\{\mathbf{p}_{m_t}^t\}$ to precoded signals $\mathbf{x}_{m_t}^t$. The N-dimensional vector $\mathbf{p}_{m_t}^t$ is the peak-cancelling signal added to the precoded signal of the m_t-th transmit antenna, while $\mathbf{p}_n \in \mathbb{C}^{M_t \times 1}$ is the frequency-domain peak-canceling signal added to the precoded signal of the n-th subcarrier. To avoid MUI, the peak-canceling signals must be projected onto the null-space of the MIMO channel, satisfying

$$\mathbf{H}_n \mathbf{p}_n = \mathbf{0}_{M_r \times 1}, \quad n \in \chi. \tag{6.20}$$

There are two methods to compute the null-space $\mathbf{V}_n$ using the singular value decomposition (SVD) [189] or by computing $\mathbf{V}_n = \mathbf{I}_n - \mathbf{H}_n^H \left(\mathbf{H}_n \mathbf{H}_n^H\right)^H$. Therefore

$$\mathbf{H}_n \mathbf{V}_n = \mathbf{0}_{M_r \times M_t - M_r}, \quad \forall n. \tag{6.21}$$

The key point is to design a peak cancelling signal in the frequency domain $\mathbf{p}_n$ in such a way that it fulfils

$$\mathbf{p}_n = \mathbf{V}_n \mathbf{e}_n. \tag{6.22}$$

After applying the clipping method to reduce the PAPR, the original frequency-domain clipping noise at the n-th subcarrier is $\mathbf{d}_n \in \mathbb{C}^{M_t \times 1}$. Then, the aim of this scheme is to solve the following convex optimization problem

$$\begin{aligned} \underset{\dot{\mathbf{e}}_n}{\text{minimize}} \quad & G(\mathbf{e}_n) = \|\mathbf{V}_n \mathbf{e}_n - \mathbf{d}_n\|_2^2, n \in \chi, \\ \text{subject to} \quad & \dot{\mathbf{e}}_n = \mathbf{0}_{(M_t - M_r) \times 1}, n \in \chi^c. \end{aligned} \tag{6.23}$$

The above formulation yields to an iterative algorithm with the peak-canceling signals constrained to be in the null-space of the corresponding MIMO channel matrices. This algorithm is referred to as ZF-PAPRnullspace. It is worth noticing that this algorithm can separate the PAPR reduction problem from the MU precoding by initializing precoded signals $\mathbf{x}_n$ according to a pre-fixed precoder.

Scheme (2) : Joint precoding and PAPR reduction using null-space [187].

In scheme (1) the PAPR reduction using null-space is performed, while applying ZF precoding before. However, scheme (2) corresponds to the joint precoding and PAPR reduction solution MU-PP-GDm proposed in [187]. In this scheme the joint precoding and PAPR reduction are done iteratively to remove

the MUI and reduce the PAPR using null-space MIMO channels and performing MU precoding. Then, the new optimization problem becomes

$$\begin{aligned} &\underset{\{\hat{\mathbf{e}}_n, \hat{\mathbf{x}}_n\}}{\text{minimize}} J(\mathbf{x}_n, \mathbf{e}_n) = F(\mathbf{x}_n) + G(\mathbf{e}_n), \qquad n \in \chi, \\ &\text{subject to } \begin{cases} \mathbf{x}_n = \mathbf{0}_{M_t \times 1}, & n \in \chi^c, \\ \dot{\mathbf{e}}_n = \mathbf{0}_{(M_t - M_r) \times 1}, & n \in \chi^c, \end{cases} \end{aligned} \tag{6.24}$$

where $F(\mathbf{x}_n) = \|\mathbf{H}_n \mathbf{x}_n - \mathbf{s}_n\|_2^2, n \in \chi$ is the cost function of MUI elimination, while $G(\mathbf{e}_n)$ is given by equation (6.23) to obtain an optimal PAPR.

An alternating minimization strategy can be used to solve (6.24), in which we alternatively minimize the objective function with respect to $\mathbf{x}_n$ and $\mathbf{e}_n$. In the $(l+1)$-th iteration, the alternating procedure can be expressed as

$$\begin{aligned} \mathbf{x}_n^{(l+1)} &= \underset{\{\mathbf{x}_n\}}{\text{argmin}} \quad J\left(\mathbf{x}_n^{(l)}, \mathbf{e}_n^{(l)}\right), \qquad n \in \chi, \\ \mathbf{e}_n^{(l+1)} &= \underset{\{\mathbf{e}_n\}}{\text{argmin}} \quad J\left(\mathbf{x}_n^{(l+1)}, \mathbf{e}_n^{(l)}\right), \quad n \in \chi. \end{aligned} \tag{6.25}$$

Scheme (3) : Joint ZF precoding, PAPR reduction and DPD [188].

The above schemes (1) and (2) use clipping method for PAPR reduction and after that, a separate DPD for PA linearization. The key idea of scheme (3) is to jointly perform MU precoding and PA non-linearity mitigation, including PAPR reduction and DPD, using the PA model directly at each transmit antenna. By using the well-known Bussgang theorem [58], one can decompose the nonlinear signal at the PA output into a linear function of the PA input and an uncorrelated distortion term. At each branch, the amplified signal $\mathbf{y}_{m_t}^t = q_{m_t} \mathbf{x}_{m_t}^t + \mathbf{d}_{m_t}^t$, where q_{m_t} is the m_t-th PA complex gain and $\mathbf{d}_{m_t}^t$ stands for the added zero-mean distortion noise with variance σ_d^2. Then, we can write the amplified signal in (6.19) as

$$\mathbf{y}_n = \mathbf{Q}_n \mathbf{x}_n + \mathbf{d}_n, \tag{6.26}$$

where $\mathbf{Q}_n = \text{diag}([q_1, q_2, \ldots, q_{M_t}])$ is the $M_t \times M_t$ square diagonal matrix with elements $\{q_{m_t}\}$ on the diagonal.

Substituting (6.26) in (6.19), we have:

$$\mathbf{r}_n = \mathbf{H}_n \mathbf{Q}_n \mathbf{x}_n + \mathbf{H}_n \mathbf{d}_n + \mathbf{b}_n. \tag{6.27}$$

By minimizing the MSE of intended symbols and PA outputs through the channel, the optimization problem can be formulated as

$$\begin{aligned} &\text{minimize } J(\mathbf{x}_n) = \|\mathbf{H}_n \mathbf{Q}_n \mathbf{x}_n + \mathbf{H}_n \mathbf{d}_n - \mathbf{s}_n\|_2^2, \\ &\text{subject to } \|\mathbf{x}_n\|_2^2 \leq P_{Tx}, \end{aligned} \tag{6.28}$$

where P_{Tx} is the total transmitted power.

Then, scheme (3) aims to search, iteratively, for the symbols $\{\mathbf{x}_{m_t}^t\}$ which can guarantee excellent transmission quality after the channel. The alternating procedure, in the $(l+1)$-th iteration, can be expressed as

$$\begin{aligned} \mathbf{x}_n^{(l+1)} &= \underset{\{\mathbf{x}_n\}}{\text{argmin}} J\left(\mathbf{x}_n^{(l)}, \mathbf{d}_n^{(l)}\right), \\ \mathbf{d}_n^{(l+1)} &= \mathcal{P}\left(\mathbf{x}_n^{(l+1)}\right) - \mathbf{Q}_n \mathbf{x}_n^{(l+1)}, \end{aligned} \tag{6.29}$$

where $\mathcal{P}(.)$ denotes the amplification operation.

The proposed algorithm is referred as MU-PNL-GDm for Multi-User (MU) precoding - Power Non-Linearities compensation (PNL) - using Gradient Descent with momentum (GDm) algorithm.

The three existing schemes introduced before proposed several solutions for PA non-linearity mitigation. However, they have high computational complexity. For scheme (1), the high complexity comes from the matrix inversion of ZF precoding and the computation of the channel null-space. For scheme (2), although the ZF precoding matrix computation is removed, the computation of null-space remains high. What is more, in scheme (3), is that there is a PA model used in each iteration, which brings high complexity for the processing.

6.3.4 Scheme (4) : Proposed scheme for joint ZF precoding and PAPR reduction without null-space.

Compared to the previously presented schemes, we propose a new scheme which can jointly apply precoding and PAPR reduction without using the high-complexity required by the null-space matrix computation. The new scheme corresponds to scheme (4) on Fig. 6.8. The key idea is to iteratively reduce jointly the MUI and the clipping noise $\{\mathbf{d}_{m_t}^t\}$, which is obtained by clipping the time-domain signals $\{\mathbf{a}_{m_t}^t\}$. Given the clipping threshold λ, the clipped signal $\bar{\mathbf{a}}_n$ at the n-th subcarrier can be obtained by

$$\bar{a}_{m_t}(k) = \begin{cases} a_{m_t}(k), \text{ if } |a_{m_t}(k)| < \lambda, \\ \lambda e^{j\phi(k)}, \text{ if } |a_{m_t}(k)| > \lambda, \end{cases} \tag{6.30}$$

where $a_{m_t}(k) = |a_{m_t}(k)|\, e^{j\phi(k)}$ and $\phi(k)$ is the phase of $a_{m_t}(k)$. The original frequency-domain clipping noise associated to the m_t-th transmit antenna is $\mathbf{d}_{m_t}^t = FFT(\bar{\mathbf{a}}_{m_t}^t - \mathbf{a}_{m_t}^t)$. Then, the effective transmission signal $\tilde{\mathbf{x}}_n$ at the n-th subcarrier in the frequency domain is represented as

$$\tilde{\mathbf{x}}_n = \mathbf{x}_n + \mathbf{d}_n, \quad n \in \chi. \tag{6.31}$$

Compared with scheme (3), here, $\mathbf{d}_n$ stands for the clipping noise instead of PA distortion noise, which can be obtained with more simplicity. To ensure desirable spectral properties of the transmitted OFDM signals, the inactivated OFDM subcarrier (indexed by χ^c) must satisfy the following shaping constraints:

$$\tilde{\mathbf{x}}_n = \mathbf{0}_{M_t \times 1}, \quad n \in \chi^c. \tag{6.32}$$

Consequently, the total MUI energy can be evaluated by $\|\mathbf{H}_n \tilde{\mathbf{x}}_n - \mathbf{s}_n\|_2^2$.

By minimizing the MSE of intended symbols $\mathbf{s}_n$ through the channel $\mathbf{H}$, the problem can be formulated as

$$\begin{aligned} &\text{minimize } J(\mathbf{x}_n) = \|\mathbf{H}_n \mathbf{x}_n + \mathbf{H}_n \mathbf{d}_n - \mathbf{s}_n\|_2^2, n \in \chi, \\ &\text{subject to } \mathbf{x}_n = \mathbf{0}_{M_t \times 1}, \quad n \in \chi^c. \end{aligned} \tag{6.33}$$

A minimization strategy can be used to solve (6.33), in which we iteratively minimize the objective function. Note that the clipping noise used in the $(l+1)$-th iteration is calculated from the previous l-th iteration. The procedure can be expressed as

$$\mathbf{x}_n^{(l+1)} = \underset{\{\mathbf{x}_n\}}{\operatorname{argmin}} J\left(\mathbf{x}_n^{(l)}, \mathbf{d}_n^{(l)}\right). \tag{6.34}$$

The search directions of the steepest gradient descent (GD) method at $l+1$ is determined by the negative gradient of the cost function J at iteration l, which is given by

$$\nabla_x J\left(\mathbf{x}_n^{(l)}, \mathbf{d}_n^{(l)}\right) = 2\mu \mathbf{H}_n^H \left(\mathbf{H}_n \mathbf{x}_n^{(l)} + \mathbf{H}_n \mathbf{d}_n^{(l)} - \mathbf{s}_n\right), \tag{6.35}$$

where μ is the adaptation step size.

The details of the proposed processing, referred to as MU-2P (for Multi-User for joint Precoding and PAPR reduction), are summarized in algorithm 2.

6.3.5 Complexity analysis

We adopt the number of complex multiplications to compare the complexity of the proposed algorithm to the one of the existing scheme (1), scheme (2) and scheme (3). For the proposed algorithm MU-2P, the computational cost is dominated by the gradient computation $\Delta \mathbf{x}_n^{(l)}$ (Line 3 of algorithm 2) and the N-point IFFT/FFT (line 5 and 6). The gradient in line 3 involves $\mathcal{O}(3|\chi| M_t M_r)$ complex multiplications. The IFFT/FFT costs $\mathcal{O}(M_t N \log(N))$ complex multiplications. Therefore, the proposed MU-2P requires a total of $\mathcal{O}(3|\chi| M_t M_r + 2M_t N \log(N))$ complex multiplications for each iteration.

For scheme (1): ZF-PAPRnullspace, it needs $\mathcal{O}\left(N(2M_t M_r^2 + M_r^3)\right)$, $\mathcal{O}(N(M_t M_r))$ and $\mathcal{O}\left(2M_t^2 M_r^2 + M_r M_t^2 + M_r^3\right)$ for ZF procoding matrix computation, ZF implementation and null-space computation. This leads to $\mathcal{O}\left(2|\chi| M_t^2 + 2M_t N \log(N)\right)$ multiplications per iteration.

Algorithm 2 Joint precoding + PAPR reduction algorithm

1: **Initialize**
$\mathbf{x}_n^{(1)} = \mathbf{0}_{M_t \times 1}$,
$\Delta\mathbf{x}_n^{(0)} = \mathbf{0}_{M_t \times 1}$,
set the maximal iteration number $maxIter$,
set the adaptation step size μ,
2: **for** $l = 1, ..., maxIter$ **do**
3: $\Delta\mathbf{x}_n^{(l)} = 2\mu\mathbf{H}_n^H \left(\mathbf{H}_n\mathbf{x}_n^{(l)} + \mathbf{H}_n\mathbf{d}_n^{(l)} - \mathbf{s}_n\right), \forall n \in \chi$,
4: $\mathbf{x}_n^{(l+1)} = \mathbf{x}_n^{(l)} - \Delta\mathbf{x}_n^{(l)}, \quad \forall n \in \chi$,
5: $\mathbf{a}_{m_t}^{t(l+1)} = IFFT\left(\mathbf{x}_{m_t}^{t(l+1)}\right), \quad \forall m_t = 1 \dots M_t$,
6: $\mathbf{d}_{m_t}^{t(l+1)} = FFT\left(\bar{\mathbf{a}}_{m_t}^{t(l+1)} - \mathbf{a}_{m_t}^{t(l+1)}\right)$
7: **end for**
8: **return** $\tilde{\mathbf{x}}_n = \mathbf{x}_n^{(\text{maxIter}+1)}$.

scheme	scheme 1	scheme 2	scheme 3	scheme 4
ZF computation	$N(2M_tM_r^2+M_r^3)$	-	-	-
ZF implementation	$N(M_tM_r)$	-	-	-
Null-space computation	$2M_t^2M_r^2 + M_rM_t^2 + M_r^3$	$2M_t^2M_r^2 + M_rM_t^2 + M_r^3$	-	-
Per iterarion	$2\lvert\chi\rvert M_t^2 + 2M_tN\log(N)$	$2\lvert\chi\rvert M_tM_r + 2\lvert\chi\rvert M_t^2 + 2M_tN\log(N)$	$3\lvert\chi\rvert M_tM_r + 2\lvert\chi\rvert M_t^2 + 2M_tN\log(N)$	$3\lvert\chi\rvert M_tM_r + 2M_tN\log(N)$
DPD	$13NM_t$	$13NM_t$	-	$13NM_t$

Table 6.5: Complexity comparison of the massive MIMO-OFDM schemes.

For scheme (2): MU-PP-GDm needs $\mathcal{O}\left(2M_t^2M_r^2 + M_rM_t^2 + M_r^3\right)$ for the null-space computation as initialization step and $\mathcal{O}\left(2|\chi|M_tM_r + 2|\chi|M_t^2 + 2M_tN\log(N)\right)$ multiplications for each iteration.

When it comes to scheme (3), the complexity of MU-PNL-GDm is $\mathcal{O}\left(3|\chi|M_tM_r + 2|\chi|M_t^2 + 2M_tN\log(N)\right)$ per iteration.

The complexities of the different schemes are summarized in Tab. 6.5. For scheme (1), (2) and (4) (the proposed scheme), a dedicated DPD block per antenna branch is used. The DPD is based on the well-known multi-layer perceptron (MLP) neural network (NN) model. The NN predistorter has two layers, one input and one output with 52 weights. The complexity of the NN DPD is the same for all three algorithms.

6.3.6 Simulation results

The performance of the previously presented schemes in multiuser massive MIMO system is evaluated by simulations. The BS is equipped with $M_t = 100$ antennas serving $M_r = 10$ single-antenna users. We consider OFDM with $N = 512$ subcarriers and use a spectral map χ, in which $|\chi| = 128$ subcarriers are used for data transmission. A 16QAM Gray mapping is considered. We use the CCDF to evaluate the PAPR reduction performance.

The wireless channel is assumed to be frequency-selective and modeled as a tap delay line with $D = 8$ taps. The time-domain channel response matrices have i.i.d. circularly symmetric Gaussian distributed entries with zero mean and unit variance. The equivalent frequency domain response $\mathbf{H}_n$ is obtained by FFT.

In order to evaluate the efficiency of our proposed scheme in term of PAPR reduction, Fig. 6.9 shows

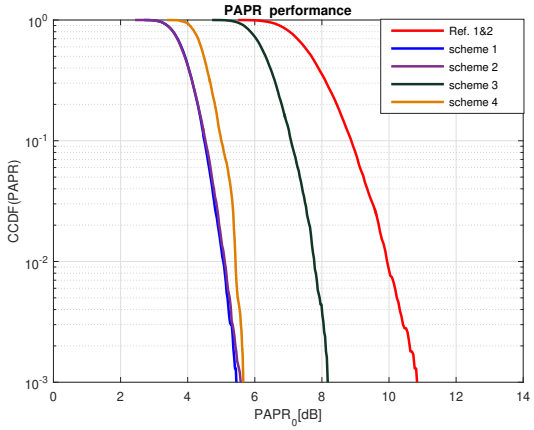

Figure 6.9: PAPR performance.

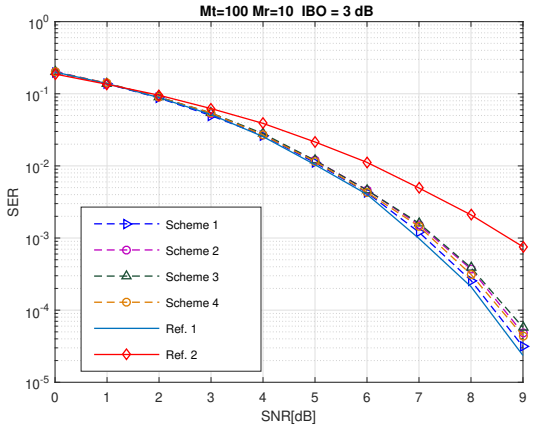

Figure 6.10: SER performance.

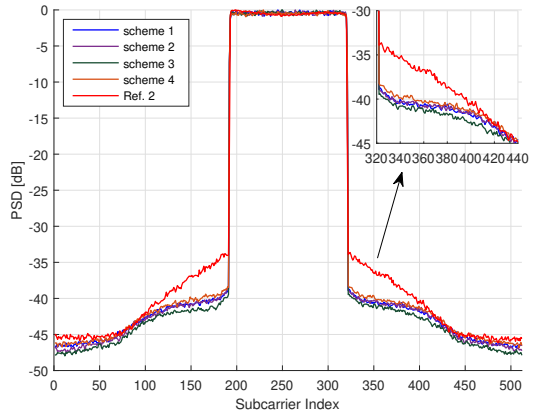

Figure 6.11: PSD performance after PA at transmitter side $IBO = 3dB$

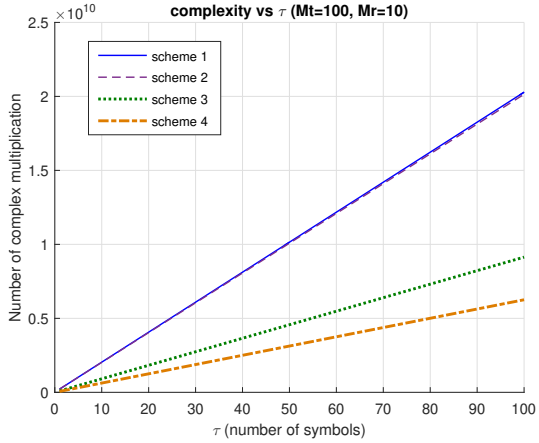

Figure 6.12: Performance complexity vs. τ.

the CCDF of the PAPR achieved by the different schemes for a same MUI level equal to $-40\ dB$[1]. Note that PAPRs associated with all M_t antennas are considered in computing the empirical CCDF. From Fig. 6.9, we can see that the PAPR gain is of 5.4 dB, 5.2 dB, 2.6 dB and 5.1 dB, when, respectively, scheme 1, scheme 2, scheme 3, scheme 4 are considered (at CCDF of 10^{-3}).

The SER vs. SNR of all the schemes is given in Fig. 6.10, where the SNR is defined as $SNR = \mathbb{E}\{\|\mathbf{x}_n\|_2^2\}/N_0$ and the PA is operated at $IBO = 3\ dB$. All schemes reduce the in-band distortion compared with ZF scheme without PAPR reduction referred as (Ref .2). We can also observe that there are little SNR performance (less than 0.5 dB) losses between all the schemes compared with the ideal scheme (Ref .1) at the level of 10^{-4}. This performance difference is primarily because we add different power on the transmitter side with the different schemes.

We compare the proposed scheme with the existing three schemes and the reference schemes. In each algorithm, the adaptation step size μ is automatically adjusted to offer the best convergence rate to the optimal PAPR. For each scheme, the value of $maxIter$ is chosen to reach a MUI of $-40\ dB$ to create a fair comparisons between all the algorithms. Fig. 6.11 shows the PSD at the receiver side for the different schemes at $IBO = 3\ dB$. The PSD spectrum is the mean on all M_r receiving antennas. From the PSD given by Fig. 6.11, we can observe that all schemes perform at nearly the same level, with a gain of 5 dB compared with (ref. 2).

According to the mentioned closed-form expressions in Tab. 6.5, it is possible to numerically assess

[1] A MUI lower than $-40\ dB$ has been chosen and corresponds to a very low penalty concerning 16 and 64-QAM symbols

the complexity of all schemes. The complexity of each scheme is computed assuming the same minimum MUI of -40 dB at the receiver side, i.e., including all the initialization stages, the iterations and the NN DPDs. To achieve a MUI of -40 dB, the ZF-PAPRnullspace, MU-PP-GDm, MU-PNL-GDm and the proposed MU-2P require 35, 32, 14 and 44 iterations, respectively.

scheme	Complexity to achieve MUI=-40 dB
scheme 1	2.1349×10^8
scheme 2	2.0133×10^8
scheme 3	9.1375×10^7
scheme 4	6.2565×10^7
scheme 4/scheme 1	29.31 %
scheme 4/scheme 2	29.5 %
scheme 4/scheme 3	68.47 %

Table 6.6: Complexity comparison for each scheme with $M_t = 100$, $M_r = 10$, $N = 512$ and $\mid \chi \mid = 256$.

First, we examine the efficiency of our proposed scheme with $M_t = 100$, $M_r = 10$, $N = 512$ and $\mid \chi \mid = 256$. Tab. 6.6 shows the complexity of different schemes. From this table we can observe, first, that the complexity of the proposed scheme (4) is lower than the other schemes. Indeed, the complexity of the proposed scheme requires 29.31%, 31.08% and 68.47% of the complexity needed by scheme (1), scheme (2) and scheme (3). This is because ZF-PAPRnullspace and MU-PP-GDm have the initialization of null-space or ZF matrix computation and for MU-PNL-GDm, there is PA implementation in each iteration.

We move now to the complexity comparison considering channel variations. Since ZF precoding matrix computation, null-space computation, the iterative algorithms and NN DPD are all sensitive to channel variations, the coherence time of the channel will play an important role in the total complexity. Fig. 6.12 shows the number of complex multiplication versus channel coherence time with $M_t = 100$ and $M_r = 10$, where τ represents the number of OFDM symbols within which the channel stays stationary. Like the previous figure, the proposed scheme has the best performance, in terms of complexity, compared with all the other schemes while schemes (1) and (2) are the most sensitive among all.

The results presented in section 6.3, have been submitted to IEEE Transaction on Vehicular Technology, in a journal paper which is under review.

6.4 Conclusion

In comparison to mixed numerologies with SISO and classical MIMO systems, where users use adjacent frequency bands, in this chapter, we first introduced new transmission schemes designed for MU massive MIMO-OFDM based 5G system that supports different services using different numerologies, while sharing the same band. The efficiency of these mixed numerologies in massive MIMO-OFDM DL & UL systems was then investigated. We derived theoretical expressions of the INI occurring in the mixed numerologies scenario. We showed that, in the massive MIMO-OFDM DL scenario, INI is only created in frequency selective channels and only when users with large sub-carriers spacing communicate with users with small SCS. However, in uplink scenario, all users suffer from INI in frequency selective channels.

Furthermore, we have verified that the theoretical INI expressions agrees with simulation findings, suggesting that INI is influenced by SCS gaps, channel selectivity, and power allocation. Last but not least, we proposed INI cancellation schemes based on the developed closed form INI expressions that can suppress the INI at the BS side without raising the users' complexity. These results demonstrated that massive MIMO-OFDM systems can accept mixed numerology transmissions while all users share the same band, indicating that this method can increase the spectrum efficiency as well as meet the needs of future wireless communication.

In the second part of this chapter, I focused on energy-efficient DL schemes for massive OFDM-MIMO, taking into account PA nonlinearities. I have presented the existing schemes in the literature and proposed a new one. The main idea of the proposed scheme is to find a trade-off between the clipping noise and the MUI which enables to transmit signals with low PAPR while maintaining acceptable transmission performance. The joint MU precoding and PAPR reduction method was formulated as a simple convex optimization problem for which an algorithm based on steepest gradient descent method was designed. The simulation results showed that the proposed algorithm allows a satisfying performance, while requiring lower computational complexities compared with the existing solutions.

Chapter 7

Future works

7.1 Introduction

The research activities I have carried during the last decade have mainly focused on topics related to improving the energy efficiency of multicarrier based transceivers in presence of NL memoryless PAs. Also, I contributed to the proposal of schemes for massive MIMO transmissions including algorithms to mitigate the interferences induced by mixed numerologies, as well as the distortions introduced by RF PAs. Most of these studies considered 5G and beyond 5G systems and scenarios.

Now that the first releases of 3GPP on 5G have been published and that the deployment of this technology is progressing almost everywhere in the world, most of the researchers and operators efforts are focused on defining the issues, specifications and scenarios for 6G in the 2030 era. Several consortia, collaborative projects and scientific events have emerged since 2018, the aim of which is to imagine and harmonize the societal and technical expectations of 6G. From these initiatives we can cite:

- **Alliances:** NGMN[1] (INT), Next G Alliance[2] (US), 6G Flagship program[3] (EU),
- **Research projects:** ICT-52 Hexa-X[4], EC Smart Networks and Services partnership[5], Japan 6G program[6], 6G research in China[7] & Huawei-ZTE[8], 6G research in LGE-KAIST & Samsung-LG[9],
- **Forums, symposiums and conferences:** IWON Global forum[10], 6G Symposium[11], 6G Wireless Summit[12],

In addition to these initiatives, there is a growing number of white papers and publications:

- **White papers:** Virginia Tech [2], 6G Flagship [3], NTT DOCOMO 6G [4]...
- **Publications:** An example of the increasing number of IEEE 6G related publications is given in table 7.1.

From the preliminary studies and prospects on 6G [2, 3, 4], I summarized in Fig. 7.1 and Fig. 7.2, some expected requirements and applications for 6G wireless technologies. In addition to the higher

[1] https://www.ngmn.org/
[2] https://nextgalliance.org/
[3] https://www.oulu.fi/6gflagship/
[4] https://hexa-x.eu
[5] https://www.eurosmart.com
[6] https://www.livemint.com/technology/tech-news/move-over-5g-japan-plans-to-launch-6g-by-2030-says-report-11579590569894.html
[7] https://www.cnbc.com/2019/11/07/china-starts-6g-development-having-just-turned-on-its-5g-mobile-network.html
[8] https://www.gizchina.com/2021/02/19/huawei-and-zte-help-china-take-the-lead-in-6g-technology/
[9] http://www.koreaherald.com/view.php?ud=20190604000610
[10] https://iowngf.org/
[11] https://www.6gworld.com/6gsymposium/
[12] https://www.6gsummit.com/

	2017	2018	2019	2020	2021, June 8^{th} 2021
Conferences	18	25	138	380	167
Journals and magazines	3	9	45	211	189

Table 7.1: 6G related IEEE publications since 2017.

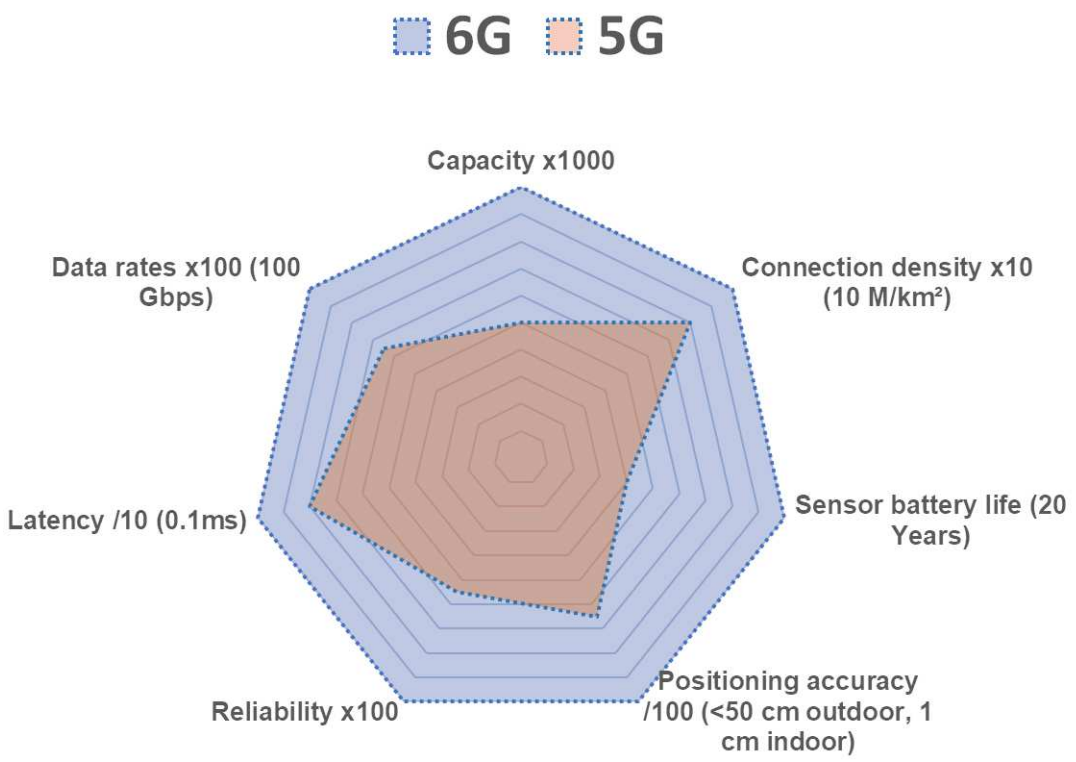

Figure 7.1: Overview on 6G requirements [2, 3, 4, 5].

requirements of 5G, new requirements that were not considered in 5G have been added and expanded more widely. Moreover, as with 5G, not all requirements need to be or can be met at the same time, but new combinations of requirements will be expected by the future new use cases.

In order to meet the new requirements of 6G, new approaches and technologies have been proposed in the literature or are being studied and developed by manufacturers or as part of collaborative research programs. Fig. 7.3 illustrates some of the 6G possible technological approaches, which are listed below:

- The extension to sub-THz and THz bands,
- A further advancement of wireless transmission technologies,
- The use of AI and ML to optimize the performance of all network elements, including the physical layer,
- The control of propagation through reconfigurable intelligent surfaces (RIS).

As perspectives of my research activities, I envision the continuation of my actual research topics, which I will extend to 6G systems whose specifications and, as seen from Fig. 7.1, will be even more demanding than those of 5G. Additionally, I intend to develop new research topics such as the introduction of Machine and Deep learning techniques to propose energy efficient transceivers which are partially or entirely based on AI and ML. Also, as another new research axis, I will be interested on RIS, which are electronically controllable for transmitting data to several users.

Fig. 7.4 summarizes the research topics that I intend to develop in the short, medium, and long term.

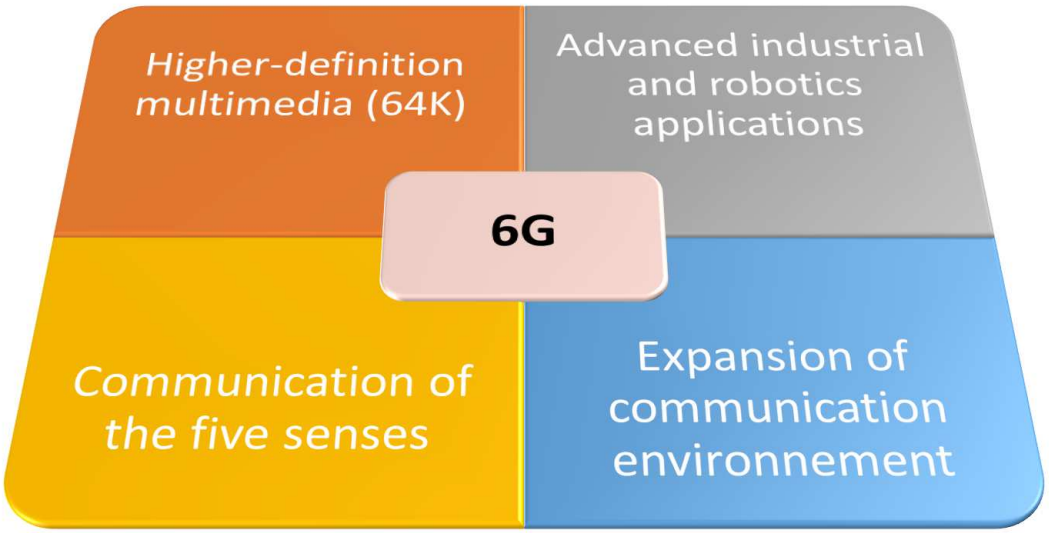

Figure 7.2: Expected 6G applications [2, 3, 4, 5].

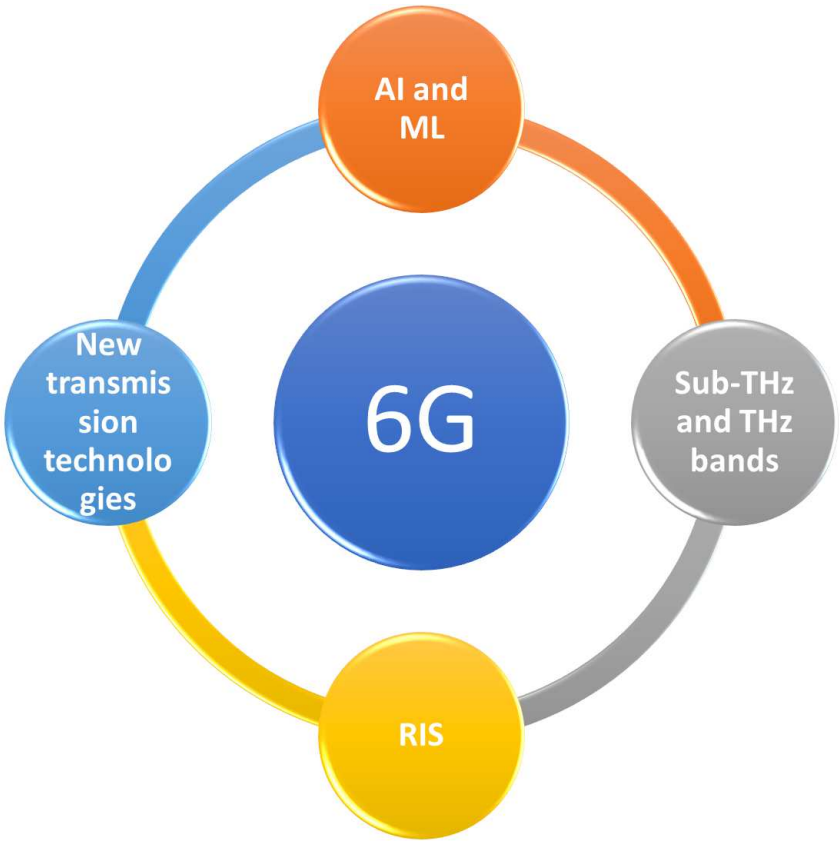

Figure 7.3: Some 6G enabling technologies.

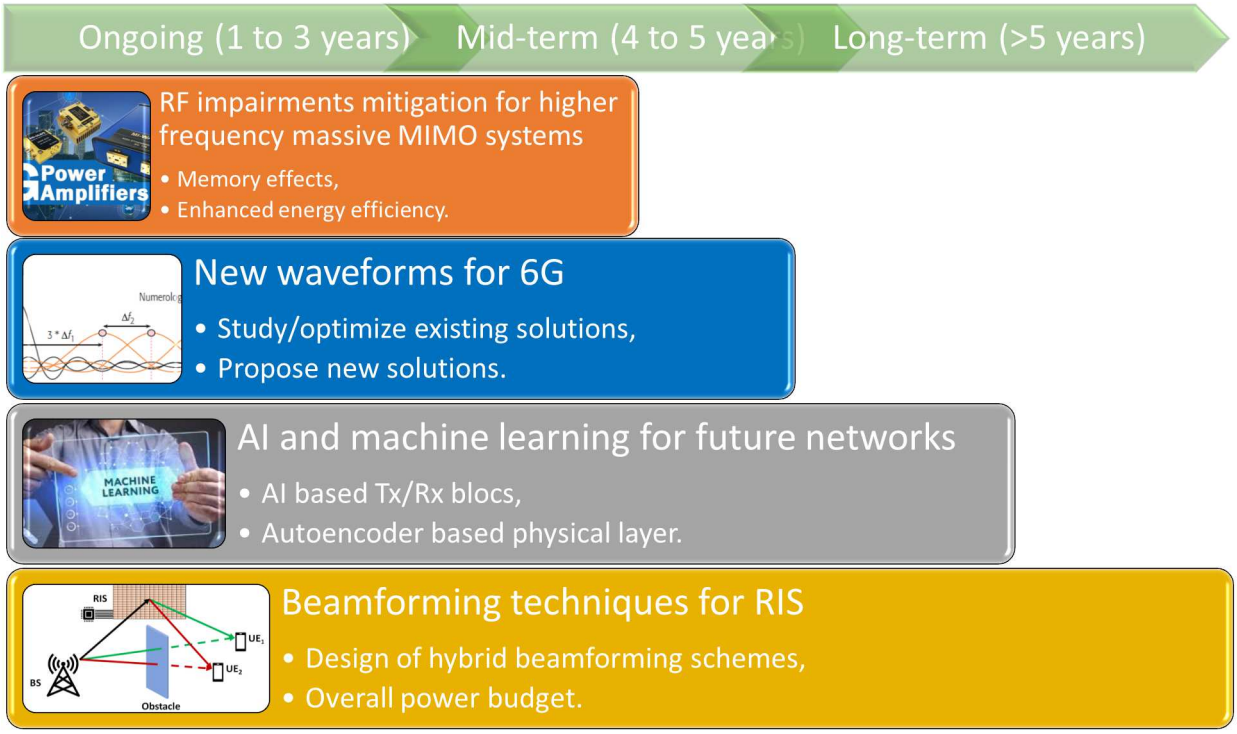

Figure 7.4: Summary of future research directions.

7.2 Mitigation of RF impairments in higher frequency massive MIMO systems

The rapid increase of connected mobile terminals in the 4G era pushed data rate requirements of 5G systems to new levels [190]. As the sub-6 GHz spectrum is congested, moving towards other ranges, such as millimeter waves (mmWaves) for 5G and beyond systems [191] as well as Sub-Tera Hertz bands [192, 193] for 6G systems, are and will be the main solutions for achieving these requirements.

In 5G NR, frequency bands up to 52.6 GHz are supported, and extension to approximately 100 GHz is examined for future releases. In addition, the U.S. Federal Communication Commission (FCC) recommends that frequencies higher than 5G allocated frequencies, such as 95 GHz to 3 THz, be considered for 6G [194]. In such high frequency bands from the upper part of the millimeter wave band to the Tera Hertz band, a remarkably wide frequency bandwidth can be utilized and is under investigation[13] to achieve extreme high data rates exceeding 100 $Gbps$ [4].

The use of higher frequency bands, as those shown by Fig. 7.5, is quite regulated and is mostly available, allowing for mobile communication systems to operate on large bandwidths. However, the propagation characteristics on this elevated frequency ranges poses many engineering challenges. Indeed, according to Friis' Law, the isotropic path loss in free-space propagation is inversely proportional to the wavelength squared and implies that path loss at higher frequency ranges is more severe than in lower ones. Nevertheless, the antenna directional gain is also inversely proportional to the wavelength squared, and, thus, employing an array of highly directional antennas more than compensates for the free-space path loss [195]. In 5G related studies, such technology has been referred to as mmWave massive MIMO [196].

Massive MIMO and high frequency bands are two attractive ideas considered to fulfil the high capacity demands of 5G and 6G communication systems. Although these technologies allow huge capacity gains, the RF transceivers employed in these frequency ranges induce several hardware impairments as noise

[13] http://www.brave-beyond5g.com/

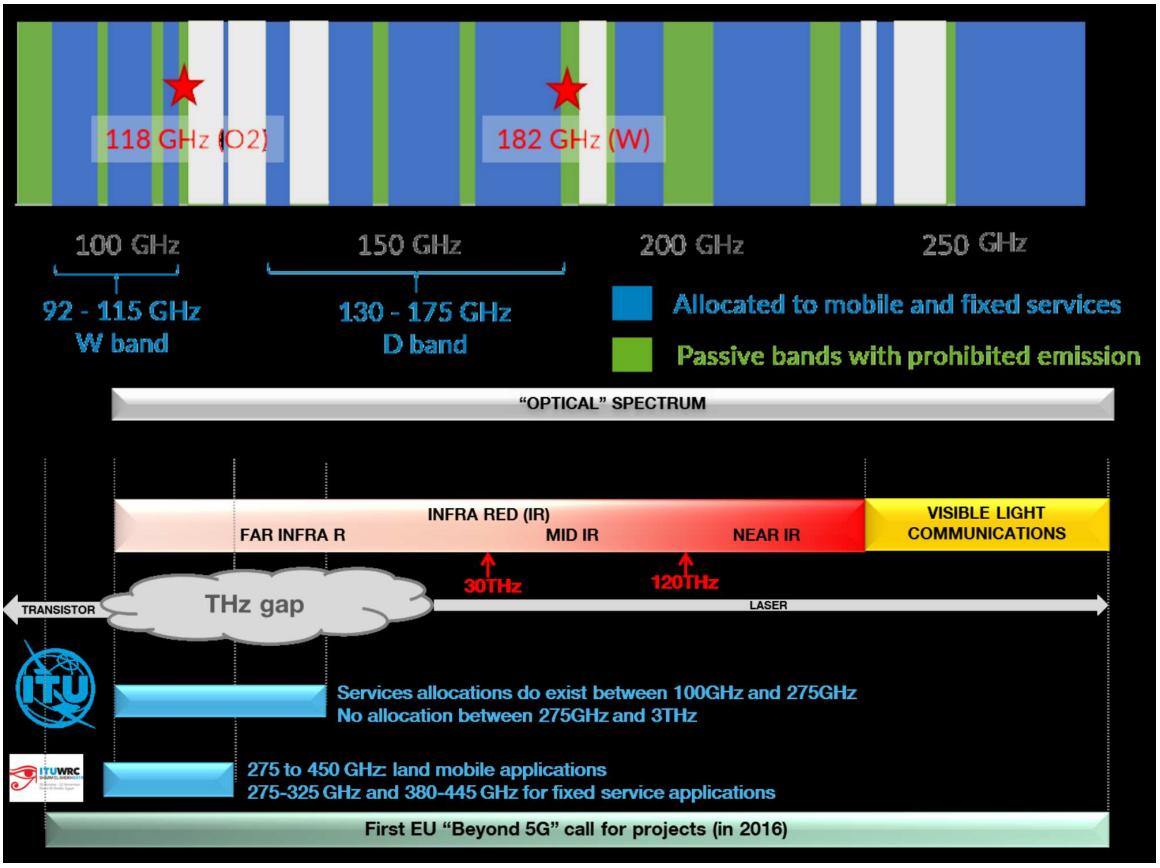

Figure 7.5: Sub-THz[14] and THz spectrum [5].

quantization (due to low resolution DAC/ADC converters [197]), nonlinear PA [198], phase noise [199] and IQ imbalance [200]. All these RF impairments lead to a strong nonlinear distortion in the transmitted signal. From these technological challenges, and as a mid term research activity, I plan to work on the following topics:

- **Impact of the memory effects of power amplifiers:** Given the large bandwidths involved in mmWaves, sub-THz and THz communications (500 MHz [201] in mmWaves bands and up to several GHz for sub-THz and THz links), the memory effects of power amplifiers can no more be neglected [202]. These effects must be considered when studying the In-band and Out-Off-Band distortions. For spectral regrowth analysis, Zhou et. al proposed in [63] theoretical analysis of the spectral regrowth induced by PA models which are based on polynomial models with memory. However, to the best of my knowledge, few contributions are made for theoretically characterizing the In-band distortions in presence of memory effects and over frequency selective channels. I aim to investigate this axis, based on some existing studies generalizing the application of Bussgang's theorem to power amplifiers exhibiting memory effects [203],

- **Improvement of the energy efficiency of transmitters/receivers:** With the rise in frequency, the envisaged waveform wavelengths are more and more smaller, where we move from 10 cm for communications at 3 GHz, to respectively 10 mm and 5 mm, for communications around 30 GHz and 60 GHz. For these wavelengths, the validity of some approaches proposed to improve the energy efficiency of power amplifiers such as LINC method or IDP becomes questionable. Indeed. for IDP method, that we have developed as part of the Khaled Tahkoubit's PhD [85], it should be interesting to investigate the problem related to the combination of amplified millimeter wave signals. On the other hand, I plan to study the interest of using IDP method in a massive MIMO context, where

significant improvement is expected in terms of energy efficiency compared to classical or LINC based schemes.

7.3 Waveform study and design for 6G communications

CP-OFDM has been selected as the reference waveform in the 4^{th} generation of wireless communication systems. This MWF has been recently confirmed, in the 15^{th} 3GPP release, to be the waveform for 5G NR. As explained in chapter 6, the main novelty in 5G NR is the association of CP-OFDM to different numerologies to addresses several users' requirements/scenarios in terms of data rates, latencies and mobilities. Indeed, 5G will address three different services named as: (1) eMBB, with data rates reaching 100 $Mbps$, (2) URLLC, with End-to-End latency lower than 1 ms and (3) mMTC, also named as Internet of Things (IoT). The increased heterogeneity of applications envisaged in beyond 5G generations, bring up to date the need to study and design advanced MWFs compared to CP-OFDM.

The waveform for 6G wireless systems should be flexible and compliant with any required bandwidth for both sub 6 GHz and higher frequency carriers. This MWF should cope with the time/frequency channels selectivities, be spectral efficient, exhibit reduced complexity and latency, be robust against time and frequency asynchronous access and present limited PAPR, enhancing so the energy efficiency of the whole transceiver. Different waveforms have been proposed in the last decades to partially reach those requirements. In addition to those presented in chapter 3, we can cite faster than Nyquist (FTN) signaling [204], Orthogonal Time Frequency Space (OTFS) [205] and Lagrange Vandermonde Division Multiplexing (LVDM) [206] to name a few. FTN, is a non-orthogonal waveform that was firstly proposed by Mazo in 1975. This MWF achieves better spectrum efficiency by increasing the symbol transmission rate faster than Nyquist limit in time domain, so higher SE can be achieved compared with classical Nyquist signaling MWFs. Regarding OTFS modulation, it has been introduced to cope with high mobility scenarios. When it turns to LVDM, this modulation generalizes ZP-OFDM while guaranteeing a perfect recovery of the transmitted complex data symbols. I plan to work on 6G MWFs, through the following directions:

Design of new waveforms. Firstly, I will continue working on the design of new waveforms satisfying flexibility (bandwidth, MIMO compatibility), high users densities, asynchronous communications, low complexity/low latency and reduced PAPR. The proposed MWFs will be compared to CP-OFDM based on several key performance indicator (KPI). The considered KPIs that will be considered are: the spectrum efficiency, the PAPR, the MIMO compatibility, the robustness to asynchronism and the overall complexity. Along with this activity, I will consider precoded filtered multicarrier schemes obtained from FFT-FBMC and BF-OFDM to reduce the PAPR while keeping the good time-frequency localization,

Study of a FTN signaling approach. Secondly, in regard to the radio access technology almost reaching the Nyquist limit in the OFDM-based technology, FTN signaling, which compresses and transmits signals non-orthogonally using a sampling rate faster than the Nyquist limit, is more and more studied. In [207], it has been shown that FTN based MWF may provide benefits in terms of PAPR reduction. As an envisaged research direction, I will investigate new PAPR reduction techniques for FTN MWF,

Optimization of existing waveforms. Thirdly, I will focus on the optimization of existing waveforms to enhance their capabilities based on the KPI defined previously. This optimization will also benefit from major advances in the field of artificial intelligence. I plan to apply advanced deep learning techniques, as well as new approaches such as reinforcement learning to optimize existing waveforms in terms of latency, PAPR... Within this task, I will also concentrate on the so-called LVDM [206] to improve its robustness in asynchronous communication scenarios. Another possible contribution could also the be proposal of advanced receivers (equalization/detection) for non-orthogonal waveforms such as FTN, FBMC-QAM and GFDM in the context of high/very high 6G mobility scenarios.

7.4 Deep learning for energy efficient future communication systems

Meeting all the challenging 6G requirements identified in section 7.1 requires a hyper-flexible network with configurable radios. In most of the prospective studies for 6G [2, 3, 4], it is proposed that AI and machine learning (ML) will be used in concert with radio sensing and positioning to learn about the static and dynamic components of the radio environment. This will be used to predict link loss events at high frequencies, to proactively decide on optimal handover instances in dense city networks and to determine optimal radio resource allocations for base stations and users.

An important question is whether AI could be used to design optimal air interfaces on the fly for a given environment and set of specific requirements. This suggests AI inspired air interfaces. However, their true performance, in particular, power and energy efficiency in real use cases is an open research problem. Indeed, existing communication systems exhibit inherent limitations in translating theory to practice when handling the complexity of optimization for emerging wireless applications with high degrees of freedom. Deep learning has a strong potential to overcome this challenge via data-driven solutions and it can improve the performance of wireless systems. As a third research perspective, I will investigate deep learning approaches to enhance the energy efficiency of future communication systems. The envisaged research topics are presented in the following:

- **AI-based pre-encoder integrating pre-distortion and PAPR reduction:** As part of Xinying Cheng's thesis, we proposed algorithms for OFDM massive MIMO context, to achieve joint multiuser pre-encoding with PAPR reduction and digital pre-distortion. These purely algorithmic solutions can present significant implementation complexities. As a short-term perspective, we have started working on solutions based on deep learning and Meta learning approaches, to reduce the complexity of the joint precoding stage integrating Multi-User Interference (MUI) cancellation along with RF impairments mitigation. An interesting idea to reach this objective is to design a meta learning neural network [208], which allows a reduced complexity and complements standard machine learning approaches. The goal is to create a meta-learning model that can be extended to a new configuration that was never learnt during the learning process. We propose to employ two neural networks. The first one, the NN Precoder, creates a precoded data vector, for a certain channel configuration, to compensate the PA nonlinearities or other hardware imperfection. The weights of the NN-Precoder associated to a channel configuration are generated by the second NN, the Meta-NN, which may be extended to any channel configuration. By doing so, we eliminate the NN Precoder's adaption and the associated computing complexity when the channel changes.

- **Communication chain based on auto-encoders:** Recent studies have shown the possibility of interpreting a communication system as an auto-encoder [209]. This approach makes it possible to develop a new way of thinking the design of the communication system as an end-to-end reconstruction task which seeks to jointly optimize the various functions of the transmitter and the receiver in a single process. An auto-encoder can therefore be seen as a neural network used for encoding and decoding a series of data. The simplest form of an auto-encoder is a multi-layered perceptron-based neural network. As shown in Fig. 7.6, the architecture is composed by an input layer, several hidden layers, and an output layer, which has the same number of nodes as the input layer. The aim is to reconstruct, at the output, the series of data presented at the input. Beyond the work published in the literature, few contributions have been made for energy efficiency purposes [210]. We started investigating these aspects as part of Meryem Benosamn's PhD and also as part of a master internship, which I am currently supervising. As a first result of this internship, we proposed an improvement of the classical autoencoder offering Gray coding capabilities and showing better BER performance than the classical M-QAM configuration. The proposed autoencoder architecture is given by Fig. 7.6. This architecture is a modified version of the autoencoder model proposed in [209] by adding pre and post-processing layers in order to map constellation points on a Gray like map, while modifying the learning loss from categorical cross-entropy to binary cross-entropy. I intend to continue this activity in the short and mid term by taking into account the PA induced RF impairments.

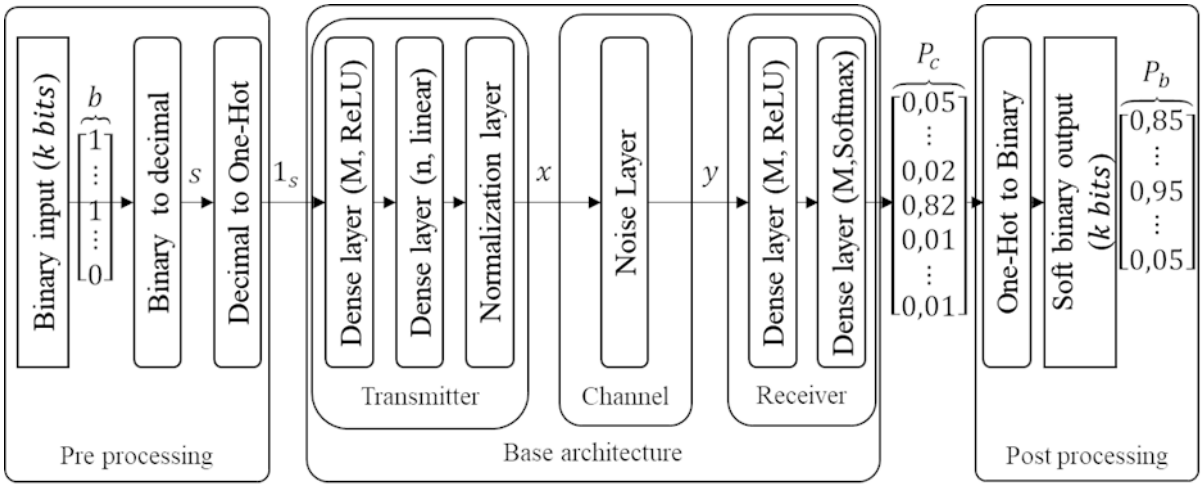

Figure 7.6: A communications system over an AWGN channel represented as an autoencoder.

7.5 Beamforming techniques for reconfigurable intelligent surfaces (RIS)

Beamforming architectures for mmWaves in massive MIMO settings are a key technology for 5G [211]. On the other hand, reconfigurable intelligent surfaces (or RIS for Reconfigurable Intelligent Surface) using reflect and transmit arrays are envisioned as low energy consumption architectures to meet future high speed communication systems [212]. This technology will allow to concentrate energy in certain directions of space, to achieve very high data rates with better energy efficiency. Compared to conventional planar antenna arrays, the radiation pattern is adjusted by activating the meta-surface diode grid, as depicted by Fig. 7.7.

Driven by a revolution in electromagnetically tunable surfaces (e.g., based on metamaterials), 6G technology plan to control signal reflections and refractions by using RIS. Open research problems range from the optimized deployment of passive reflectors and metamaterial-coated smart surfaces to AI-powered operation of reconfigurable RIS[15]. As a first step of studies, fundamental analysis to understand the performance of RIS and smart surfaces, in terms of the rate, latency, reliability, and coverage is required. Another important research direction is environmental AI whereby smart surfaces learn and autonomously reconfigure their material parameters. Challenges include how to focus signals with different angles of incidence in large metamaterial surfaces, requiring controllability of reflection/refraction coefficients. ML-driven smart surfaces in mobile environments may require continuous retraining, in which the access to sufficient training data, high computational capabilities, and guaranteed low training convergence are needed. Holographic radio could be made possible with 6G by using RIS and similar structures [3]. Holographic RF allows the control of the entire physical space and the full closed loop of the electromagnetic field through spatial spectral holography and spatial wave field synthesis.

In 2020, CNAM, Orange, CEA-Leti, IEMN and INSA-IETR have won a national ANR research project which started in February 2021. This project is entitled MESANGES for Metasurface-based Electronically Steerable Antenna arrays for Next Generation EHF Systems. This project will investigate and implement two main types of metasurfaces based systems: reflectarrays [213] and transmitarrays [214]. Reflect and transmitarray antennas, thanks to the spatial feeding mechanism and the possibility to integrate tunable device to control the aperture phase distribution, are an extremely attractive technology for the future high-performance and smart communication networks operating up to sub-THz frequencies. As stated previously, reflect- or a transmitarray is composed of a focal system illuminating a planar or conformal array of elements also called unit-cells. PIN diodes or other technologies of RF switches are integrated on the unit-cells to implement beamforming functions. Both structures are used generally to

[15] https://5g-ppp.eu/rise-6g/

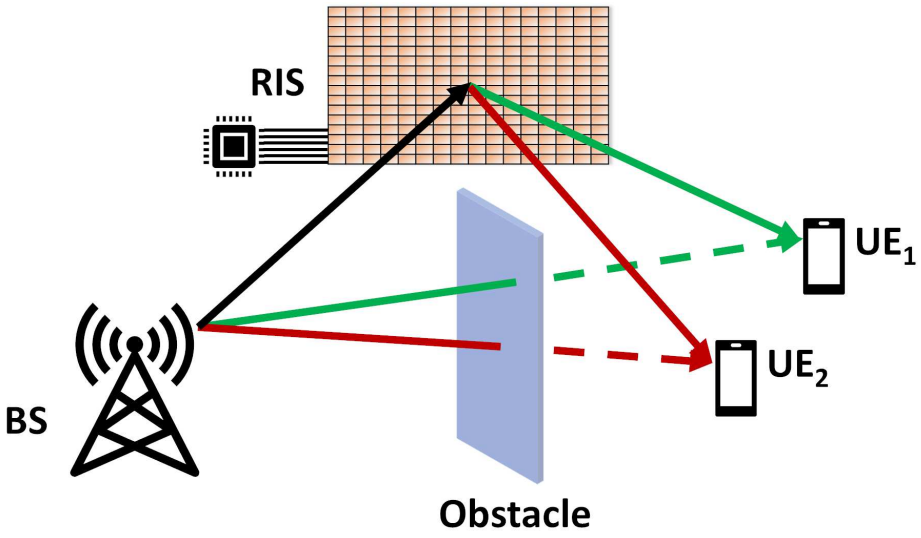

Figure 7.7: Typical RIS based communication scenario.

deviate and to focus beams on desired directions or generate shaped patterns and multi beams. The main difference between the two solutions is that, in the case of reflectarrays, the electromagnetic wave does not pass through the surface as for transmitarrays, but it is reflected onto it. In both cases challenges will lie in the design of the surface's elements for mmWaves and sub-THz bands, then on the control of the numerous PIN diodes connected. Optimization algorithms are thus necessary to efficiently create beams towards the desired direction.

As part of this ANR project, I will focus on the design of hybrid beamforming schemes applied to both reflectarrays and transmitarrays. The main difference with respect to classical massive MIMO is that only one or few sources are active and that the radiation pattern diagram for both reflectarray and transmitarray is adjusted by the activation of the grid of diodes of the metasurface [215]. Another open issue is the beam management and the limited exchange of information between the receivers and the source. I envision the study of different approaches for beam management. A first approach could be to perform two or more phases (large beams and then beam refinement) [216]. Another solution is to exploit the time/space sparsity of the channel in mmWaves and see the beam management problem as a sparse signal recovery problem. The problem can be solved using compressed sensing based algorithms where only the strongest channel coefficients are fed back to the transmitter in order to compute a precoding matrix and select the grid of diodes of the metasurface.

7.6 Conclusion

This chapter concludes my "Habilitation à diriger les Recherches" (HDR) thesis. In this chapter, I have presented the main research perspectives in the short, medium, and long term. These perspectives are centered around four topics, the first two being a continuation of the activities carried out over the last years. These topics will focus on the analysis/synthesis of waveforms for 6G systems, as well as the proposal of solutions to improve the energy efficiency of transmitters/receivers in mmWaves, sub-THz and THz bands in the presence of power amplifiers and/or other dirty RF phenomenon. As a third topic of my future research, I will investigate techniques based on machine learning to improve the energy efficiency of transceivers when interpreting the communication system as an auto-encoder. Least but not last, I plan to develop, over the next four-five years, a new research direction on Reconfigurable Intelligent Surfaces (RIS). Specifically, I will focus on the beamforming algorithms for the steering of the transmit and reflect arrays for both single and multi-user scenarios. We are currently in the process of recruiting a PhD student who will work on this topic.

Bibliography

[1] Z. Chen, K. Li, K. Jin, C. Huang, P. Li, and L. Geng. A 2.6 GHz Class-AB GaN Power Amplifier with Maximum Output Power of 56 W Achieving 70% Power Added Efficiency. In *2018 1st Workshop on Wide Bandgap Power Devices and Applications in Asia (WiPDA Asia)*, pages 328–331, 2018. (Cited on pages 8 and 118.)

[2] W. Saad, M. Bennis, and M. Chen. A Vision of 6G Wireless Systems: Applications, Trends, Technologies, and Open Research Problems. *IEEE Network*, 34(3):134–142, 2020. (Cited on pages 8, 143, 144, 145 and 149.)

[3] P. Ahokangas, J. Van De Beek, H. Alves, and M. Bennis. Key drivers and research challenges for 6G ubiquitous wireless intelligence. *White paper*, 2019. (Cited on pages 8, 143, 144, 145, 149 and 150.)

[4] INC. NTT DOCOMO. 5G Evolution and 6G. *White paper*, 2020. (Cited on pages 8, 143, 144, 145, 146 and 149.)

[5] E. Hardouin. 6G overview. Technical report, Orange, 2021. (Cited on pages 8, 144, 145 and 147.)

[6] ETSI TS 100 292-2. Terrestrial trunked radio (TETRA); Voice plus Data (V+D); Part 2: Air interface (AI). Technical report. (Cited on pages 9, 109 and 110.)

[7] B. Debail and H. Shaiek. Radiated sound field analysis of loudspeaker systems: discrete geometrical distribution of circular membranes versus co-incident annular rings. In *Proceedings of the* 119^{th} *convention of the Audio Engineering Society*, October 2006. (Cited on page 44.)

[8] H. Shaiek, B. Debail, and J. M. Boucher. Activation signal filtering device for e.g. professional listening system, has digital filtering unit with channel separation unit under constraint, where separation unit has separator filters covering frequency band between channels. Technical report, Cabasse, May 2006. Patent n° FR20060004533. (Cited on page 45.)

[9] H. Shaiek, B. Debail, Y. Kerneis, J. M. Boucher, and P. Y. Diquelou. Enhanced control of sound field radiated by co-axial loudspeaker systems using digital signal processing techniques. In *Proceedings of the* 120^{th} *convention of the Audio Engineering Society*, May 2006. (Cited on page 45.)

[10] H. Shaiek and J. M. Boucher. Optimizing the Directivity of Multiway Loudspeaker Systems. *EURASIP Journal on Audio, Speech, and Music Processing*, pages 1–10, 2010. (Cited on page 45.)

[11] S. A. White. Design of a biquadratic peaking or notch filter for audio equalization. *JAES*, 34(6):479–483, June 1986. (Cited on page 45.)

[12] G. Ndo, H. Shaiek, M. Jaidane, and J. M. Boucher. An hybrid approach of low frequency room equalization: Notch filters based on common acoustical pole modeling. In *2007 15th European Signal Processing Conference*, pages 1600–1604, 2007. (Cited on page 47.)

[13] K. Lakhdhar, M. Jaidane, H. Shaiek, and J. M. Boucher. Iterative equalization of room transfer function using biquadratic filters. In *2009 IEEE Instrumentation and Measurement Technology Conference*, pages 1463–1466, 2009. (Cited on page 47.)

[14] H. Shaiek, J. M. Boucher, B. Debail, and Y. Kerneis. Design and real-time implementation of a digital filter bank dedicated to co-axial loudspeaker systems. In *IEEE 3rd ISIVC*, September 2006. (Cited on page 47.)

[15] H. Shaiek, B. Debail, Y. Kerneis, J. M. Boucher, and P. Y. Diquelou. An optimized full-bandwidth 20Hz-20kHz digitally controlled co-axial source. In *Proceedings of the* 121^{th} *convention of the Audio Engineering Society*, October 2006. (Cited on page 47.)

[16] D. Kerneis P. Y. Diquelou and H. Shaiek. Method for developing correction filters for correcting the acoustic modes of a room. Technical report, Canon, October 2012. Patent n° WO2012045927. (Cited on page 48.)

[17] E. Dahlman, G. Mildh, S. Parkvall, J. Peisa, J. Sachs, Y. Selén, and J. Sköld. 5G wireless access: requirements and realization. *IEEE Communications Magazine*, 52(12):42–47, 2014. (Cited on pages 48 and 56.)

[18] Research Brief. Exponential data growth - constant ict footprints. Technical report, Ericson white paper, June 2019. (Cited on page 49.)

[19] S. G. Andrae. Total consumer power consumption forecast. Technical report, Nordic Digital Business Summit, October 2017. (Cited on pages 49 and 56.)

[20] W. Vereecken, W. V. Heddeghem, M. Deruyck, B. Puype, B. Lannoo, W. Joseph, D. Colle, L. Martens, and P. Demeester. Power consumption in telecommunication networks: overview and reduction strategies. *IEEE Communications Magazine*, 49(6):62–69, 2011. (Cited on page 49.)

[21] M. Jens and L. Dag. The Energy and Carbon Footprint of the Global ICT and E&M Sectors 2010–2015. *Sustainability*, 10(9), 2018. (Cited on pages 49 and 56.)

[22] 3GPP TR 38.802. Technical Specification Group Radio Access Network; Study on New Radio (NR) access technology. Technical report, 3GPP, 2017. (Cited on pages 50 and 60.)

[23] 3GPP TSG RAN WG1. Numerology requirements. Technical report, 3GPP, April 2016. (Cited on pages 50, 60, 78 and 123.)

[24] Y. Medjahdi, M. Terré, D. Le Ruyet, D. Roviras, and A. Dziri. Performance analysis in the downlink of asynchronous OFDM/FBMC based multi-cellular networks. *IEEE transactions on wireless communications*, 10(8):2630–2639, 2011. (Cited on page 51.)

[25] Incorporatedn Qualcomm. R1-162199 - waveform candidates. Technical report, RG246552, June 2017. (Cited on pages 51 and 64.)

[26] V. Vakilian, T. Wild, F. Schaich, S. ten Brink, and J. F. Frigon. Universal-filtered multi-carrier technique for wireless systems beyond LTE. In *Proc. IEEE Globecom Workshops (GC Wkshps)*, pages 223–228, Dec 2013. (Cited on pages 51 and 65.)

[27] J. Abdoli, M. Jia, and J. Ma. Filtered OFDM: A new waveform for future wireless systems. In *Proc. IEEE 16th International Workshop on Signal Processing Advances in Wireless Communications (SPAWC)*, pages 66–70, June 2015. (Cited on page 51.)

[28] J. Van de Beek and F. Berggren. N-continuous OFDM. *IEEE Communications Letters*, 13(1):1–3, January 2009. (Cited on pages 51 and 65.)

[29] G. Cherubini, E. Eleftheriou, S. Oker, and J. M. Cioffi. Filter bank modulation techniques for very high speed digital subscriber lines. *IEEE Communications Magazine*, 38(5):98–104, May 2000. (Cited on pages 51 and 65.)

[30] M. Bellanger, D. Le Ruyet, D. Roviras, M. Terré, J. Nossek, L. Baltar, Q. Bai, D. Waldhauser, M. Renfors, and T. Ihalainen. FBMC physical layer: a primer. *PHYDYAS, January*, 2010. (Cited on pages 51 and 68.)

[31] M. Bellanger, D. Mattera, and M. Tanda. Lapped-OFDM as an alternative to CP-OFDM for 5G asynchronous access and cognitive radio. In *Proc. IEEE Vehicular Technology Conference (VTC Spring)*, pages 1–5. IEEE, 2015. (Cited on pages 51 and 66.)

[32] H. Lin and P. Siohan. Multi-carrier modulation analysis and WCP-COQAM proposal. *EURASIP Journal on Advances in Signal Processing*, 2014(1):1, 2014. (Cited on pages 51, 52 and 67.)

[33] M. J. Abdoli, M. Jia, and J. Ma. Weighted circularly convolved filtering in OFDM/OQAM. In *Proc. IEEE 24th Annual International Symposium on Personal, Indoor, and Mobile Radio Communications (PIMRC)*, pages 657–661, Sept 2013. (Cited on pages 51 and 67.)

[34] Y. Yun, C. Kim, K. Kim, Z. Ho, B. Lee, and J. Y. Seol. A new waveform enabling enhanced QAM-FBMC systems. In *Proc. IEEE 16th International Workshop on Signal Processing Advances in Wireless Communications (SPAWC)*, pages 116–120. IEEE, 2015. (Cited on pages 51 and 68.)

[35] G. Fettweis, M. Krondorf, and S. Bittner. GFDM - generalized frequency division multiplexing. In *Proc. IEEE 69th Vehicular Technology Conference (VTC)*, pages 1–4, April 2009. (Cited on pages 52 and 68.)

[36] R. Zakaria and D. Le Ruyet. A novel filter-bank multicarrier scheme to mitigate the intrinsic interference: Application to MIMO systems. *IEEE Transactions on Wireless Communications*, 11(3):1112 –1123, march 2012. (Cited on pages 52 and 67.)

[37] R. Gerzaguet, N. Bartzoudis, L. Baltar, V. Berg, J. B. Doré, D. Kténas, O. Font-Bach, X. Mestre, M. Payaró, M. Färber, and K. Roth. The 5G candidate waveform race: a comparison of complexity and performance. *EURASIP Journal on Wireless Communications and Networking*, 2017(1):13, 2017. (Cited on pages 52 and 68.)

[38] R. Zayani, Y. Medjahdi, H. Shaiek, and D. Roviras. WOLA-OFDM: A potential candidate for asynchronous 5G. In *2016 IEEE Globecom Workshops (GC Wkshps)*, pages 1–5, 2016. (Cited on pages 52, 65 and 67.)

[39] Y. Medjahdi, R. Zayani, H. Shaïek, and D. Roviras. WOLA processing: A useful tool for windowed waveforms in 5G with relaxed synchronicity. In *2017 IEEE International Conference on Communications Workshops (ICC Workshops)*, pages 393–398, 2017. (Cited on page 52.)

[40] Y. Medjahdi, S. Traverso, R. Gerzaguet, H. Shaïek, R. Zayani, D. Demmer, R. Zakaria, J. Doré, M. Ben Mabrouk, D. Le Ruyet, Y. Louët, and D. Roviras. On the road to 5G: Comparative study of physical layer in MTC context. *IEEE Access*, 5:26556–26581, 2017. (Cited on pages 52, 55, 69 and 111.)

[41] J. Medbo and P. Schramm. Channel models for hiperlan/2 in different indoor scenarios. Technical report, ETSI EP BRAN 3ERIO85B, March 1998. (Cited on page 53.)

[42] Y. Medjahdi, Y. Louet, M. B. Mabrouk, D. Roviras, R. Zakaria, H. Shaiek, D. L. Ruyet, S. Traverso, R. Gerzaguet, D. Demmer, J. Dore, and R. Zayani. Impact of selective channels on post-OFDM waveforms for 5G machine type communications. In *2018 15th International Symposium on Wireless Communication Systems (ISWCS)*, pages 1–5, 2018. (Cited on pages 53 and 69.)

[43] Y. Medjahdi, M. Terre, D. Le Ruyet, D. Roviras, J. A. Nossek, and L. Baltar. Inter-cell interference analysis for ofdm/fbmc systems. In *2009 IEEE 10th Workshop on Signal Processing Advances in Wireless Communications*, pages 598–602, 2009. (Cited on page 53.)

[44] R. Chauvat. Etude de liaisons SISO, SIMO, MISO et MIMO à base de formes d'ondes FBMC-OQAM et de récepteurs Widely Linear. Technical report, PhD Thesis, CNAM, March 2017. (Cited on pages 53, 77 and 80.)

[45] H. Fhima, R. Zayani, H. Shaiek, D. Roviras, B. S. Cheng, and R Bouallegue. Comparison of Linear, Widely Linear and Fresh equalizers for FBMC-OQAM Systems with different numerologies. *Wireless Pers Commun*, June 2020. (Cited on page 53.)

[46] H. Fhima, R. Zayani, H. Shaïek, D. Roviras, B. S. Chang, and R. Bouallegue. Widely linear equalizer performance with multiple independent interferences. In *2017 IEEE Symposium on Computers and Communications (ISCC)*, pages 912–917, 2017. (Cited on page 53.)

[47] B. S. Chang, C. A. F. da Rocha, H. Fhima, R. Zayani, H. Shaiek, and D. Roviras. On the performance of a widely linear SC-FDE system under multiple independent interferences. In *2017 IEEE 28th Annual International Symposium on Personal, Indoor, and Mobile Radio Communications (PIMRC)*, pages 1–5, 2017. (Cited on page 53.)

[48] H. Fhima, B. S. Chang, R. Zayani, H. Shaiek, D. Roviras, and R. Bouallegue. Performance of Linear and Widely Linear equalizers for FBMC/OQAM modulation. In *2018 25th International Conference on Telecommunications (ICT)*, pages 605–609, 2018. (Cited on page 53.)

[49] H. Fhima, H. Shaïek, R. Zayani, D. Roviras, B. S. Chang, and R. Bouallegue. Analysis of Widely Linear equalization over frequency selective channels with multiple interferences. In *2018 14th International Conference on Wireless and Mobile Computing, Networking and Communications (WiMob)*, pages 83–88, 2018. (Cited on page 53.)

[50] J. Bussgang. Crosscorrelation functions of amplitude-distorted gaussian signals. Technical report, Cambridge: Research laboratory of electronics, Massachusetts Institute of Technology, 1952. (Cited on page 55.)

[51] H. Bouhadda, H. Shaiek, Y. Medjahdi, D. Roviras, R. Zayani, and R. Bouallegue. Sensitivity analysis of FBMC signals to non linear phase distortion. In *2014 IEEE International Conference on Communications Workshops (ICC)*, pages 73–78, 2014. (Cited on pages 55 and 66.)

[52] D. Dardari, V. Tralli, and A. Vaccari. A theoretical characterization of nonlinear distortion effects in ofdm systems. *IEEE Transactions on Communications*, 48(10):1755–1764, 2000. (Cited on page 55.)

[53] H. Bouhadda, H. Shaiek, D. Roviras, R. Zayani, Y. Medjahdi, and R. Bouallegue. Theoretical analysis of BER performance of non-linearly amplified FBMC/OQAM and OFDM signals. *EURASIP Journal on Advances in Signal Processing*, pages 1–16, 2016. (Cited on pages 55 and 90.)

[54] R. Zayani, H. Shaïek, D. Roviras, and Y. Medjahdi. Closed-form BER expression for (QAM or OQAM)-based OFDM system with HPA nonlinearity over Rayleigh fading channel. *IEEE Wireless Communications Letters*, 4(1):38–41, 2015. (Cited on pages 55, 94 and 95.)

[55] R4-163314. Realistic power amplifier model for the new radio evaluation. In *3GPP TSG-RAN WG4 Meeting No. 79*. 3GPP, 2016. (Cited on pages 55 and 92.)

[56] R4-163314 3GPP TSG-RAN WG4 Meeting No. 79. Realistic power amplifier model for the new radio evaluation. Technical report, 3GPP, May 2016. (Cited on page 55.)

[57] H. Shaiek, D. Roviras, Y. Medjahdi, R. Zayani, M. Ben Mabrouk, and Y. Louet. Performance of the candidate waveforms in the presence of power amplifier. Technical report, WONG5 Document Number D3.1, April 2017. (Cited on page 55.)

[58] H. Shaiek, R. Zayani, Y. Medjahdi, and D. Roviras. Analytical analysis of SER for beyond 5G post-OFDM waveforms in presence of high-power amplifiers. *IEEE Access*, 7:29441–29452, January 2019. (Cited on pages 55, 93 and 136.)

[59] J. Stern, J. de Barbeyrac, and R. Poggi. *Méthodes pratiques d'étude des fonctions aléatoires*. Editions Dunod, 1967. (Cited on page 55.)

[60] C. L. Nikias and A. P. Petropulu. *Higher-order spectral analysis*. Englewood Cliffs, NJ: Prentice-Hall, 1993. (Cited on pages 55 and 56.)

[61] M. Khodjet-Kesba, C. Saber, D. Roviras, and Y. Medjahdi. Multicarrier interference evaluation with jointly non-linear amplification and timing errors. In *2011 IEEE 73rd Vehicular Technology Conference (VTC Spring)*, pages 1–5, 2011. (Cited on page 55.)

[62] S. Sall, H. Shaiek, D. Roviras, and Y. Medjahdi. Analysis of the nonlinear spectral re-growth in FBMC systems for cognitive radio context. In *ISWCS 2013; The Tenth International Symposium on Wireless Communication Systems*, pages 1–5, 2013. (Cited on pages 56, 96 and 97.)

[63] G. T. Zhou and R. Raich. Spectral analysis of polynomial nonlinearity with applications to RF power amplifiers. *EURASIP Journal on Applied Signal Processing*, 2004(256395):1931–1840, 2004. (Cited on pages 56, 89 and 147.)

[64] K. Bulusu, H. Shaiek, and D. Roviras. Prediction of spectral regrowth for FBMC-OQAM system using cumulants. In *2014 IEEE 10th International Conference on Wireless and Mobile Computing, Networking and Communications (WiMob)*, pages 402–406, 2014. (Cited on pages 56, 96 and 132.)

[65] M. Brandon. Joint optimization of linearization methods at the transmitter for multi-carrier modulations. Technical report, PhD Thesis, ETIS, Cergy Pontoise University, October 2012. (Cited on page 56.)

[66] K. Bulusu, H. Shaiek, D. Roviras, and R. Zayani. Reduction of PAPR for FBMC-OQAM systems using dispersive SLM technique. In *2014 11th International Symposium on Wireless Communications Systems (ISWCS)*, pages 568–572, 2014. (Cited on pages 57 and 103.)

[67] K. Bulusu, M. Renfors, J. Yli-Kaakinen, H. Shaiek, and D. Roviras. Enhanced multicarrier techniques for narrowband and broadband PMR coexistence. *Transactions on Emerging Telecommunications Technologies*, pages 1–14, 2016. (Cited on pages 58 and 110.)

[68] K. Bulusu, H. Shaiek, and D. Roviras. Potency of trellis-based SLM over symbol-by-symbol approach in reducing PAPR for FBMC-OQAM signals. In *2015 IEEE International Conference on Communications (ICC)*, pages 4757–4762, 2015. (Cited on pages 58, 104 and 132.)

[69] K. Bulusu, H. Shaiek, and D. Roviras. Reduction of PAPR of FBMC-OQAM systems by dispersive tone reservation technique. In *2015 International Symposium on Wireless Communication Systems (ISWCS)*, pages 561–565, 2015. (Cited on pages 58 and 107.)

[70] K. Bulusu, H. Shaiek, and D. Roviras. PA linearization of FBMC-OQAM signals with overlapped recursive error correcting predistortion. In *2016 International Symposium on Wireless Communication Systems (ISWCS)*, pages 533–537, 2016. (Cited on pages 58 and 109.)

[71] K. Bulusu, P. Maddila, H. Shaiek, and D. Roviras. HPA linearization for FBMC-OQAM signals with fast convergence-digital predistortion. In *2019 16th International Symposium on Wireless Communication Systems (ISWCS)*, pages 133–138, 2019. (Cited on pages 58 and 109.)

[72] K. Bulusu, H. Shaiek, and D. Roviras. HPA linearization for next generation broadcasting systems with fast convergence-digital predistortion. *IEEE Transactions on Broadcasting*, 2021. (Cited on pages 58 and 109.)

[73] Y. Medjahdi, D. Le Ruyet, F. Bader, and L. Martinod. Integrating LTE broadband system in PMR band: OFDM vs. FBMC coexistence capabilities and performances. In *2014 11th International Symposium on Wireless Communications Systems (ISWCS)*, pages 643–648, 2014. (Cited on pages 58, 109 and 110.)

[74] K. Bulusu, H. Shaiek, and D. Roviras. Impact of HPA non-linearity on coexistence of FBMC-OQAM systems with PMR/PPDR systems. In *2016 IEEE 83rd Vehicular Technology Conference (VTC Spring)*, pages 1–5, 2016. (Cited on pages 58 and 110.)

[75] M. Renfors, X. Mestre, E. Kofidis, and F. Bader. Contributors. In *Orthogonal Waveforms and Filter Banks for Future Communication Systems*. Academic Press. (Cited on pages 58, 77 and 102.)

[76] K. Tani, Y. Medjahdi, H. Shaiek, R. Zayani, and D. Roviras. PAPR reduction of post-OFDM waveforms contenders for 5G Beyond using SLM and TR algorithms. In *2018 25th International Conference on Telecommunications (ICT)*, pages 104–109, 2018. (Cited on pages 58 and 112.)

[77] Y. Louet, D. Roviras, A. Nafkha, H. Shaiek, and R. Zayani. Global power amplifier efficiency evaluation with PAPR reduction method for Post-OFDM waveforms. In *2018 15th International Symposium on Wireless Communication Systems (ISWCS)*, pages 1–5, 2018. (Cited on pages 58, 112 and 113.)

[78] K. Tahkoubit, A. Ali-Pacha, H. Shaiek, and D. Roviras. PAPR reduction of BF-OFDM waveform using DFT-Spread technique. In *2019 16th International Symposium on Wireless Communication Systems (ISWCS)*, pages 406–410, 2019. (Cited on page 58.)

[79] R. Zayani, H. Shaiek, C. Alexandre, A. Kielys, X. Cheng, X. Fu, and D. Roviras. A testbed for experimental performance evaluation of multicarrier waveforms in presence of RF PA. In *2018 15th International Symposium on Wireless Communication Systems (ISWCS)*, pages 1–6, 2018. (Cited on pages 59 and 117.)

[80] R. Zayani, H. Shaiek, X. Cheng, X. Fu, C. Alexandre, and D. Roviras. Experimental testbed of Post-OFDM waveforms toward future wireless networks. *IEEE Access*, 6:67665–67680, 2018. (Cited on pages 59 and 117.)

[81] O. A. Gouba and Y. Louët. A joint approach for PAPR reduction and predistortion by adding signal in cognitive radio. In *8th International Conference on Cognitive Radio Oriented Wireless Networks*, pages 220–225, 2013. (Cited on pages 59 and 113.)

[82] P. N. Landin, W. Van Moer, M. Isaksson, and P. Handel. Peak-power controlled digital predistorters for RF power amplifiers. *IEEE Transactions on Microwave Theory and Techniques*, 60(11):3582–3590, 2012. (Cited on pages 59 and 113.)

[83] R. Zayani, H. Shaiek, D. Roviras, and K. Bulusu. Method for conditioning a signal for amplification thereof, method for amplification, associated conditioning device and amplification device. Technical report, CNAM, October 2017. Patent n° PCT/FR2017/052845. (Cited on pages 59 and 114.)

[84] R. Zayani, H. Shaïek, and D. Roviras. Ping-pong joint optimization of PAPR reduction and HPA linearization in OFDM systems. *IEEE Transactions on Broadcasting*, 65(2):308–315, 2019. (Cited on pages 59 and 114.)

[85] K. Tahkoubit, A. Ali-Pacha, H. Shaiek, and D. Roviras. Iterative dichotomy PAPR reduction method for multicarrier waveforms. *IEEE Communications Letters*, 23(11):2073–2076, 2019. (Cited on pages 60, 119 and 147.)

[86] K. Tahkoubit, H. Shaiek, D. Roviras, and A. Ali-Pacha. Energy efficiency comparison of Outphasing and IDP techniques with non-linear power amplifiers. In *2020 3rd International Conference on Advanced Communication Technologies and Networking (CommNet)*, pages 1–5, 2020. (Cited on pages 60 and 121.)

[87] X. Cheng, R. Zayani, H. Shaiek, and D. Roviras. Inter-numerology interference analysis and cancellation for massive MIMO-OFDM downlink systems. *IEEE Access*, 7:177164–177176, 2019. (Cited on pages 61 and 125.)

[88] X. Cheng, R. Zayani, H. Shaiek, and D. Roviras. Analysis and Cancellation of Mixed-Numerologies Interference for Massive MIMO-OFDM UL. *IEEE wireless communications letters*, 9(4):470–474, January 2020. (Cited on pages 61, 127 and 128.)

[89] B. Saltzberg. Performance of an efficient parallel data transmission system. *IEEE Transactions on Communication Technology*, 15(6):805–811, 1967. (Cited on pages 63 and 66.)

[90] T. Wild, F. Schaich, and Y. Chen. 5G air interface design based on Universal Filtered (UF-)OFDM. In *Proc. IEEE International Conference on Digital Signal Processing (DSP)*, pages 699–704, Aug 2014. (Cited on page 65.)

[91] B. Muquet, Zhengdao Wang, G. B. Giannakis, M. de Courville, and P. Duhamel. Cyclic prefixing or zero padding for wireless multicarrier transmissions? *IEEE Transactions on Communications*, 50(12):2136–2148, Dec 2002. (Cited on page 65.)

[92] F. Schaich and T. Wild. Relaxed synchronization support of universal filtered multi-carrier including autonomous timing advance. In *Proc. IEEE 11th International Symposium on Wireless Communications Systems (ISWCS)*, pages 203–208, Aug 2014. (Cited on page 65.)

[93] Huawei HiSilicon. f-OFDM Scheme and filter design. In *R1-165425*, May 2016. (Cited on page 65.)

[94] J. van de Beek and F. Berggren. EVM-constrained OFDM precoding for reduction of out-of-band emission. In *Proc. IEEE 70th Vehicular Technology Conference Fall*, pages 1–5, Sept 2009. (Cited on page 65.)

[95] S. Traverso. A family of square-root nyquist filter with low group delay and high stopband attenuation. *IEEE Communications Letters*, 20(6):1136–1139, June 2016. (Cited on page 66.)

[96] A. Viholainen, T. Ihalainen, T. H. Stitz, M. Renfors, and M. Bellanger. Prototype filter design for filter bank based multicarrier transmission. In *Proc. 17th European Signal Processing Conference (Eusipco)*, pages 1359–1363. IEEE, 2009. (Cited on page 66.)

[97] M. G. Bellanger. Spicification and design of prototype filter for filter bank based multicarrier transmission. In *IEEE International Confrence on Acoustic, Speech and Signal Processing*, pages 2417–2420, May 2001. (Cited on page 66.)

[98] F. Schaich, T. Wild, and Yejian Chen. Waveform contenders for 5G - suitability for short packet and low latency transmissions. In *Proc. IEEE 79th Vehicular Technology Conference (VTC Spring)*, pages 1–5, May 2014. (Cited on page 67.)

[99] M. Bellanger. Efficiency of filter bank multicarrier techniques in burst radio transmission. In *Proc. IEEE Global Telecommunications Conference (GLOBECOM)*, pages 1–4, Dec 2010. (Cited on page 67.)

[100] B. Farhang-Boroujeny. OFDM versus filter bank multicarrier. *IEEE Signal Processing Magazine*, 28(3):92–112, May 2011. (Cited on page 67.)

[101] R. Zakaria and D. Le Ruyet. A novel FBMC scheme for spatial multiplexing with maximum likelihood detection. In *Proc. 7th International Symposium on Wireless Communication Systems (ISWCS)*, pages 461 –465, sept. 2010. (Cited on page 67.)

[102] R. Zakaria and D. Le Ruyet. Theoretical analysis of the power spectral density for FFT-FBMC signals. *IEEE Communications Letters*, 20(9):1748–1751, Sept 2016. (Cited on page 68.)

[103] R. Zakaria and D. Le Ruyet. FFT-FBMC equalization in selective channels. *IEEE Signal Processing Letters*, PP(99):1–1, 2017. (Cited on page 68.)

[104] D. Demmer, R. Gerzaguet, J. B. Doré, D. Le Ruyet, and D. Kténas. Block-Filtered OFDM: an exhaustive waveform to overcome the stakes of future wireless technologies. In *Proc. IEEE International Conference on Communications (ICC)*, Paris, France, May 2017. (Cited on page 68.)

[105] C. Lélé, P. Siohan, and R. Legouable. The Alamouti scheme with CDMA-OFDM/OQAM. *EURASIP Journal on Advances in Signal Processing*, 2010(1):703513, 2010. (Cited on page 68.)

[106] R. Zakaria and D. Le Ruyet. Intrinsic interference reduction in a filter bank-based multicarrier using QAM modulation . *Physical Communication*, 2014. (Cited on page 68.)

[107] R. Zakaria, D. Le Ruyet, and Y. Medjahdi. On ISI cancellation in MIMO-ML detection using FBMC/QAM modulation. In *Proc. IEEE International Symposium on Wireless Communication Systems (ISWCS)*, pages 949 –953, aug. 2012. (Cited on page 68.)

[108] O. E. Agazzi and N. Seshadri. On the use of tentative decisions to cancel intersymbol interference and nonlinear distortion (with application to magnetic recording channels). *IEEE Transactions on Information Theory*, 43(2):394 –408, mar 1997. (Cited on page 68.)

[109] S. Van Beneden, J. Riani, and J.W.M. Bergmans. Cancellation of linear intersymbol interference for two-dimensional storage systems. In *IEEE International Conference on Communications (ICC)*, volume 7, pages 3173 –3178, june 2006. (Cited on page 68.)

[110] N. Michailow, I. Gaspar, S. Krone, M. Lentmaier, and G. Fettweis. Generalized frequency division multiplexing: Analysis of an alternative multi-carrier technique for next generation cellular systems. In *International Symposium on Wireless Communication Systems (ISWCS)*, pages 171–175, Aug 2012. (Cited on page 68.)

[111] N. Michailow, S. Krone, M. Lentmaier, and G. Fettweis. Bit error rate performance of generalized frequency division multiplexing. In *Proc. IEEE Vehicular Technology Conference (VTC Fall)*, pages 1–5, Sept 2012. (Cited on page 69.)

[112] S. G. Krantz. *Handbook of complex variables*. Birkhäuser Basel, 1999. (Cited on page 75.)

[113] H. Gerstacker, R. Schober, and A. Lampe. Receivers with widely linear processing for frequency-selective channels. *IEEE Transactions on Communications*, 51(9):1512–1523, 2003. (Cited on page 78.)

[114] R. Dayana and R. Kumar. Co-operative cyclo-stationary feature detection with universal filtered multi-carrier spectrum sensing for cognitive radio network. In *2016 IEEE International Conference on Recent Trends in Electronics, Information Communication Technology (RTEICT)*, pages 1647–1650, May 2016. (Cited on pages 78 and 80.)

[115] V. Lazov and G. Vandersteen. Cyclo-stationary process analysis within telecom applications. In *2016 IEEE International Instrumentation and Measurement Technology Conference Proceedings*, pages 1–6, May 2016. (Cited on pages 78 and 80.)

[116] P. Chevalier, J. P. Delmas, and R. Chauvat. Reception filter impact on widely linear fresh receiver performance for SAIC/MAIC with frequency offsets. In *2016 IEEE Sensor Array and Multichannel Signal Processing Workshop (SAM)*, pages 1–5. IEEE, 2016. (Cited on pages 78 and 80.)

[117] R. Chauvat, P. Chevalier, and J. P. Delmas. Widely linear fresh receiver for saic/maic with frequency offsets. In *2015 International Symposium on Wireless Communication Systems (ISWCS)*, pages 536–540. IEEE, 2015. (Cited on pages 78 and 80.)

[118] M. Elgenedy, M. Sayed, N. Al-Dhahir, and R. C. Chabaan. Cyclostationary noise mitigation for simo powerline communications. *IEEE Access*, 6:5460–5484, 2018. (Cited on page 78.)

[119] Z. E. Ankarali, B. Peköz, and H. Arslan. Flexible radio access beyond 5G: a future projection on waveform, numerology, and frame design principles. *IEEE Access*, 5:18295–18309, 2017. (Cited on page 78.)

[120] A. Ikhlef and J. Louveaux. An enhanced mmse per subchannel equalizer for highly frequency selective channels for fbmc/oqam systems. In *2009 IEEE 10th Workshop on Signal Processing Advances in Wireless Communications*, pages 186–190. IEEE, 2009. (Cited on page 79.)

[121] B. Picinbono and P. Chevalier. Widely linear estimation with complex data. *IEEE transactions on Signal Processing*, 43(8):2030–2033, 1995. (Cited on page 79.)

[122] W. A. Gardner. Cyclic wiener filtering: theory and method. *IEEE Transactions on communications*, 41(1):151–163, 1993. (Cited on page 80.)

[123] G.T. Zhou and R. Raich. Spectral analysis of polynomial nonlinearity with applications to rf power amplifiers. *EURASIP Journal on Applied Signal Processing*, 2004(256395):1931–1840, 2004. (Cited on pages 85, 87, 95 and 98.)

[124] J. H. K. Vuolevi, T. Rahkonen, and J. P. A. Manninen. Measurement technique for characterizing memory effects in the rf power amplifiers. *IEEE Trans. on Microw. Theory and Tech*, 49(8):1383–1380, 2001. (Cited on pages 85 and 87.)

[125] W. Bosch and G. Gatti. Measurement and simulation of memory effects in predistortion linearizers. *IEEE Trans. on Microw. Theory and Tech*, 37(12):1885–1890, 1989. (Cited on page 85.)

[126] C. Rapp. Effects of HPA nonlinearity on 4-DPSK-OFDM signal for digital sound broadcasting systems. *2nd European Conference on Satellite Communications*, pages 38–45, Oct. 1991. (Cited on page 88.)

[127] A. A. Saleh. Frequency-independent and frequency-dependent nonlinear models of TWT amplifiers. *IEEE Transactions on Communications*, 29(11):1715–1720, Nov. 1981. (Cited on page 88.)

[128] J. J. Bussgang. *Crosscorrelation functions of amplitude-distorted gaussian signals.* Research laboratory of electronics, Massachusetts Institute of Technology, Cambridge, 1952. (Cited on page 88.)

[129] D. Dardari, V. Tralli, and A. Vaccari. A Theoretical characterization of nonlinear distortion effects in OFDM systems. *IEEE transactions on Communications*, 48(10):1755–1764, October 2000. (Cited on pages 88 and 89.)

[130] R. Raich, H. Qian, and G.T. Zhou. Orthogonal polynomials for power amplifier modeling and predistorter design. *IEEE transactions on Vehicular Technologies*, 53:1468–1479, September 2004. (Cited on page 89.)

[131] R. Zayani, H. Shaiek, D. Roviras, and Y. Medjahdi. BER analysis of FBMC-OQAM systems with phase estimation error. *IET Communications*, 11(15):2269–2273, January 2017. (Cited on page 92.)

[132] J. G. Proakis. *Digital Communications.* 5th ed. McGrawHill, New York, 2001. (Cited on page 93.)

[133] T. Ihalainen, T. H. Stitz, and M. Renforse. Channel equalization in filter bank based multicarrier modulation for wireless communications. *EURASIP Journal on Advances in Signal Processing*, 2007(049389), 2007. (Cited on page 95.)

[134] A. Skrzypczak, P. Siohan, and J-P. Javaudin. Power Spectral Density and Cubic Metric for the OFDM/OQAM Modulation. In *in Proc. of ISSPIT*, Vancouver, Canada, Sep. 2006. (Cited on pages 95 and 96.)

[135] S. Benedetto and E. Biglieri. *Principles of digital transmission with wireless applications.* Kluwer Academic/Plenum Publishers, New York, 1999. (Cited on page 96.)

[136] G. T. Zhou, H. Qian, L Ding, and R. Raich. On baseband representation of a bandpass nonlinearity. *IEEE Transactions on Signal Processing*, 53(8):2953–2957, 2005. (Cited on page 96.)

[137] Deliverable D 8.1. Application of the FBMC physical layer in a cognitive radio scenario. Technical report, FP 7 PHYDYAS Project, www.ict-phydyas.org 2019. (Cited on page 97.)

[138] H. Cramer. *Mathematical methods of statistics.* Princeton University Press, UK, 1946. (Cited on page 98.)

[139] R. A. Fisher and J. J. Wishart. The derivation of the pattern formulae of two-way partitions from those of simpler patterns. In *Proceedings of the London Mathematical Society*, 1932. (Cited on page 98.)

[140] K. C. Bulusu. *Performance analysis and PAPR reduction techniques for filter-bank based multi-carrier systems with non-linear power amplifiers.* PhD thesis, 2016. (Cited on page 99.)

[141] H. G. Ryu, B. I. Jin, and I. B. Kim. PAPR reduction using soft clipping and ACI rejection in OFDM system. *IEEE Transactions on Consumer Electronics*, 48(1):17–22, Aug. 2002. (Cited on page 101.)

[142] J. Tellado. *Multicarrier Modulation with Low PAR: Applications to DSL and Wirelesss.* Kluwer Academic Publishers, 2000. (Cited on page 101.)

[143] J. Tellado. *Peak to average ratio Rreduction for multi-carrier modulation.* PhD thesis, Stanford University, Stanford, CA, USA, Sep. 1999. (Cited on page 101.)

[144] Z. X. Yang, H. D. Fang, and C. Y. Pan. ACE with frame interleaving scheme to reduce peak-to-average power ratio in OFDM systems. *IEEE Transactions on Broadcasting*, 51(41):571–575, Mar. 2005. (Cited on page 101.)

[145] S. H. Muller and J. B. Huber. OFDM with reduced peak-to-average power ratio by optimum combination of partial transmit sequences. *IEEE Electronics Letters*, 33(5):368—-369, Feb. 1997. (Cited on page 101.)

[146] R. W. Bauml, R. F. H. Fischer, and J. B. Huber. Reducing the peak-to-average power ratio of multicarrier modulation by selected mapping. *IEEE Electronics Letters*, 32(22):2056–2057, Oct. 1996. (Cited on page 101.)

[147] T. A. Wilkinson and A. E. Jones. Minimisation of the peak-to-mean envelope power ratio of multicarrier transmission schemes by block coding. *IEEE Vehicular Technology Conference*, 2:925–829, Feb. 1995. (Cited on page 101.)

[148] H. S. Hee and L. J. Hong. An overview of peak-to-average power ratio reduction techniques for multicarrier transmission. *IEEE Transactions on Wireless Communications*, 12(2):56–65, Apr. 2005. (Cited on page 101.)

[149] T. Jiang and Y. Wu. An overview: Peak-to-average power ratio of OFDM signals. *IEEE Transactions on Broadcasting*, 54(2):257–268, Jun. 2008. (Cited on page 101.)

[150] P. Kenington. *High-linearity* RF *amplifier design.* Artech House, Boston, 2000. (Cited on page 102.)

[151] A. Katz, J. Wood, and D. Chokola. The evolution of PA linearization. 17(2):32–40, February 2016. (Cited on page 102.)

[152] K. Bulusu, H. Shaiek, and D. Roviras. Reducing the PAPR in FBMC-OQAM systems with Low Latency Trellis-based SLM Technique. *EURASIP Journal on Advances in Signal Processing*, pages 1–18, 2016. (Cited on page 104.)

[153] R. Bellamen. *Applied dynamic programming.* Princeton, 1962. (Cited on page 106.)

[154] J. Tellado and J. Cioffi. Peak power reduction for multicarrier transmission. *IEEE CTMC, GLOBECOM*, Nov. 1998. (Cited on page 106.)

[155] A. Gatherer and M. Polley. Controlling clipping probability in DMT transmission. *Asilomar Conference record*, 1:578—-584, Nov. 1997. (Cited on page 106.)

[156] P. B. Kenington. *High-linearity RF amplifier design.* Artech house, 2000. (Cited on page 107.)

[157] F. M. Ghannouchi and O. Hammi. Behavioral modeling and predistortion. *IEEE Microwave Magazine*, 10(7):52–64, 2009. (Cited on page 107.)

[158] S. Boumaiza, J. Li, M. Jaidane-Saidane, and F. M. Ghannouchi. Adaptive digital/RF predistortion using a nonuniform LUT indexing function with built-in dependence on the amplifier nonlinearity. *IEEE Transactions on Microwave Theory Techniques*, 52(12):2670–2677, 2004. (Cited on page 107.)

[159] R. Zayani, Y. Medjahdi, H. Bouhadda, H. Shaiek, D. Roviras, and R. Bouallegue. Adaptive predistortion techniques for non-linearly amplified FBMC-OQAM signals. In *2014 IEEE 79th Vehicular Technology Conference (VTC Spring)*, pages 1–5, 2014. (Cited on page 107.)

[160] O. A. Gouba and Y. Louet. Digital predistortion expressed as an adding signal technique in OFDM context. *IEEE International New Circuits and Systems Conference*, pages 1–4, Jun. 2013. (Cited on page 107.)

[161] Pasternack PE15A4017. Accessed: Jun. 10, 2018. [online]. available: https://www.pasternack.com/images/productpdf/pe15a4017.pdf. Technical report. (Cited on pages 112 and 116.)

[162] T. Jiang, C. Ni, C. Xu, and Q. Qi. Curve fitting based tone reservation method with low complexity for papr reduction in ofdm systems. *IEEE Communications Letters*, 18(5):805–808, 2014. (Cited on page 113.)

[163] USRP-2942 Specifications. Accessed: Jun. 10, 2018. [online]. available: https://www.ni.com/pdf/manuals/374410d.pdf. Technical report. (Cited on page 115.)

[164] P. Garcia-Dúcar, J. de Mingo, P. L. Carro, and A. Valdovinos. Design and experimental evaluation of a LINC transmitter for OFDM systems. *IEEE Transactions on Wireless Communications*, 2010. (Cited on page 117.)

[165] A. Sahin and H. Arslan. Multi-User Aware Frame Structure for OFDMA Based System. In *2012 IEEE Vehicular Technology Conference (VTC Fall)*, pages 1–5, Sep. 2012. (Cited on page 123.)

[166] S. Lien, S. Shieh, Y. Huang, B. Su, Y. Hsu, and H. Wei. 5G New Radio: Waveform, frame Structure, multiple access, and initial access. *IEEE Communications Magazine*, 55(6):64–71, Jun. 2017. (Cited on page 123.)

[167] P. Guan, D. Wu, T. Tian, J. Zhou, X. Zhang, L. Gu, A. Benjebbour, M. Iwabuchi, and Y. Kishiyama. 5G field trials: Ofdm-based waveforms and mixed numerologies. *IEEE Journal on Selected Areas in Communications*, 35(6):1234–1243, Jun. 2017. (Cited on page 123.)

[168] L. Zhang, A. Ijaz, P. Xiao, A. Quddus, and R. Tafazolli. Subband filtered multi-carrier systems for multi-service wireless communications. *IEEE Transactions on Wireless Communications*, 16(3):1893–1907, Mar. 2017. (Cited on pages 123 and 124.)

[169] L. Zhang, A. Ijaz, P. Xiao, and R. Tafazolli. Multi-service system: An enabler of flexible 5G Air Interface. *IEEE Communications Magazine*, 55(10):152–159, Oct. 2017. (Cited on page 123.)

[170] A. Yazar and H. Arslan. Reliability enhancement in multi-numerology-based 5G new radio using INI-aware scheduling. *EURASIP Journal on Wireless Communications and Networking*, 2019(1):110, May 2019. (Cited on page 123.)

[171] X. Zhang, L. Zhang, P. Xiao, D. Ma, J. Wei, and Y. Xin. Mixed numerologies interference analysis and inter-numerology interference cancellation for windowed ofdm systems. *IEEE Transactions on Vehicular Technology*, 67(8):7047–7061, Aug. 2018. (Cited on pages 123, 124 and 125.)

[172] A. B. Kihero, M. S. J. Solaija, A. Yazar, and H. Arslan. Inter-numerology interference analysis for 5G and beyond. In *2018 IEEE Globecom Workshops (GC Wkshps)*, pages 1–6, Dec. 2018. (Cited on page 123.)

[173] S. Rajagopal and M. S. Rahman. Multi-user MIMO with flexible numerology for 5G. *CoRR*, abs/1610.03056, 2016. (Cited on pages 123 and 125.)

[174] J. Choi, B. Kim, K. Lee, and D. Hong. A transceiver design for spectrum sharing in mixed numerology environments. *IEEE Transactions on Wireless Communications*, 18(5):2707–2721, May 2019. (Cited on page 123.)

[175] E. G. Larsson, O. Edfors, F. Tufvesson, and T. L. Marzetta. Massive MIMO for next generation wireless systems. *IEEE Communications Magazine*, 52(2):186–195, Feb. 2014. (Cited on page 129.)

[176] J. Vieira, F. Rusek, O. Edfors, S. Malkowsky, L. Liu, and F. Tufvesson. Reciprocity calibration for massive MIMO: Proposal, modeling, and validation. *IEEE Transactions on Wireless Communications*, 16(5):3042–3056, May 2017. (Cited on page 129.)

[177] 3GPP TR 38.901. Study on channel model for frequencies from 0.5 to 100 GHz (Release 14). Technical report, 3GPP, 2018. (Cited on pages 130 and 132.)

[178] J. Guerreiro, R. Dinis, and P. Montezuma. Massive MIMO with nonlinear amplification: Signal characterization and performance evaluation. In *2016 IEEE Global Communications Conference (GLOBECOM)*, pages 1–6. IEEE, 2016. (Cited on page 133.)

[179] A. A. Khan, P. Uthansakul, P. Duangmanee, and M. Uthansakul. Energy efficient design of massive mimo by considering the effects of nonlinear amplifiers. *Energies*, 11(5):1045, 2018. (Cited on page 133.)

[180] C. Mollén, U. Gustavsson, T. Eriksson, and E. G. Larsson. Spatial characteristics of distortion radiated from antenna arrays with transceiver nonlinearities. *IEEE Transactions on Wireless Communications*, 17(10):6663–6679, 2018. (Cited on page 133.)

[181] S. F. Mohammed, A. Chockalingam, and B. S. Rajan. A low-complexity precoder for large multiuser miso systems. In *VTC Spring 2008-IEEE Vehicular Technology Conference*, pages 797–801. IEEE, 2008. (Cited on page 133.)

[182] C. Siegl and R. FH. Fischer. Selected basis for par reduction in multi-user downlink scenarios using lattice-reduction-aided precoding. *EURASIP Journal on advances in signal processing*, 2011(1):1–11, 2011. (Cited on page 133.)

[183] H. Prabhu, O. Edfors, J. Rodrigues, L. Liu, and F. Rusek. A low-complex peak-to-average power reduction scheme for OFDM based massive MIMO systems. In *2014 6th international symposium on communications, control and signal processing (ISCCSP)*, pages 114–117. IEEE, 2014. (Cited on page 133.)

[184] C. Ni, Y. Ma, and T. Jiang. A novel adaptive tone reservation scheme for PAPR reduction in large-scale multi-user MIMO-OFDM systems. *IEEE Wireless Communications Letters*, 5(5):480–483, 2016. (Cited on page 133.)

[185] H. Bao, J. Fang, Q. Wan, Z. Chen, H. Li, and S. Li. An efficient Bayesian PAPR reduction method for OFDM-based massive MIMO systems. *IEEE Transactions on Wireless Communications*, 15(6):4183–4195, 2016. (Cited on page 133.)

[186] H. Bao, J. Fang, Q. Wan, Z. Chen, and T. Jiang. An ADMM approach for PAPR reduction for large-scale MIMO-OFDM systems. *IEEE Transactions on Vehicular Technology*, 67(8):7407–7418, 2018. (Cited on page 133.)

[187] R. Zayani, H. Shaïek, and D. Roviras. PAPR-Aware Massive MIMO-OFDM Downlink. *IEEE Access*, 7:25474–25484, 2019. (Cited on pages 133 and 135.)

[188] R. Zayani, H. Shaïek, and D. Roviras. Efficient precoding for massive MIMO downlink under PA nonlinearities. *IEEE Communications Letters*, 23(9):1611–1615, 2019. (Cited on pages 133 and 136.)

[189] H. Sun, J. Guo, and L. Fang. Improved singular value decomposition (TopSVD) for source number estimation of low SNR in blind source separation. *IEEE Access*, 5:26460–26465, 2017. (Cited on page 135.)

[190] C. X. Wang, F. Haider, X. Gao, X. H. You, Y. Yang, D. Yuan, H. M. Aggoune, H. Haas, S. Fletcher, and E. Hepsaydir. Cellular architecture and key technologies for 5g wireless communication networks. *IEEE Communications Magazine*, 52(2):122–130, 2014. (Cited on page 146.)

[191] L. Wei, R. Q. Hu, Y. Qian, and G. Wu. Key elements to enable millimeter wave communications for 5g wireless systems. *IEEE Wireless Communications*, 21(6):136–143, 2014. (Cited on page 146.)

[192] S. Bicaïs and J. B. Doré. Design of digital communications for strong phase noise channels. *IEEE Open Journal of Vehicular Technology*, 1:227–243, 2020. (Cited on page 146.)

[193] M. Saad, A. C. Al Ghouwaye, H. Hijazi, F. Bader, and J. Palicot. Mimo techniques for wireless terabits systems under sub-thz channel with rf impairments. In *2020 IEEE International Conference on Communications Workshops (ICC Workshops)*, pages 1–6, 2020. (Cited on page 146.)

[194] FCC takes steps to open spectrum horizons for new services and technologies. Technical report, FCC News Release, 2019. (Cited on page 146.)

[195] R. W. Heath, N. González-Prelcic, S. Rangan, W. Roh, and A. M. Sayeed. An overview of signal processing techniques for millimeter wave mimo systems. *IEEE Journal of Selected Topics in Signal Processing*, 10(3):436–453, 2016. (Cited on page 146.)

[196] E. G. Larsson, O. Edfors, F. Tufvesson, and T. L. Marzetta. Massive mimo for next generation wireless systems. *IEEE Communications Magazine*, 52(2):186–195, 2014. (Cited on page 146.)

[197] J. Zhang, L. Dai, X. Li, Y. Liu, and L. Hanzo. On Low-resolution ADCs in practical 5G millimeter-wave massive MIMO systems. *IEEE Communications Magazine*, 56(7):205–211, 2018. (Cited on page 147.)

[198] D. Zhao and P. Reynaert. A 60-GHz dual-mode Class AB power amplifier in 40-nm CMOS. *IEEE Journal of Solid-State Circuits*, 48(10):2323–2337, 2013. (Cited on page 147.)

[199] S. Bicais and J. B. Doré. Phase noise model selection for Sub-THz Communications. In *2019 IEEE Global Communications Conference (GLOBECOM)*, pages 1–6, 2019. (Cited on page 147.)

[200] L. Fan, Y. Li, and M. Zhao. Joint IQ imbalance and PA nonlinearity pre-distortion for highly integrated millimeter-wave transmitters. In *2014 IEEE Globecom Workshops (GC Wkshps)*, pages 399–404, 2014. (Cited on page 147.)

[201] C. Yu, Q. Lu, H. Sun, X. Wu, and X. W. Zhu. Digital predistortion of Ultra-Broadband mmWave power amplifiers with limited Tx/Feedback loop/baseband bandwidth. *Wireless Communications and Mobile Computing*, 2018. (Cited on page 147.)

[202] O. Hammi, M. Younes, and F. M. Ghannouchi. Metrics and methods for benchmarking of RF transmitter behavioral models with application to the development of a hybrid memory polynomial model. *IEEE Transactions on Broadcasting*, 56(3):350–357, 2010. (Cited on page 147.)

[203] N. Y. Ermolova and O. Tirkkonen. Theoretical characterization of memory polynomial models with gaussian inputs. *IEEE Signal Processing Letters*, 16(8):651–654, Aug 2009. (Cited on page 147.)

[204] J. E. Mazo. Faster-than-nyquist signaling. *The Bell System Technical Journal*, 54(8):1451–1462, 1975. (Cited on page 148.)

[205] R. Hadani and A. Monk. OTFS: A new generation of modulation addressing the challenges of 5G. *arXiv preprint arXiv:1802.02623*. (Cited on page 148.)

[206] K. Tourki, R. Zakaria, and M. Debbah. Lagrange vandermonde division multiplexing. In *ICC 2020 - 2020 IEEE International Conference on Communications (ICC)*, pages 1–6, 2020. (Cited on page 148.)

[207] J. A. Lucciardi, N. Thomas, M. L. Boucheret, C. Poulliat, and G. Mesnager. Trade-off between spectral efficiency increase and PAPR reduction when using FTN signaling: Impact of non linearities. In *2016 IEEE International Conference on Communications (ICC)*, pages 1–7, 2016. (Cited on page 148.)

[208] J. Vanschoren. Meta-learning : A survey. *arXiv preprint arXiv :1810.03548*, 2018. (Cited on page 149.)

[209] T. O'Shea and J. Hoydis. An introduction to deep learning for the physical layer. *IEEE Transactions on Cognitive Communications and Networking*, 3(4):563–575, 2017. (Cited on page 149.)

[210] M. Vahdat, K. P. Roshandeh, M. Ardakani, and H. Jiang. PAPR reduction scheme for deep learning-based communication systems using autoencoders. In *2020 IEEE 91st Vehicular Technology Conference (VTC2020-Spring)*, pages 1–5, 2020. (Cited on page 149.)

[211] L. N. Ribeiro, S. Schwarz, M. Rupp, and A. L. F. De Almeida. Energy efficiency of mmwave massive mimo precoding with low-resolution dacs. *IEEE Journal of Selected Topics in Signal Processing*, 12(2):298–312, 2018. (Cited on page 150.)

[212] M. Di Renzo, A. Zappone, M. Debbah, M. S. Alouini, C. Yuen, J. De Rosny, and S. Tretyakov. Smart radio environments empowered by reconfigurable intelligent surfaces: How it works, state of research, and the road ahead. *IEEE Journal on Selected Areas in Communications*, 38(11):2450–2525, 2020. (Cited on page 150.)

[213] M. H. Dahri, M. I. Abbasi, M. H. Jamaluddin, and M. R. Kamarudin. A Review of high gain and high efficiency reflectarrays for 5G communications. *IEEE Access*, 6:5973–5985, 2018. (Cited on page 150.)

[214] A. Clemente, L. D. Palma, F. Diaby, L. Dussopt, K. Pham, and R. Sauleau. Electronically-steerable transmitarray antennas for Ka-Band. In *2019 13th European Conference on Antennas and Propagation (EuCAP)*, pages 1–4, 2019. (Cited on page 150.)

[215] D. C. Sawyer, D. Sell, R. P. Jenkins, E. B. Whiting, J. A. Fan, and H. W. Douglas. Review of numerical optimization techniques for meta-device design. *Opt. Mater. Express*, 9(4):1842–1863, Apr 2019. (Cited on page 151.)

[216] M. Giordani, M. Polese, A. Roy, D. Castor, and M. Zorzi. A Tutorial on beam management for 3GPP NR at mmWave frequencies. *IEEE Communications Surveys Tutorials*, 21(1):173–196, 2019. (Cited on page 151.)

Multi-carrier waveforms for 5G and beyond systems: from PA impairments to energy efficiency enhancement

Abstract: This report draws my professional career by focusing on the activities carried since 2011. The first part is an extended Curriculum Vitae presenting various information about my research activities, namely the supervision, publications, collaborations as well as the research projects in which I have been involved.

In the second part of this report, which is structured in six chapters, I presented the research activities carried as associate professor at CNAM. During this period I have been working on post-Orthogonal Frequency Division Multiplexing (OFDM) Multi-Carrier Waveforms (MWFs) for 5G and beyond systems, with important efforts to characterize and mitigate power amplifier (PA) distortions in Single Input Single Output (SISO) and massive Multiple Input Multiple Output (MIMO) scenarios. For each research activity, I have presented the projects under which the work has been carried, along with the different collaborations carried out, the main achievements and related publications.

As a first research direction, I worked, within the framework of the ANR WONG5 national research project, on the study and proposal of the most suitable post-OFDM waveforms for critical machine type communications. This use case is one of the scenarios envisioned in future 5G communications and requires extra reduced latency, below 1 ms, as well as relaxed constraint on users synchronization. As this later constraint can difficulty be fulfilled with conventional 4G/5G CP-OFDM waveform, I contributed to the study and proposal of alternative solutions based on windowing/filterinfg the transmitted/received signals. In parallel to this study, I focused on advanced equalization structures for FBMC-OQAM over frequency selective channels.

The time domain signals from the vast majority of the MWFs candidate for 5G exhibit significant fluctuations in instantaneous power compared to the average power, characterized by the Peak to Average Power ratio (PAPR). This characteristic makes these MWFs very sensitive to the non-linearities induced by the Radio Frequency (RF) power amplifiers. As a second research topic, I focused on the characterization of the In-Band (IB) and Out-Of-Band (OOB) distortions induced by memoryless measured or modeled PA. The carried studies made it possible to characterize the transmission errors as well as the induced spectral regrowth. This information is essential for engineers working on RF chain specifications for 5G and beyond systems.

The high PAPR of MWFs strongly compromises the energy efficiency of 4G, 5G and beyond systems. As a third research topic, I proposed solutions to improve the energy efficiency of several post-OFDM MWFs based transceivers. The first family of the proposed solutions aims to reduce the PAPR and/or pre-distort the signal before amplification in a dissociated or joint manner. The second approach that we have proposed, to improve the energy efficiency of post-OFDM MWFs, modifies the architecture of the PA and splits the multi-carrier signal into several sub-signals with lower PAPRs which can be amplified with better energy efficiency.

Among the prominent technologies proposed to reach the 5G New Radio (NR) requirements, massive MIMO and mixed numerology have been retained to support various configurations on top of OFDM waveform. In this direction, we proposed a first contribution related to the analysis and cancellation of the interference caused by users using different numerologies in massive MIMO OFDM systems. Another contribution that we made, in this field, is the proposal of low complexity energy efficient emitters architectures combining MIMO precoding, PAPR reduction and Digital Pre-Distortion (DPD).

As future works, I intend to focus on the design of new waveforms for 6G systems, as well as the proposal of solutions to improve the energy efficiency of transceivers in mmWaves, sub-THz and THz bands. These solutions can be based on advanced learning techniques or on Reconfigurable Intelligent Surfaces (RIS).

Keywords: 5G & beyond systems, multi-carrier waveforms, power amplifiers, energy efficiency, PAPR reduction, digital pre-distortion, MIMO, mixed numerology, deep learning, reconfigurable intelligent surfaces.